— INTERNATIONAL SOCIETY FOR —
ISMRM
MAGNETIC RESONANCE IN MEDICINE

ONE
COMMUNITY
FOR CLINICIANS
AND SCIENTISTS

Footprints of the **ISMRM** in the MR Path

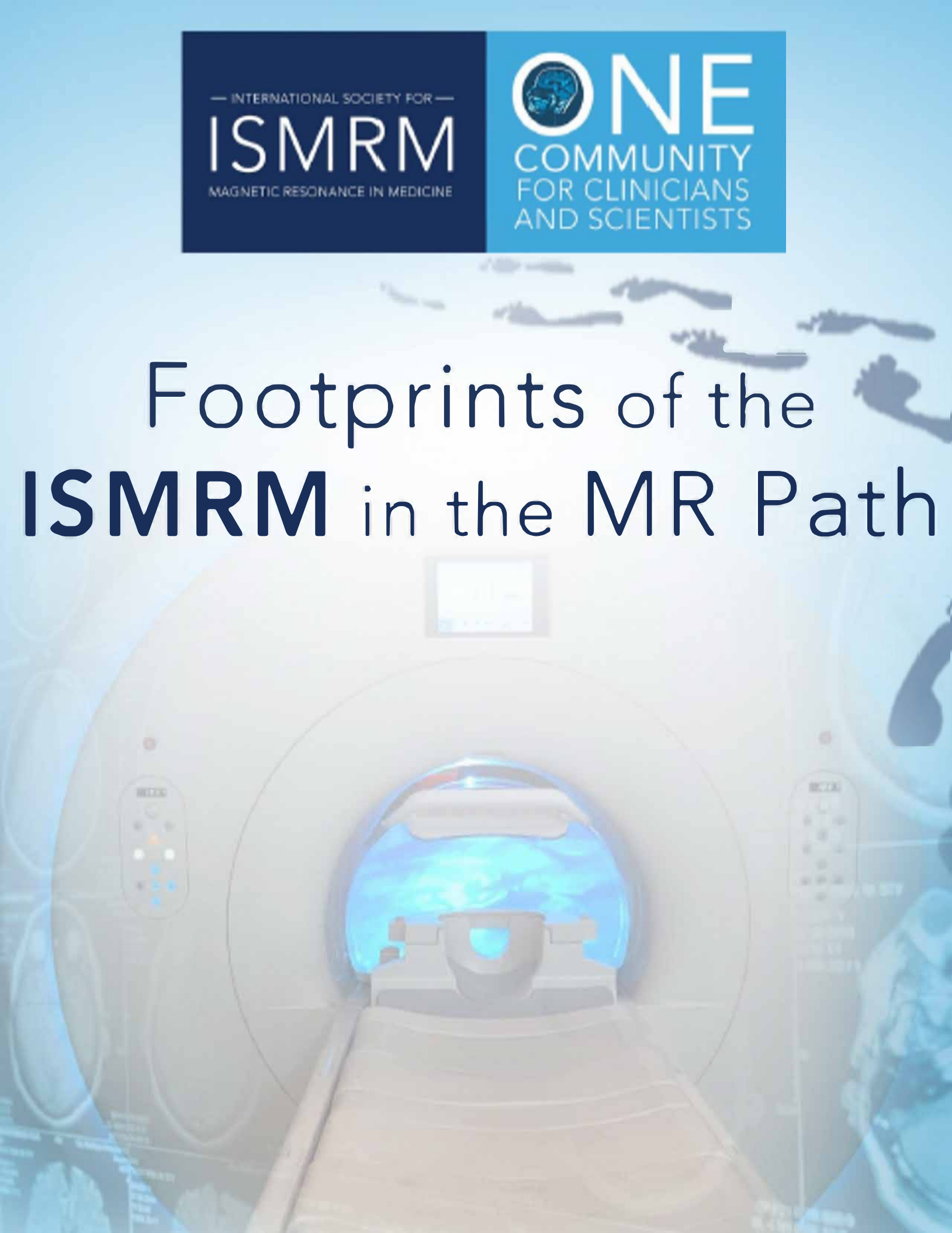

The Annual Meetings of the ISMRM (and its predecessor Societies, the Society of Magnetic Resonance in Medicine, SMRM, and the Society of Magnetic Resonance Imaging, SMRI) go all the way back to 1982, which was the year the 1st SMRM Annual Meeting took place in Boston, USA (August 16–18, 1982); 1983 was the year of the 1st SMRI Annual Meeting (Colorado Springs, USA). The Proceedings of all these historical meetings are now available online on the ISMRM website. These Proceedings provide an amazing footprint in the arc of our history as a Society, and the importance of our Annual Meetings as the avenue of choice for presenting new MR methods, tools, and applications of aspects of our field that have greatly impacted and transformed how MR is used today, and which have become 'classic' contributions. This is something the ISMRM should be very proud of, testimony to the role we have played helping MR leaders shape our field. It is indeed at our Annual Meetings where MR advances are most often first shown and/or conceived.

As it is often said, you must look at the past if you want to understand the future; by exploring the influential aspects of our past, it can help us envision what the future may look like and inspire us to dream high about it.

The project has involved broad consultation and led to a shortlist of 100 'classic' abstracts to celebrate the 40th anniversary of the Annual Meetings. If one thinks that we have well over 100,000 abstracts having been presented at our Annual Meetings over the years, the task of selecting a shortlist of 'classics' is indeed daunting. This is by no means "the list" of classics, but just the start of this project – a first trailer of our history.

After working on this project, I feel a bit like archaeologists from old times who had just discovered a new site, and the more they searched, the more amazing and influential material they found! This is just the start of our journey to unearth the footprints of ISMRM in the MR path, and there will be a follow up project(s) to address some of the gaps and diversity aspects we identified on the list.

We hope you will enjoy reading this collection.

Kind regards,

Fernando Calamante

2021-2022 ISMRM President

Year	Page / Abstract number	Authors	First Author's Institute	Title
1982	SMRM, p24	Brasch RC, Nitecki DE, London D, Tozer TN, Doemeny J, Tuck LD, Wolff S	University of California San Francisco, US	Evaluation of nitroxide stable free radicals for contrast enhancement in NMR imaging
1982	SMRM, p94	Mansfield P, Ordidge RJ, Rzedzian RR, Doyle M, Guilfoyle D	University of Nottingham, UK	Real-time dynamic imaging by NMR
1982	SMRM, p102	Maudsley AA, Hilal SK, Simon HE, Perman WH	Columbia University, US	Multinuclear NMR imaging
1982	SMRM, p105	Mendonça Dias MH, Lauterbur PC, Brown EJ	State University of New York at Stony Brook, US	The use of paramagnetic contrast agents in NMR imaging II: In vivo studies
1983	SMRM, p116	Edelstein WA, Mueller OM, Bottomley PA, Hart HR, Schenck JF, Smith LS, O'Donnel M, Leue WM, Redington RW	GE, US	NMR images of the whole human trunk at 64 MHz.
1983	SMRM, p230	Maudsley AA, Hilal SK, Simon HE, Wittekoek S	Columbia University, US	Multinuclear applications of chemical shift imaging
1984	SMRM, p63	Bottomley PA	GE, US	RF power deposition in NMR imaging
1984	SMRM, p74	Bottomley PA, Foster TE, Vatis D, Darrow RD, Mueller OM, Edelstein WA, Hardy CJ	GE, US	Depth resolved surface coil spectroscopy (DRESS) for in vivo 1H, 31P, and 13C NMR.
1984	SMRM, p193	Dixon WT, Faul DD	Washington University in St. Louis, US	Proton spectroscopic imaging at 0.35T
1984	SMRM, p291	Haase A, Frahm J, Hänicke W, Matthaei D	Max-Planck Institute, DE	Chemical shift selection (CHESS) imaging
1984	SMRM, p342	Hoult DI, Silver MS, Joseph RI	NIH, US	A highly selective 180° pulse
1984	SMRM, p559	Norris DG	University of Aberdeen, UK	Phase encoded NMR flow imaging
1985	SMRM, p618	Wedeen VJ, Rosen BR, Buxton R, Edelman, RR, Meuli R, Brady TJ	Massachusetts General Hospital, US	MRI angiography and flow volume quantification
1985	SMRM, p887	Mendonça-Dias MH, Bernardo ML, Muller RN, Acuff V, Lauterbur PC	State University of New York at Stony Brook, US	Ferromagnetic particles as contrast agents for magnetic resonance imaging
1985	SMRM, p935	Ahn CB, Rew CY, Kim JH, Nalcioglu O, Cho ZH	Korea Advanced Institute of Science, KR	A new high speed spiral-scan echo planar (SEPI) NMR imaging

1985	SMRM, p980	Haase A, Frahm J, Matthaei D, Hänicke W, Merboldt KD	Max-Planck Institute, DE	Rapid images and NMR movies
1985	SMRM, p988	Hennig J	University of Freiburg, DE	RARE-imaging: a fast imaging method for clinical routine
1985	SMRM, p1024	Margosian P	Siemens AG, DE	Faster MR imaging – imaging with half the data
1985	SMRM, p1094	Hayes CE, Edelstein WA, Schenck JF, Mueller OM, Eash M	GE, US	Highly homogeneous, efficient resonator for high field imaging
1985	SMRM, p1238	Le Bihan D, Breton E, Syrota A	Hopital d'Orsay, FR	In-vivo magnetic resonance imaging of self-diffusion
1986	SMRM, p7	Le Bihan D, Breton E, Guéron M	Ecole Polytechnique, FR	Separation of perfusion and diffusion in intra-voxel incoherent motion (IVIM) MR imaging
1987	SMRI, p107	Pattany PM, Duerk JL, McNally JM	Picker lnternatilonal, US	Motion artifact suppression technique (MAST™) in multislice MR imaging
1987	SMRM, p898	Szumowski J, Plewes DB, Dumoulin CL, Souza SP	University of Rochester, US	“SIMA” - Simultaneous multislice acquisition for magnetic resonance imaging
1988	SMRI, p38	Tasciyan T, Farzaneh F, Lee JN, Wright RC, Riederer SJ	Duke University, US	Selections of phase encodings in MR fluoroscopy
1988	SMRM, p154	Wolff SD, Balaban RS	NHLBI, US	Magnetization transfer contrast (MTC) in 1H-NMR imaging
1988	SMRM, p159	Bruhn H, Frahm J, Gyngell ML, Merboldt KD, Hänicke W, Sauter R	Max-Planck Institute, DE	Localized proton spectroscopy of patients with cerebral infarction
1988	SMRM, p237	Mansfield P, Chapman B, Coxon R, Glover P, Howseman AM, Ordidge RJ, Stehling MJ, Turner R	University of Nottingham, UK	Advances in echo-planar imaging
1988	SMRM, p653	Meyer C, Pauly J, Macovski A, Nishimura D	Stanford University, US	Simultaneous spatial and spectral selective excitation
1988	SMRM, p725	Dumoulin CL, Souza SP	GE, US	Three dimensional phase contrast angiography
1988	SMRM, p875	Roemer PB, Edelstein WA, Souza SP, Hayes CE, Mueller OM	GE, US	Simultaneous multiple surface coil NMR imaging
1989	SMRI, p434	Ehman RL, Felmlee JP, Riederer SJ, Korin HW	Mayo Clinic, US	Adaptive correction of MR motion artifacts: A method utilizing interleaved navigation echoes

1989	SMRM, p2	Axel L	University of Pennsylvania, US	Quantitative cardiac wall motion
1989	SMRM, p28	Pauly J, Conolly S, Nishimura D, Macovski A	Stanford University, US	Slice-selective excitation for very short T_2 species
1989	SMRM, p42	Cohen Y, Mintorovitch J, Chileuitt L, Pereira B, Shimizu H, Weinstein P, Moseley ME	University of California San Francisco, US	Early detection of ischemic injury: comparison of diffusion- and T2-weighted MRI and spectroscopy during regional cerebral ischemia in cats
1989	SMRM, p101	Pelc NJ, Shimakawa A, Glover GH	GE, US	Phase contrast cine MRI
1989	SMRM, p103	Keller P, Drayer B, Fram E, Williams K, Dumoulin C, Souza S	Barrow Neurological Institute, US	Initial experience with very thin slice two-dimensional MR angiography
1989	SMRM, p136	Moseley ME, Cohen Y, Mintorovitch J, Chileuitts L, Shimizu H, Tsuruda J, Norman D, Weinstein P	University of California San Francisco, US	Evidence of anisotropic self-diffusion in cat brain
1989	SMRM, p741	Ogawa S, Lee TM	AT&T Bell Labs, US	Oxygenation sensitive contrast in magnetic resonance imaging of brain at high fields
1989	SMRM, p744	Larsson, HBW, Stubgaard M, Frederiksen JL, Jensen M, Henriksen O, Paulson O	Hvidovre Hospital, DK	Quantitation of blood-brain barrier defect using MRI and Gadolinium-DTPA in acute multiple sclerosis
1989	SMRM, p805	Tofts PS, Kermode AG, Barker G	Institute of Neurology, UK	Measurement of the blood-brain barrier permeability using dynamic Gd-DTPA scanning
1990	SMRM, p432	Mugler JP, Brookeman JR	University of Virginia, US	Three-dimensional magnetization prepared rapid gradient echo (3D MP RAGE) imaging
1990	SMRM, p1289	Detre JA, Leigh JS, Williams DS, Korestsky AP	University of Pennsylvania, US	Quantitative NMR imaging of perfusion in rat brain
1991	SMRM, p115	Belliveau JW, Kennedy DN, McKinstry RC, Buchbinder BR, Weisskoff RM, Cohen MS, Vevea JM, Brady TJ, Rosen BR	Massachusetts General Hospital, US	Functional mapping of the human visual cortex by nuclear magnetic resonance imaging
1991	SMRM, p917	MacKay AL, Whittal KP, Cover KS, Li DKB, Paty DW	University of British Columbia, CA	In Vivo T_2 relaxation measurements of brain may provide myelin concentration
1992	SMRM, p104	Dumoulin CL, Souza SP, Darrow RD	GE, US	Tracking of an invasive device within an MR imaging system
1992	SMRM, p211	Meyer C, Hu B, Nishimura D, Macovski A	Stanford University, US	Fast spiral coronary artery imaging

1992	SMRM, p301	Kwong KK, Belliveau JW, Chesler DA, Goldberg IE, Stern CE, Baker JR, Weisskoff RM, Benson R, Poncelet BP, Hoppel BE, Kennedy DN, Turner R, Cohen MS, Brady TJ, Rosen BR	Massachusetts General Hospital, US	Real time imaging of perfusion change and blood oxygenation change with EPI
1992	SMRM, p302	Bandettini PA, Wong EC, Hinks RS, Tikofsky RS, Hyde JS	Medical College of Wisconsin, US	Time-course gradient-echo EPI of localized signal enhancement in the human brain during task activation
1992	SMRM, p303	Ogawa S, Tank DW, Menon R, Ellermann JM, Kim SG, Merkle H, Ugurbil K	AT&T Bell Labs, US	Functional brain mapping using MRI: Intrinsic signal changes accompanying sensory stimulation
1992	SMRM, p670	Provencher SW, Michaelis T, Hänicke W, Frahm J	Max-Planck Institute, DE	Automated determination of metabolite concentrations from localized in vivo proton NMR spectra
1992	SMRM, p1221	Basser PJ, Le Bihan D	NIH, US	Fiber orientation mapping in an anisotropic medium with NMR diffusion spectroscopy
1992	SMRM, p4803	Ishihara Y, Calderon A, Watanabe H, Mori K, Okamoto K, Suzuki Y, Sato K, Kuroda K, Nakagawa N, Tsutsumi S	Toshiba, JP	A precise and fast temperature mapping using water proton chemical shift
1993	SMRM, p249	Warach S, Wielopolski P, Edelman RR	Beth Israel Hospital, US	Identification and characterization of the ischemic penumbra of acute human stroke using echo planar diffusion and perfusion imaging
1993	SMRM, p710	Liang ZP, Lauterbur PC	University of Illinois at Urbana-Champaign, US	(k, t)-space sampling considerations for imaging of time-varying functions
1994	SMR, p72	Warach S, Darby DG, Thangaraj DV, Nobre AC, Sanes JA, Edelman RR	Beth Israel Hospital, US	Applications of EPISTAR for mapping functional changes in relative cerebral blood flow
1994	SMR, p330	Jezzard P, Karni A, Meyer G, Adams M, Prinster A, Ungerleider L, Turner R	NIH, US	Practice makes perfect: a functional MRI study of long term motor cortex plasticity
1995	SMR, p189	Muthupillai R, Lomas DJ, Rossman PJ, Greenleaf JF, Manduca A, Riederer SJ, Ehman RL	Mayo Clinic, US	Magnetic resonance imaging of acoustic strain waves

1995	SMR, p875	Østergaard L, Weisskoff RM, Chesler DA, Kwong K, Sorensen G, Davis TL, Boxerman JL, Gyldensted C, Rosen BR	Aarhus University Hospital, DK	High resolution measurement of cerebral plasma flow, mean transit time and volume using dynamic imaging of Gd-DTPA bolus passages
1997	ISMRM, p135	Bernstein MA, Zhou X, King KF, Ganin A, Pelc NJ, Glover GH	GE, US	Shading artifacts in phase contrast angiography induced by maxwell terms: analysis and correction
1997	ISMRM, p898	Buxton RB, Wong EC, Frank LR	University of California San Diego, US	A biomechanical interpretation of the BOLD signal time course: the balloon model
1997	ISMRM, p2022	Sodickson DK, Manning WJ	Beth Israel Deaconess Medical Center, US	Simultaneous acquisition of spatial harmonics (SMASH): ultra-fast imaging with RF coil arrays
1997	ISMRM, p2332	Mugler JP, Driehuys B, Brookeman JR, Cates GD, Berr SS, Bryant RG, Daniel TM, de Lange EE, Erickson CJ, Happer W, Hinton DP, Maier T, Saam BT, Sauer KL, Wagshul ME	University of Virginia, US	MR imaging of the human lungs using hyperpolarized ^{129}Xe gas
1998	ISMRM, p358	DelaBarre L, Garwood M	University of Minnesota, US	LASER: adiabatic single shot localization with J-refocusing
1998	ISMRM, p579	Pruessmann KP, Weiger M, Scheidegger MB, Boesiger P	University of Zurich, CH	Coil sensitivity encoding for fast MRI
1998	ISMRM, p1226	Basser, PJ	NIH, US	Fiber-tractography via diffusion tensor MRI (DT-MRI)
1999	ISMRM, p320	Mori S, Xue R, Crain B, Solaiyappan M, Chacko VP, van Zijl PCM	Johns Hopkins University, US	3D reconstruction of axonal fibers from diffusion tensor imaging using fiber assignment by continuous tracking (FACT)
1999	ISMRM, p1282	Bundy J, Simonetti O, Laub G, Finn JP	Siemens, US	Segmented trueFISP cine imaging of the heart
2000	ISMRM, p82	Wedeen VJ, Reese TG, Tuch DS, Weigel MR, Dou JG, Weiskoff RM, Chessler D	Massachusetts General Hospital, US	Mapping fiber orientation spectra in cerebral white matter with Fourier-transform diffusion MRI
2000	ISMRM, p213	Simonetti O, Kim RJ, Fieno DS, Hillenbrand H, Wu E, Bundy JM, Finn JP, Judd RM	Siemens, US	2D and 3D segmented TurboFLASH for the visualization of myocardial injury
2000	ISMRM, p221	Nieminen MT, Rieppo J, Töyräs J, Hakumäki JM, Silvennoinen MJ, Hyttinen MM, Helminen J, Jurvelin JS	University of Kuopio, FI	T_2 reveals spatial collagen architecture in articular cartilage: a comparative quantitative MRI and polarized light microscopic study

2000	ISMRM, p379	Ward KM, Aletras AH, Balaban RS	NIH, US	Proton chemical exchange dependent saturation transfer (CEST): evaluation as a mechanism for non-metal based exogenous MRI contrast agent
2000	ISMRM, p383	Bulte JWM, Zhang SC, van Gelderen P, Lewis BK, Duncan ID, Frank JA	NIH, US	3D MR tracking of magnetically labeled oligosphere transplants: initial in vivo experience in the LE (shaker) rat brain
2001	ISMRM, p8	Griswold M, Jakob P, Heidemann R, Nittka M, Wang J, Kiefer B, Haase A	Wurzburg University, DE	Push-button PPA reconstructions: generalized autocalibrating partially parallel acquisitions (GRAPPA)
2001	ISMRM, p10	Gupta A, Liang ZP	University of Illinois at Urbana-Champaign, US	Dynamic imaging by temporal modeling with principal component analysis
2002	ISMRM, p189	Katscher U, Börnert P, Leussler C, van den Brink J	Philips Research, DE	Theory and experimental verification of transmit SENSE
2002	ISMRM, p720	Zhou J, Payen JF, Wilson DA, Traystman RJ, van Zijl PCM	Johns Hopkins University, US	Detection of pH Effects in the water signal through selective saturation transfer via exchangeable amide protons of mobile intracellular proteins: protein proton transfer imaging (PPTI)
2003	ISMRM, p618	Glunde K, Chacko V, Bhujwalla Z	Johns Hopkins University, US	Mechanisms of indomethacin-induced alterations in choline phospholipid metabolism of non-malignant versus malignant human mammary epithelial cells
2003	ISMRM, p742	Lu H, Golay X, Pekar J, van Zijl PCM	Johns Hopkins University, US	Vascular-space-occupancy (VASO) dependent fMRI
2003	ISMRM, p2154	Jensen JH, Helpern JA	New York University, US	Quantifying non-gaussian water diffusion by means of pulsed-field-gradient MRI
2004	ISMRM, p502	Dresner M, Fidler J, Ehman R	Mayo Clinic, US	MR elastography of in vivo human liver
2005	ISMRM, p37	Garcia DM, de Bazelaire C, Alsop D	Beth Israel Deaconess Medical Center, US	Pseudo-continuous flow driven adiabatic inversion for arterial spin labeling
2005	ISMRM, p408	Grazioso R, Ladebeck R, Schmand M, Krieg R	CPS Innovations, Inc., US	APD-based PET for combined MR-PET imaging
2006	ISMRM, p213	Vaughan T, Snyder C, DelaBarre L, Bolinger L, Tian J, Andersen P, Strupp J, Adriany G, Ugurbil K	University of Minnesota, US	7T body imaging: first results

2006	ISMRM, p293	Nunes RG, Hajnal JV, Golay X, Larkman DJ	Hammersmith Hospital, UK	Simultaneous slice excitation and reconstruction for single shot EPI
2006	ISMRM, p695	Lustig M, Donoho DL, Pauly JM	Stanford University, US	Rapid MR imaging with "compressed sensing" and randomly under-sampled 3D FT trajectories
2006	ISMRM, p892	Yacoub E, Ugurbil K, Harel N	University of Minnesota, US	Detection of orientation specific activation zones in human V1 using fMRI
2007	ISMRM, p204	Duyn JH, van Gelderen P, Li TQ, de Zwart JA, Koretsky AP, Fukunaga M	NIH, US	High-Field MRI of brain cortical substructure based on signal phase
2008	ISMRM, p323	Ling W, Regatte RR, Navon G, Jerschow A	Tel Aviv University, IL	gagCEST & NOE: assessment of glycosaminoglycan concentration in vivo
2008	ISMRM, p434	Brunner DO, De Zanche N, Paska J, Fröhlich J, Pruessmann KP	University of Zurich, CH	Traveling wave MR on a whole-body system
2008	ISMRM, p642	Shmueli K, van Gelderen P, Li TQ, Duyn JH	NIH, US	High resolution human brain susceptibility maps calculated from 7 Tesla MRI phase data
2008	ISMRM, p643	Liu T, Spincemaille P, de Rochefort L, Kressler BM, Wang Y	Cornell University, US	Multiple orientation acquisition to invert dipole field for quantitative susceptibility mapping
2008	ISMRM, p2366	Moeller S, Auerbach E, van de Moortele PF, Adriany G, Ugurbil K	University of Minnesota, US	fMRI with 16 fold reduction using multibanded multislice sampling
2009	ISMRM, p594	Overweg J, Raaymakers B, Lagendijk J, Brown K	Philips Research, DE	System for MRI guided radiotherapy
2009	ISMRM, p2812	Doneva M, Sénégas J, Börnert P, Eggers H, Mertins A	University of Luebeck, DE	Accelerated MR parameter mapping using compressed sensing with model-based sparsifying transform
2010	ISMRM, p87	Sacolick L, Wiesinger F, Dixon W, Hancu I, Vogel MW	GE Research, DE	B1 mapping by Bloch-Siegert shift
2010	ISMRM, p551	Setsompop K, Gagoski BA, Polimeni J, Witzel T, Wedeen VJ, Wald LL	Massachusetts General Hospital, US	Blipped CAIPIRHINA for simultaneous multi-slice EPI with reduced g-factor penalty
2012	ISMRM, p288	Ma D, Gulani V, Seiberlich N, Duerk J, Griswold M	Case Western Reserve University, US	MR Fingerprinting (MRF): a novel quantitative approach to MRI
2016	ISMRM, p1088	Hammernik K, Knoll F, Sodickson DK, Pock T	Graz University of Technology, AU	Learning a variational model for compressed sensing MRI reconstruction

2016	ISMRM, p1778	Wang S, Su Z, Ying L, Peng X, Liang D	Shenzhen Institutes of Advanced Technologies, CN	Exploiting deep convolutional neural network for fast magnetic resonance imaging
2016	ISMRM, p1801	Kwon K, Kim D, Seo H, Cho J, Kim B, Park H	KAIST, KR	Learning-based reconstruction using artificial neural network for higher acceleration

Authors:

Fernando Calamante

ISMRM President 2021-2022

The University of Sydney, Sydney, AU

Stefano Mandija

Chair of the Footprints of the ISMRM in the MR path sub-committee

Assistant Professor, Radiotherapy Department, UMC Utrecht, Utrecht, NL.

Chao Ma

Vice- chair of the Footprints of the ISMRM in the MR path sub-committee

Assistant Professor, Massachusetts General Hospital, Boston, US

Ruiliang Bai

Sub-committee member

Associate Professor, Zhejiang University School of Medicine, CN

Li Feng

Sub-committee member

Associate Professor, Department of Radiology, Icahn School of Medicine at Mount Sinai, New York, US

Francesco Giganti

Sub-committee member

Associate Professor, Faculty of Medical Sciences, University College London, London, UK

Hong-Hsi Lee

Sub-committee member

Instructor at Massachusetts General Hospital, Boston, US

Andrada Ianus

Sub-committee member

Junior Leader Postdoctoral Fellow, Champalimaud Foundation, Lisbon, PT

Fei Li

Sub-committee member

Associate Professor, Huaxi MR Research Center, Department of Radiology, West China Hospital of Sichuan University, Chengdu, CN

Thomas Welton

Sub-committee member

Junior Principal Investigator, National Neuroscience Institute, Singapore, SG

Project Stakeholders and Advisory groups:

ISMRM Executive Director Roberta Kravitz

ISMRM EDI Committee Elizabeth A. Morris

ISMRM Vice-President Scott Reeder

ISMRM Vice-President Elect Derek Jones

ISMRM AMPC 2022 Chair Steven Sourbron

ISMRM Chair of the Web Editorial Board Wally Block

ISMRM Study Groups

ISMRM Board of Trustees

ISMRM Past Presidents

ISMRM Chapters' Governing Committees

ISMRM Gold Medalists and Silver Medalists

ISMRM AMPC Table Chairs

ISMRM Historical Archives Committee

MRM Editor in Chief Peter Jezzard

JMRI Editor in Chief Mark Schweitzer

SMRM, 1982.

EVALUATION OF NITROXIDE STABLE FREE RADICALS FOR CONTRAST ENHANCEMENT IN NMR IMAGING.

R.C. Brasch, D.E. Nitecki, D. London, T.N. Tozer, J. Doemeny L.D. Tuck, S. Wolff (University of California San Francisco, California, 94143).

The aims of this study were to determine by animal experimentation the potential diagnostic utility and the pharmacology of nitroxide stable free radicals (NSFR) used in vivo as NMR contrast agents.

METHODS: NMR images were obtained using both a small animal scanner and a large human NMR scanner (3.5 MHz) at UCSF (1). NSFR solutions were imaged in varying concentrations within test tubes to determine their relative strength as NMR contrast agents; animals were imaged before and after NSFR intravenous administration. The metabolism and excretion of NSFR were studied in rats and cats with measurement of proton relaxation effect within various biologic fluids and tissues using electron spin resonance (ESR) spectrometry.

RESULTS: NSFR are paramagnetic and demonstrate relatively strong proton relaxation enhancement by virtue of an unpaired electron in an outer molecular orbital. The magnetic moment of an unpaired electron promotes both spin lattice and spin-spin relaxation of surrounding protons; T_1 and T_2 decrease. Within tissues these affects result in an increase in intensity on the NMR image using relatively low concentrations of NSFR. A 0.5 millimolar concentration of NSFR in water has a notably stronger intensity signal than water or urine; the intensity image of a 10.0 millimolar NSFR solution is very bright. The proton relaxation enhancement of NSFR is comparable to that from cupric (Cu^{+2}) and ferrous (Fe^{+2}) ions in similar concentrations.

Unlike the paramagnetic ions, the potential for chemical conjugation of NSFR makes them well-suited for labeling of target specific biomolecules. By coupling NSFR to substances of known specificity it seems possible to make them selective for different tissues and receptors.

A piperidine NSFR molecule was tested for biologic stability by incubation in urine and serum; there was virtually no loss of paramagnetic activity in 24 hours. NSFR were also evaluated as NMR contrast enhancers by intravenous injection into rats in a concentration of 0.5 g/kg body weight. There was a substantial increase above baseline in the intensity signal from the renal parenchyma and from the urine within the renal collecting structures.

The renal clearance of NSFR was studied by injecting intravenously 1 g/kg into a cat with sequential collection of urine and plasma. NSFR concentrations in these biologic fluids

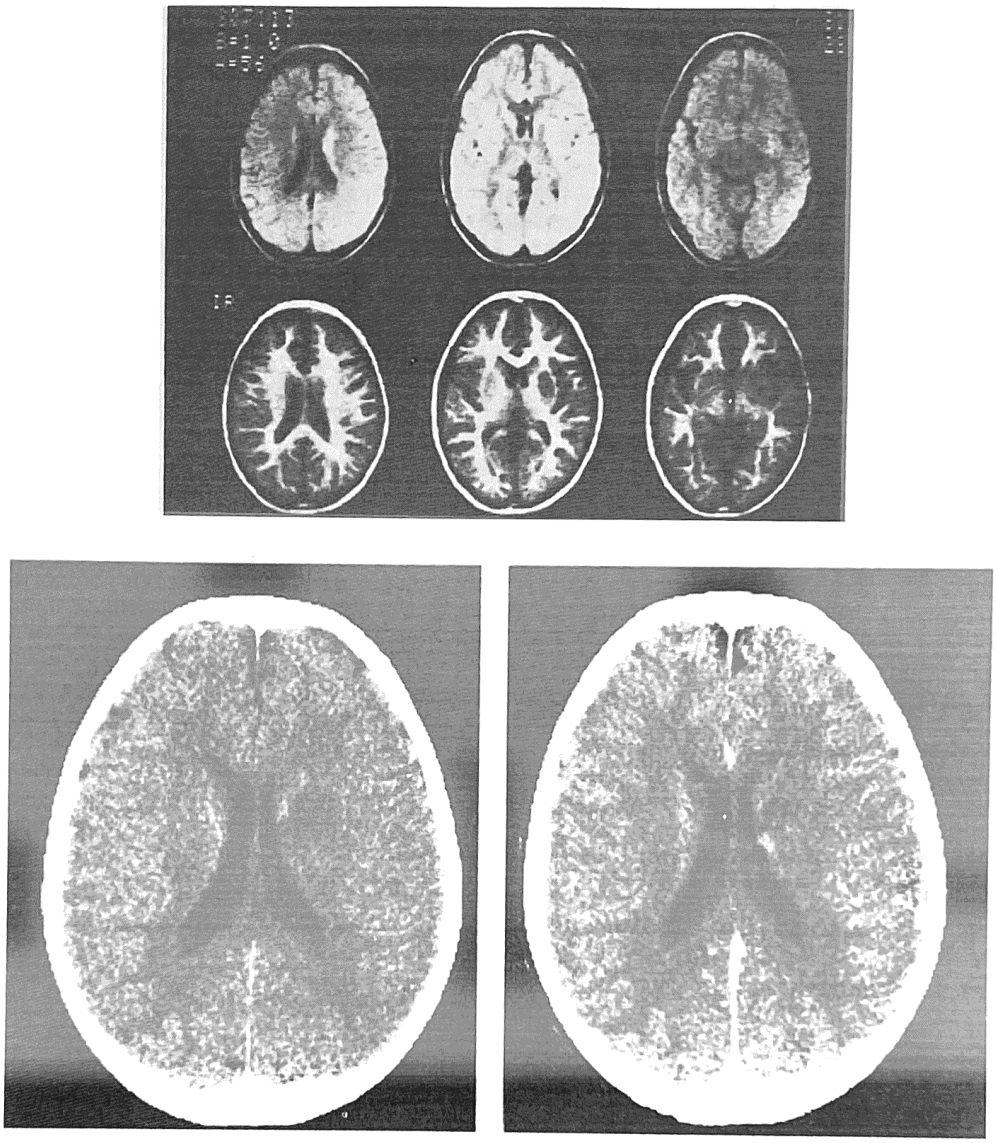

Figure 1. Transverse NMR images through the head of a patient with a left basal ganglion infarct. The top row are spin echo images; the bottom row are inversion recovery images. The left images are the most cephalic. The lesion is best seen in the center plane. It appears as an area of increased intensity in the spin echo image and as an area of decreased intensity in the inversion recovery image. The lesion is not as well seen in the corresponding CT scan (pre and post contrast injection).

as determined by ESR spectroscopy showed a half-life of approximately 38 minutes. The renal clearance was 9.8 ml per minute, a value approximating the glomerular filtration rate in the cat.

Rats having experimentally-induced unilateral hydronephrosis, renal ischemia, or renal vein thrombosis, were imaged before and after NSFR contrast enhancement. Because the NSFR renal concentration and the contrast enhancement are dependent upon renal function, the NSFR-enhanced renal images showed an intensity differential between the normal kidney and the contralateral, diseased kidney. This differential renal function was obvious on the NSFR-enhanced NMR images of the surgically treated rats but could not always be identified on the nonenhanced images. Thus, the use of NSFR as a NMR urographic contrast agent provided a direct means for functional assessment of the kidneys.

CONCLUSIONS: Nitroxide stable free radicals demonstrate several of the characteristics sought for an NMR contrast agent. NSFR are strongly paramagnetic and chemically stable. NSFR in vivo are rapidly excreted by glomerular filtration and this behavior can be used in consort with NMR imaging to demonstrate renal anatomy and to estimate renal function. Because NSFR are chemically versatile and can be covalently bound to a variety of biomolecules, they may be used as targeted contrast agents to help in the specific evaluation of multiple organs and bodily functions. Although NSFR are now manufactured only in very small amounts and accordingly are quite expensive, it seems likely that these agents could be produced inexpensively when manufactured on a large industrial scale.

REFERENCES

1. Kaufman L, Crooks L, Margulis AR, (eds.). Nuclear Magnetic Resonance Imaging in Medicine. New York, Igaku-Shoin, 1981.
2. McConnell HM. Molecular Motion in Biological Membranes. Spin Labeling, Theory and Applications, LJ Berliner (ed.). Academic Press, New York, New York, pp. 525-560, 1976.

REAL-TIME DYNAMIC IMAGING BY NMR

P. Mansfield, R.J. Ordidge, R.R. Rzedzian, M. Doyle and D. Guilfoyle, Department of Physics, University of Nottingham, Nottingham, U.K. and R.E. Coupland, Department of Human Morphology, Queen's Medical School, Nottingham.

In a radically new imaging method of ours, proposed in 1977, the entire spin distribution within a selected plane through a specimen can be read out in digital form in a single experiment[1,2]. Depending on intrinsic factors like the spin-spin interaction time T_2 and on experimental parameters like field gradient strengths, the imaging time can vary from typically 10 - 100 msec. The method exploits the properties of spin echoes and is therefore often referred to as echo-planar (EP) imaging. The details of this method together with most of the other imaging techniques are described elsewhere[3]. The first real-time NMR movie images were obtained last year (1981) with a small scale probe on a rabbit[4]. Each frame is taken in 32 msec and when viewed separately clearly demonstrates the snapshot ability of EP imaging to freeze cardiac motion. For the rabbit, the heart beat period was about 200 msec. Recent experiments using a larger probe have enabled us to study heart and breathing motions of an anaesthetized piglet. In this case the object field was 20 x 20 cm^2. The heart beat period for these medium sized animals is around 600 msec. Movie images have been produced for several cross-sectional slices through the thorax, starting just above the heart and progressing to just below the apex. The slice thickness in all pig images is 8.6 mm. Nine frames from a movie sequence through the middle of the heart are shown in Fig.1. Other movie loops have been produced through the thorax of a smaller piglet over a wider region including the diaphragm. These loops clearly demonstrate movement of the diaphragm due to breathing. The apparatus has also been used to study motion in the human brain. A movie loop shows the anterior horns of the ventricles as dark regions which appear to change thickness by about 3 - 4 mm. The CSF though rich in protons, has a long T_1 around 1.0 sec and does not show due to the short repetition period of 300 msec used here. However, in other data with a much longer repetition period of 2.0 sec, the ventricles show up as bright regions as expected from the high mobile proton content. Current work in progress includes a further scaling of the apparatus to take human subjects. Improvements in data handling, including an array processor, will enable virtually instant display of incoming data.

References

1. Mansfield P. Multi-planar image formation using NMR spin echoes. J Phys C, 10: L55-58, 1977
2. Ordidge RJ, Mansfield P, Coupland RE. Rapid Biomedical imaging by NMR. Brit J Radiol, 54: 850-855, 1981.

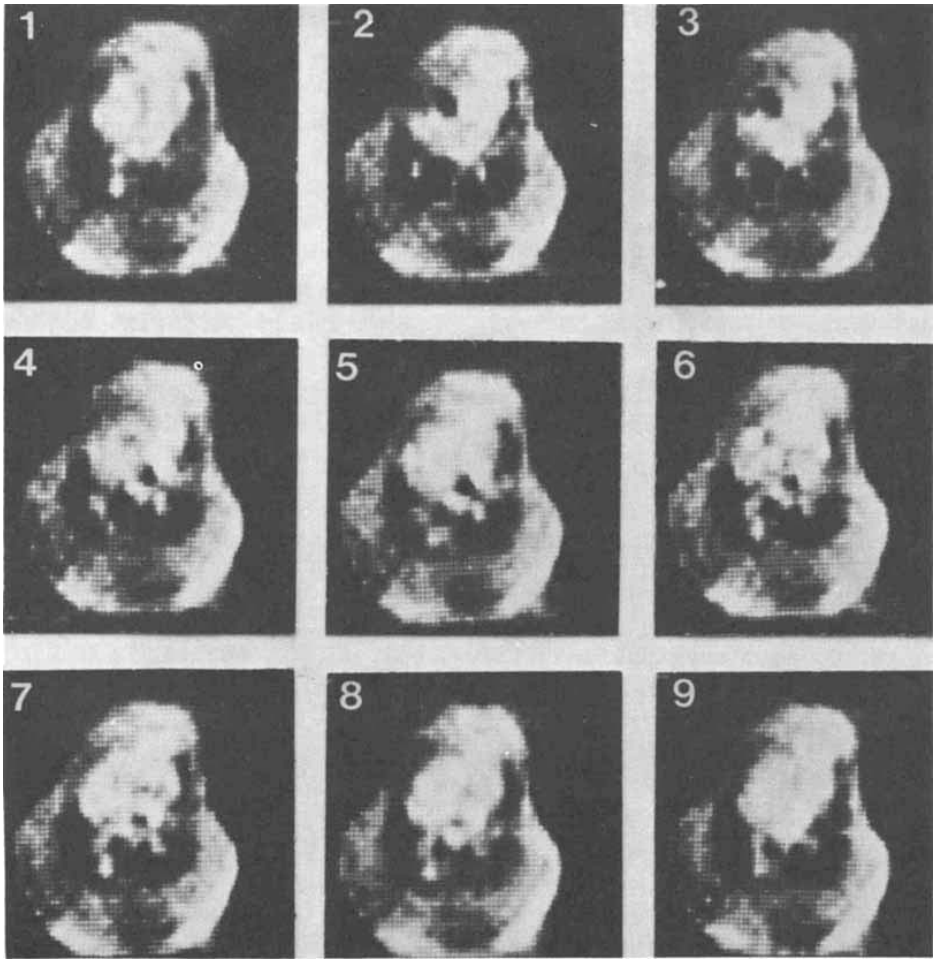

Fig. 1. Sequence from a movie loop showing thoracic cross-sections of a live piglet. The plane passes midway through the heart. Anterior aspect uppermost. Each frame corresponds to a different phase of the cardiac cycle starting with frame 1 at the r-wave and progressing through to 86% of the cycle in frame 9. All show the general outline of the thorax and lung field. The dark spot within the heart mass in frames 2 and 3 is moving blood within the left ventricle. Frames 5 - 7 indicate blood flow within the right atrium.

---

3. Mansfield P, Morris PG. NMR Imaging in Biomedicine. Special Supp.2, Waugh JS, ed. Advances in Magnetic Resonance. Academic Press, N.Y. 1982.
4. Ordidge RJ, Mansfield P, Doyle M, Coupland RE. Real-time moving images by NMR. Radiol 142: 244, 1982.

SMRM, 1982.

102

MULTINUCLEAR NMR IMAGING

A. A. Maudsley, S. K. Hilal, H. E. Simon, and W. H. Perman
(Department of Radiology, The Neurological Institute, Columbia University)

Sodium was imaged in the live cat using a superconducting magnet with a 30cm warm bore and operating at 27 kG. Also, experiments on physical phantoms were conducted for obtaining a spatially resolved high resolution spectroscopy of phosphorus using "four-dimensional NMR".

The NMR images of the sodium molecule in the normal cat show a very bright image of the eyes. They also show the cerebrospinal fluid in the subarachnoid space with a spatial resolution of approximately 3mm. A stroke model was developed and some of the preliminary results of this model will be presented.

The four-dimensional NMR images of the phosphorus compounds resulted in separate images for inorganic phosphate, sodium pyrophosphate and phosphocreatine. A separate image of each of the compounds was possible. This study on phosphorus was conducted in a physical phantom. The detail of the method will be presented.

This paper represents the first in vivo images of the sodium nucleus. The potential clinical application of this method in the characterization of an infarcted brain or a neoplasm is important. Since sodium is primarily in the extracellular space, an increase in sodium concentration would represent either expansion of the extracellular space, such as in edema, or irreversible damage to the cells with diffusion of the sodium molecule in the intracellular space.

THE USE OF PARAMAGNETIC CONTRAST AGENTS IN NMR IMAGING. II: In vivo studies.

M.H. Mendonça Dias*, P C. Lauterbur*#, and E.J. Brown, Jr.+
Department of Chemistry*, Department of Radiology#, and Department of Medicine-Cardiology Division+, State University of New York at Stony Brook, Stony Brook, New York, 11794.

a)-Fast experiments with local coils.
An important question concerning the use of Mn^{2+} as a paramagnetic contrast agent in tissues is whether the effects are the same in vivo as in vitro. Studies done in vivo and post-mortem on rat liver, using as receiver a local surface coil and a sequence of pulses 180°, τ ,90°, from a large transmitter coil, have shown that the T_1 does not change with death or for several hours afterward. In Fig. 1 we present one example, for one experiment of only one hour.The rate of uptake and washout of relatively large dosages of manganese is also of interest, and that has been studied, by monitoring, with a temporal resolution of one to three seconds, the T_1 changes (using the technique described above) on exposed livers of rats, using a local surface coil as receiver, and in the flowing blood of dogs, using a solenoidal coil. The results are shown in Figs. 2-4.

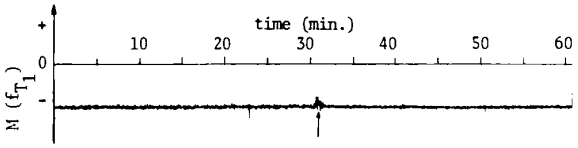

Figure-1 (the arrow represents the moment of death)

Fig.2 shows the effect of three consecutive injections of $MnCl_2$ on the T_1 of a rat liver. Fig. 4 shows the rate of clearance of manganese from the blood of a dog (in both cases the dosage of manganese injected was .05mM/Kg). Fig. 3 is a comparison with previous results obtained by taking blood samples from a dog and measuring the values of T_1 in a sample tube.

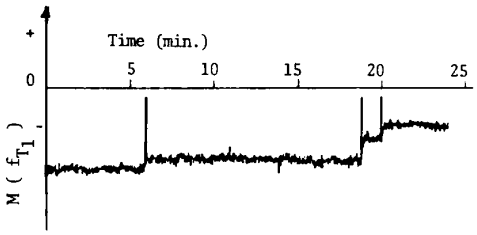

Figure 2

b)-Manganese acute toxicity.
After several years of work with rats and dogs, it seems likely that the acute toxicity of Mn^{2+} is primarily cardiac. The ECG of dogs and rats have been monitored. We observed that for rats dosages of .1 mM/Kg are almost always lethal (iv injection), but that the

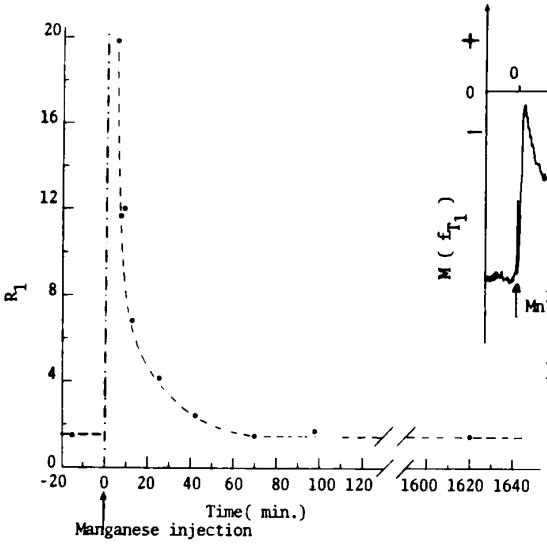

Figure 3

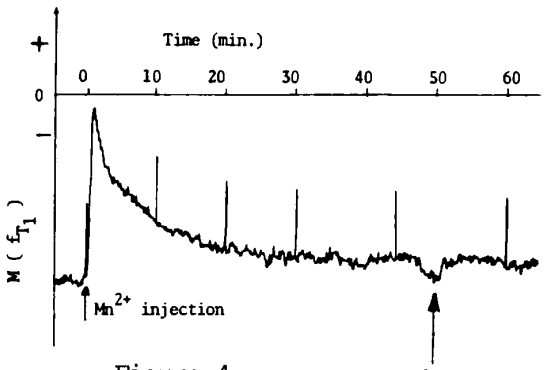

Figure 4

Disturbance produced by a magnetic hypodermic needle.

effects can be suppressed if EDTA is injected a few minutes after the manganese. For rats a dose of .05 mM/Kg does not appear to induce any abnormalities in the ECG.

c)-Other possible paramagnetic contrast agents.
Other metal ions, such as Ni^{2+}, Fe^{3+}, and Gd^{3+}, are also potentially good paramagnetic contrast agents, but the acute toxicity of nickel and even iron are higher than that of manganese. Besides, iron is present in the body at very high levels, which can be a disadvantage. In the case of gadolinium there is no data available about its physiological effects or levels of chronic or acute toxicity.
Further efforts need to be directed to the search for the most suitable contrast agents, keeping in mind that the biggest challenge and, in all likelihood, the most serious and difficult problem in this field will be to find contrast agents for which the toxicity is low enough to make possible their eventual use in medical diagnosis.

Acknowledgements: We wish to thank M. Bernardo and K. Hedges for their advice and help with computer programs and use of the equipment, and Ruth Heidelberger and Virgil Acuff for invaluable technical assistance.
This work was supported by Grant No. HL19851, awarded by the National Heart, Lung, and Blood Institute, DHHS.

SMRM, 1983.

NMR IMAGES OF THE WHOLE HUMAN TRUNK AT 64 MHZ

W. A. EDELSTEIN, O. M. MUELLER, P. A. BOTTOMLEY, H. R. HART, J. F. SCHENCK, L. S. SMITH, M. O'DONNELL, W. M. LEUE AND R. W. REDINGTON

GENERAL ELECTRIC CORPORATE RESEARCH AND DEVELOPMENT CENTER
SCHENECTADY, NY 12301

Proton NMR images of the whole human torso have been produced in a magnetic field of 1.5 T, corresponding to a Larmor frequency of 64 MHz. The imaging aperture is .5 m. RF attenuation and phase shift effects are not a serious impediment to the production of such images as had been earlier predicted.

The pulse sequence used is a modified "spin warp" 2-D Fourier transform technique[1] which contains a selective 90^{o} pulse followed by a nonselective 180^{o} pulse to produce a spin echo. The 180^{o} pulse has a peak power of about 1.9 kW, and at the present duty cycle, the total average power deposition to the subject (from both RF pulses) is about 12 W.

Figure 1 shows an image taken at the level of the kidneys. It is a saturation recovery sequence with repetition period 200 ms and total imaging time 102 s. The image has been made with a 256x256 pixel raster with a resolution of about 2 mm. The slice thickness is approximately 7 mm. No corrections have been made for attenuation or phase shift effects.

REFERENCE

1. W. A. Edelstein, P. A. Bottomley, H. R. Hart, W. M. Leue J. F. Schenck and R. W. Redington, Proc. International Symposium on NMR Imaging, R. L. Witcofski, N. Karstaedt and C. L. Partain, eds. (Bowman Gray School of Medicine, NC, 1982), p. 139.

Figure 1. 7 mm thick transaxial section through human trunk at level of kidneys.

SMRM, 1983.

MULTINUCLEAR APPLICATIONS OF CHEMICAL SHIFT IMAGING

A.A. Maudsley, S.K. Hilal, H.E. Simon, S. Wittekoek
Columbia University College of Physicians & Surgeons
Neurological Institute, 710 W. 168th St., New York,NY 10032

Imaging of separate chemically shifted NMR spectral lines is possible by using an extension of the Fourier imaging experiment, whereby the NMR signal is observed in the absence of any field gradient with spatial selection performed during an earlier, phase-encoding, time period (1). We have used a spin echo pulse sequence where a selective pulse is used to select a single slice perpendicular to the z-axis and spatial discrimination within the plane is achieved by successive applications of the phase-encoding gradients applied along the x and y axes. The NMR signal is then recalled by a 180 degree pulse and observed in the absence of any field gradients. The Fourier transform of the resultant three-dimensional data set provides the NMR spectrum for each point in x and y, allowing separation of different chemically shifted lines.

Since field inhomogeneity changes the resonance frequencies by different amounts at different locations over the object, these effects must be corrected for in order to obtain a true image of the distributions of each spectral line. Measurement of the magnetic field variation over the imaging region is done by using the same experimental sequence (2) with an object of constant spin density and, preferably, a single NMR resonance line, for example, a large bottle or water in the case of proton imaging. This data set can then be used to correct for the effects of field inhomogeneity on the chemical shift data. Further data processing techniques include integration of selected planes (along the frequency axis) for each resonance line, in order to reduce the number of images to simplify data analysis.

Results will be shown for proton and phosphorus NMR observation obtained *in vivo*. Figure 1 shows a proton chemical shift image of a single section through the head of a cat. Successive images represent spin density distributions from proton-containing groups with increasing chemical shifts, which, broadly speaking, are the signals from water, from CH_2 groups

and from CH_3 groups, in order of increasing frequency.

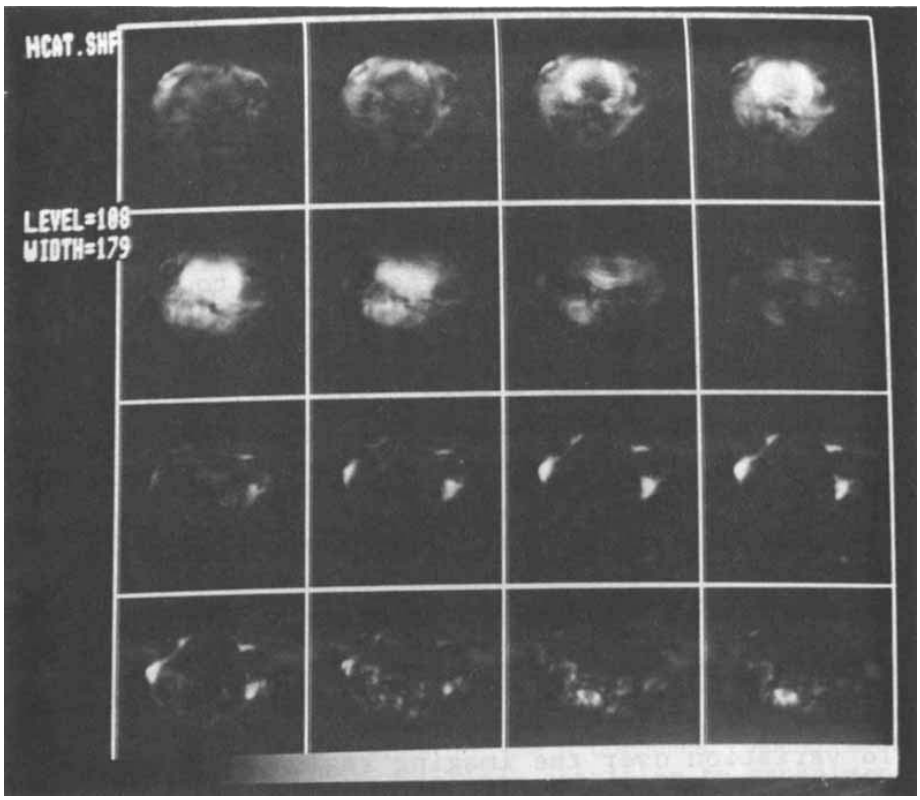

Figure 1

Proton chemical shift imaging through a single section in the head of a cat. A strong water signal from the brain can be seen at lower frequencies and various signals arising from fats at the higher frequencies.

REFERENCES

1. Maudsley AA, Hilal SK, Perman WH, Simon HE: J Magn Reson *51*: 147-152, 1983

2. Maudsley AA, Oppelt A, Ganssen A: Siemens Research and Development Reports *8*: 326, 1979

SMRM, 1984.

RF POWER DEPOSITION IN NMR IMAGING

Paul A. Bottomley,
General Electric Corporate Research and Development Center
Schenectady, New York 12301

RF power is deposited in the body during the NMR pulses applied in imaging experiments owing to the finite but small electrical conductivity of biological tissue in the NMR frequency range(1,2). Power is principally deposited as joule heating associated with eddy currents induced by the RF magnetic field. Power deposition from electric fields associated with RF transmitter coils are negligible when efficient transmitter coil designs are employed(3), as is the power deposited via NMR relaxation(4). The specific power absorption rate (SAR, W/kg) in biological tissue is a function of sample size, sample geometry, NMR frequency (ν, Hz), RF pulse length (τ,s for a $\pi/2$ pulse), pulse repetition period (t, s), RF pulse sequence, tissue resistivity (ρ,Ωm), and dielectric constant. For a homogeneous tissue cylinder with RF field directed axially, or for a homogeneous sphere, the peak (surface) SAR (P) is approximately

$$P(peak) = \frac{K\nu^2R^2}{\rho s \tau t} \qquad (1)$$

where $K = 6.8 \times 10^{-19}$, R (m) is the sample radius and s is the specific gravity of the tissue(2). Since current UK and USA RF exposure guidelines cite both peak and total body average SAR's, the (theoretical) relations P(peak) = 2P(average) for a homogeneous cylinder, and P(peak) = 2.5 P (average) for a homogeneous sphere, are useful for estimating both values given only one.

Empirical testing of the above dependencies for the human torso was performed at 64 MHz with nine volunteers weighing between 65 and 102 Kg using the method of measuring the change of RF coil quality factor (Q) with and without the subject present(5). The patient position was adjusted for maximum Q change which occurred with the coil centered about the umbilicus. The NMR coil used produced an RF field orthogonal to the cylindrical axis. Whilst equation (1) is inappropriate for this configuration, this is by far the most commonly employed experimental geometry in superconducting magnet based systems.

Figure 1 shows that the total average power (W) increases as the $(1.8\pm.3)^{th}$ power of total body mass (m). Equation(1) suggests that $W \propto R^4$. Since $R \propto m^{1/2}$ for a fixed sample length, $W \propto m^2$ is consistent with the measurement. If it is assumed that the peak power is absorbed at the surface(1,2), P(peak) can be estimated from the slope of the W versus mean torso radius curve. Thus

P(peak) = $\frac{\partial W}{\partial R}$. δR, where δR is a small change in R, and we obtain empirically P(peak) = 3(±1.5) P(average). Examination of this result and the figure 1 measurements in the context of the published(2) peak surface SAR curves for the torso with the pulse sequence timing parameters used here, indicates that the actual power deposited is about 2-fold lower than that estimated from reference(2). The disagreement is not surprising given the differences in geometric configuration, the heterogeneity and compartmentation of the human sample, and the use of the worse case resistivity (muscle) for computing in the curves.

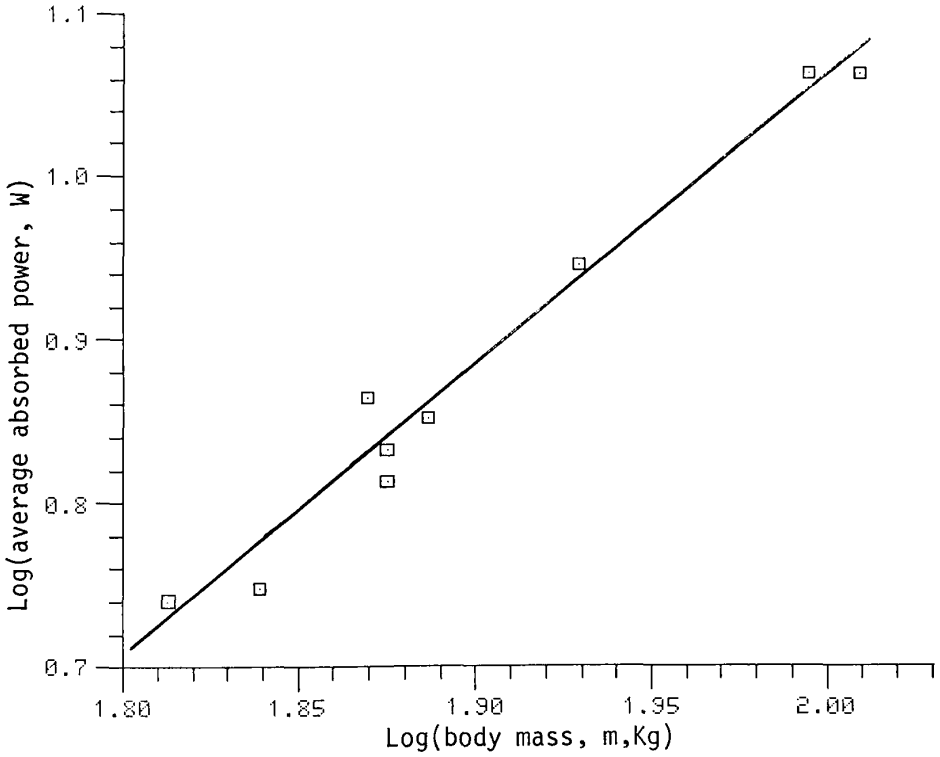

Figure 1: Average absorbed RF power W(W) measured at 64 MHz as a function of body mass (m,kg; log. scales, courtesy R.W. Redington).

Equation (1) also assumes a uniform RF field across the sample. The slight increase in the RF field towards the sample center observed in theoretical calculations (1,5), might suggest the development of "hotter spots" of power deposition in interior

locations. However computation of the power deposition in a .2 m radius liver cylinder (Figure 2) indicates that the quadratic dependence of the SAR dominates so the SAR decreases monotonically and rapidly to zero at the cylinder center. This result is unaltered in a given tissue if the model is extended to concentric layers of different tissues since the eddy currents also follow concentric paths.

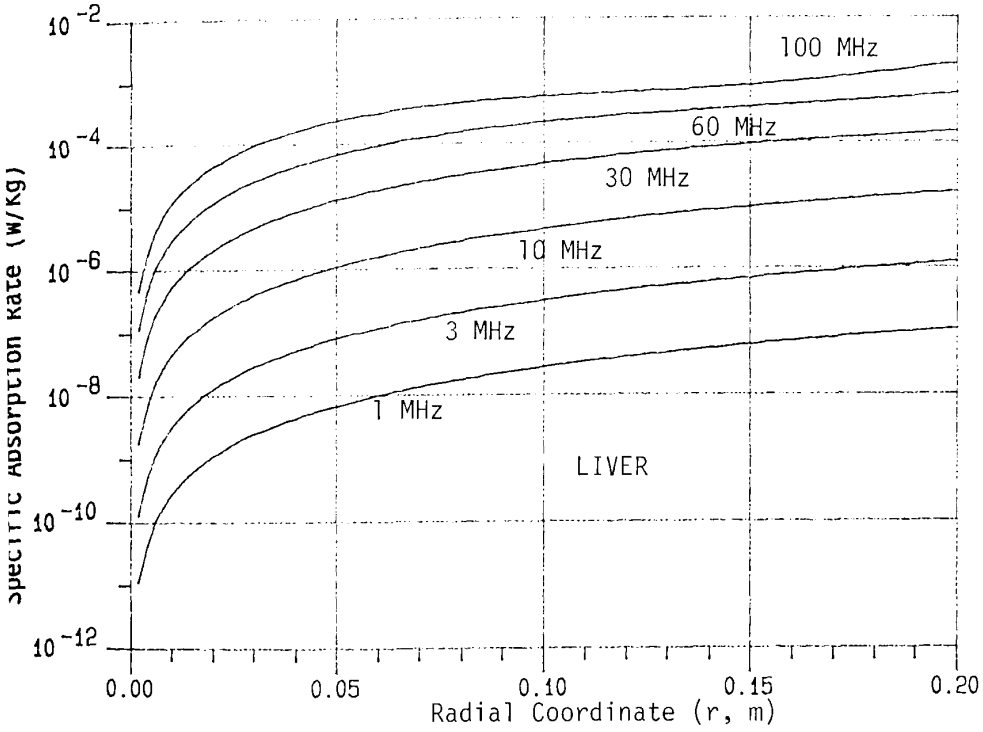

Figure 2: SAR in a .2 m radius homogeneous liver cylinder as function of radial position and NMR frequency (MHz) with $\tau t=10^{-2}s^2$, computed from equations (10) and (11) of reference (2).

1) P.A. Bottomley, E.R. Andrew. Phys. Med. Biol. 23,630 (1978).
2) P.A. Bottomley, W.A. Edelstein. Med. Phys. 8,510(1981).
3) D.I. Hoult, P.C. Lauterbur. J. Magn Reson. 34,425(1979).
4) P.K. Grannell, P. Mansfield. Phys. Med. Biol., 20,477(1975).
5) P. Mansfield, P.G. Morris. NMR imaging in biomedicine (Academic, NY, 1982).

DEPTH RESOLVED SURFACE COIL SPECTROSCOPY (DRESS) FOR IN VIVO ^{1}H, ^{31}P AND ^{13}C NMR

P. A. Bottomley, T. H. Foster, D. Vatis, R. D. Darrow,
O. M. Mueller, W. A. Edelstein and C. J. Hardy
General Electric Corporate Research and Development Center
PO Box 8, Schenectady, NY 12301

Surface coils offer improved signal-to-noise ratios over large volume coils for detecting localized NMR spectra because of their improved filling factors and because their restricted spatial sensitivity significantly reduces the detected Johnson noise from the sample. A serious problem encountered when using surface coils for studying tissues lying deep beneath the sample surface in situ is undesirable contributions to the spectra from intervening surface tissues (1-6), and indeed several remedies have been proposed to improve surface coil localization (4-6).

We propose and demonstrate here an alternative technique for eliminating surface tissue contributions, and for providing accurately controlled depth resolved surface coil spectra (DRESS) for in vivo applications. The method utilizes either a conventional volume RF coil or a large surface coil for providing a uniform RF excitation field over the sensitive volume and a smaller diameter surface coil which is used for detection only. Depth resolution is achieved by incorporating at least one selective excitation pulse in the RF pulse sequence. The selective excitation pulse is applied during the presence of a magnetic field gradient pulse whose direction is coaxial with the surface coil to excite a flat plane of nuclei parallel to the plane of the surface coil. The extent of the sensitive volume within the selected plane is determined only by the diameter of the surface detection coil and the distance of the coil from the sensitive plane. The sensitive volume is approximated by a disk lying at the intersection of the three-dimensional surface coil sensitivity profile (3) in a uniform excitation field, and the selected plane.

^{31}P spectra from the surface of the head and the brain (35 mm deep) are compared with a spatially unresolved spectrum in the Figure. The slice thickness was 12 mm, the diameter of the surface detection coil was 65 mm, the resonance frequency was 25.3 MHz, and a 1 s pulse repetition period was used. Experiments were done on a 1.5 T, 1 m bore NMR research system (1). The brain, and spatially unresolved spectra were recorded in 10 min., 20 min., and 5 min. respectively. The brain spectrum and the surface spectrum exhibit significantly different phosphocreatine (PCr) to adenosine triphosphate (ATP) ratios and relative levels of

phosphodiesters (PD), inorganic phosphate or blood sugar phosphate (Pi), and sugar phosphates (SP). The surface spectram in fact resembles a muscle spectrum (1).

1. P. A. Bottomley, H. R. Hart, W. A. Edelstein, J. F. Schenck, L. S. Smith, W. M. Leue, O. M. Mueller, R. W. Redington. Radiol. 150, 441 (1984).
2. P. A. Bottomley, W. A. Edelstein, H. R. Hart, J. F. Schenck, L. S. Smith. Magn. Reson. Med. (in press 1984).
3. J. L. Evelhoch, M. G. Crowley, J J. H. Ackerman, J. Magn. Reson. 56, 110 (1984).
4. R. E. Gordon, P. E. Hanley, D. Shaw, D. G. Gadian, G. K. Radda, O. P. Styles, P. J. Bore, L. Chan, Nature, 287, 736 (1980).
5. M. R. Bendall, R. E. Gordon, J. Magn. Reson. 153, 365(1983).
6. A. Haase, C. Malloy, G. K. Radda, J. Magn. Reson. 55, 164 (1983).

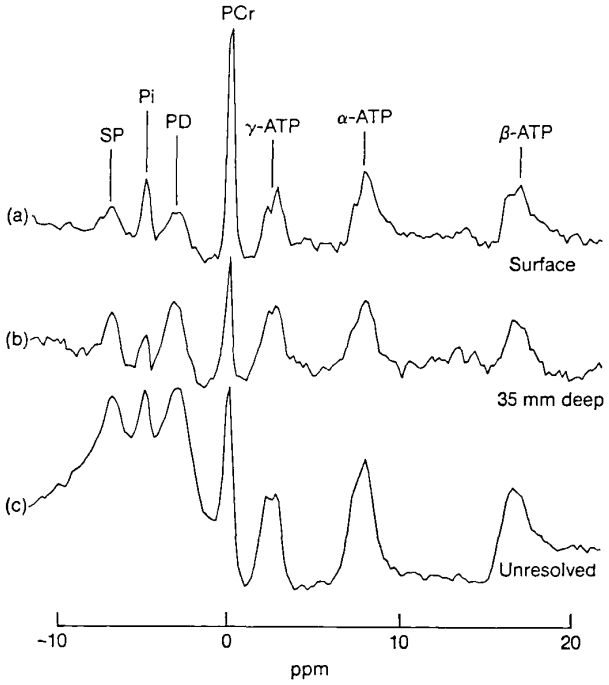

^{31}P DRESS from the surface of the human head (a), and 35 mm deep (b). The surface coil was located above the temple. (c) is a spatially unresolved spectrum recorded with the gradient turned off. A 3 Hz line broadening exponential filter was applied to each spectrum, but no baseline flattening was attempted. The spectrometer gains are in the ratio 2:4:1 for (a), (b), and (c) respectively.

SMRM, 1984.

Proton Spectroscopic Imaging at 0.35 T

W. Thomas Dixon
Mallinckrodt Institute of Radiology
Washington University School of Medicine

David D. Faul
Siemens Medical Systems, Inc.

A spin-echo imaging pulse sequence has been modified so that useful spectroscopic information is encoded into clinical images obtained at 0.35 T (1). The new type of image produced with this technique shows the difference between the water and fat intensities. When, in addition, a normal spin-echo image is obtained, then pure fat and pure water images can be computed. The technique provides both new parameters for tissue characterization and improved contrast between some organs. Although the imaging speed, spatial resolution and signal-to-noise ratio are comparable to ordinary imaging, the generation of pure fat and pure water intensity images requires an additional correction for the effects of magnetic field inhomogeneity.

The method is implemented by shifting the position of the 180^{o} RF pulse in time by ΔT as shown in Fig. 1. The time ΔT is equal to $1/4\Delta\nu$ where $\Delta\nu$ is the chemical shift between fat and water in Hz. In a conventional spin-echo imaging pulse sequence the read-out gradient G_{RO} focuses an echo at a time T_{GE} ("GE" means gradient echo) corresponding to T_{HE} ("HE" means Hahn echo), the time at which an echo would occur if the RF acted alone. With the modified pulse sequence the echo peaks at a time T'_{GE} which is not equal to T'_{HE}. The echo produced by the modified pulse sequence occurs when the phase difference between the fat and water magnetization vectors is 180^{o}, while that produced by the normal pulse sequence occurs when the phase difference is zero. The results obtained with this technique can be improved by correcting the phase error in the image obtained with the modified pulse sequence. This phase error results from field inhomogeneities across the image acting during the interval between T'_{HE} and T'_{GE}.

The modified pulse sequence has been used clinically to demonstrate fatty infiltration of the liver (2). Figs. 2a and 2b compare images made with the normal and modified pulse sequences, respectively. Metastatic lesions of the liver are more apparent in the image formed with the modified pulse sequence where the metastates produce a mottling.

These results show that clinically useful spectroscopic information can be encoded into images at a field strength used by today's commercial systems. The technique is applicable to all regions of the body and is compatible with multiple-slice imaging.

References

1. Dixon WT. Simple proton spectroscopic imaging. Radiology, submitted for publication, 1984.

2. Lee JKT, Dixon WT, Ling D, Levitt RG, and Murphy WA, Jr. Demonstration of fatty infiltration of the liver by proton spectroscopic imaging: preliminary observations. Radiology, accepted for publication, 1984.

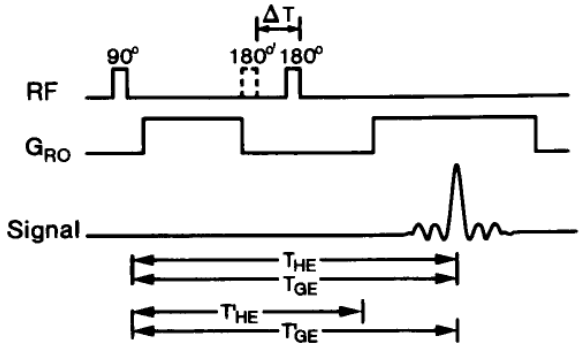

Fig. 1 Diagram showing the modification of the spin-echo pulse sequence described in this report. The position of the 180^{O} RF pulse is changed to 180^{O}'.

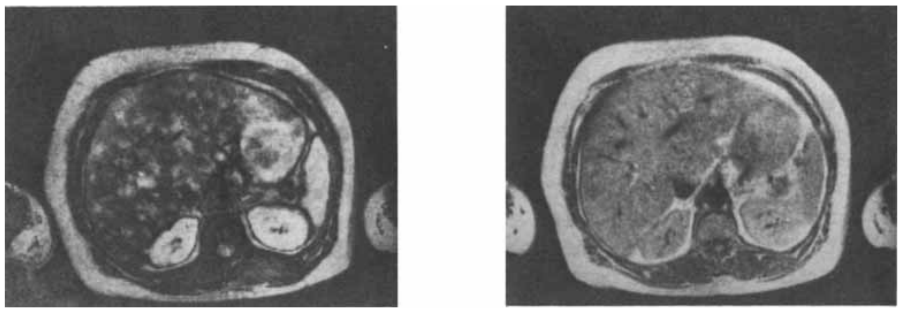

a b

Fig. 2 MR images made with a spin-echo pulse sequence (40 ms echo time, 1.5 s repetition time, 4 averages, 0.35 T) where a) shows the result of imaging with a conventional spin-echo pulse sequence and b) shows the result obtained with the modified spin-echo pulse sequence shown above.

SMRM, 1984.

Chemical Shift Selection (CHESS) Imaging

A. Haase, J. Frahm, W. Hänicke, D. Matthaei
Max-Planck-Institut für biophysikalische Chemie
Postfach 2841, D-3400 Göttingen, W.-Germany

There are several reasons for the separation of water and lipid proton signals in ^{1}H-NMR imaging:

(1) the chemical shift dispersion in high-field NMR imaging,
(2) the quantitative evaluation and interpretation of proton relaxation times, and
(3) the diagnostic implications of "water" and "fat" distributions.

In general, water and lipid proton resonances can be distinguished by their relaxation times or chemical shifts. Here we propose methods for obtaining separate images which are applicable in cases where a chemical shift difference is observed over the entire imaging volume (i.e. within a homogeneous region of the magnet). The technique employs an initial chemical shift selection period which may either be based on selective excitation or saturation pulse sequences followed by a conventional imaging sequence. Results on phantoms, animals, and humans are presented using presaturation of water or lipid resonances combined with standard 2D-Fourier imaging in the spin-warp modification.

In conclusion, the new CHESS imaging strategy shows the following advantages:

(1) it is simple and allows combination with any imaging principle without changing the imaging pulse sequence,
(2) it is direct and needs only a single imaging experiment to obtain either a "water" or a "fat" image,
(3) the number and the widths of the selected chemical shift ranges can be adjusted by proper CHESS pulse sequences prior to imaging,
(4) the method is applicable to imaging of other nuclei.

SMRM, 1984.

A Highly Selective 180° Pulse

by
D.I. Hoult*, M.S. Silver+ and R.I. Joseph+
*Biomedical Engineering and Instrumentation Branch
Division of Research Services
National Institutes of Health
Bethesda, Maryland 20205

+Department of Electrical Engineering and Computer Science
The Johns Hopkins University
Baltimore, Maryland 21218

The generation of highly selective 90° and 180° pulses is a problem which has received considerable attention in recent years in the areas of both NMR spectroscopy and imaging. While good solutions are available for 90° flip angles, until recently no result of comparable quality was available for the case of a 180° flip. However, we have found, using mathematics analogous to that employed in the analysis of the optical phenomenon of self-induced transparency, that a driving function of the form

$$\Omega = \Omega_0(\text{sech } \beta t)^{1+i\mu} \quad ; \beta, \mu \text{ constants}$$

produces an excellently defined, localized population inversion, as may be seen from the figure. Here $\Omega = -\gamma(B_{1x} + i B_{1y})$ represents the irradiating field in the rotating frame, and γ is the gyromagnetic ratio. Important as this result is, of greater import is the fact that above a critical threshold, the inversion is independent of the amplitude Ω_0 of the driving function. This remarkable result, (which has an analogue in the theory of coherent optics) has been verified over a 30dB range and it implies, among other things, that the dependency of flip angle on B_1 homogeneity is removable.

The key to insight into the result lies in the fact that when the driving function Ω is employed, the Bloch Equations may be reduced to the hypergeometric equation, and the magnetization's evolution may then be expressed as a function of Gaussian series ${}_2F_1$ whose convergence depends on the various parameters. In remarking that the flip angle is independent of applied power, we are merely making a statement about the final resting place of the magnetization; doubtless the trajectory executed during the course of the selective pulse varies greatly with the pulse amplitude.

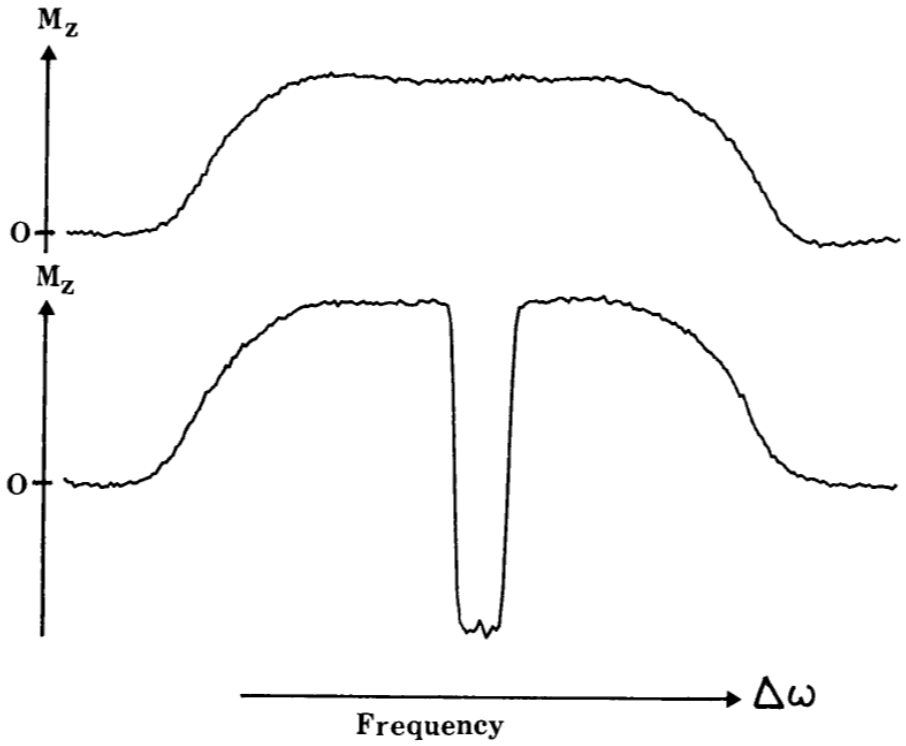

SELECTIVE POPULATION INVERSION

SMRM, 1984.

PHASE ENCODED NMR FLOW IMAGING

D. G. Norris, (University of Aberdeen, Scotland)

Purpose of Study: The practical implementation of a new method of NMR flow imaging (Moran, 1983) is described.

Methods: The technique employs a series of bi-polar field gradient pulses to phase-encode fluid moving in the direction of the gradient. These pulses were incorporated in our spin-warp pulse sequence as shown in figure 1. In our implementation 8 images are collected as a 64 x 64 matrix of complex numbers. The magnitude of the flow pulse used in each image was stepped linearly between images as shown in figure 1. The reason for collecting 8 images is because the phase shift due to spins moving with constant velocity is proportional to the magnitude of the flow-pulse, whereas the phase shift due to main field inhomogeneities is identical for each image. A series of complex 8 point Fourier transforms taking as input the complex pixel values z(i,j) from each of the 8 images will yield 8 transformed images. If the spins in a particular pixel are stationary then the 8 point Fourier transform will give a sharp maximum value for that pixel in the 5th of the 8 transformed images, if the spins are moving with velocity v then the set of transformed images will have a maximum value in image number n where $(n-5) \propto v$.

Results: The 8 transformed images shown in figure 2 were obtained on the Aberdeen Mark I imager (Hutchison et al 1980). A phantom consisting of several turns of plastic tubing (internal diameter = 10 mm), containing water doped with copper sulphate to give a T_1 of about 400 ms, was imaged. The solution was driven through the tubing at a constant velocity of .6 ms^{-1} whilst the flow pulses were applied in the direction across the page in figure 2. The maximum field gradient used was 11.7mTm^{-1} applied for 1.4 ms in each pulse.

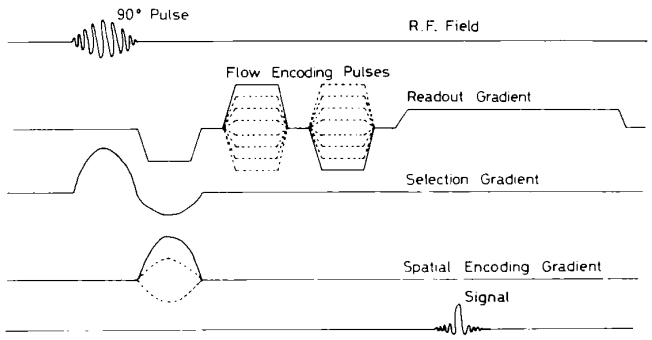

Figure 1.

Figure 2

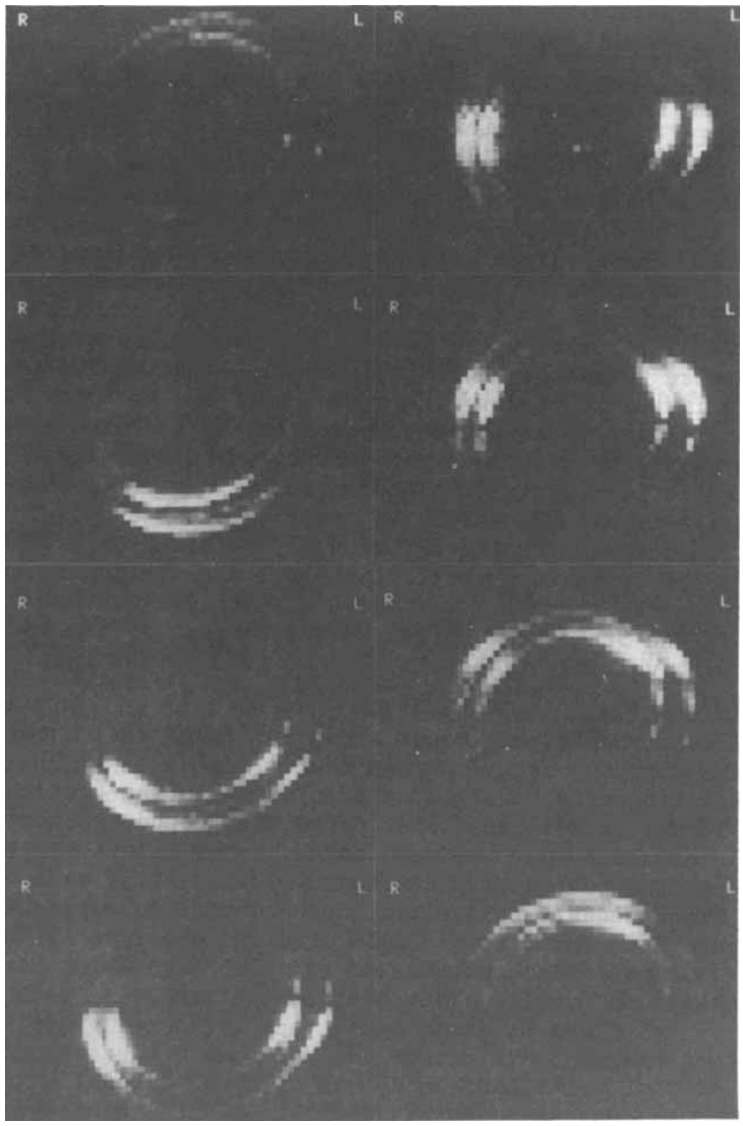

References:

1. MORAN, P.R. (1938) A flow velocity interlace for NMR imaging in humans. Mag. Res. Imaging, 1, 197-203.

2. HUTCHISON, J.M.S., EDELSTEIN, W.A. and JOHNSON, G. (1980). A whole-body NMR imaging machine. J.Phys.E: Sci Instrum. 13, 947-955.

SMRM, 1985.

MRI ANGIOGRAPHY AND FLOW VOLUME QUANTITATION

V.J. Wedeen, B.R. Rosen, R. Buxton, R.R. Edelman, R. Meuli, and T.J. Brady*

From the Department of Radiology and the *Medical Service, Massachusetts General Hospital, Boston, MA 02114

Introduction: A method for projective MR flow imaging with phase contrast is developed. The strategy is to use a 2DFT spin-echo imaging pulse sequence to induce small velocity-dependent phase shifts. The readout image gradient of these sequences does the work according to the relationship of Carr, Purcell (1) and Hahn (2): $\Delta\phi = 1/4\,\gamma G T E^2$. Using phase-sensitive signal detection and image reconstruction, image data can be split into two components. With care, all signal from stationary protons can be placed in the real channel. Hence, any data in the imaginary channel will have originated in the moving protons. This accomplishes the task of background suppression in one step. When a projective image is produced by these means, only voxels which intersect a flowing vessel will show non-zero data.

Methods: Two forms of the method are demonstrated. In one form, flow dependent contrast is maximized in order to isolate and identify vascular anatomy. This is done by cultivating moving proton phase shifts close to 90^{o}. The result in the MRI analog of contrast angiography. In the other form, some contrast is sacrificed for the sake of flow volume quantitation. Phase shifts are kept less than about 45^{o}, in which regime the approximation $\sin\theta = \theta$ is valid (3). In this case, the contribution any proton makes to the image data, positive, negative, or zero, is proportional to its velocity. Thus two protons moving at velocity V or one proton moving at 2V would give the same flow signal. If we can assume that the moving fluid has uniform MR characteristics (relaxation times and density, i.e., signal per unit mass), then the image intensity is proportional to the net flow volume. Each pixel represents the flux across its corresponding voxel.

Results: Image data validating both techniques are presented. Angiographic in-vivo images at 0.14 T showed the course of the femoral artery in a human from the upper thigh to the popliteal bifurcation in the calf. Studies were gated; definition and contrast were improved by subtraction of systolic images from diastolic (Figure, right). Images demonstrating the carotid arteries and jugular veins of a dog are also presented. These studies employed echo times ranging from 5.5 to 9 msec and total imaging times of approximately 8 minutes. A modification of this method has recently been implemented at 0.6 T.

The volume quantitative mode was validated by means of flow phantoms at 0.14 T. The expected proportionality between

image intensity and flow volume was corroborated. Furthermore, flow image data were found not to depend on several variables including 1) image resolution (voxel size); 2) orientation of the flow in the image; and 3) short-term flow variations such as pulsatility and turbulence, contingent upon adequate sampling. These properties are consequences of the elementary linear relationship between signal and flow. They are cooperative and should endow clinical flow volume imaging with unusually high specificity and reproducibility.

References:
1. Carr HY, Purcell EM, Phys. Rev., 94, 630, 1954.
2. Hahn EL, J. Geophys. Res., 65, 776, 1960.
3. Moran PR, Magn. Res. Imaging, 1, 197, 1983.

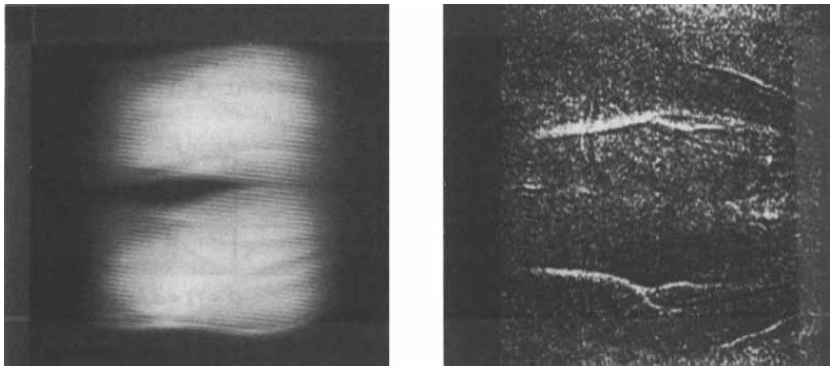

Magnitude (left) and background suppressed (right) reconstructions of lower extremities showing the bifurcations of the popliteal arteries bilaterally.

SMRM, 1985.

FERROMAGNETIC PARTICLES AS CONTRAST AGENTS FOR MAGNETIC RESONANCE IMAGING

M. Helena Mendonça-Dias, Marcelino L. Bernardo, Jr., Robert N. Muller , Virgil Acuff and Paul C. Lauterbur
Department of Chemistry, State University of New York at Stony Brook, Stony Brook, N.Y. 11794

Small ferromagnetic particles in suspension are expected to induce in their vicinity fluctuations in the value of the local magnetic fields, which will affect the shapes and widths of the NMR signals from the surrounding material. These effects will depend upon the strength of the local induced magnetic fields and also upon diffusion phenomena. We have examined the water proton signals from gels containing magnetite (Fe_3O_4), and found some simple empirical correlations, although a full theoretical treatment has not yet been carried out. Fig. 1A shows an example of such correlations, and in Fig. 1B we present an image which shows the variations in signal intensities resulting from spin-echo sequences. The phantom used consisted of a set of gel suspensions of 1.5μm magnetite particles with concentrations of ferromagnetic material (up to 600 micromoles/liter).

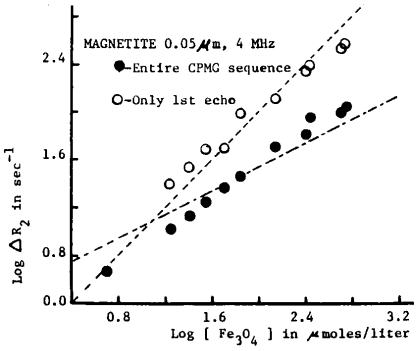

Figure 1 A

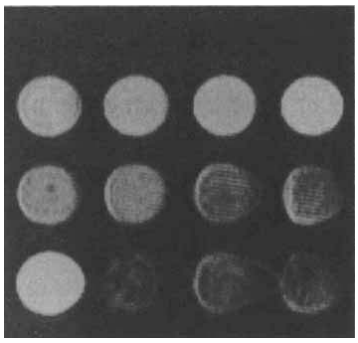

Figure 1B

It is also expected that such particles will induce similar effects in organs and tissues of living animals, and will be useful in magnetic resonance medical imaging, for those diagnostic procedures now carried out by gamma emission imaging, using radioactive colloids and microspheres. To evaluate such possibilities we have injected 0.05μm particles of magnetite into the veins of rats and dogs, and imaged them 0.094 and 0.6 tesla, respectively.

Although it is expected that small particles will be removed from circulation through the reticuloendothelial system, some deposition may also occur in the lungs, as it seems apparent from Fig.2.

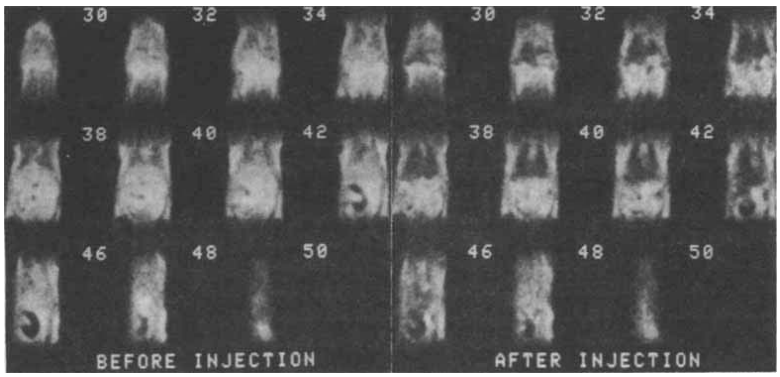

Figure 2: Coronal slices from 3D images of a rat, obtained at 0.094 T, before and 1 hour after an iv injection of 10 mg/Kg of body weight of 0.05 μm magnetite particles, using a spin-echo sequence (RT=1 sec; echo time=30 msec)

In figure 3 we present 2D transverse slices through the upper abdomen of a dog, obtained at 0.6 T using the same experimental conditions reported for the rat.

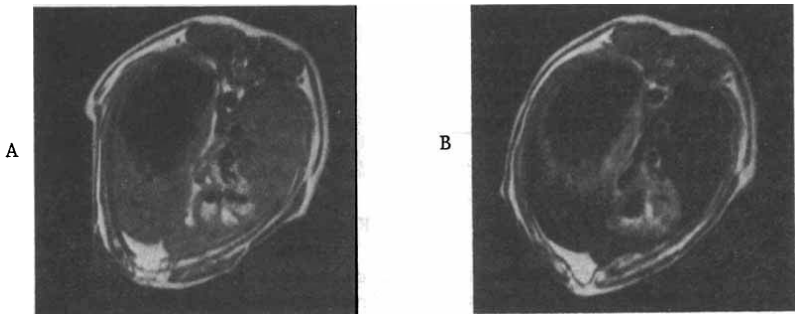

Figure 3: A-before injection; B-1hour after injection

Ackowledgement: We wish to ackowledge the Department of Radiology, North Shore University Hospital, Manhasset, N.Y. 11030, for allowing us to use their 0.6T NMR imaging system during the week ends.

SMRM, 1985.

A New High Speed Spiral-scan Echo Planar (SEPI) NMR Imaging-I

C.B.Ahn, C.Y.Rew, J.H.Kim, O.Nalcioglu*, and Z.H.Cho*

Dept. of Electrical Science
Korea Advanced Institute of Science, Seoul, Korea

Abstract

A new high speed imaging technique using Spiral-scan Echo Planar Imaging (SEPI) is proposed and experimentally examined. In the new proposed technique, two linearly increasing sinusoidal gradient fields are applied simultaneously. This results in a spiral scan trajectory in the spatial frequency domain (K-domain) covering the entire frequency domain uniformly (see Fig.1). Advantages of the method are: (a) Circularly symmetric T_2 weighting, resulting in circular symmetric point spread function in the image, (b) elimination of discontinuities in gradient waveforms together with small gradient fields at the beginning, which in turn will reduce initial transients as well as steady state distortions, and (c) effective rapid spiral scan from d.c. to high frequency in a continuous fashion to ensure multiple pulsing with interlacing technique for the further resolution improvement without T_2 decay image degradation. Using the spiral trajectory, reconstruction of SEPI is performed by the convolution backprojection of the projection data that is obtained by a sequence of processes after the fast Fourier transform for the radially arranged data sets.

Finally, in Fig.2, a two dimensional slice of a phantom image is shown. The phantom image was obtained in 64 msec using 64X64 matrix.

* Also at Dept. of Radiological Science, University of California, Irvine, CA92717, USA

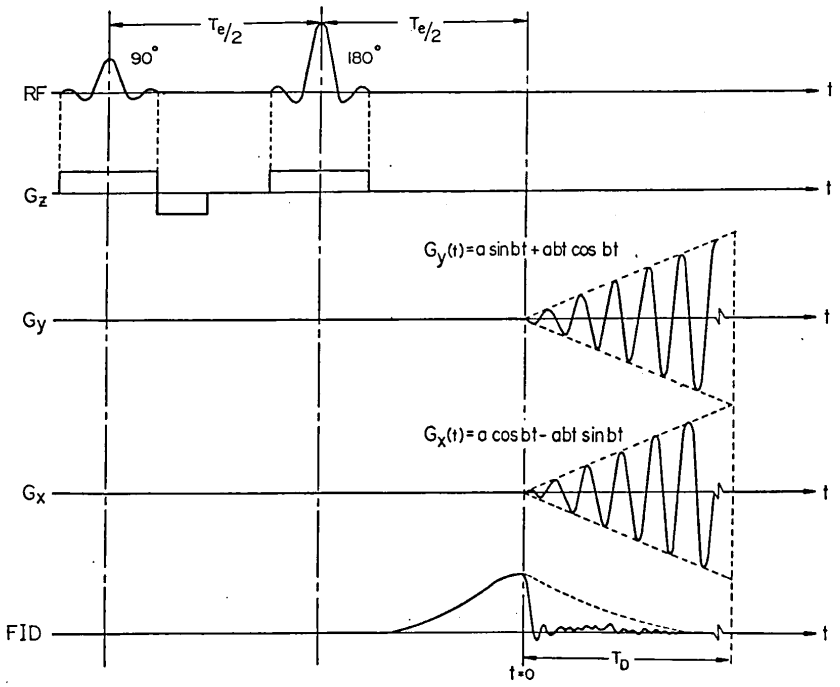

Fig.1 The pulse sequence for the spiral scan EPI (SEPI) technique.

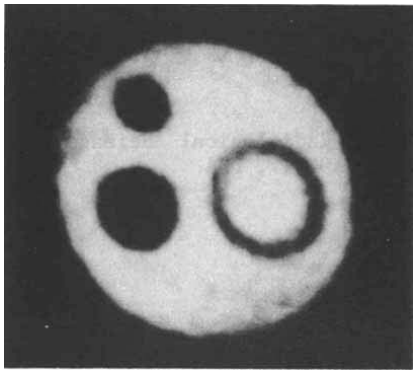

Fig.2 An experimentally reconstructed phantom image using a 64X64 matrix size within a total measurement time of 64 msec using the KAIS 1.5 KG resistive magnet system.

SMRM, 1985.

RAPID IMAGES AND NMR MOVIES

A. Haase, J. Frahm, D. Matthaei, W. Hänicke, K.-D. Merboldt
Max-Planck-Institute for Biophysical Chemistry, P.O. Box 2841,
D-3400 Göttingen, FRG

Purpose

To provide a method for single-shot NMR imaging which fulfills the following conditions:

- variable compromise between time resolution and spatial resolution
- no need for extremely short gradient switching times (i.e. applicable to superconducting magnets)
- low RF power (i.e. applicable at high field strengths)
- no limitation due to T_2 or T_{2eff}
- 2DFT reconstruction algorithm

Methods

We will present two solutions to the above problem which are based on the use of two different types of NMR signals. The first technique, single-shot STEAM imaging (STEAM = Stimulated Echo Acquisition Mode), employs a multiple partial readout of longitudinal magnetizations stored after application of two 90^{o} RF pulses (see Fig. 1). The second technique, FLASH imaging (FLASH = Fast Low Angle Shot Imaging) takes advantage of a related idea using gradient echoes. Specific properties are:

Single Shot STEAM Imaging:

- time limitation due to T_1 (i.e. emphasis of long T_1 values)
- spin echo properties with respect to inhomogeneities of the static magnetic field B_o

FLASH Imaging:

- no time limitation (i.e. arbitrary compromises between time resolution and spatial resolution)
- optimal signal-to-noise ratio
- good homogeneity of B_o required
- NMR movies possible

Results

Both techniques are applicable to high-field NMR imaging using superconducting magnets. Experiments have been carried out at 2.3 Tesla. Single shot STEAM imaging provides good access to short measuring times (ca. 100 ms - 1 s) but the images are limited in S/N. FLASH images exhibit excellent S/N but require measuring times of at least 400 ms (32 * 64 pixel) using our actual gradient system (see Fig. 2). FLASH NMR movies have been recorded by means of continous imaging without waiting between successive image acquisitions and without degrading the image quality. NMR movies of phantoms, animals, and humans will be demonstrated.

Conclusions

High quality images with measuring times of 1-2 seconds are accessible. NMR movies can be recorded without image degradation.

Using homogeneous high-field magnets and improved gradient systems, FLASH imaging may become a routine imaging experiment.

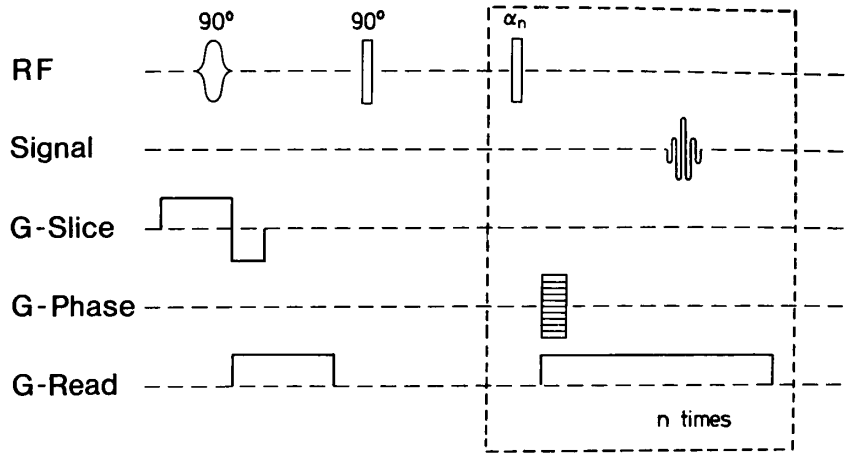

Fig. 1: Schematic diagram of a rapid STEAM imaging sequence

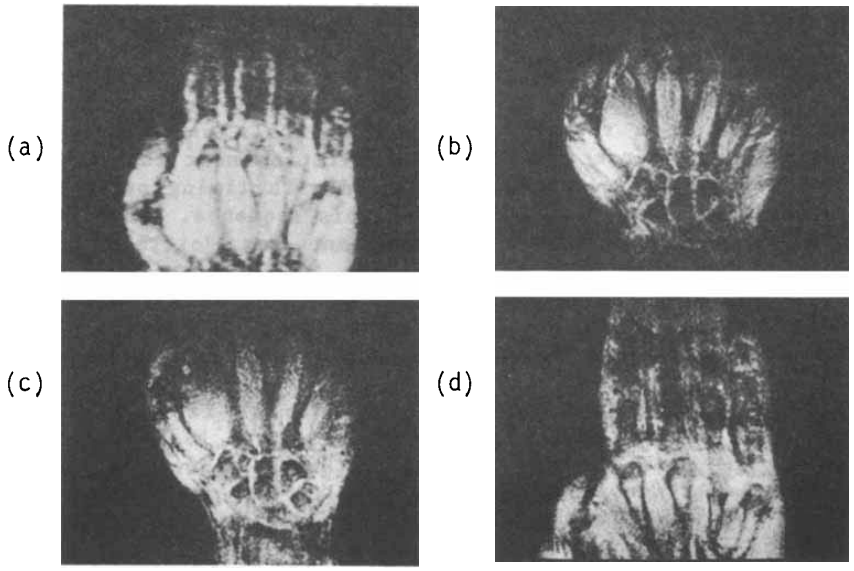

Fig. 2: FLASH NMR images of horizontal slices of thickness 6 mm through the human hand. (a) measuring time: 1 sec, spatial resolution 64 * 128, (b)-(d) measuring time: 2 sec, spatial resolution 128 * 128

SMRM, 1985.

RARE - Imaging : A Fast Imaging Method for Clinical Routine

J. Hennig, University of Freiburg

In order to reduce the long patient investigation times in MRI,we have devellopped a method to acquire sufficient data for a 256 x 256 image with down to one excitation of the spin system. The method is based on the principle of echo imaging, where each echo in a long echotrain is encoded differently for spatial coordinates. Due to the nature of the data sampling, the image contrast is determined mainly by the relaxation time T_2,which makes it especially suited to detect lesions with long T_2.The contrast can be varied widely and optimized to detect lesions with certain relaxation times.RARE (= Rapid Acquisition with Relaxation Enhancement) works equally well in combination with Inversion - Recovery and Partial Saturation methods to give additional T_1 - contrast.

Contrary to other methods for faster data acquisition,the gain in imaging speed has not necessarily to be paid for by a loss in signal - to - noise.An explicit mathematical treatment, confirmed by the direct comparison of a RARE - image with a conventional 2DFT- image of the same slice of a patient shows, that the signal amplitudes are the same for structures with long T_2.The efficiency of the method regarding the signal sampled per unit of time is therefore more than an order of magnitude better for those structures than that of normal 2DFT- imaging.

Since the implementation of RARE on our .23 T iron shielded resistive system,we have investigated more than 400 patients with this method. Apart from the general usefulness

in patient positioning,we have found, that the possibility to detect and locate lesions after only a few seconds investigation time is excellent, especially in the head, where lesions with long T_2 are dominant.

The very good data sampling properties of RARE can be used to make heavily T_2-weighted images of very thin slices with very high signal to noise by accumulation in a few minutes, making this domain accessible to low field imaging.

SMRM, 1985.

Faster MR Imaging -- Imaging with Half the Data

Paul Margosian, Ph.D.
(Siemens AG, Henkestrasse 127, 8520 Erlangen,
West Germany)

The simplest method for reducing data acquisition time for MR imaging is to use only half (or approximately half) the normal number of measurements. Three such methods are described in this report. These are as follows:

(1) Use the central 128 data lines (for 256 imaging), sinc interpolate. In this method only the central 128 steps of the phase encoding gradient are used (with the normal 256 samples on each line), this data is placed in the center of a 256 x 256 matrix which is otherwise zero, and the normal FFT reconstruction performed (amplitude image). For this (old and well known) method, the cost of taking only half the data is that spatial resolution in the phase encoding direction is reduced by a factor of two. The theory for this is well known, images are shown for comparison with the other two methods. It is necessary to make a Hamming rolloff over the outer 8 data points (in the truncated direction) in order to minimize "ringing" artifacts. This method is robust and simple, but is not so esthetically pleasing.

(2) Use the upper (or lower) half of the phase encoding steps, place into a 256x256 matrix which is otherwise empty, reconstruct (complex FFT), take the real part. The imaginary part of this reconstruction is quite far from the desired image, so it is important to remove phase errors that mix real and imaginary parts of the reconstruction. It is also necessary to make a rolloff of the raw data (over the central few lines) in order to remove ringing artifacts. A few extra data lines are needed in order to make this rolloff possible. This method works well for spin-echo data for both low and high field machines.

For this "Half Fourier" method, full spatial resolution is retained, at the cost of reducing signal to noise ratio by almost a factor of two. In this method the phase information has been used to keep full resolution. The image quality obtained is sensitive to phase errors in the data.

(3) Use every second step of the phase encoding gradients, place the data lines in their correct places in an otherwise empty matrix, interpolate to fill the gaps (at least a cubic is needed), and take at least 8 extra data lines near the center (this means that 16 central measurements are taken with no gaps), reconstruct (FFT amplitude reconstruction). When this method is used, the data is fundamentally undersampled causing two ghost images in the transform; the interpolations and use of some extra data serve to reduce the amplitude of these ghost images. With this method, full spatial resolution is retained with almost no loss in signal to noise ratio, but at the cost of making two faint ghost images, as previously mentioned. This method is not as sensitive to phase errors as is method (2).

Conclusions: Each "Half-data" method (really 53% for methods (2) and (3)) has virtues and drawbacks. For all methods, data acquisition time is reduced by a factor of two. Method (1) is the easiest to try but costs a factor of two in spatial resolution. Method (2) provides the best (cosmetically) images (full spatial resolution retained) as long as there are not severe phase errors, but is the most complicated to try and costs almost a factor of two in signal to noise. Method (3) is simple to try and keeps almost full spatial resolution and signal to noise ratio, but at the cost of two faint "ghost" images.

SMRM, 1985.

HIGHLY HOMOGENEOUS, EFFICIENT RESONATOR FOR HIGH FIELD IMAGING

Cecil E. Hayes,* William A. Edelstein,** John F. Schenck,**
Otward M. Mueller** and Matthew Eash*
*GE Medical System, Milwaukee, WI
**GE Corporate Research & Development, Schenectady, NY

We have designed an RF resonator which combines good signal sensitivity and high homogeneity with the ability to perform quadrature excitation and reception. The coil is highly efficient; that is, coil losses are small compared to patient losses. The RF field homogeneity, which is significantly better than of a saddle coil or slotted tube resonator, permits accurate multi-echo pulse sequences. Use of quadrature excitation and reception reduces RF power deposition and improves the signal-to-noise ratio (SNR) (1).

A uniform transverse B_1 field can be produced in a long cylinder by a surface current which runs along the length of the cylinder and is proportional to $\sin\phi$, where ϕ is the azimuthal angle. Our design (2), which we call the "birdcage" resonator (Fig. 1), automatically develops the desired sinusoidally weighted currents at resonance in N evenly spaced, parallel conductors on the surface of a cylinder. Each version behaves like a lumped element transmission line which is connected to form a closed circle. The low pass birdcage in Fig. 1(a) is analogous to an N section, low pass LC filter (Fig. 2), where the inductors represent the short segments of the birdcage end rings. Likewise the high pass birdcage in Fig. 1(b) corresponds to a high pass LC filter where the inductors arise from the straight, parallel conductors. In both such structures the desired resonance consists of a standing wave with wavelength equal to the circumference of the closed circle. Two standing wave patterns are possible and can both coexist in the same resonator without interfering with each other. If the standing wave has surface currents proportional to $\sin\phi$, it produces a B_1 field in the x direction. Currents proportional to $\cos\phi$ produce a B_1 along y. Quadrature operation utilizes both of these modes simultaneously.

Figure 3 compares computed field intensity contour lines in the transverse midplane for a saddle coil and for a sixteen segment birdcage resonator. The regions of field inhomogeneity extend into the sample volume for distances comparable to the separation between conductors. More conductors could be added to the birdcage to eliminate nearly all of the field strength ripples. The chief remaining source of inhomogeneity in the birdcage arises from its finite length. The higher magnetic energy stored near

the saddle coil wires but outside the sample volume tends to degrade that coil's filling factor compared to that of the birdcage. The many turns of the birdcage are effectively connected in parallel. Therefore the birdcage has low inductance and low coil losses. The ratio of empty coil Q to loaded Q is typically greater than five. Hence the coil losses contribute less than 11% of the observed noise voltage.

With quadrature excitation in human subjects, the power required was 50 to 70% of that required by a linear oscillating B_1 field. With quadrature reception the SNR was improved by a factor of 1.33 compared to linear reception (3). Use of quadrature excitation and reception also reduces RF penetration artifacts at 1.5T.

REFERENCES

1. C.-N. Chen, D.I. Hoult and V.J. Sank, J. Magn. Reson. 54, 324 (1983).
2. C.E. Hayes, W.A. Edelstein, J.F. Schenck, O.M. Mueller and M. Eash, J. Magn. Reson. July 1985.
3. G.H. Glover, C.E. Hayes, N.J. Pelc, W.A. Edelstein. O.M. Mueller, H.R. Hart, C.J. Hardy, M. O'Donnell & W.D. Barber, J. Magn. Reson. (in press).

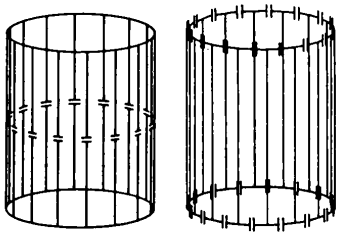

Fig. 1(a) Low pass birdcage

Fig. 1(b) High pass birdcage

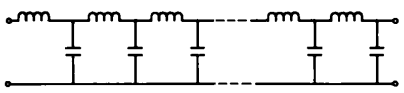

Fig.2. Low pass filter

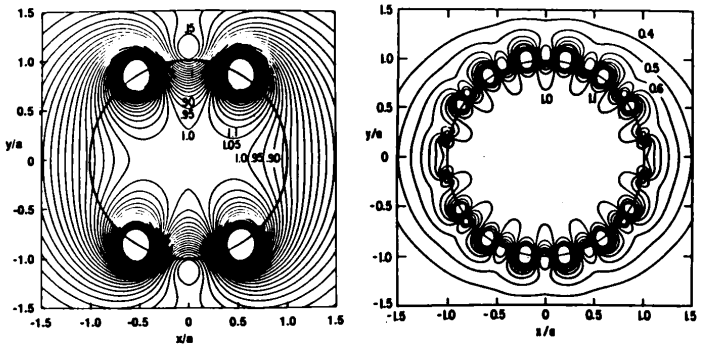

Fig.3. Field intensity for saddle coil and birdcage resonator.

SMRM, 1985.

IN-VIVO MAGNETIC RESONANCE IMAGING OF SELF-DIFFUSION

D. Le Bihan, E. Breton*, and A.Syrota
Département de Biologie du Commissariat à l'Energie Atomique, Hôpital d'Orsay, 91406 Orsay, France
*THOMSON-CGR, 551 rue de la Minière, 78530 Buc, France.

Purpose : To obtain calculated in-vivo self-diffusion images from two spin-echo sequences, ρ, T_1 and T_2 being eliminated.
Introduction : NMR studies of diffusion in biological systems have provided significant results, particularly when attempting to appreciate restricted diffusion of water (1). These studies require constant or pulsed (Stejskal-Tanner method (2)) field gradients. Such measures are possible in Magnetic Resonance Imaging (MRI) as recently demonstrated (3). We are proposing a method to obtain calculated in-vivo self-diffusion images from just two 2DFT spin-echo sequences. Knowing the gradients used in the two sequences, the diffusion coefficient in each voxel is then calculated. We tested this technique on phantoms and used it on normal volunteers.
Method : It rests on two acquisitions : The first is a multi-echo 2DFT spin-echo sequence with n echoes. A short inter-echo time TE' is used to minimize diffusion effect. The second is a single-echo 2DFT spin-echo sequence with long TE and higher gradients to maximize diffusion effect. When dividing the n^{th} echo signal (S_n) of the first sequence by the single-echo signal (S_1) of the second sequence, the effects of ρ, T_1 and T_2 are eliminated if nTE' = TE. Then the quantity (S_n/S_1) only depends on the diffusion coefficient (D) and $D = \ln(S_n/S_1)/(b_1 - b_n)$ is shown as an image. The b factors are entirely determined by gradient pulse parameters :

$$b_k = \gamma^2 \sum_{i=1}^{k} \sum_{j=1}^{N_i} G_{ij}^2 d_{ij}^2 \left[\frac{d_{ij}+d'_{ij}}{3} + I_{ij}\right]$$

where γ = gyro-magnetic factor, k = number of echoes, N_i = number of gradient pulse pairs on each axis (slice-selective, readout, phase-encoding) during i^{th} inter-echo delay. d and I are respectively gradient pulse length and separation time as shown in the following scheme :

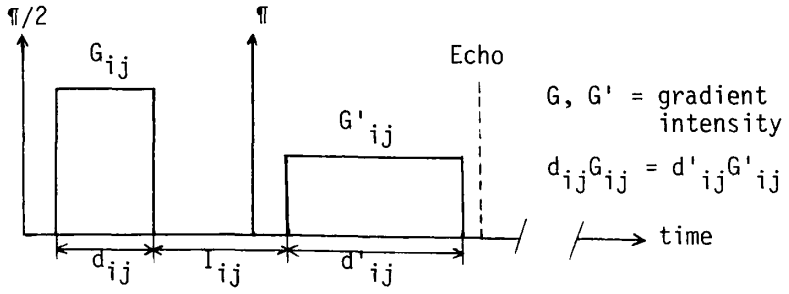

Results : The results obtained on phantoms and normal volunteers are shown. Acquisition parameters were : magnetic field 0.35 T and 0.5 T, 256 x 256 matrix, multi-slice mode, TE = 112 ms (single echo-sequence), TE = 28 ms and n = 4 (multi-echo sequence). In the single-echo sequence, readout gradient has been increased to maximize the diffusion effect and the b_1/b_n ratio.

Calculated contribution of each gradient to the b factors :

gradient	$b_1 = 2.08\ 10^8 s.m^{-2}$	$b_n = 1.59\ 10^6 s.m^{-2}$
readout	99.9 %	81.0 %
slice-selective	.3 %	4.6 %
phase-encoding	< .8 %	< 14.4 %

Measures on the calculated image of a phantom containing several tubes of acetone and water :

fluid	S_n/S_1	D(calculated) $(10^{-9} m^2 s^{-1})$	D (literature) $(10^{-9} m^2 s^{-1})$
water	1.62	2.34±.10	2.25 - 2.51 (4)
acetone	2.36	4.16±.15	4.47 (5)

Fig. 1 : Calculated diffusion image. Coronal head section of a normal volunteer.

As this method only requires a special single-echo sequence added to a standard multi-echo sequence commonly used by radiologists, clinical and physiological studies can be performed easily and rapidly.

References

1. Cooper RL, Chang DB, Young AC, Martin CJ, Ancker Johnson B, Biophys. J. 14, 161-177, 1974
2. Stejskal EO, Tanner JE, J. Chem. Phys. 242, 288-292, 1965
3. Wesbey G, Moseley M, Ehman R. Biomedical Magnetic Resonance, James TL, Margulis AR, Ed. Radiology Research and Education Foundation, San Francisco, 1984
4. James TL, McDonald, J. Magn. Reson. 11, 58-61, 1973
5. Cantor DM, Jonas J, J. Magn. Reson. 28, 157-162, 1977

SMRM, 1986.

SEPARATION OF PERFUSION AND DIFFUSION IN INTRA-VOXEL INCOHERENT MOTION (IVIM) MR IMAGING

D. Le Bihan, E. Breton*, M. Guéron
Groupe de Biophysique, Ecole Polytechnique, Palaiseau, France.
*Thomson-CGR, Buc, France.

Introduction : We designate as intra-voxel incoherent motions, the movements of molecules which, within a single voxel and during the measurement sequence, involve velocities in various directions and/or of various amplitudes. In a magnetic field gradient, these motions will produce distributed phase shifts, resulting in spin-echo attenuation, in addition to that from T2 relaxation during the spin-echo delay TE. In biological tissues, these motions are molecular diffusion and microcirculation of blood in the capillary network (1). The spin-echo attenuation S(TE)/S(0) due to diffusion is :

$$S(TE)/S(0) = \exp(-TE/T2).\exp(-b.D)$$

where D is the diffusion coefficient (typically 2.5 10^{-3} mm²/s for pure water at 40°C), and b is a factor depending only on the set of gradient pulses used in the spin-echo imaging sequence (2-3). For the capillary flow, the spin-echo amplitude is greater reduced by a term F(v), which may be evaluated as a function of the mean blood velocity (1-4 mm/s) (4) and of capillary geometry. If the direction of blood changes several times during the measurement sequence, $F(v) = \exp(-b.D^*)$ (macro-diffusion). The pseudo-diffusion coefficient D* is estimated to be typically in the range of 5-100 10^{-3} mm²/s. If the blood flow can be considered to take place in straight capillary segments during the measurement sequence, and if the segments are isotropically distributed, one finds $F(v) = |\mathrm{sinc}(c.v.)|$, where factor c depends only on the set of gradient pulses. Our simple model of biological tissues includes a volumic fraction f (typically a few percent) of water in blood flowing in open capillaries, and a fraction (1-f) of static (diffusing only), intra- and extracellular water, both assumed as having the same value for D and T2. The spin-echo attenuation in a single voxel is thus :

$$S(TE)/S(0) = \exp(-TE/T2).\exp(-b.D).[(1-f) + f.F(v)]$$

Method : IVIM images were generated on the basis of an apparent diffusion coefficient (ADC) from two images S and S' differently sensitized to these motions (2-3) :

$$ADC(x,y,z) = [\mathrm{Log}(S(x,y,z)/S'(x,y,z)]/[b'-b] \quad [1]$$

Use of ratio S/S' allows the effects of spin density, T1 and T2 to be eliminated (TR = TR' = 1 s, TE = TE' = 140 ms). The diffusion coefficient D and the perfusion factor f can be separately obtained by using three sequences. The first is a standard 2D-FT spin-echo sequence in which the effect of intra-voxel

motions is negligible. The others have additional, motion-probing, gradient pulses on the readout axis (2). The strength (0.34 G/cm and 0.48 G/cm) and duration (2 x 40 ms) of these pulses are great enough to eliminate the contribution of the flowing component ($f.F(v)<<1$), whereas the contribution of the static (diffusing) component is moderately reduced. Thus application of [1] to the second and third sequences gives an image of the ADC which is the image of the diffusion coefficient D. The ADC obtained from the first two images is :

$$ADC = D - [Log(1-f)]/[b'-b]$$

From the two ADC images, we obtain a calculated image of f.

Results : Models of different capillary geometry were computed to support the theoretical analysis, i.e. function F(v). A phantom was developed and imaged in view of evaluating quantitatively and separately diffusion and microcirculation. The phantom was a chromatographic column packed with Sephadex G100. Water flow was maintained in the interstitial volume, whereas intrabead water only diffused. The plot of Log(S/S') vs (b'-b) for several values of b' was linear as expected. The slope gave the known diffusion coefficient, and the intersection at b'-b = 0 gave f (here the interstitial volume). The method was then applied to human subjects. Images were generated at 0.5 T in a high-resolution multisection mode. The diffusion image and the perfusion image of a bone tumor were correlated with contrast-enhanced CT and digital subtraction angiography.

Conclusion : IVIM MR imaging appears as a very useful method for the quantitative evaluation of both the diffusion coefficient and perfusion in tissues.

References :

1-Budinger T.F.,Knittel B.L.,Bruner P.,Harrison C. Abstracts of the 4th Annual Meeting of the SMRM, 577, London 1985.
2-Le Bihan D.,Breton E.,Syrota A. Abstracts of the 4th Annual Meeting of the SMRM, 1238, London 1985.
3-Le Bihan D.,Breton E.,C.R.Acad.Sc.Paris;301,II,15,1109, 1985.
4-Lee J,In:Gabor K.,Burton M.A., Ed. Microcirculation Baltimore, University Park Press, 335-364, 1976.

LOWER EXTREMITY - BONE TUMOR

SE 1000/40

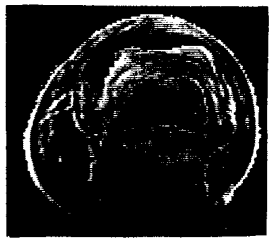

Diffusion image

Perfusion image

Tpm-B7

MOTION ARTIFACT SUPPRESSION TECHNIQUE (MAST™) IN MULTISLICE MR IMAGING

P. M. Pattany, M.Sc., J. L. Duerk, Ph.D., and J. M. McNally, Ph.D.

Clinical Science Center, Picker International, Highland Heights, Ohio

Artifacts and signal loss due to object motion and blood flow obscure the fine detail structure in 2DFT multislice imaging when using long TE/TR spin echo sequences. This is due to incomplete rephasing of the moving object at the end of the slice select gradient and at the center of data collection gradient.

Complete rephasing of the static and dynamic material within the slice is achieved by setting Ø to zero in the equation shown below.

$$\emptyset = \int_0 \gamma\, G(t)\, X(t)\, dt = 0 \quad \ldots\ldots\ldots \quad 1$$

where: γ Gyromagnetic ratio
$G(t)$ Gradient pulses applied at a given time t in a given gradient profile.
$X(t)$ Position of the material at a given time t.

The term X(t) can be expanded in a Taylor series as shown below.

$$X(t) = X_o + \frac{Xt}{1!} + \frac{Xt^2}{2!} + \frac{Xt^3}{3!} + \ldots \text{etc}$$

Each order of the above Taylor series equation has been integrated seperately using equation 1, thus completely rephasing static and dynamic material in the slice direction and read direction.

These studies include gradient profile simulation. Comparison of orbits, liver and lumbar spine images obtained with the conventional spin echo sequences and motion artifact suppression technique sequences are presented to show artifact reduction as higher order terms of X(t) are incorporated in the new sequence profiles.

The images obtained with the motion artifact suppression technique reduces/eliminates the artifact due to cardiac, respiratory, orbit and CSF and blood flow motions and signal intensity of the CSF is highlighted.

Reference:

1. Motion Artifact Suppression Technique (MAST™*) of Magnetic Resonance Imaging. P. M. Pattany, J. M. McNally. Patent Apllicalton Number 766, 757. Filed August 16, 1986.

* MAST is a trademark of Picker International.

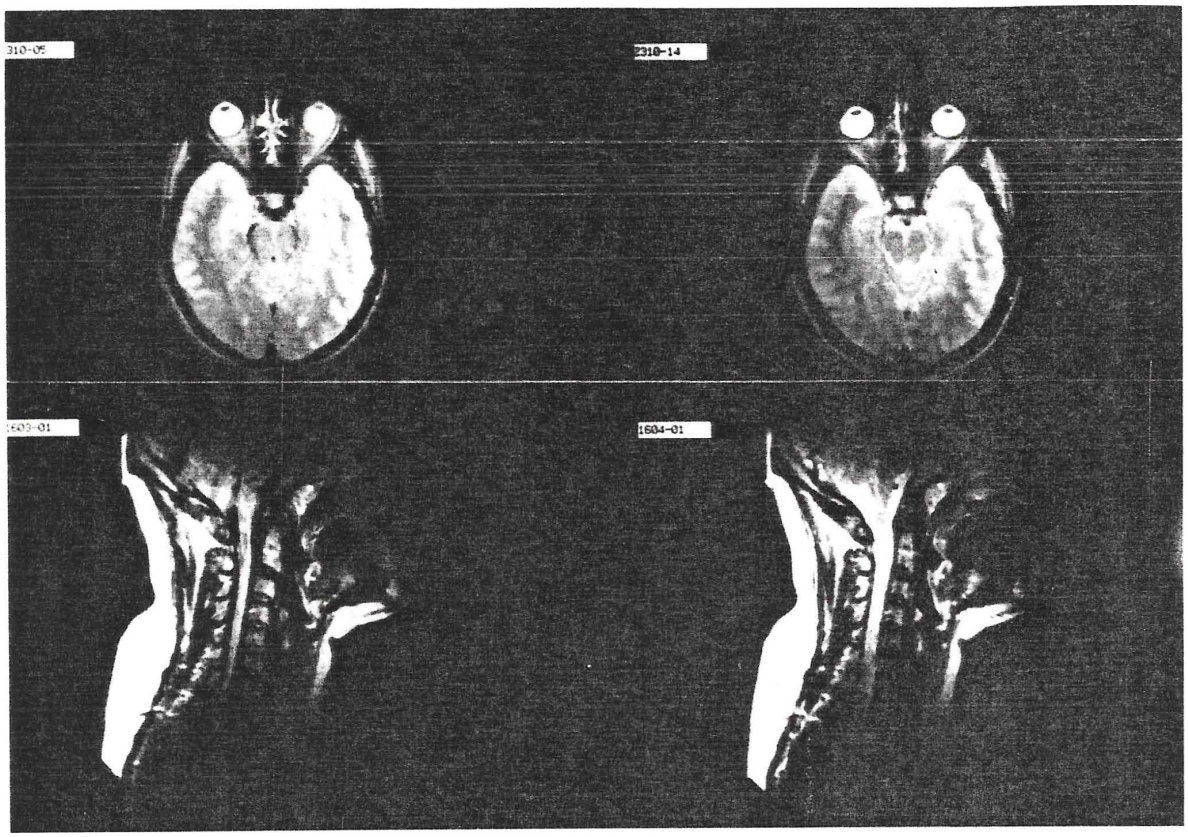

Conventional Spin Echo
Sequence
TR 2000 mSec
TE 100 mSec
1 Excitation
256 Views

MAST™
Spin Echo Sequence
TR 2000 mSec
TE 100 mSec
1 Excitation
256 Views

"SIMA" - Simultaneous Multislice Acquisition for Magnetic Resonance Imaging

J. Szumowski, D.B. Plewes, C.L. Dumoulin*, S.P. Souza**
Department of Radiology, University of Rochester, Rochester, N.Y.
*Corporate Research and Development Laboratories, General Electric Company
Schenectady, N.Y.

Clinical multislice techniques provides an efficient method of decreasing imaging time per slice over single slice sequences of the same TR with the number of slices available proportional to TR. This typically requires long TR values for a clinically reasonable number of acquired slices. It can be shown that short TR spin echo sequences provides maximum contrast/noise for a given scan time (CNR) for most tissue pairs of interest. This suggests that short TR's should be used to exploit these contrast advantages; however, in the limit of decreasing TR, multislice sequences become serial single slice acquisitions.

A better approach to short TR multislice imaging can be achieved with 3-D Fourier volume sequences which provide a signal/noise advantage. In practice, Fourier volume imaging for a limited number of slices suffers from two limitations. The location of slices are contiguous which may result in a more dense sampling of the object than clinically necessary. Furthermore, for symmetric studies such as imaging of the knees, breasts or TMJ, multiple thin slices would need to be collected in two separate scans. Secondly, anisotropic Fourier volume imaging can exhibit severe undersampling artefacts which become clinically apparent as the number of slices become small.

In this presentation we propose a different approach to volume imaging where several slices are simultaneously excited and detected by applying selective pulses which are modulated to provide a multifrequency excitation pattern. The corresponding RF phase modulation can be derived from the convolution properties of the Fourier transform. To illustrate this scheme of Simultaneous Multislice Acquisition (SIMA), Figure 1 outlines the excitation pattern for 4 slices. By application of the four excitation patterns and by appropriate data manipulation of the acquired data, the individual slices can be calculated with the Hadamard transform similar to that discussed by Maudsley (1).

This technique provides many potential advantages over multislice or Fourier volume imaging. In particular, the location and separations between slices can be more flexible than with Fourier methods. Furthermore, the sampling limitations of Fourier volume technique are not present, allowing a limited (4-16) number of slices to be acquired.

This provides a corresponding increase in signal/noise over the serial single slice acquisition for those cases where short TR is desired. In addition, this method can be applied to provide a multislice capability to intrinsically single slice methods such as Inner Volume imaging (2) and some chemical shift imaging methods (3,4). The primary limitation of this technique is due to increased RF power requirements necessary to excite several slices simultaneously. This problem can be overcome by exploring the method of RF excitation power reduction proposed by Connolly et al.(5).

We have implemented this method on a 1.5 T Signa imager and will review the details of implementation, discuss the technique capabilities and compare its imaging features to those of standard multislice techniques.

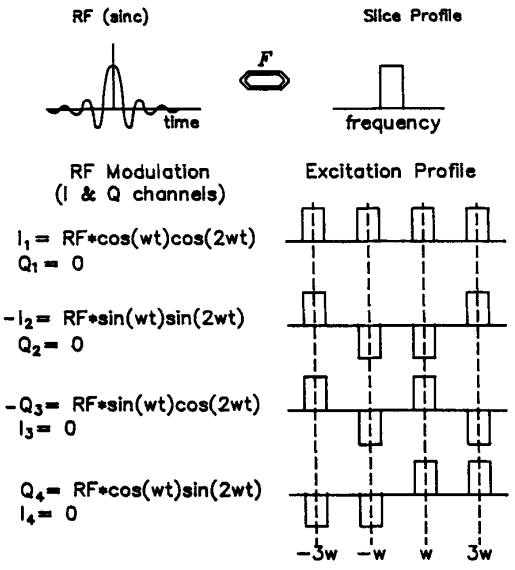

Figure 1. RF modulation (left) which generates multislice excitation profile (right) for 4 slices. The approach can be readily extended to 2^N number of planes.

References

1. Maudsley, A.A., JMR, 41,112,1980.
2. Feinberg, D.A., et al. Radiol., 156,743, 1985.
3. Kunz, D., Magn. Reson. Med., 3,639, 1986.
4. Joseph, PM., JCAT, 5,651,1985.
5. Connolly, S., Nishimura, D., Macovski, A., 5th SMRI Meeting, San Antonio, March 1987

** General Electric Consulting Services
Schenectady, New York 12305

P38

SELECTIONS OF PHASE ENCODINGS IN MR FLUOROSCOPY

T Tasciyan, F Farzaneh, JN Lee, RC Wright, SJ Riederer
Duke University Medical Center, Department of Radiology

In MR Fluoroscopy, images can be produced continuously at rates as high as 30/second. This is accomplished by applying a limited number N of phase encodings to a basic FLASH sequence and using a special reconstruction scheme. The encodings are applied repeatedly and the images are reconstructed by sliding a window of width N along the acquired data. Testing the method on a dynamic phantom has revealed that the motion depicted by successive reconstructed images may be in slight discrepancy with the actual movement of the phantom, the former being less smooth. To observe and smooth the character of the motion in the reconstructed images, further phantom studies have been carried out using a) different numbers of limited phase encodings; b) different distributions of phase encodings; c) different directions of motion; i.e., motion along readout vs. motion along phase encoding.

One alternative in tracking motion smoothly is to simply record a limited number of phase encodings, repeating each at an interval of N*TR, automatically updating in frequent intervals. For this case, a tradeoff exists between spatial resolution and time resolution dictated by the velocity of the phantom. The phantom used consisted of a vial 2cm in diameter and 8cm in length rolling at a velocity of 5cm/sec. The use of only 24 phase encodings along the long dimension of the vial portrayed the motion well, giving adequate spatial resolution at 12 images/sec.

Since the lower frequency phase encodings determine the crude shape of the image and hence the gross location of the phantom, another scheme updates the lower frequencies more often, sampling the encodings nonuniformly. With N limited phase encodings and K lower frequency encodings, the first reordering scheme N,K,N,K,... for N fixed and K variable gives best results when 1/3 K/N 1/2. The second reordering scheme updates at an even higher rate by recording first odd then even phase encodings: N/2odd, K/2odd, N/2even, K/2even, ... However, this distribution artifactually doubles the phantom as the sliding window can contain odd low frequency phase encodings from one position and even low frequency phase encodings from another.

Presently, the results are being extended to phantoms with different velocities.

SMRM, 1988.

Magnetization transfer contrast (MTC) in ^{1}H-NMR imaging.

S.D. Wolff and R.S. Balaban
Laboratory of Cardiac Energetics, NHLBI Bethesda MD 20892

Introduction: Tissue water protons are in dynamic exchange and interaction with numerous molecules and structures. In these studies we have attempted to image the molecules exchanging magnetization with "bulk" water spins using magnetization transfer experiments.

Materials and Methods: The rationale for these experiments using magnetization transfer for imaging exchange processes has been previously published from this laboratory using ^{31}P(1). To detect magnetization exchange with ^{1}H water, spins in exchange with water are selectively irradiated and the effect on the instensity and T_1 of water ^{1}H is observed. Images of this exchange can be obtained as either ratio images, collected with and without irradiation(1), or by imaging the T_1 effects of the irradiation with a T_1 sensitive imaging sequence. All experiments were conducted on a GE CSI instrument at 4.7 Tesla. The rabbit kidney model used in these studies has been described elsewhere (2).

Results: Using this approach we have been successful in ratio imaging mM concentrations of urea and ammonia in water phantoms by irradiating the urea or ammonia resonances and observing the effect on the large (110 M) proton resonance. This method results in an enormous gain in the detection of metabolites like urea and ammonia since the effect on the water peak is much larger that the magnitude of the metabolites alone. However, in attempting to use this method in vivo, an interesting complication was observed. Over a broad range in frequencies surrounding the main water resonance, irradiation resulted in a specific decrease in the water resonance (i.e. Ms/Mo <1). A plot of one such experiment on the kidney in vivo is shown in Figure 1.

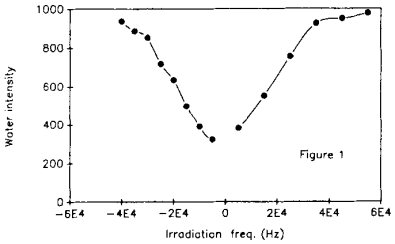

Here the magnitude of the water resonance as a function of irradiation frequency (0.4 watts for 4 sec) is plotted. The effect of this irradiation was roughly symmetrical around water with an approximate half width of 30000 Hz. This effect was not seen in water phantoms and was reproduced in tissue removed for the animal and placed in a sample tube.

The effect of this irradiation was specific for water. Figure 2 shows proton spectra without (A) and with (B) irradiation(10KHz below the water frequency). The water resonance(i) was decreased 40% while trimethylamine(ii) and fat(iii) resonances were unaffected even though the irradiation was closer in frequency to these metabolites than water. A striking effect on water T_1 was also observed by the irradiation, further indicating the specific nature of this interaction. Under conditions identical to those used in Figure 2, the T_1 of renal water was 1.2 sec in control and 0.45 sec after irradiation. Irradiation could result in a >10 fold decrease in overall water T_1 depending on the strength and frequency of the irradiation.

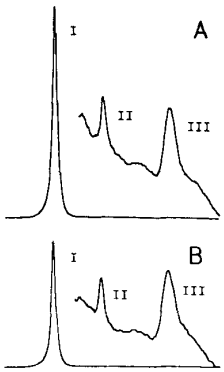

This T_1 effect was used to image the kidney in vivo. Using this approach, high contrast images of the different zones of the kidney were obtained with low level irradiation of the "hump". These high contrast images demonstrate that the magnitude of the water magnetization transfer is different in different tissue types resulting in excellent image contrast based on this exchange process.

Discussion: These data demonstrate that exchange between metabolites and water as well as water-water exchange can be imaged using magnetization transfer techniques. In vivo, this exchange processes is dominated by the interaction of water with a very broad component in the NMR spectrum (~30000 Hz). Simple modeling of this phenomenon suggests that this could be due to exchange of water with a broad component associated with protein or lipid structures with a rate constant on the order of 1 sec^{-1}. These calculations also indicate that this interaction could be an important component of water T_1 and T_2 in tissues. Summary: This new form of "contrast", MTC, could be useful in the imaging of different tissue conditions where the interaction of water with the protein and lipid matrix may be disrupted such as in edema or forms of cancer.

References: 1) Hsieh, P.S., and R.S. Balaban. J. Magn. Res. 74:574,1987. 2) Wolff, S.D. and R.S. Balaban. J. Magn.Res. 75:190,1987.

SMRM, 1988.

Localized Proton Spectroscopy of Patients with Cerebral Infarction

H. Bruhn, J. Frahm, M.L. Gyngell, K.D. Merboldt, W. Hänicke, R. Sauter*)
MPI für biophysikalische Chemie, Postfach 2841, D-3400 Göttingen, FRG
*) Siemens AG, UB Med, Henkestr. 127, D-8520 Erlangen, FRG

Purpose

To noninvasively assess the metabolic consequences of acute stroke in man using image-selected localized proton spectroscopy.

Methods

Following FLASH MRI to determine the position and size of a lesion, localized STEAM spectroscopy was performed using echo times of 50 ms and 270 ms and repetition times of 1.5 s. Typically, proton spectra were recorded from 3x3x3 cm^3 volumes in about 6 minutes. Details of the stimulated echo localization sequence and its implementation on a conventional 1.5 T Siemens Magnetom are reported in a further presentation.

Results

The Figures compare localized proton NMR spectra from the insular area of a normal volunteer (bottom) with spectra from acutely infarcted regions of two arteriosclerotic patients of similar age (43 years). The patients were investigated 4 days (left frontal cortex) and 26 weeks (right occipital area) after infarction, respectively.

The proton spectra of early post-ischemic brain tissue in vivo are characterized by
- a complete loss of N-acetyl aspartate (NAA),
- a reduction of the total creatine signal by about 50% to 5 mM, and
- a dramatic increase of lactic acid (here to about 16 mM)

Older infarctions present with
- a strong increase of the lipid signals
- a significant reduction of NAA depending on the extent of cell damage, and
- no enhanced lactic acid.

Discussion

The present study directly reveals for the first time that an acute cerebral infarction results in an early loss of NAA. This 'long-term' neurotransmitter appears to be characteristic for functional neural tissue. Its loss is in agreement with death of neuronal cells. In fact, the corresponding production of large concentrations of lactic acid is readily assessed. This observation lends itself to an estimate of the degree of focal hypoxia in the follow-up of a stroke patient so that the adequacy of therapy could be directly monitored.

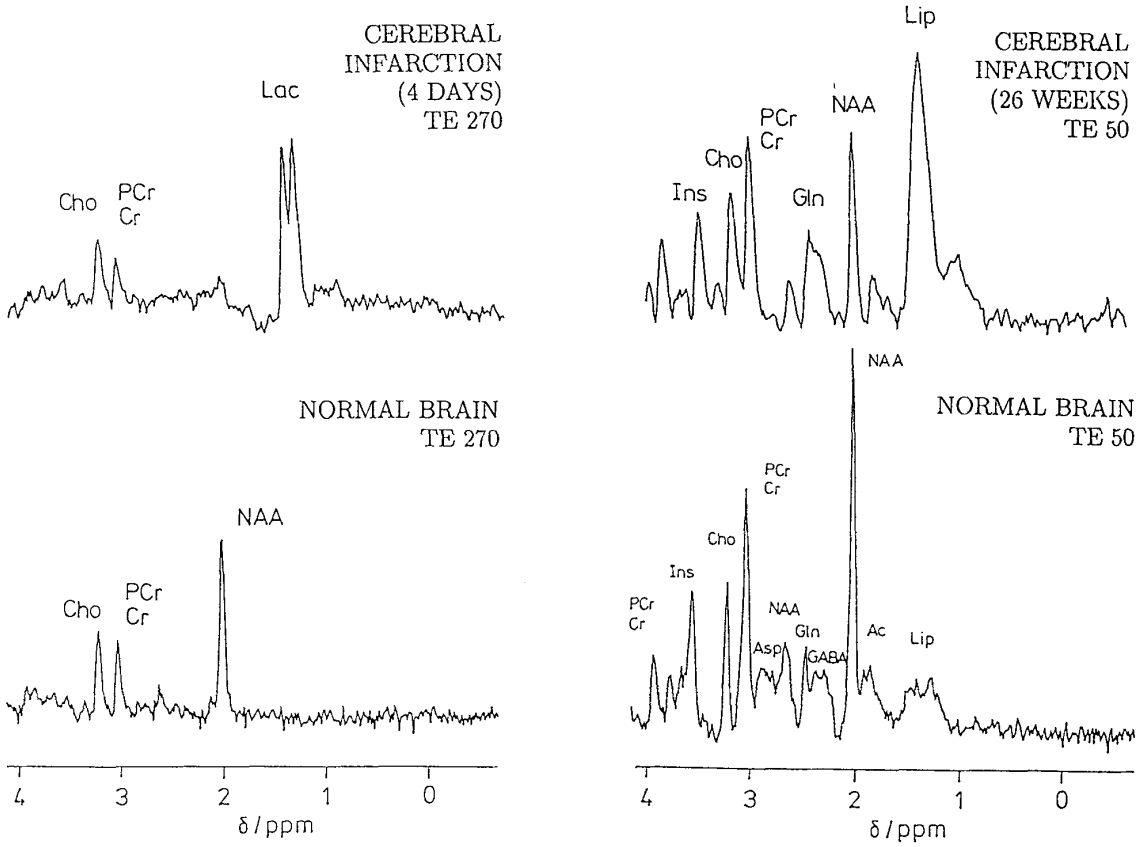

Advances in Echo-Planar Imaging

P. Mansfield, B. Chapman, R. Coxon, P. Glover, A.M. Howseman, R.J. Ordidge., M.K. Stehling and R. Turner
Department of Physics, University of Nottingham, Nottingham, England.

Introduction

Echo-planar imaging (EPI) is a snap-shot technique[1,2] capable of producing complete images in times ranging from 10 to 100 ms. The precise timing depends on T2. For example in biological tissue with an average T2 of 30 ms one may wish to produce images in less than this time if full spin density maps are required. If, however, T2 discrimination is required longer imaging times may be used which effectively filter out the short T2 components in an image.

Several minor variants of the EPI method have been described[3,4] which have a number of practical advantages. The first is the blipped echo-planar single-shot technique (BEST)[3]. This technique effectively scans half the k-plane in a one pass parallel raster which means that images can be extracted from data in a single shot lasting typically 60 ms. (Note, however, that although the original echo-planar k-plane raster scan is a zig-zag, one shot images may also be succesfully obtained from this experiment). Since only half k-space is scanned, the images produced are real.

Method

A simple modification of BEST which we call modulus-BEST (MBEST) scans all of the k-plane, thereby producing a modulus image which is insensitive to phase errors and is, therefore, experimentally more robust. The disadvantage of MBEST is that it takes twice as long as BEST for the same spatial resolution and gradient strengths. An advantage of MBEST is that it produces images which are intrinsically T2 weighted and edge enhanced. However, a difficulty is that there is no control over this weighting.

T2 weighting may be introduced into BEST by a suitable pre-pulse procedure. Similar pre-pulse procedures allow fat and water separation of our images[5].

Results and Conclusions

The BEST and MBEST techniques have been implemented with proton resonances on our imaging machine running at an operating frequency of 22 MHz. With BEST, images comprising 128 x 128 pixels are produced in 64 ms. By doubling the broadening gradient in BEST we have been able to produce one shot images with a pixel resolution of 1.5 x 3.0 mm which corresponds to an equivalent array size of 128 x 256 pixels. With MBEST, images comprising 128 x 64 pixels produced in 64 ms. By extending the imaging time to 128 ms head images comprising 128 x 128 pixels may be produced.

Whole body results obtained in adult volunteers and patients will be presented.

We thank the Medical Research Council, the Department of Health and Social Security and the British Heart Foundation for financial support of the echo-planar imaging programme. We also thank Analogic Inc. and Oxford Magnet Technology for providing some equipment.

We are particularly grateful to A. Blamire and P. Gibbs for their help in various phases of this project.

References

1. Mansfield, P., J.Phys. C. 10, L55-L58, 1977.
2. Mansfield, P. and Morris P.G., NMR Imaging in Biomedicine, Academic Press, NY, 1982.
3. Chapman, B., Turner, R., Ordidge, R.J., Doyle, M., Cawley, M.G., Coxon, R., Glover, P. and Mansfield, P., Magn. Res. Med. 5, 246-254, 1987.
4. Howseman, A.M., Stehling, M.K., Chapman, B., Coxon, R., Turner, R., Ordidge, R.J., Cawley, M.G., Glover, P., Mansfield, P. and Coupland, R.E., Brit. J. Radiol. (to be published).
5. Ordidge, R.J. et al (to be published).

SMRM, 1988.

Simultaneous Spatial and Spectral Selective Excitation

Craig Meyer, John Pauly, Albert Macovski, and Dwight Nishimura
Magnetic Resonance Systems Research Laboratory, Stanford University

Many techniques for forming water/fat images using spectrally-selective excitation sequences have been studied. Most of these combine a spatially-selective pulse with a spectrally-selective pulse [1]; multi-slice acquisition is impossible with these techniques. One recent technique uses two offset spatially-selective pulses [2],[3]. However, for many applications a single pulse that is simultaneously spatially selective and spectrally selective is preferable to a combination of pulses. Using the **k**-space interpretation of small-tip excitation introduced by Pauly *et al* [4], we have designed such a pulse. We have applied the pulse to square-spiral fast imaging, where separate water/fat acquisition is necessary because of long readout times [5].

The problem of designing a pulse that is spatially and spectrally selective is similar to the problem of designing a pulse that is selective in two spatial dimensions [4]. For a spatial/spectral pulse the excitation is constrained to move linearly with time along the k_w axis, an axis conjugate to resonant frequency. In order to generate an adequate sampling structure, in (k_z, k_w) space, one must oscillate the slice-select gradient. We use a sinusoidal oscillation that is easy to generate, although other forms of oscillation can be used. This produces a **k**-trajectory analogous to sinusoidal echo-planar imaging. We have investigated various forms of **k**-space weighting. Fig. 1 shows the RF and gradient waveforms for a pulse that has Gaussian weighting on both k_z and k_w. The equations for this pulse are given below.

$$G_z(t) = G\cos\Omega(t-T)$$

$$k_z(t) = \frac{\gamma G}{\Omega}\sin\Omega(t-T), \quad k_w(t) = T - t$$

$$B_1(t) = B_1 e^{-\pi\left[\frac{\sin\Omega(t-T)}{A}\right]^2} e^{-\pi\left[\frac{t-(T/2)}{B}\right]^2} |\dot{\mathbf{k}}(t)|$$

Fig. 2 shows the simulated spatial slice profiles for both water and fat for the $\pi/2$ pulse in Fig. 1, demonstrating good suppression of the fat component. Fig. 3 gives the spectral response of the pulse over a range of $\pm$ 550 Hz, calculated by integrating over the spatial slice at each frequency. Note the good suppression for a range of frequencies around 230 Hz, the difference frequency between water and fat at 1.5 T. Note also the aliasing islands centered at $\pm$ 460 Hz, the gradient modulation frequency. We have implemented this pulse on a GE Signa 1.5 T scanner. With a 0.6 G/cm 460 Hz gradient, the slice width was less than 1.5 cm.

Some of the advantages and applications of this pulse are as follows: (1) Using this pulse, square-spiral fast images free of spectral artifacts are formed within a breath-holding interval. (2) Water/fat fast imaging using FID's rather than spin echoes is possible. (3) Spatial multi-slice water/fat imaging is possible with a single excitation pulse. (4) No delay between water and fat images is necessary, so "spectral multi-slice" imaging is possible. (5) A spatial/spectral $\pi/2$ pulse can be combined with a π pulse that performs another function, such as field-of-view restriction. (6) Off-resonance slices are not spatially offset, so a version of this pulse can be used to eliminate slice misregistration artifacts in conventional imaging. (7) The pulse is self-refocusing in z.

References

[1] P. M. Joseph, *J. Comput. Assist. Tomogr.*, **9(4)**, 651-658, 1985.
[2] H. W. Park, D. J. Kim, and Z. H. Cho, *Magn. Reson. Med.*, **4**, 526-536, 1987.
[3] A. Volk, B. Tiffon, J. Mispelter, and J. Lhoste, *J. Magn. Reson.*, **71**, 168-174, 1987.
[4] J. Pauly, D. Nishimura, and A. Macovski, *J. Magn. Reson.*, to appear, 1988.
[5] C. H. Meyer and A. Macovski, in *Proc. Sixth SMRM*, p. 230, 1987.

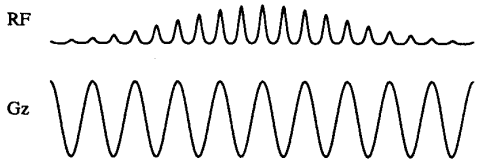

Figure 1: RF and Gradient waveforms.

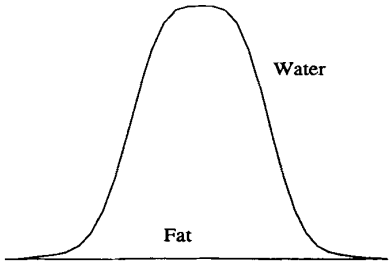

Figure 2: Spatial slice profiles for water and fat.

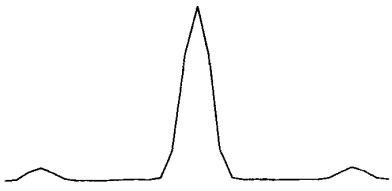

Figure 3: Spectral response over $\pm$ 550 Hz.

Three Dimensional Phase Contrast Angiography

C. L. Dumoulin and S. P. Souza*
General Electric Company, Corporate Research and Development Center, Schenectady, New York and *GE Consulting Services Corp., Albany, NY

The technique of phase contrast angiography (1-2) has been extended to a third spatial dimension. Previously this technique was limited to the acquisition of projections through the region of interest. While useful, projective methods are limited in that only a predetermined projection angle can be acquired in a given scan. The three dimensional technique described below overcomes this limitation and allows the data to be viewed in a variety of formats.

The basic principle of phase contrast angiography is the velocity induced phase shift which occurs when transverse spin magnetization moves in the presence of a magnetic field gradient. This phase shift can be exploited by applying a gradient pulse which consists of two lobes of equal amplitude and opposite polarity. Such a bipolar pulse induces a phase shift which is directly proportional to velocity. Consequently, stationary spin magnetization experiences no phase shift, and its signal can be readily separated from the signal of flowing spin magnetization by modulating the phase of the bipolar gradient.

In the technique presented here, a 3D-GRASS scan is augmented with bipolar flow encoding gradients as shown in figure 1. The phase of the rf is held constant and the polarity of the flow encoding pulse is changed at specific points during the scan. One modulation strategy which we have found to be very useful is to invert the polarity of the flow encoding pulse each time the phase encoding pulse in the slowly sampled dimension is incremented. This permits the acquisition of single acquisition data (NEX=1) and allows the simultaneous detection of flowing and stationary spin magnetization since only the flowing spin information is modulated. If the field-of-view in the modulation dimension is restricted to be more than twice the excitation volume, the flow image and the stationary tissue image do not overlap.

In addition to the conveniences of retrospective analysis of vascular structure and the simultaneous acquisition of stationary spin images which include vessel walls and plaques, the 3D technique presented here partially overcomes one of the most severe problems of projective phase contrast techniques. This problem arises from the fact that the projective voxels are by definition very large in one dimension and a dispersion of spin velocities in that dimension results in a dispersion of velocity induced phase shifts. This phase dispersion can cause a reduction or even loss of signal. In the 3D phase contrast angiography procedure, the voxel sizes are quite small and the phase dispersion across a voxel is minimized.

The 3D technique provides very high quality angiographic images which can be presented in a number of ways. For example, the data can be presented as a series of thin sections which can be rapidly paged to provide vessel cross-sections. In addition, the 3D image can be collapsed into a 2D projection whose projection angle can be retrospectively determined. The data can also be subjected to more sophisticated data analysis treatments such as the extraction of a surface of interest (3).

1. C. L. Dumoulin and H. R. Hart, Radiology, 161:717 (1986).

2. C. L. Dumoulin, S. P. Souza and H. R. Hart, Magn. Reson. Med., 5:238 (1987).

Figure 1: 3DFT Phase Contrast Angiography

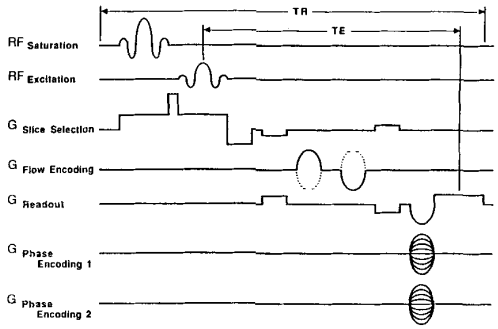

Simultaneous Multiple Surface Coil NMR Imaging

P. B. Roemer, W. A. Edelstein, S. P. Souza[1], C. E. Hayes[2], O. M. Mueller
GE Corporate Research and Development Center, Schenectady, NY
[1] GE Consulting Services Corporation, Albany. NY
[2] GE Medical Systems, Milwuakee Wisconsin

We have developed a method of simultaneously receiving NMR signals from a multitude of closely positioned RF coils. The techniques can be applied to a linear or two-dimensional array of surface coils. In order to accomplish this task, some serious problems of mutual interaction between many coils have been solved. We are now able to image large fields of view with high signal-to-noise and resolution with no penalty in imaging time. 512x512, 48 cm FOV saggital images of the spine taken using the coil array in Fig. 1 show the high SNR of a small 12 cm surface coil over the entire 48 cm field-of-view.

Previous work [1,2] has shown that a single surface coil of diameter ~d gives the highest possible signal-to-noise ratio (SNR) for a volume around depth d inside an infinite conducting half space. However, a single surface coil can only effectively image a region whose lateral dimensions are comparable to the diameter of the surface coil. The object here is to use an array of surface coils to image an extended region but maintain the high SNR of a single surface coil. Data should be collected simultaneously so that there is no penalty in imaging time.

By appropriately overlapping surface coils the mutual inductance between adjacent coils is forced to zero. By connecting all coils to low input impedance, low noise preamplifiers, the interaction to the next nearest neighbors is reduced to negligible levels. In this way coils can be operated simultaneously and independently.

When data is collected simultaneously from an arbitrary set of coils there is correlated and uncorrelated noise. If one is to realize the benefits of a multiple coil system the data from each coil must be acquired separately and optimally combined in the computer on a point by point basis. In this way every point in the image has the maximum possible SNR.

Fig. 1 shows a block diagram of a four coil system built for imaging a 48 cm field of view along the spine. The data from the four coils is acquired simultaneously and images are reconstructed from each coil. With knowledge of the correlated and uncorrelated noise between coils, the images are combined into a single image that has the SNR of the small coil and a field of view corresponding to the overall size of the array.

1. Edelstein WA, Foster TH, Schenck JS. SMRM 4th Annual Meeting, p. 964, 1985.

2. Roemer PB, Edesltein WA. SMRM 6th Annaul Meeting, p. 410, 1987.

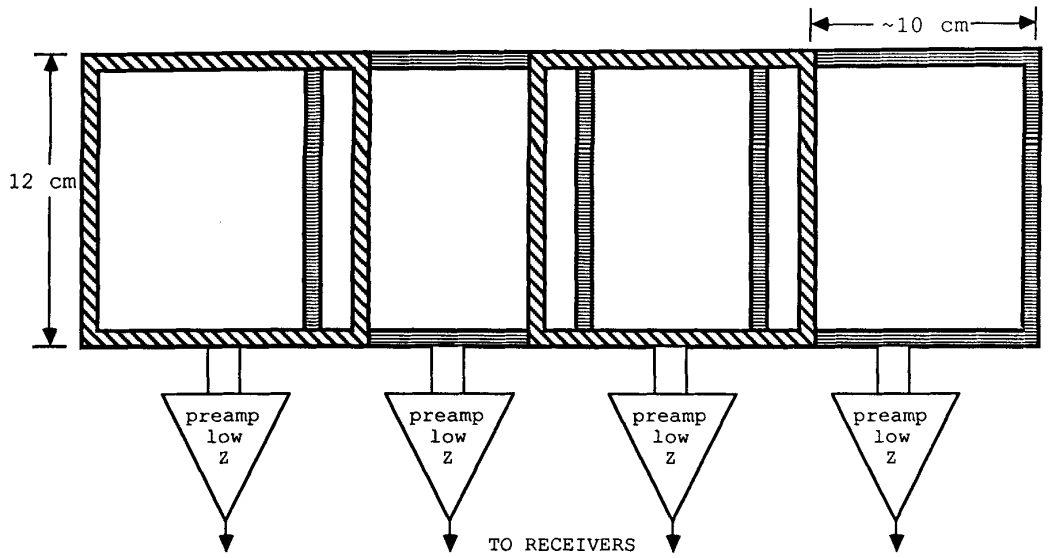

FIGURE 1. Four element spine coil. Nearest neighbor interactions are eliminated by overlap. Next nearest neighbor and more distant coil interactions are reduced to negligible levels by connection to low input impedance (< 5 ohms) preamplifiers.

ADAPTIVE CORRECTION OF MR MOTION ARTIFACTS: A METHOD UTILIZING INTERLEAVED NAVIGATION ECHOES

RL Ehman, JP Felmlee, SJ Riederer, HW Korin
Mayo Clinic and Foundation, Rochester, MN. 55905

Physiological motion remains a major problem in clinical magnetic resonance imaging. During image acquisition, the effects of motion can be characterized as a temporal modulation of bulk phase and spin density distribution within an image volume. This modulation is caused by view-to-view changes in the position of structures in the field of view, and by variable phase shifts caused by intraview motion of tissue and flowing blood. While the temporal pattern of modulation is unique to each data acquisition, our analysis has indicated that the perturbations at any given instant are similar in magnitude in many volume elements within the field of view. This is due to the global nature of the most important tissue motions.

We have developed and tested a new corrective technique consisting of a set of operators which can adaptively correct raw image data for global view-to-view tissue motion and for bulk phase shifts caused by variable intraview tissue motion. These operators essentially transfer the frame of reference of the image coordinate system from the "table-top frame" to the "visceral frame".

A prerequisite for calculating the correction operators is an accurate record of tissue motion during image acquisition. We have obtained this in a number of ways, but one of the most successful has been the use of an interleaved, specially encoded "Navigator echo". Post-processing of the navigation echo data provides information about spatial and phase displacements of the visceral frame of reference with respect to the table-top frame. These data are then folded into the correction algorithm to yield a unique operator to apply to each succeeding line of spin echo image data.

We have assessed the performance of this adaptive correction system in a variety of motion phantom studies. These have demonstrated a reduction by more than 70% in the intensity of motion artifacts arising from structures with physiologically realistic motions. In contrast to other techniques (except gating), the new method has the unique capacity to reduce motion unsharpness. Experiments were performed in which intraview motion was the major cause of artifact formation. The adaptive phase shift correction provided by this method was found to be superior to first order gradient moment nulling in reducing intensity loss and artifact formation due to intraview motion.

Initial testing of the correction technique in human imaging studies has been encouraging, and systematic evaluation is now in progress.

SMRM, 1989.

Quantitative Cardiac Wall Motion

Leon Axel, Ph.D., M.D.

Radiology Dept., University of Pennsylvania, Philadelphia, PA 19104 USA

The function of the heart is to pump; many cardiac diseases produce abnormal patterns of contraction. The ability to quantitatively study heart wall motion could help diagnose heart disease and provide a way to follow its therapy. Traditional angiographic approaches to cardiac imaging provide only projection views of the endocardial surface. Implantation of radiopaque markers in the heart wall permits tracking the motion of the implantation sites, but is both invasive and limited to a few sites. Tomographic imaging with ultrasound permits the study of wall thickening but can produce the appearance of inplane motion by passive motion of the curved wall through the imaging plane. Rapid x-ray CT can provide chamber sizes and regional wall thickening, but requires the case of intravascular contrast agents and special purpose scanners; it is also subject to potential errors from through-plane motion.

Magnetic resonance imaging (MRI) provides good contrast between blood and heart wall without the need for contrast agents, permitting measurement of chamber sizes and wall thickening with conventional cardiac-gated MRI. While useful for measuring global cardiac functions, such as stroke volume, and wall thickening, wall measurement with MRI is still subject to possible errors due to through-plane motion. Also, the overall uniform appearance of the heart wall prevents any measurement of within-wall motion or rotary components of heart wall motion.

The ability of MRI techniques to selectively alter the magnetization of a desired region has been used to create a noninvasive magnetic tag of the region that allows its motion to be followed in subsequent images as a corresponding region of altered signal in the images. The tag will last for times on the order of the Tl time, i.e., an appreciable fraction of the heart cycle time for myocardium.

One method of magnetic tagging is to use conventional selective excitation to alter the magnetization in a desired plane perpendicular to the image plane; the intersection of the tagged and imaging planes will create a stripe in the image whose motion can be followed (1). For example, a "star" of such stripes can be produced in conjunction with a short axis view of the heart in order to permit studying rotational motions of the heart wall. A limitation of the use of selective excitation for tagging is the need to deposit each tagging stripe individually, limiting the number of stripes that can be practically produced.

An alternative method of magnetically tagging the heart is to use nonselective RF pulses in combination with magnetic field gradient pulses to produce a regular pattern of spatial modulation of magnetization (SPAMM), in effect, producing a large number of parallel tagging stripes at once (2). Using multiple pulse sequences can yield sharp-edged stripes, permitting production of two-dimensional tagging grids (3), which can be used ot study regional deformation of the heart wall.

Synchronization of magnetic tagging with a specific phase of the cardiac cycle, in conjunction with imaging at different delays, permits following the time course of cardiac contraction. This tagging can be used with either conventional spin echo or rapid gradient echo imaging. The quantitative analysis of stripe displacements can yield both rigid body and deformation (intrinsic) components of wall motion.

Preliminary experience with tagged heart images shows complex but consistent patterns of regional motion in normals. In patients with ischemic heart disease there has been good agreement in regions of altered motion with other imaging techniques.

In summary, MRI offers powerful new techniques for the measurement of heart wall motion.

References

1. Zerhouni, E.,D. Parrish, W.J. Rogers, A. Yang, E.P. Shapiro. Radiology, 169, 59, 1988.

2. Axel, L., L. Dougherty . Radiology, (in press).

3. Axel, L., L. Dougherty . Radiology, (in press).

Slice-Selective Excitation for Very Short T_2 Species

John Pauly, Steven Conolly, Dwight Nishimura, and Albert Macovski
Magnetic Resonance Systems Research Laboratory
Stanford University, Stanford CA 94305

In conventional slice-selective spin-warp imaging there is an inherent delay between the peak of the RF main lobe when the bulk of the transverse magnetization is created, and the peak of the echo where most of the energy in the raw data is collected. This delay is called the echo time T_E, and is illustrated in Fig. 1. The minimum T_2 that can effectively be imaged is on the order of T_E. On commercial imaging machines T_E can reduced to approximately 3 ms by using partial **k**-space data collection, and an offset RF pulse with a reduced refocussing lobe. However the slice profile suffers.

We have proposed another approach [1]. All of the gradient lobes between the dotted lines in Fig. 1 are simply eliminated. The T_E is then limited only by the time required to shut down the RF system, about 250 μs on our 1.5T GE Signa System. The phase-encode lobe, the dephase lobe, and the first half of the readout lobe are eliminated by using projection-reconstruction acquisition gradients. The elimination of the second half of the slice select gradient and the refocussing lobe is accomplished by using a new slice-selection pulse presented here.

Slice selection is performed by a sequence of two excitations, each followed by the same acquisition gradients. Each of these excitations is half of a conventional slice selection pulse, the first with a positive gradient, and the second with a negative gradient. Each covers half of excitation **k**-space. When the two acquisitions are added the result is the same as applying a single complete excitation pulse.

The proposed pulse sequence is illustrated in Fig. 2. Gradient rise times are significant on the time scale of this pulse sequence. This is apparent in both the excitation and readout gradients. The last part of the RF occurs during the falling edge of the slice select gradient. The RF waveform has been compensated using the VERSE algorithm [2] to produce a half sinc **k**-space weighting. Similarly data is acquired on rising edge of the readout gradients. This non-uniform **k**-space sampling is corrected in reconstruction.

This pulse sequence has a number of advantages. It can be run as an SSFP sequence to acquire an image in a few seconds. This is important where respiratory motion is a problem. The very short T_E minimizes both susceptibility effects, and flow dephasing.

In phantom studies we have demonstrated that species with T_2's of 1 ms can easily be imaged on a stock commercial scanner. Studies of human volunteers have demonstrated the ability to image tissues that have very short T_2's, such as the lungs.

References

[1] J. Pauly, S. Conolly, D. Nishimura, and A. Macovski, *Submitted to Mag. Res. Med.*

[2] S. Conolly, D. Nishimura, A. Macovski, and G. Glover, *J. Magn. Reson.*, **78**,440, 1988.

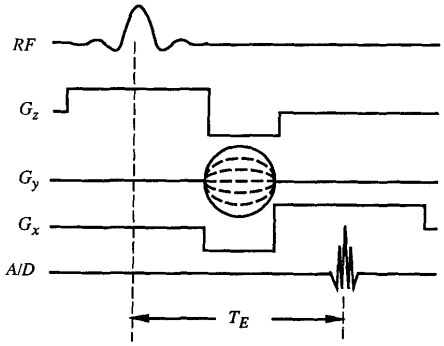

Fig. 1. T_E in Conventional Slice-Selective Spin-Warp Imaging

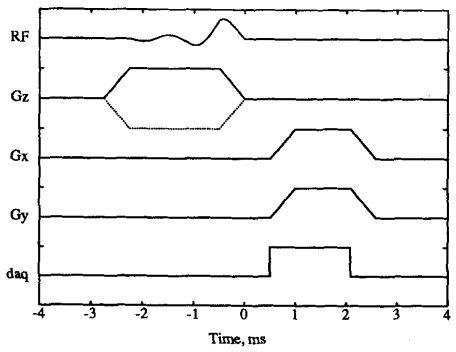

Fig. 2. Proposed Short T_2 Pulse Sequence

SMRM, 1989.

Early Detection of Ischemic Injury: Comparison of Diffusion- and T2-weighted MRI and Spectroscopy During Regional Cerebral Ischemia in Cats

Y. Cohen[2], J. Mintorovitch[2], L. Chileuitt[3], B. Pereira[3], H. Shimizu[3], P. Weinstein[3] and M.E. Moseley[1]. Dept of [1]Radiology, [2]Pharm Chemistry, and [3]Neurosurgery, Univ of California, San Francisco, Ca 94143

INTRODUCTION. In the first several hours following an ischemic insult, the injury is characterized by a breakdown of cell membrane Na^+/K^+ homeostasis, a resulting osmotic increase of intracellular water, a loss of high-energy phosphates and an increase in lactate. While spectroscopy and spin-echo MRI have been used to study the early effects of ischemia, the diffusion behavior of water protons during early ischemia is largely unknown. The purpose of this study was to evaluate the utility of the new technique of diffusion MRI compared to the conventional approach of using T2-weighted MRI as well as P-31 and H-1 MRS in the study early ischemic injury.

METHODS. The transorbital occlusion model of the right middle cerebral artery (MCAO) supplemented by bilateral carotid artery occlusion was used in a total of ten fed cats. A General Electric CSI (2 Tesla) unit, equipped with Acustar self-shielded gradient coils (± 20 gauss/cm) was used. P-31 and H-1 MRS was performed with a double-tuned surface coil positioned over the MCA territory after scalp and muscle retraction. The surface coil was passively-decoupled from a low-pass birdcage proton imaging coil. Multi-slice T2-weighted images (TR 2800, TE 80 and 160, 3 mm slices), MRS spectra, and diffusion-weighted images were obtained sequentually for six hours following MCAO. Non-gated multi-slice coronal and axial spin-echo diffusion-weighted images (TR 1800, TE 80, 3 mm slices) were acquired with gradient durations of 20 msec, gradient separations of 40 msec and very large gradient *b* values (1) of 2800 sec/mm^2. The direction of the diffusion gradient was varied between the x,y, and z axes. Diffusion phantoms of water, corn oil and cyclohexane were used to indicate the accuracy of the measurements.

RESULTS. Using large gradient *b* values, the diffusion images showed no signal from cerebrospinal fluid (CSF) or pulsatile blood flow, thus eliminating the need for cardiac gating. Within one hour following MCAO, the appearance of the diffusion-weighted images was characterized by a mass-effect and a well-defined large hyperintensity in the gray matter and basal ganglia of the occluded side. This hyperintensity exhibited slower diffusion compared to contralateral hemisphere ($D = 0.3 \pm 0.1 \times 10^{-5}$ cm^2/sec versus $0.6 \pm 0.1 \times 10^{-5}$ cm^2/sec for normal gray matter). The hyperintensity seen on the diffusion-weighted images correlated well with increases in the MRS peak areas for lactate and inorganic phosphate from the spectra. After one hour of ischemia, the ratio of shifted inorganic phosphate (Pii) to phosphocreatine (PCr) was 2.0 ± 0.4. The ratio of lactate to N-acetylasparate (NAA) using a water-surpressed spin-echo sequence (TE = 128 msec) was 1.0 ± 0.2. However, at the same time point, T2-weighted MRI showed only mass-effect and no significant abnormality in signal intensity from the occluded hemisphere. After six hours of ischemia, no large further changes were observed in the P-31 and H-1 spectra. T2-weighted images showed progressive hyperintensity from the occluded gray matter and basal ganglia. This hyperintensity reached a maximum relative image intensity (TR 2800, TE 80) difference (occluded versus normal hemisphere) of 35% ± 15% at 6 hours. The corresponding diffusion-weighted image intensity differences were 80% ± 10%. Finally, pre- and immediate post-mortem diffusion images showed no significant changes for either normal or ischemic tissues. After two hours post-mortem, however, diffusion-weighted signal intensities increased an average of 60%.

CONCLUSIONS. Diffusion-weighted MRI using large *b* values was useful in producing maps of slow water diffusion devoid of CSF and pulsatile protons. This technique was superior to T2-weighted MRI in the detection of early (one hour or less) ischemic events. Further, the contrast (image intensity differences) from abnormal to normal tissues was greater for diffusion-weighted images than for the T2-weighted spin-echo images at any time point. We attribute the hyperintensity of ischemic regions in the diffusion-weighted images to local increases in the restricted intracellular water. This is supported by the lower apparent diffusion values observed in ischemic compared to normal brain tissues.

REFERENCES: (1). Le Bihan D., Breton E., Lallemand D., et al. *Radiology*, **168**, 497, 1988.

SMRM, 1989.

Phase Contrast Cine MRI

Norbert J. Pelc Sc.D., Ann Shimakawa, M.S., and Gary H. Glover, Ph.D.
GE Medical Systems, Milwaukee, WI 53201 USA

Introduction:

A phase contrast cine MRI method that allows dynamic quantitative studies of fluid flow has been developed. The technique, dubbed VINNIE, consists of a modified pulse sequence and data processing software. The physical principles underlying the technique are fundamentally similar to those in the method developed by Nayler *et. al.*[1]

Method:

The pulse sequence is a derivative of the cine MRI sequence in which the spectrometer cycles asynchronously at a constant rate and the phase encoding increments are timed from the cardiac cycle trigger[2]. Within each cardiac period, acquisitions for up to two planes (sections) are interleaved. In addition, each plane is interrogated in an interleaved manner with two sequence types which contain different flow encoding. The differential flow encoding consists of different first moments of the magnetic field gradient in a selected direction. The other gradient directions are moment nulled. The magnitude of the moment difference (flow sensitivity) is also selectable.

For example, in an interleaved two plane acquisition, the first plane is measured with the first flow encoding, followed by the second plane with the first flow encoding, followed by the first plane with the second flow encoding, followed by the second plane with the second flow encoding. This set of sequences is repeated with the same phase encoding throughout the entire cardiac cycle. Upon detection of a cardiac trigger, the phase encoding value is incremented. The technique is compatible with respiratory motion compensation. Acquisitions for additional planes can be concatenated into a single longer scan. The scan time can be as short as 128 cardiac periods. For a sequence time of 27 msec and a single plane acquisition the temporal resolution is approximately 54 msec. If two planes are interleaved the temporal resolution is 108 msec.

The data for each of the planes and each of the flow encodings are separately sorted and interpolated into data sets for a selectable number of cardiac phases. Magnitude and phase reconstructions of each of the data sets are performed. The magnitude images are essentially equivalent to conventional cine MRI images. The magnitude images from both flow experiments at each cardiac phase can be averaged to improve the SNR. For each plane and each phase of the cardiac cycle, the phase images are subtracted to produce images representing flow velocity in the direction of the selected flow encoding. Corrections for the effects of residual eddy currents can be performed at this stage. The resulting images can be used to quantitatively portray flow. Images in which each phase difference image is multiplied by the corresponding magnitude image can also be generated and are more aesthetic since flowing fluids are highlighted and the background noise level is suppressed.

Results:

The technique has been used to study pulsatile CSF flow as well as flow in arterial and venous structures. The reasonable scan time and automated processing make this technique clinically viable. However, the flow information is gathered at the expense of a factor of 2 in temporal resolution or a doubling of the total scan time. Thus, the technique is not a direct replacement for cine MRI and should be used when its unique flow information is desirable.

References:

1. Nayler, G.L., Firmin, G.L., and Longmore, D.B., J. Comput. Assist. Tomogr, 10, 715, 1986.
2. Glover, G.H., and Pelc, N.J., Mag. Res. Annual 1988, 299, 1988.

SMRM, 1989.

Initial Experience with Very Thin Slice Two-Dimensional MR Angiography

Paul Keller, Ph.D., Burton Drayer, M.D., Evan Fram, M.D., Kenneth Williams, M.D., Charles Dumoulin, Ph.D.,* Steven Souza, Ph.D.,* Barrow Neurological Institute, *GE Corporate Research and Development, Schenectady, NY 12301, USA

Introduction

Time-of-flight based MR angiographic (MRA) techniques rely upon "tagging" of spins outside of the observed region, and the detecting the tag within the observed volume. This tagging may be passive, i.e. washin of spins with full longitudinal magnetization (1,2), or active by inversion (3), or presaturation (4). One disadvantage of this approach is that T1 relaxation results in loss of active tags over time, while progressive saturation of spins passing through an imaging volume results in the loss of a passive tag. In order to minimize this problem, we developed a 2D gradient-echo pulse sequence for the sequential acquisition of very thin slices (2). Unlike 3DFT-volume acquisitions, this results in a very thin excitation volume, effectively eliminating saturation effects. The combination of a short TR and a high flip angle results in diminished signal intensity from stationary spins. The passive tag of flow-related enhancement (FRE) then yields high signal for spins flowing out-of-plane.

Here we wish to report on-going improvements in the pulse sequence and initial experience with this 2D-MRA method both in normal volunteers and in patients. The technique was used to evaluate both extracranial and intracranial vasculature, and correlated with conventional angiography.

Methods

MRA was performed on a 1.5 Tesla General Electric Signa MR instrument. A 2DFT gradient recalled echo sequence is utilized in which transverse magnetization was disrupted by a 10 ms spoiling gradient which is stepped from 5 mT/m to zero in concert with update of the phase encoding gradient. Thin slices (1.5 mm) are obtained using an RF bandwidth of 625 Hz in conjunction with a gradient of 9.8 mT/m. TR of 50 ms, TE of 9.5 - 13.3 ms, and flip angle of 40^{o}-60^{o} are utilized. Constant velocity flow compensation is employed on the slice and read axes. A presaturation band superior to the acquisition slice is used in neck examinations to remove venous structures. The position of the presaturation band incremented along with the acquisition slice.

The patient population studied were those who were scheduled to undergo conventional angiography of the head or neck, and a routine MRI examination. Normal volunteers also underwent MRA examination.

Results

Technical improvements to date have permitted the reduction of TE from 13.3 ms to 9.5 ms by asymmetric echo sampling and half-Fourier reconstruction. Shortened echo times have resulted in reduction in motion induced dephasing and susceptibility effects adjacent to air and bone, significantly reducing artifacts and increasing intraluminal signal.

Very good correlation has so far been found for carotid artery pathology. A wide spectrum of carotid and vertebrobasilar pathology has been studied including normals, arteriosclerotic narrowing, fibromuscular dysplasia, dissection, and occlusion. Intracranially, cases of arteriovenous malformations, stenoses, aneurysms and sinus thrombosis have been studied by MRA. In general, correlation with angiography has been very good.

Acknowledgement

The authors are grateful to Dr. Gary Glover of General Electric Medical Systems for providing the half-echo reconstruction program.

References

1. Masaryk, T.J., M. T. Modic, G. W. Lenz, E. M. Haake. Radiol., 166, 461, 1988.

2. Keller, P.J., B. P. Drayer, E. K. Fram, C. L. Dumoulin, S. P. Souza. Magn. Reson. Imaging, 7, Supplement 1, 186, 1989.

3. Nishimura, D. G., A. Macovski, J. M. Pauly. Magn. Reson. Med., 7, 472, 1988.

4. Dumoulin, C. L., H. E. Cline, S. P. Souza, W. Wagle, M. F. Walker. Magn. Reson. Med., In Press, 1989.

SMRM, 1989.

Evidence of Anisotropic Self-Diffusion in Cat Brain

M.E. Moseley[1], Y. Cohen[2], J. Mintorovitch[2], L. Chileuitt[3], H. Shimizu[3], J. Tsuruda[1], D. Norman[1], P. Weinstein[3]
Dept of [1]Radiology, [2]Pharm Chemistry, and [3]Neurosurgery, Univ of California, San Francisco, Ca 94143

INTRODUCTION.

Diffusion imaging, which measures the microscopic motion of water protons in tissues, has attracted considerable interest (1,2). The advantages of measuring diffusion using magnetic resonance are that the time that diffusion takes place can be accurately controlled as can the direction of observed diffusion. Further, the diffusion pathlengths or displacements can be estimated from the Einstein equation.

One important application of diffusion imaging is that of the brain water motion. As the strength and duration of the diffusion gradient pulses is increased, diffusion of fast-moving protons such as those found in cerebrospinal fluid (CSF) and pulsatile blood become apparent as signal loss on the observed image. With sufficient diffusion gradient strengths and durations (measured as the gradient *b* value (2)), the signal intensity from fast-moving protons in the diffusion-weighted image drops out, leaving only slower-diffusing proton image intensities.

The purpose of the present study was to examine the diffusion behavior of brain water found in normal gray and white matter in the cat brain as the diffusion gradient strength, duration and principally, the diffusion gradient direction was varied.

METHODS.

A total of six fed cats was examined. A General Electric CSI (2 Tesla) unit, equipped with Acustar self-shielded gradient coils (± 20 gauss/cm) was used. Cardiac-gated and non-gated multi-slice coronal, sagittal and axial spin-echo diffusion-weighted images (TR 1500-1800 msec, TE 50 - 100 msec, 3 mm slices) were acquired with gradient durations of 15 - 40 msec, gradient separations of 20 - 80 msec and large gradient *b* values of 1400 - 5600 sec/mm^2. The direction of the diffusion gradient was varied between the x,y, and z axes. Diffusion phantoms of water, corn oil and cyclohexane were used to indicate the accuracy of the measurements.

RESULTS.

Using large gradient *b* values above 1000 sec/mm^2, the diffusion images showed no intensity from cerebrospinal fluid (CSF) or from blood flow, thus eliminating the need for cardiac gating in these experiments. No differences in the gated versus non-gated diffusion-weighted images were observed at these and higher *b* values.

No clear evidence of anisotropic water diffusion was found in either gray matter or in basal ganglia tissues at the *b* values chosen. However, very large directional differences in both diffusion-weighted image intensity and in calculated diffusion values were observed in cortical and in deep white matter. Faster diffusion of water protons in white matter was seen when the direction of the applied diffusion gradient was parallel to the orientation of the white matter. Water diffusion in white matter perpendicular to the gradient direction was significantly slower. This effect was proportional to both the gradient duration and the gradient strength. This effect was seen in all axial, sagittal, and coronal images.

Calculated diffusion values (gradient pulse separation = 40 msec) for gray matter and basal ganglia were 0.6 to 0.9 x 10^{-5} cm^2/sec. In deep white matter, water diffusion oriented along the direction of the applied gradient was $0.7 \pm 0.1 \times 10^{-5}$ cm^2/sec. Diffusion of the same water perpendicular to the direction of the applied gradient varied from 0.3×10^{-5} cm^2/sec to 0.5×10^{-5} cm^2/sec.

This orientation effect was seen in both pre- and post-mortem images.

CONCLUSIONS.

Diffusion-weighted MRI using large *b* values is useful in producing maps of slow water diffusion devoid of CSF and pulsatile protons. Images of exquisite gray/white matter contrast can be obtained depending upon the direction of the applied diffusion gradient. Our conclusions are that the observed white matter diffusional anisotropy may be due to water translations along and against white matter myelin fibers. Potential applications of this technique include determination of white matter orientations and it's changes in neonate development and in white matter diseases such as gliomas or demyelination.

REFERENCES:

(1). Ahn CB, Lee SY, Nalcioglu O. *Med Phys*, **13**, 789, 1986.
(2). Le Bihan D, Breton E, Lallemand D, et al. *Radiology*, **168**, 497, 1988.

Oxygenation Sensitive Contrast in Magnetic Resonance Image of Brain at High Fields

S. Ogawa and T. M. Lee
AT&T Bell Laboratories, Murray Hill, NJ 07974

At high fields (7T and 8.4T), water proton MRI of rodent brain has been shown to give a high image contrast which is very sensitive to the level of oxygenation in the blood (1). The contrast depicts anatomical details of the brain by numerous dark lines of various sizes. These dark lines represent vessels in the image slice and appear when the deoxyhemoglobin content in the blood increases. With diamagnetic oxy and CO hemoglobins, they do not appear. The contrast is observable in gradient echo images but is absent in spin echo images. The local field induced by the magnetic susceptibility change in the blood due to paramagnetic deoxyhemoglobin causes the reduction of signal by the intra voxel dephasing of the water signal. The area of the reduced signal intensity includes not only the blood vessel but also the surrounding tissue. Actually as shown in a series of *in vitro* experiments, the latter is the major component of the darken area at the high field used in this study. Therefore the size of the dark line is larger than the size of the blood vessel by a factor of nearly 2. This effect is not present when the blood vessel runs parallel to the main field. A typical example of a coronal slice image of a rat brain is shown in Fig. 1. The plane of the slice is normal to the main field. The contrast depends on the state of the anesthetization, the intake of oxygen and the consumption of oxygen in the brain.

Anatomical aspects of brain organization can be studied by these images, especially in anoxy brain where the contrast is highest. There are many blood vessels at the boundaries of the organizational elements of brain and also in the ventricles. These blood vessels give strong dark lines and the brain organization can be clearly visualized in the image. One can find close resemblance in these images to the histological slice pictures published in the rat brain atlas (2).

When there is a pathological condition present in a brain, it could appear in the image as a dark area in a case of hemorrhage or as localized dark lines in a case of stroke. When there happens cell death in a localized area, a white area could appear because of no oxygen consumption in the area.

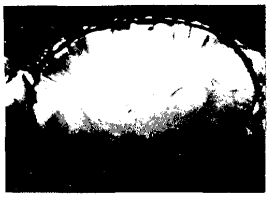

Fig. 1
A coronal slice image of a rat brain anesthetized with thiopental. The image was obtained with a simple gradient echo sequence with a field gradient of 4 to 5 gauss/cm at 8.4T main field. The voxel size was 65μ x 65μ x 700μ at the signal acquisition.

Most challenging problems to study with this MRI are those physiological activities of brain which could manifest in distinct changes of regional oxygen consumption and therefore in localized contrast enhancements in the image.

Some examples of images will be presented to illustrate the possible usages of this MRI for anatomical, pathological and physiological studies of brain.

1. S. Ogawa, T. M. Lee, A. S. Nayak, and P. Glynn, J. Mag. Res. Med. submitted for publication.
2. G. Paxinos and C. Watson, in "The Rat Brain", Academic Press, Orlando, 1986.

SMRM, 1989.

Quantitation of Blood-Brain Barrier defect using MRI and Gadolinium-DTPA in Acute Multiple Sclerosis.

H.B.W.Larsson, M.Stubgaard, J.L.Frederiksen, M.Jensen, O.Henriksen, O.Paulson.
Dept. of Magnetic Resonance, Hvidovre Hospital, University of Copenhagen, Denmark.

It is now widely accepted that it is possible to detect a deficient blood-brain barrier (BBB) in newly developed MS lesions by use of magnetic resonance imaging (MRI) and gadolinium-DTPA (Gd-DTPA). As deficient BBB could be an important step in the pathogenesis and/or the ethiology of MS, there is an increasing demand for quantification of the degree of BBB defect by use of MRI and Gd-DTPA. We have developed a model taking into account the non-linearity between the MR signal and concentration of Gd-DTPA. Furthermore there was no need for external calibration procedures relating the MR signal to the concentration of Gd-DTPA.

Method:

Gd-DTPA was given as a bolus injection in a vein, and blood was sampled from the brachial artery during the experiment. The concentration of Gd-DTPA in the blood samples was measured by neutron activation. The basic capillary model concerning the diffusion of Gd-DTPA across the BBB is described by the equation:

$$\frac{dC_{br}(t)}{dt} = PS(\bar{C}_c(t) - \frac{C_{br}(t)}{\lambda}) \quad I$$

($C_{br}(t)$: concentration of Gd-DTPA in the plaque, PS: permeability surface area product, $\bar{C}_c(t)$: mean capillary plasma concentration of Gd-DTPA, λ : appearent volume of distribution of Gd-DTPA in the lesion, t: time after Gd-DTPA infusion). Using equation (I) together with E=1-exp(-PS/F) (E: extration of Gd-DTPA, F: plasma floow) and $C_a(t)=A\exp(-\alpha t)$ (C_a: artery plasma concentration, A: amplitude, α: rate of decrease of Gd-DTPA in plasma) and $\delta_1(S(t)-S(0)) \approx C_{br}(t)$ (δ_1: unknown local determined constant, S: MR signal) or $\delta_2(R_1(t)-R_1(0)) = C_{br}(t)$ (δ_2: unknown local determined constant, $R_1 = 1/T_1$) we could calculate the final expressions:

$$S(t)-S(0) \approx \frac{\dot{S}(0)}{\frac{EF}{\lambda} - \alpha}(\exp(-\alpha t) - \exp(\frac{-EFt}{\lambda})) \quad II$$

$$R_1(t)-R_1(0) = \frac{\dot{R}_1(0)}{\frac{EF}{\lambda} - \alpha}(\exp(-\alpha t) - \exp(-\frac{EFt}{\lambda})) \quad III$$

($\dot{S}(0)$ and $\dot{R}_1(0)$ are the initial increase in the MR signal and longitudinal relaxation rate respectively). From equation (II) or (III) the permeability $\frac{EF}{\lambda}$ could be found by non-linear regression analysis. The enhancement was monitored for about 1 h with a CPMG sequence (TE= 30,60,90,120 ms; TR=0.5 s;Ma=256 R. Data were acquired with a temporal resolution of 68 s. The sequence was also run just before Gd-DTPA infusion, given S(0). From the four-echoes sequence the apparent R_2 was calculated. Furthermore, T_1 was measured before Gd-DTPA infusion with partial saturation inversion recovery giving $R_1(0)$. From the temporal sequence of MR signal and $R_1(0)$ and the apparent $R_2(t)$, $R_1(t)$ could easily be calculated. To prove the correctness of this procedure a phantom experiment was performed. The regression line between T_1 estimated indirectly in this way in the phantom and T_1 ref of the phantom was $T_1^{in} = 1.00\ T_1^{ref} - 45$ (ms), and the correlation coefficient was 0.9989 ($p<0.0001$).

Results:

The model was applied in two patients with acute MS-attack. The first patient showed enhancement in one lesion and EF/λ was $7.17\ 10^{-4}\ s^{-1} \pm 0.31\ 10^{-4}\ s^{-1}$, and the other patient showed enhancement in two lesions, $15.0 \cdot 10^{-4}\ s^{-1} \pm 1.9 \cdot 10^{-4}\ s^{-1}$ and $19.0 \cdot 10^{-4}\ s^{-1} \pm 1.7 \cdot 10^{-4}\ s^{-1}$. No significant difference was found between the calculated permeability based on S(t) compared to calculated permeability based on $R_1(t)$. The experimental data fitted the theoretical curve very well, see Fig. 1.

Conclusion:

MRI seems very suitable for investigation and quantification of BBB defects. It also gives great spatial resulution, anatomical details, can be repeated and is relatively cheap. The major drawback is the need for catheterization of an artery, however, this may also be solved.

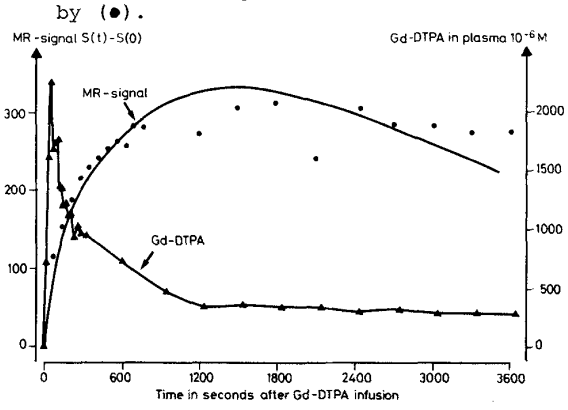

Fig. 1: The MR signal difference S(t) -S(0) and the plasma concentration of Gd-DTPA shown as a function of time after Gd-DTPA infusion. The smooth curve represent equation (II) fitted to the observed MR signal: S(t) - S(0) denoted by (•).

SMRM, 1989.

Measurement of the Blood-Brain Barrier Permeability using Dynamic Gd-DTPA Scanning

Paul S. Tofts, Allan G. Kermode and Gareth Barker.
Multiple Sclerosis NMR Research Group, Institute of Neurology, Queen Square, London WC1N 3BG, U.K.

Introduction

Gd-DTPA has been used to qualitatively visualise whether the blood brain barrier (BBB) is breached, for example in active multiple sclerosis (MS) and in tumours. Dynamic scanning, in which the signal enhancement is measured as a function of time after injection of a bolus of Gd-DTPA, shows that MS lesions may vary in the time to peak enhancement, and in the degree of enhancement. A quantitative model of signal enhancement vs time has been developed, based on compartmental analysis.

Gd-DTPA tracer is known to distribute into 3 compartments:

a) plasma

b) whole body extracellular space (ecs) and

c) lesion leakage space within the brain.

Two parameters relevant to the natural history of the lesion are estimated:

1) k_i, the blood brain barrier (BBB) permeability surface area product per unit volume, or influx constant. This is defined as the flow of tracer across the membrane, per unit volume of the tissue, for unit concentration difference between the plasma and the brain.

2) v_i, the leakage space per unit volume of tissue ($0 \le v_i < 1$). This is the fraction of the lesion volume which is available for the tracer to leak into; it may correspond to the extracellular space in the lesion.

Theory

The mathematical model involves the following steps:

1) Flow of tracer from capillary plasma to the lesion leakage space is

$$v_l \, dC_l/dt = k_i(C_p - C_l) \qquad [1]$$

where C_p and C_l are [tracer] in plasma and in lesion leakage space respectively.

2) Plasma concentration $C_p(t)$ is known to decay biexponentially. The initial fast component ($t_{1/2} \approx 12$min) corresponds to equilibration between plasma and whole body ecs; the final (slow) component ($t_{1/2} \approx 90$min) corresponds to renal extraction of the tracer from these two linked compartments.

3) Solution of equation [1] gives a triexponential for $C_l(t)$

4) The dependence of T_1 and T_2 on [Gd] and hence on C_l is known.

5) Dependence of IR or SE signal on T_1 and T_2 is known.

By adjusting k_i and v_l, early- or late-enhancing curves can be simulated as seen in practice. These curves can be fitted to measured curves, with k_i and v_l as free parameters.

Method

The patient is scanned with an SE/IR combination to determine spin density and T_1 of the lesion. Gd-DTPA is injected and repeated IR scans made. The patient is kept still in the scanner during the whole procedure, with aid of SNOD[1]. Injection is carried out in situ.

Results

An early enhancing lesion (plateau at 10min) gave $k_i = 0.056\text{min}^{-1}$; $v_l = 0.18$. A late enhancing lesion (45min) gave $k_i = 0.012\text{min}^{-1}$; $v_l = 0.41$. The values of v_l are similar to measurements of ecs using multi-echo biexponential T_2 analysis, and suggest that the Gd-DTPA leakage space is the extra cellular space.

Discussion

This represents a true physiological measurement of BBB permeability, independent of MRI scan sequence or field strength.

References

1. Tofts, P.S., Kermode, A.G., MacManus, D.G., Robinson, W.H. Simple nasal orientation device (SNOD) eliminates head movement in cooperative patients. Abstract submitted to this conference.

Three-Dimensional Magnetization Prepared Rapid Gradient Echo (3D MP RAGE) Imaging

John P. Mugler III, James R. Brookeman
Departments of Radiology and Biomedical Engineering, University of Virginia
Charlottesville, Virginia 22908 USA

Description of Technique

Three-**D**imensional **M**agnetization **P**repared **RA**pid **G**radient **E**cho imaging (3D MP RAGE) is a novel technique applicable for 3-dimensional imaging *throughout* the body (1). The sequence begins with a magnetization preparation (MP) period as employed by Haase (2,3) in conjunction with the snapshot FLASH technique. For example, an inversion pulse followed by a delay yields T1-dependent contrast, and a 90°-180°-90° pulse set gives T2-dependent contrast.

After the longitudinal magnetization is encoded with the desired contrast during the MP period, a rapid gradient-echo (RAGE) sequence is used to *sample* the prepared magnetization. The sampling sequence may be any of the well-known rapid gradient-echo techniques such as: FLASH, snapshot FLASH, GRASS, FISP, FAST, FFE, etc. A fraction of the desired 3D k-space volume is acquired by a given RAGE acquisition.

A magnetization recovery period follows each RAGE acquisition. The duration of the recovery period is determined by the desired contrast properties, the T1 relaxation times of the tissues, and the state of the longitudinal magnetization at the end of the gradient-echo acquisition. The complete 3D MP RAGE data set is formed by repeating the prepare-acquire-recovery cycle until the desired k-space volume is covered. A trigger signal may initiate each cycle for imaging structures subject to periodic motion such as the liver or heart.

The structure of the 3D MP RAGE sequence provides several inherent advantages over existing 3D acquisition methods which operate in a steady state mode. (By steady state we mean sequences which are based on either a steady state of the longitudinal component of the magnetization (e.g. standard spin-echo or FLASH), or a steady state of the complete magnetization vector (e.g. FISP or GRASS).) The advantages of 3D MP RAGE include:

1. The cyclic nature of the sequence makes it naturally applicable to imaging structures subject to periodic motion such as the liver or heart using respiratory or cardiac triggering, respectively. When the magnetization recovery period is sufficiently long with respect to tissue T1 values, variations in total cycle length as occur with changes in heart or respiratory rates do not adversely affect the images. To our knowledge, this is the first technique that produces relatively high resolution 3D image sets of the abdomen with minimal respiratory artifacts in an imaging period acceptable for routine clinical use.
2. By employing a separate magnetization preparation, given tissue contrasts can be obtained in much shorter imaging times than are possible with existing steady state techniques. In addition, the images are not prone to the transverse coherence artifacts that have plagued some current 3D techniques.
3. The *dead* times in the preparation and recovery periods can be used for secondary magnetization preparations (e.g. spatial or chemical presaturation).

Imaging Results

The 3D MP RAGE sequence has been implemented on a standard 1.5 Tesla whole-body imager (Siemens Magnetom 63SP, Siemens Medical Systems, Iselin NJ). In our preliminary investigations we have acquired high quality 3D image sets of the abdomen, pelvis, legs, head, and C-spine. We will discuss the imaging parameters for the abdomen and head.

Abdomen: 3D image sets of the abdomen showing minimal respiratory artifacts were acquired in 7.2 min. The image matrix was 128 (350mm) by 128 (350mm) by 256 (700mm), yielding cubic voxels 2.7mm on a side. The magnetization preparation was an inversion pulse followed by a 350ms delay which produced strong T1-weighting. Each RAGE acquisition acquired 128 lines in 1024ms (TR/TE 8/3.3, FLASH type sequence, 10° flip angle) and was performed at end expiration. The recovery period was 2 sec. Since each RAGE acquisition was only 1 sec., image artifacts from stomach, bowel, and cardiac motions appear predominantly in one phase-encoding direction.

Head: 3D image sets of the head showing excellent gray/white contrast were acquired in 5.9 min. The image matrix was 128 (180mm) by 128 (250mm) by 256 (250mm), yielding 1.4mm by 2.0mm by 1.0mm voxels. The magnetization preparation was an inversion pulse followed by a 500ms delay which produced strong T1-weighting. Each RAGE acquisition acquired 128 lines in 1280ms (TR/TE 10/4.15, FLASH type sequence, 10° flip angle). The recovery period was 1 sec. The images display excellent gray/white contrast compared to the standard T1-dependent imaging sequences we currently employ (400/15 2D spin-echo and 30/5 3D FLASH). Due to the very short TE of the RAGE acquisition and the small voxel sizes, the images do not show any significant susceptibility artifacts at air/soft tissue and bone/soft tissue interfaces. This sequence is currently in clinical evaluation for the imaging of pituitary tumors.

Conclusions

Initial experience with the 3D MP RAGE sequence shows promise that it will be a noteworthy addition to the existing arsenal of MR imaging techniques. For given voxel sizes and certain contrast properties, the 3D MP RAGE technique can generate 3D image sets substantially faster than existing techniques. Particularly exciting is the possibility of generating high quality 3-dimensional image sets of the abdomen. We are also currently investigating the T2-weighted versions of 3D MP RAGE.

References

1. Mugler III, J.P., J.R. Brookeman. submitted to *Magn. Reson. Med.*
2. Haase, A. *Magn. Reson. Med.* **13**, 77 (1990).
3. Haase, A., D. Matthaei, R. Bartkowski, et al. *J. Comput. Assist. Tomogr.* **13**, 1036 (1989).

SMRM, 1990.

Quantitative NMR Imaging of Perfusion in Rat Brain

John A. Detre and John S. Leigh, Dept. Biochem. and Biophys, University of Pennsylvania, Phila.,PA
Donald S. Williams and Alan P. Korestsky, Pittsburgh NMR Center and Dept. Biol. Sci., CMU, Pittsburgh, PA

Measurement of perfusion is important for the functional assessment of organs *in vivo*. Here we report the use of ^{1}H NMR imaging to generate quantitative perfusion maps in the rat brain at 4.7T. Blood water flowing to the brain is saturated in the neck with a slice-selective saturation imaging sequence, creating an endogenous tracer in the form of proximally saturated spins. Because proton T_1 times are relatively long in blood and brain, saturated spins exchange with bulk water in the brain, and a steady state is created where the regional concentration of saturated spins is determined by the regional blood flow and regional T_1. Distal saturation applied equidistantly outside the brain serves as a control for effects of the saturation pulses.

The Bloch equation describing the Z magnetization in brain, M_b, can be modified to include flow as described by eqn. 1. FM_a and fM_b/λ refer respectively to spins entering and leaving the brain due to blood flow (f=flow, λ=blood:brain partition coefficient, M_a=arterial inflow). A well mixed compartment is assumed such that the the quantity of spins leaving the brain by venous flow, fM_v, has been replaced by the amount fM_b/λ.

$$\frac{dM_b}{dt} = \frac{M_b^0 - M_b}{T_1} + fM_a - \frac{f}{\lambda} M_b \quad (1)$$

Solving for flow yields:

$$f = \frac{1}{T_{1app}} \left(1 - \frac{M_b}{M_b^0}\right) \quad (2)$$

where λ is in units of cc blood/g brain, T_{1app} is in seconds and M_b/M_b^0 is a unitless ratio. This determination of flow is independent of how M_b and M_b^0 are sampled.

Methods: Rats were anaesthesized with 5% Halothane, intubated and maintained on 50% O_2/50% N_2O and 1-2 % Halothane. A femoral arterial line was used to monitor blood pressure and sample blood gases. Temperature was maintained at 37°C with a heated water pad.

Images were obtained on a Bruker 4.7T, 40 cm bore Biospec II spectrometer operating at 200 MHz. The head was placed in an 6 cm ^{1}H imaging coil. A 64 X 64 spin echo imaging sequence was used, with TE=13 msec, TR=2 sec slth=2 mm, FOV=50mm, and NA=2. Saturation during the TR period was performed using slice selective (1 cm) 90° pulses applied every 30 msec, each followed by an x,y, or z gradient homospoil pulse. Saturation was applied either proximal to the brain in the neck region, or to a control region outside the brain. Spoiler gradients were also applied around the 180° pulse in the imaging sequence to eliminate signal from moving spins, while minimally attenuating diffusing spins.

For T_{1app} determinations the TR time was varied from 0.5 to 4 sec. Maps were calculated by fitting each pixel to the exponential: $M=M^0(1-e^{-TR/T1app})+C$. Images were processed with 2 point smoothing and interpolated to a 256 X 256 matrix. Negative flow values were discarded.Two sets of control and proximal saturation images were summed resulting in a total flow imaging time of 16 min.

Results: A perfusion map of the rat brain was obtained according to eqn. 2. The flow image is displayed on a scale in units of cc·100g^{-1}·min^{-1}. A value of 0.9 cc/g for the λ of water was used[1]. The average CBF value over the whole brain is 106 cc·100g^{-1}·min^{-1}, in agreement with the value for CBF in rat brain under halothane anesthesia of 105 cc·100g^{-1}·min^{-1} previously reported in the literature[2]. Individual pixel flow values range from 46 to 222 cc·100g^{-1}·min^{-1}. Flow values are increased in the periphery of the brain, consistent with increased cortical flow.

This technique allows regional perfusion maps to be measured noninvasively, with the resolution of ^{1}H MRI, and should be readily applicable to human studies.

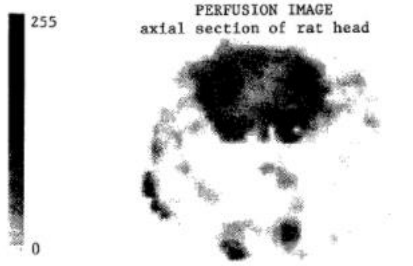

References
[1]Herscovitch and Raichle, *J Cereb Blood Flow Metab* **5**, 65, 1985.
[2]Harp et al., *Acta Anaesth Scand* **20**, 83,1976

SMRM, 1991.

FUNCTIONAL MAPPING OF THE HUMAN VISUAL CORTEX BY NUCLEAR MAGNETIC RESONANCE IMAGING

J.W. BELLIVEAU, D.N. KENNEDY, R.C. MCKINSTRY, B.R. BUCHBINDER, R.M.WEISSKOFF, M.S. COHEN, J.M. VEVEA, T.J. BRADY, B.R. ROSEN

MGH-NMR Center, Department of Radiology, Massachusetts General Hospital and Harvard Medical School, Boston, MA 02114, U.S.A.

Introduction

We present the first functional NMR maps of human task activation, using a well-established visual stimulus paradigm. Dynamic susceptibility-contrast imaging was used to obtain regional cerebral blood volume (CBV) maps of the brain during resting and activated states. During photic stimulation, localized increases in blood volume were detected in the primary visual cortex. Areas of the brain activated by visual stimulation were correlated directly to the underlying anatomy, permitting demarcation of activated versus nonactivated cortex.

Local alterations in neuronal activity occur during task performance and induce local changes in cerebral perfusion which can be used to map the location of component mental operations. Because cerebral hemodynamic state in nonactivated brain areas is quite stable over time, a resting-state functional image can be subtracted from a stimulated-state image to create a new image depicting local changes caused by the activation task. The human visual cortex was investigated using photic stimulation, a robust stimulus which produces regional changes in perfusion of 30-50% (1, 2). Dynamic susceptibility-contrast NMR imaging using intravenously administered Gd-(DTPA)$^{2-}$ (i.e., Magnevist) was used to obtain regional cerebral blood volume maps of the human brain during resting and activated states (3, 4). High-resolution three-dimensional T1-weighted anatomic images were also obtained for correlation of the functional images to the underlying neural substrate. Functional and anatomic data sets were translated into proportionately measured stereotactic coordinates relating to the line between the anterior and posterior commissures (AC-PC line or bicommissural line) (5). This allows direct correlation to reported standardized PET maps of the visual cortex.

Methods and Results

Seven normal subjects underwent dynamic NMR imaging using a prototype high-speed imaging device (1.5 Tesla GE Signa modified by ANMR, Woburn, MA) based on a variation of the echo planar imaging (EPI) technique first described by Mansfield (6). Approval for these studies was obtained from the MGH Subcommittee on Human Studies. Light-proof, stimulating goggles (Grass S10VS) were placed over the subject's eyes and the subject further screened from any ambient light. The stimulus rate was fixed for maximum response (1, 2) at 7.8 Hz. A surface coil over the occipital pole was used to improve signal-to-noise (≈ 170/1) within the visual cortex. A parasagittal slice from the 3-D T1-weighted data set (1 x 1 x 1.5 mm) was used to identify the plane of the calcarine fissure bilaterally.

Two doses of 0.1 mmol/kg Gd(DTPA)$^{2-}$, with and without 7.8 Hz photic stimulation, were administered via antecubital vein bolus injection (4 sec, using a Medrad power injector) for a total dose not exceeding 0.2 mmol/kg. The rapid injection was well tolerated. A series of images oriented parallel to the calcarine fissures were collected at 750 msec intervals using a lipid-suppressed spin echo EPI pulse sequence (TE=100 msec, TR=750 msec, 64 msec image acquisition window) before, during, and following contrast agent injection. A slice thickness of from 7-10 mm was used, with in-plane resolution of either 1.5 x 1.5 or 3 x 3 mm.

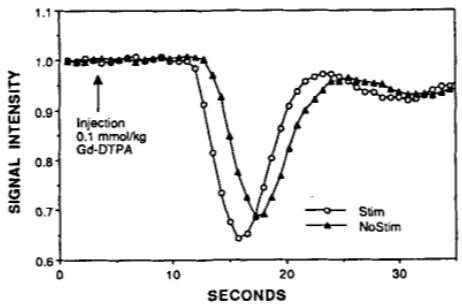

Figure 1 displays the measured NMR signal changes in a region-of-interest within the visual cortex in a single subject, during resting (darkness) and stimulated conditions. These time series images were used to generate functional relative CBV maps of the brain. Changes in brain signal intensity occurring during cerebral transit of the high magnetic susceptibility Gd(DTPA)$^{2-}$ were converted into contrast agent concentration-time curves (3, 4). The area under the concentration-time curve, corrected for recirculation via gamma-variate fitting, is proportional to the local CBV. These calculations were performed on a voxel-by-voxel basis to generate images of relative CBV. The resulting resting and activated functional CBV images were subtracted to reveal areas involved in cognitive processing of the task.

The subtraction images vividly show an area of increased blood volume located in the primary visual cortex (V1 + V2). During photic stimulation in our seven subjects, we measured an average increase in CBV of 32 ± 10 %. Paired t-test analysis of the data shows a high level of significance ($p < 0.001$). Stereotactic results demonstrate that MR determined regions of activity fall within PET determined center-of-mass coordinates of the primary visual system. Using the center of the AC-PC line in proportionately measured stereotactic coordinates, the average MR determined center-of-mass location lies –65.5 ± 10.3 mm along the antero-posterior axis and +7.8 ± 2.8 mm along the vertical axis for the left hemisphere; and –64.4 ± 7.6 mm along the antero-posterior axis and +7.4 ± 1.6 mm along the vertical axis for the right hemisphere. Moreover, sharp demarcation of the activated region corresponded well to the anatomically determined gray/white borders. This result is in agreement with previous autoradiographic experience in animals, which shows sharp boundaries between functionally distinct regions.

Discussion

In vivo measurement of activated human visual cortex by dynamic contrast enhanced NMR is demonstrated. Of future importance, the sensitivity of our MR technique to changes in blood volume, as distinct from blood flow shown in previous radionuclide studies, offers the potential to perform continuous serial imaging of cortical function with subsecond temporal resolution. This is true because blood volume changes as shown here can be assessed with intravascular contrast agents at equilibrium within the vascular space (7). The ability to perform complete 2-D images in times as short as 50 milliseconds implies that the hemodynamic response time of neural activation, ~100 msec (8), will ultimately limit the temporal resolution of this technique. This combination of time-resolved functional imaging with precise anatomical localization promises to provide the highest resolution functional maps of the living brain to date, with complete three-dimensional imaging of the brain possible using multislice acquisition (6). The use of dynamic susceptibility-contrast NMR imaging should lead to greater understanding of the unique structure-function correlates involved in neural information processing and the development of a NMR based functional neuroanatomy.

1. Fox PT and Raichle ME, *J Neurophysiol* **51,** 1109 (1984).
2. Fox PT and Raichle ME, *Ann Neurol* **17,** 303 (1985).
3. Belliveau JW, Rosen BR, et al., *Magn Reson Med* **14,** 538 (1990).
4. Belliveau JW, Cohen MS, et al., *J. Neuroimaging* **1,** 36 (1991).
5. Talairach J, et al., "Atlas d'Anatomie Stereotaxique du Telencephale," Masson, Paris, 1967.
6. Cohen MS and Weisskoff RM, *Magn Reson Imag* **9,** (1991).
7. Moseley M, White D, et al., *in* "Society of Magnetic Resonance in Medicine, Ninth Annual Meeting" New York, New York, USA, 1990.
8. Sandman CA, OHalloran JP, and Isenhart R, *Science* **224,** 1355 (1984).

SMRM, 1991.

Invivo T_2 Relaxation Measurements of Brain may Provide Myelin Concentration

A.L. MacKay, K.P. Whittall, K.S. Cover, D.K.B. Li. and D.W. Paty, Departments of Radiology, Physics and Neurology, University of British Columbia, Vancouver, Canada

Introduction

Spin -spin(T_2) relaxation, which plays an important role in the tissue contrast observed in neurological MR images, is measured from the relaxation decay curve; i.e. a plot of signal intensity versus TE. In clinical MRI, only one or two points on the T_2 relaxation decay curve are sampled (e.g. images acquired at TE30 and TE80). It is our conviction that much more information about the tissue of interest may be obtained by more complete sampling of the relaxation decay curve.

Recent invitro relaxation studies using solid state NMR spectrometers on cat brain (1) and on Guinea pig CNS tissue (2) have identified two T_2 components in white matter; one component with a T_2 of 10 to 20 ms was assigned to water compartmentalized in myelin and the other component to the rest of the tissue water. Since all the water in CNS tissue possesses T_2 times greater than 10 ms, it should be accessible to invivo MR studies. The goal of the present study was to measure spin -spin relaxation in the brain invivo in order to see if the shorter T_2 component was resolvable and to assess the assignment of this component to myelin water.

Methods

Invivo T_2 measurement was carried out with a single slice 32 echo CPMG imaging sequence operating with TR 3000 ms, TE 15 ms to 480 ms, a slice thickness of 10 mm, a FOV of 20 mm, an image matrix of 256x128 and two averages. This pulse sequence, which used nonselective composite 180 pulses and a series of sign alternating and incrementally increasing gradient crusher pulses along the slice select direction (3), provided accurate T_2 times for water phantoms and for a study of multiexponential relaxation in log sections (4) when compared to spectrometer values. In the present study, measurements were made with a GE Signa 1.5T MRI scanner using the head coil and axial slice selection on normal volunteers and volunteers with multiple sclerosis.

Linear inverse theory models (5) with a minimum number of apriori assumptions were employed to analyze the relaxation decay curves. The explicit assumptions made were that the decay curve was the sum of exponential components and that the distribution of T_2 times varied smoothly with T_2 time. No limits were placed on the number of components. CPMG decay curve fits obtained using inverse theory were substantially better than those from fits to one, two or three discrete exponential components. Two means of displaying the linear inverse theory results have been investigated; i) plots of amplitude versus T_2 for a given region of interest and ii) images of various aspects of the individual T_2 plots for each pixel e.g. the amplitude of the shorter T_2 component (related to myelin content) or the integrated amplitude of the entire T_2 plot (related to total water content).

Results

The invivo relaxation results for grey and white matter were in agreement with previous invitro studies (1,2). The T_2 plots were readily separable into two regions: one from water with a T_2 time less than 60 ms and the other from water with a T_2 time greater than 60 ms. Our results support the assignment of the shorter T_2 component to water associated with myelin. This assignment is based upon the following: 1) the lower water concentration in myelin would indicate a shorter T_2, 2) the multilamellar structure of the myelin is likely to provide a diffusion barrier for water;i.e. water is compartmentalized in the sheath, 3) the amount of water (about 20% of the total water in white matter) is consistent with what one would expect to be associated with the myelin, 4) this T_2 component is much smaller or absent in grey matter and is greater in white matter regions with higher myelin density; e.g. the corpus callosum and the internal capsule, and 5) many of the multiple sclerosis lesions showed a reduced amplitude of this T_2 peak suggesting demyelination. In invitro studies (2), EAE lesions histologically found to be demyelinated had a smaller proportion of the shorter T_2 component.

The longer T_2 peak (80-100ms) which we measure in normal white and grey matter corresponds to the remainder of the tissue water. We have noted that in multiple sclerosis lesions this peak shifts to longer T_2 times. The cerebral spinal fluid signal exhibited a much longer T_2 time and was therefore readily distinguishable from tissue water.

Conclusions

From invivo spin -spin relaxation measurements, we have identified a reservoir of water in brain with a relatively short T_2 time. Preliminary evidence suggests that this component may be water in the myelin sheath. If this assignment is correct, such T_2 measurements may enable quantitative invivo determinations of myelin concentration. This would be valuable for multiple sclerosis investigations since active inflammatory lesions could be distinguished from chronic demyelinated lesions.

References

1) Menon, R.S. and Allen, P.S. Magn. Res. Med. in press.
2) Stewart, W.A., Whittall, K.P., MacKay, A.L., Moore, W., Hall, L.D., and Paty, D.W. submitted to Magn. Res. Med.
3) Crawley, A.P., and Henkelman, R.M. Magn. Res. Med. **4**, 34, 1987.
4) MacKay, A.L., Araujo, C.J., Whittall, K.P. and Hailey, J.R.T. 9 th SMRM, 588, 1990.
5) Whittall, K.P. and MacKay, A.L. J. Magn. Res. **84**, 1989.

SMRM, 1992.

Tracking of an Invasive Device within an MR imaging system

C.L. Dumoulin, S.P. Souza and R.D. Darrow
General Electric Research and Development Center, Schenectady NY 12301

Introduction

X-ray fluoroscopes are used routinely to monitor the placement of catheters during diagnostic and therapeutic vascular procedures. Modern X-ray fluoroscopes are optimized to use as low an X-ray dose as possible. Nevertheless, some procedures can be very long and the accumulated X-ray dose to the patient can become significant. The long term exposure of the attending medical staff is perhaps of greater concern since they participate in these procedures as often as several times a day.

MR imaging does not suffer from the dose limitations of X-ray, nor does it offer the temporal resolution of X-ray fluoroscopy. Nevertheless, interventional applications of MR are beginning to arise and it would be useful to follow interventional devices such as catheters, biopsy needles, guide wires, endoscopes and the like in real-time during these procedures.

A system is described which can be used to follow the path of a catheter or other interventional device during an MR exam. The system consists of an rf coil placed external to the patient (typically the standard body coil) and a very small rf coil placed on the tip of the device. One of these coils acts as a transmitter causing nutation of the spin magnetization. The other coil acts as a receiver. The NMR signal is detected in the presence of a magnetic field gradient and the location along the direction of the applied magnetic field gradient is calculated. Subsequent measurements in the orthogonal directions permits the three-dimensional localization of a point on the interventional device.

Methods and Results

A small rf coil is attached to an invasive device. The coil is a simple nonresonant loop (<<1mm diameter) connected via a coaxial cable to a preamplifier. This coil detects NMR signals from its immediate vicinity, but is insensitive to signals coming from more than a few diameters away.

The pulse sequence shown in figure 1 is used to determine the location of the rf coil. In this pulse sequence the body coil is used to excite all the spins within its active volume. Gradient recalled echoes are then generated by applying magnetic field gradient pulses on one of the three orthogonal gradient axes. The coordinates of the location are obtained by calculating one dimensional Fourier transforms of the acquired data and finding the peak signal corresponding to the coil position.

Tracking of the coil has been achieved within a 20cm x 20cm x 20cm volume having a 512 x 512 x 512 resolution. The location of a single coil was determined and displayed in real time at a rate of 20 times a second.

The device position was also determined by simultaneously acquiring signals detected by the coil on the interventional device and by the standard imaging coil on independent receivers. Images were separately reconstructed from the data acquired by the coils. The tracking image has signal intensity only at the location of the device. Since the receiver channel used by the interventional device is independent of the channel used for subject image acquisition, both the image and device position are detected with the same rf and gradient pulses thereby insuring accurate registration.

Discussion

Due to reciprocity the roles of the transmitter and receiver can be reversed. For example, the transmitter coil can be placed on the invasive device and the receiver coil can be placed outside the body.

The device tracking system described above uses the spins in the body to generate the NMR signal. Spins of a different gyromagnetic ratio can be used if the small coil on the interventional device encompasses a small sample. This would permit simultaneous imaging and tracking.

Additional coils can be placed at other locations on the interventional device to provide information on the orientation of the tip and the location of the rest of the device. Information from these coils can be either multiplexed or can be detected by independent receiver systems.

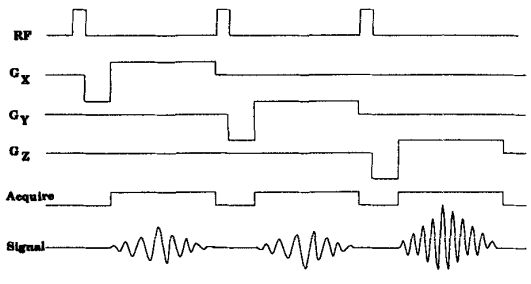

Figure 1. Pulse sequence diagram to detect location of an interventional device.

SMRM, 1992.

Fast Spiral Coronary Artery Imaging

CRAIG MEYER*, BOB HU†, DWIGHT NISHIMURA*, AND ALBERT MACOVSKI*‡
*Departments of *Electrical Engineering and ‡Radiology and*
†Division of Cardiovascular Medicine, Stanford University

We have developed a flow-independent method for imaging the coronary arteries within a breath-hold on a standard whole-body MR imager. Other researchers have recently made significant progress in imaging the coronary arteries by other methods, including fast selective inversion recovery [1] and oblique gradient-echo methods [2,3]. Our technique is based on interleaved spiral k-space scanning and forms a cardiac-gated image in 20 heartbeats. The spiral readouts have good flow properties and generate minimal flow artifacts. The oblique slices are positioned so that the arteries are in the plane and so that the chamber blood does not obscure the arteries. Fat suppression by a spectral-spatial pulse improves the visualization of the arteries.

Fig. 1 shows the spiral imaging sequence, with a 15.5 ms spectral-spatial pulse and 17.5 ms spiral readout gradients. The 20-interleave sequence generates an image with 1.08 mm by 1.08 mm resolution over 20 cm, using a surface coil for FOV restriction. We numerically optimized the readout gradients under gradient amplitude and risetime constraints. We reconstruct the images using a gridding procedure, which involves convolving the data in a 2D array and then performing a 2D FFT.

Spiral gradients have good flow properties, meaning that flowing material is imaged well, even though the readouts are relatively long. There are at least three reasons for the good flow properties of spirals: (1) the x-axis moments of all orders are near zero whenever the k_x axis is crossed (and similarly for the y axis), (2) the center of k space is collected at the start of the scan before any transverse gradients have been played and thus with zero transverse moments of all orders, and (3) coherent "phase-encoding" ghosts do not appear when there are amplitude or phase variations from excitation to excitation, because the interleaving pattern is spiral instead of rectilinear. Fig. 2 shows the moments of the readout gradients of Fig. 1.

We have successfully imaged several coronary arteries, including the LAD and the RCA, in normal volunteers and patients with known coronary artery disease. We will need to do more patient studies before determining if the technique can visualize lesions adequately.

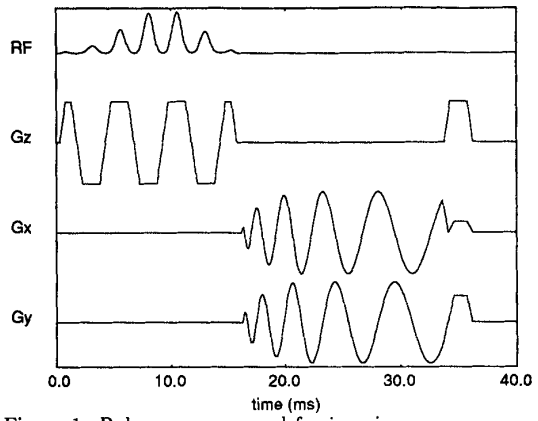

Figure 1: Pulse sequence used for imaging coronary arteries on a 1.5 T GE Signa system.

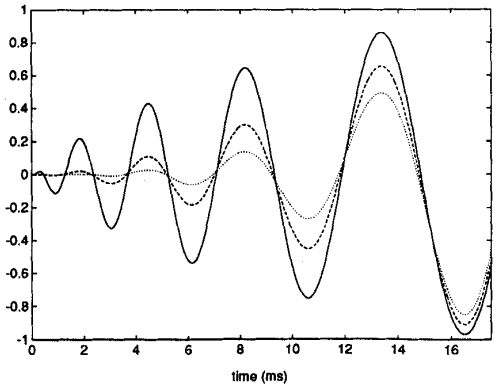

Figure 2: The first three moments of the x gradient of Fig. 1. The solid line is k_x, the dashed line is the first moment, and the dotted line is the second moment.

References

[1] S. WANG, B. HU, A. MACOVSKI, AND D. NISHIMURA, *Magn. Reson. Med.* **18**, p. 417, 1991.
[2] D. BURSTEIN, *JMRI* **1**, p. 337, 1991.
[3] R. EDELMAN, W. MANNING, D. BURSTEIN, AND S. PAULIN, *Radiology* **181**, p. 641, 1991.

SMRM, 1992.

Real Time Imaging of Perfusion Change and Blood Oxygenation Change with EPI

K.K. KWONG, J.W. BELLIVEAU, D.A. CHESLER, I.E. GOLDBERG, C.E. STERN, J.R. BAKER, R.M. WEISSKOFF, R. BENSON, B.P. PONCELET, B.E. HOPPEL, D.N. KENNEDY, R. TURNER*, M.S. COHEN, T.J. BRADY, B. R. ROSEN
Massachusetts General Hospital NMR Center, Dept. of Radiology, Charlestown, MA 02129
*N.I.H. Laboratory of Cardiac Energetics, NHLBI, Bethesda, MD 20892

Introduction

Completely non-invasive, real time (at a frame resolution of seconds) tomographic movies of dynamic human visual system and motor system activity are demonstrated. These images are based on single shot EPI techniques sensitive to changes in either cerebral blood flow (CBF) or blood oxygenation. Given the close correspondence in both space and time between cerebral hemodynamic changes and neuronal activation, these data provide the highest spatial and temporal resolution tomographic maps of human brain activity reported to date.

Methods

Changes in blood oxygenation were detected using a T2* sensitive gradient echo (GE) imaging sequence (TR=3000 ms, TE=40ms). Blood flow changes were evaluated using a spin echo inversion recovery, T1-sensitive pulse sequence (TI=1100 ms, TR=3500 ms, TE=42 ms). The primary visual cortex of our normal volunteers was evaluated using well established patterned-flash photic stimulation. Special care was taken to minimize subject movement between scans by using a snugly fitting head holder. A receive-only RF surface coil was used to improve signal-to-noise (similar results were obtained, albeit with reduced S/N, using a quadrature head volume coil). Single slice images (4-10mm thickness) with 3 x 3 mm in-plane resolution was positioned along the banks of the calcarine fissures. A series of images were acquired continuously with the same imaging pulse sequence (either GE or IR) during task activation. Cine display of subtraction images (activated minus baseline) directly demonstrates activity-induced changes in brain MR signal observed at a temporal resolution of seconds. Similarly, human primary motor cortex (M1) activation was studied with the gradient echo sequence using a hand squeezing paradigm.

Results

During 8 Hz (where the largest MR signal response occurred) patterned-flash photic stimulation, a significant increase in signal intensity (paired *t*-test, $P < 0.001$) of 1.8 ± 0.9% for IR (Fig.1) and 1.8 ± 0.8% for GE (Fig.2) was observed in the primary visual cortex (V1) of seven normal volunteers. The mean rise-time constant of the signal change was 4.4 ± 2.2 seconds for the GE images and 8.9 ± 2.8 seconds for the IR images. Similar signal changes were observed within the human primary motor cortex (M1) (Fig.3) during a hand squeezing task. These data are consistent with concurrent experimental data showing similar changes in using animal models during hypercapnia induced increased blood flow.

Discussion

The relationship between T1 and regional blood flow was characterized by Detre *et al.*: $1/T1app = 1/T1 + f/\lambda$ where T1app is the observed (apparent) longitudinal relaxation time with flow effects included, T1 is the true tissue longitudinal relaxation time in the absence of flow, f is the flow in ml/gm/min, and λ is the brain–blood partition coefficient of water [~0.95 ml/gm]. If we assume that the true tissue T1 remains constant, a change in blood flow Δf will lead to a change in the observed T1app as: $\Delta(1/T1app) = \Delta f/\lambda$. Thus, the MR signal change can be used to estimate the change in blood flow. For an IR sequence with TI ≈ T1, our 2% change in MR signal intensity implies a change in flow of ~ 50 ml/100gm/min, within range of previous PET data. Applying a single imaging sequence repeatedly at the same slice location removes the problem of magnetization transfer as well as other systematic bias. The method of matching blood flow change here with T1 change is thus extremely robust.

Our gradient echo data suggest that the increased signal on T2*- weighted images reflects an increase in venous blood oxygenation. Since CBF (and hence oxygen delivery) changes exceed cerebral blood volume changes by 2-4 times, while blood oxygen extraction increases only slightly, the total paramagnetic blood deoxyhemoglobin content within brain tissue voxels will decrease with brain activation, even though the volume of blood increases. The resulting decrease in the tissue-blood magnetic susceptibility difference leads to less intervoxel dephasing within brain tissue voxels and hence *increased* signal on T2*–weighted images. Physiological data suggests that photic stimulation will reduce the volume susceptibility difference ($\Delta\chi$) between deoxygenated blood and the surrounding brain from 3.2×10^{-8} to 1.9×10^{-8} (cgs). Modeling the cerebral vasculature as randomly oriented cylinders, an initial blood volume of 4% should produce a 2% signal increase in GE images at TE=40 msec.

The advent of MRI techniques utilizing intrinsic blood-tissue contrast, promises the development of a functional human neuroanatomy of unprecedented spatial-temporal resolution.

Fig.1 Photic Stimulation -- IR Images

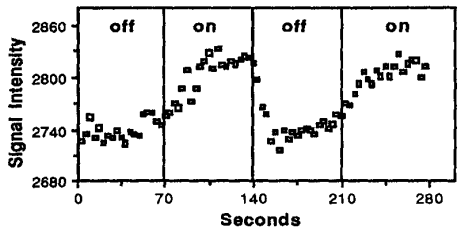

Fig 2. Photic Stimulation -- GE Images

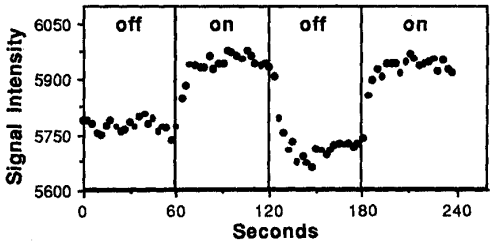

Fig.3 Motor Response Time Course

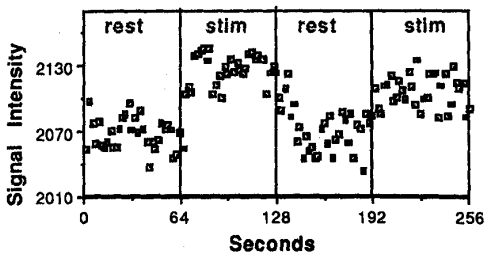

SMRM, 1992.

Time-Course Gradient-Echo EPI of Localized Signal Enhancement in the Human Brain During Task Activation

P. A. Bandettini*, E. C. Wong*, R. S. Hinks‡, R. S. Tikofsky*, and J. S. Hyde*
*Dept. of Radiology, Medical College of Wisconsin, Milwaukee, WI and ‡GE Medical Systems, Milwaukee, WI

PURPOSE:

We demonstrate that time course, long-TE, gradient echo EPI is an effective tool in localizing, without the use of contrast agents, human brain function associated with task activation.

INTRODUCTION:

Blood is a unique source of physiological contrast in MRI due to its oxygenation-sensitive paramagnetic characteristics. Deoxyhemoglobin contains paramagnetic iron while oxyhemoglobin contains diamagnetic oxygen-bound iron (1). It has been demonstrated that the paramagnetic contribution of deoxyhemoglobin affects the susceptibility of whole blood (1-4). Microscopic B_0 field inhomogeneities within and around vessels are created by this susceptibility differential. A spin-echo is attenuated by dephasing due to diffusion of spins through field inhomogeneities while a gradient-echo is additionally attenuated by dephasing due to static field inhomogeneities, independent of diffusion.

Recent work demonstrates the sensitivity of gradient-echo imaging to blood oxygenation changes (3,5). Furthermore, preliminary success using gradient-echo EPI in observing signal changes in the visual cortex during photic stimulation has been reported (2).

METHOD:

Imaging was performed on a standard clinical GE 1.5 Tesla Signa system using either a 30.5 cm i.d. three-axis local gradient coil or a 33.0 cm i.d. prototype GE z-axis local gradient coil. A blipped, gradient-echo EPI pulse sequence, having an initial $\pi/2$ pulse and an effective TE, (kx, ky) = (0, 0), of 50 ms, was employed. Data acquisition time was 40 ms to acquire a 64 x 64 image. The FOV ranged from 20 to 24 cm. Slice thickness was 25 mm to ensure that the region of activation was completely contained in the slice. A series of up to 128 sequential images of the same plane in the brain was obtained using an inter-scan delay or TR of 2 to 3 s.

Each time course series was generally divided in time into three segments. During the first and last segment, the subject was instructed to remain completely relaxed. During the middle segment, the subject was instructed to perform the well-established sensory and motor cortex activation paradigm of touching each finger to thumb in a self-paced and repetitive manner. Fingers on one or both hands were used.

All post-processing was performed on a Sun SPARCstation 1+. Brain activity images were obtained by calculating the cross correlation between the time response of each voxel and the ideal response to the task activation. The cross-correlation calculation was performed for each voxel and displayed in an image array, termed the brain activity image. Voxel values that change in a manner temporally correlated to the finger movement activity had the highest values in the brain activity images. Plots of signal intensity versus image number from activated regions, demonstrating the temporal characteristics of the signal enhancement, were also made. The fractional signal change in the activated region was calculated from a 4-voxel volume in each image series using:

$$\%\Delta S = ((Sa - Sr) / Sr) \times 100$$

averaged activated state signal, and Sr is the averaged resting state signal. The change in relaxation rate, ΔR_2^*, associated with task activation was calculated using the relationship (6):

$$-\ln(Sa / Sr) / TE = \Delta R_2^*$$

RESULTS:

A total of 24 experiments were performed on 6 healthy volunteers. An increase of 4.3% ± 0.3% in signal was observed in the areas functionally associated with the task during activation. The calculated ΔR_2^* during activation is $-0.8 \pm 0.1\ s^{-1}$.

The areas of signal enhancement correspond with regions known to be associated with the finger movement task. Figure 1 shows a typical plot of signal intensity versus sequential image number (TR = 2 s) from an ROI in the primary motor cortex contralateral to the hand performing the task. Finger movement takes place during the time between the vertical arrows. Preliminary results using spin-echo EPI show no significant signal enhancement during task activation.

CONCLUSIONS:

The observed increase in signal intensity in the activated region of brain is potentially explained qualitatively by findings that, during local brain stimulation, oxygen delivery to the activated region exceeds metabolic need (7). The overabundance of oxygen-rich blood leads to a decrease in the local oxygen extraction fraction, directly suggesting a local increase in blood pO_2 and a local decrease in the concentration of deoxyhemoglobin. Such a decrease in deoxyhemoglobin concentration decreases the vessel-tissue susceptibility differential, allowing increased spin coherence and thus increased signal. Time course gradient-echo EPI is a powerful new noninvasive tool for assessment of regional cerebral activation with high temporal and spatial resolution.

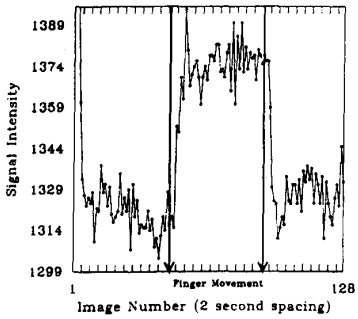

Figure 1

REFERENCES:

1. Thulborn, K.R., Waterton, P.M., Matthiews, P.M., and Radda, G.K., *Biochim. Biophys. Acta 714, 265, (1982).*
2. Brady, T.J. *SMRM abstr. 1: 2, (1991).*
3. Ogawa S. and Lee, T., *Mag. Res. Med. 14: 68, (1990).*
4. Weisskoff R. and Kiihne, S., *SMRM abstr. 2: 689, (1991).*
5. Turner R., Le Bihan, D., Moonen, C.T., et. al. *Mag. Res. Med., 22: 159, (1991).*
6. Rosen, B.R., Belliveau, J.W., and Chien, D., *Mag. Res. Quart. 5: 263, (1989).*
7. Fox, P. and Raichle, M.E., *PNAS, USA, 83: 1140*

SMRM, 1992.

Functional Brain Mapping using MRI: Intrinsic Signal Changes Accompanying Sensory Stimulation

S. Ogawa[1], D. W. Tank[1], R. Menon[2], J. M. Ellermann[2], S. G. Kim[2], H. Merkle[2] and K. Ugurbil[2]
[1]AT&T Bell Labs., Murray Hill, NJ and [2]Univ. of Minnesota Medical School, Minneapolis, MN

We report that visual stimulation produces an easily detectable (5-20%) transient increase in the intensity of water proton magnetic resonance signals in human primary visual cortex in gradient echo images obtained with FISP sequences (40 ms echo time) at 4T field strength. Our experiments were motivated by the previous observation that magnetic resonance images of rodent brains at high (7T) field showed proton signal intensity alterations which were Blood Oxygenation Level Dependent (BOLD) in regions of close proximity to local blood vessels (1, 2). The possibility of using deoxyhemoglobin induced magnetic susceptibility changes to map human sensory and mental operations is suggested by the increasing evidence that an increase in regional cerebral blood flow (rCBF) and a local elevation in human brain venous blood oxygenation accompanies an increase in neuronal activity (3, 4).

Materials and Methods Magnetic resonance images were acquired with a 4T whole body system using a curved surface r.f. coil (14 cm in diameter). Consecutive gradient echo images (85 images with two visual stimulation periods/run) were obtained from the average of two scans using a FISP pulse sequence (TE=40 ms; TR= 45 ms; voxel size=1.6x3.1x10 mm^3; time interval between scans=2 s; one image /~10 s). The plots of signal intensity change versus image number were digitally filtered (gaussian filter: 2 point width). Heart rate and arterial blood oxygenation were monitored throughout an imaging session.

RESULTS Experiments were performed on 6 normal human volunteers (48 visual stimulation periods; 12 sagittal; 36 oblique image planes). In whole field visual stimulation experiments (10 Hz LED illumination), difference images between stimulation and non-stimulation periods showed that signal increases produced by stimulation occurred in areas predominantly occupied by gray matter in the visual cortex. This was easily shown by a comparison with inversion recovery-T_1 weighted images which enhanced white matter signals preferentially.

The temporal responses of the signal at a few locations (1, 2 visual cortex; 3 outside visual cortex) are shown in Fig. 1 for an experiment on an obliquely angled plane. The largest fractional changes in signal intensity in an imaging series ranged 5-20% (mean 8.2%; s.d. 3.3%) . Although global changes in signal intensity were observed with heart rate variation, in all experiments reported here heart rates did not show any change during and after stimulation. The signal intensity during non stimulation periods fluctuated with a standard deviation of 2%. This fluctuation contained contributions from instrumental noise and physiology related variations.

Figure 2 shows a result of hemi field (Left and Right) visual stimulation observed at a rostral site in the right occipital pole. This demonstrates that functional maps within a brain region can be determined by this BOLD imaging.

Fig.1 Whole field stim. Fig.2 Hemi field stim.

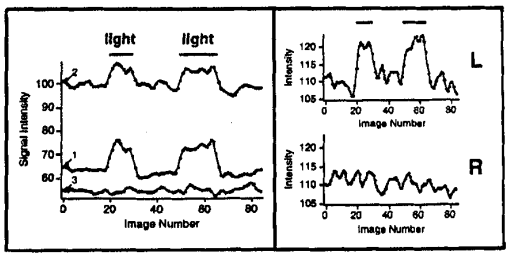

At a short TE (8 ms), with all other acquisition parameters held constant, the fractional signal change induced by visual stimulation was diminished, although the overall signal intensity was high. This result indicates that the signal change observed upon stimulation is not due to a T_1 or T_1*(flow effect) process, but is consistent with a change in T_2* (or T_2). We suggest the signal increase during stimulation is produced by a local increase in venous blood oxygenation that changes T_2*.

From the dependence of image signal intensity on venous blood oxygenation measured in rodent brains at 7T, a rough estimate of the signal change at 4T for a 50% increase in rCBF was 4%. The changes we observed in the present study were much larger. This may indicate that rCBF increases in the gray matter may be significantly higher than the value of 30-75% determined by a PET study under a similar stimulus paradigm. Because of the limited resolution, PET experiments necessarily average gray matter and white matter.

CONCLUSIONS Imaging methods that enhance BOLD contrast can be used to map human mental operations. When combined with rapid gradient echo MRI methods, dynamic functional brain mapping should be possible with a temporal resolution determined by the neural-hemodynamic response time.

REFERENCES

1. Ogawa, S., Lee, T.M., Nayak, A.S. & Glynn, P., *Magn. Reson. Med.*, 14, 68, 1990
2. Ogawa, S., Lee, T.M., Kay, A.R. & Tank, D.W., *Proc. Natl. Acad. Sci. USA*, 87, 9868, 1990
3. Fox, P.T., Raichle, M.E., Mintun, M.A. & Dence, C., *Science*, 241, 462, 1988
4. Frostig, R.D., Lieke, E.E., Ts'o, D.Y. & Grinvald, A., *Proc. Natl Acad. Sci. USA*, 87, 6082, 1990

Automated Determination of Metabolite Concentrations from Localized *In Vivo* Proton NMR Spectra

Stephen W. Provencher, Thomas Michaelis, Wolfgang Hänicke, and Jens Frahm
Max-Planck-Institut für biophysikalische Chemie, Postfach 2841, D-3400 Göttingen, Germany

Introduction

The reliable determination of metabolites and their concentrations is of fundamental importance in biochemical and clinical MRS. The usual procedure of integrating over individual peaks of spectra is hampered by the complexity of the overlapping metabolite spectra, particularly at the relatively low fields used *in vivo* [1]. However, this complexity can be turned into an advantage by analyzing the *in vivo* spectrum as a linear combination of a basis set of *complete* spectra (not individual peaks) of model metabolite solutions *in vitro*. The complexity (high information content) of the metabolite spectra results in a highly unique analysis, since two metabolites with overlapping peaks at one chemical shift can still be separated because of their different structures at other chemical shifts. By using the same experimental conditions for the model *in vitro* spectra as for the *in vivo* spectra [1], the complicated spin-spin couplings, J modulations, etc. are automatically accounted for in the analysis. A similar stategy is now widely used in the analysis of circular dichroism spectra for protein secondary structure [2].

The method has been automated to take the time-domain *in vivo* data as input and to output the metabolite concentrations and their estimated uncertainties, with no user interaction. This should improve reproducibility and ease the exchange of data, since subjective steps such as interactive visual phasing of the *in vivo* spectra are no longer necessary.

Methods

Model spectra of 13 cerebral metabolites were measured as in [1]. Conditions were the same as *in vivo*, except that the concentrations were five to ten times higher, resulting in a significantly lower noise level in the model spectra.

The *in vivo* spectrum is then analyzed as a sum of the phased model spectra convoluted to account for the difference between $1/T_2^*$ of the *in vivo* and model spectra. This $\Delta(1/T_2^*)$ parameter and the zero- and first-order phase corrections for the *in vivo* spectrum are determined automatically by a constrained nonlinear least-squares procedure. A highly restricted nonnegatively constrained deconvolution [3] for slight variations in the line shapes and small relative shifts (a maximum of two grid points) on the ppm-axes of the spectra is simultaneously performed. A primitive two-parameter linear background, has been used, but a better model, e.g., for incomplete water suppression, could be included.

Results and Discussion

Test analyses of spectra from model mixtures were encouraging, both at physiological and higher concentrations; e.g., a 50 mM equimolar mixture of NAA, glutamate, and glutamine yielded relative concentrations of 1 : 1.01 : 1.03, and a 1 : 1: 0 mixture yielded 1 : 0.97: 0.02, despite the similarity between the spectra of glutamine and glutamate. Concentrations of the other 10 metabolites were small with large estimated relative uncertainties.

Figure 1 shows a typical 2.0 T localized ^{1}H spectrum of human gray matter *in vivo* [1]. The data (dotted) are well fit (solid) by the 13 model spectra, and the results are consistent internally and with conventional single-peak integrations. Figure 2 shows the same spectrum analyzed with choline removed from the basis set. The concentrations of most of the metabolites do not change much and are thus robust to this extreme deficiency in the basis set. Only taurine increases in a futile attempt to fit the choline peak, but the other taurine peaks around 3.3–3.4 ppm prevent this, and it is still clear that something important is yet to be discovered.

Future work will include the development of an experimental protocol that will allow accurate determination of absolute (rather than just relative) concentrations *in vivo*.

References

1. Michaelis, T. *et al, NMR Biomed.*, **4**, 90, 1991.
2. Provencher, S.W. *et al, Biochemistry*, **20**, 33, 1981.
3. Provencher, S.W. *Comput. Phys. Commun.*, **27**, 213, 229, 1982.

Fig. 1: With choline

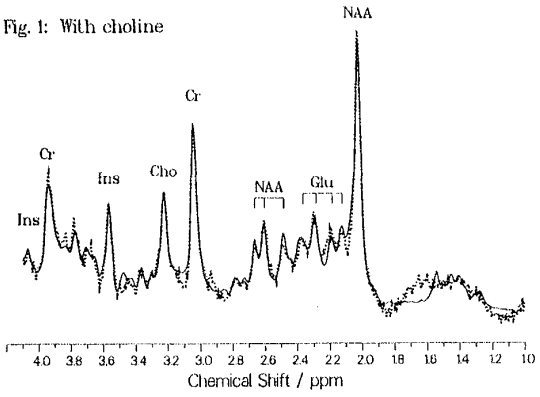

Fig. 2: Without choline

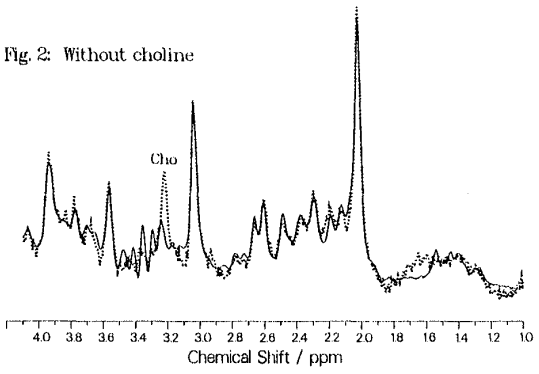

Fiber orientation mapping in an anisotropic medium with NMR diffusion spectroscopy

Peter J. Basser°, Denis LeBihan†
°Biomedical Engineering and Instrumentation Program, and
†Diagnostic Radiology Department, Warren G. Magnuson Clinical Center, NIH, Bethesda, MD 20892 USA

Purpose: The diagonal and off-diagonal components of the apparent self-diffusion tensor [1], $\underline{D}$, are used to construct a diffusion ellipsoid for a voxel that depicts both orientation of tissue microstructures, such as muscle fibers, and mean diffusion distances. New weighting parameters are also suggested for structural NMR imaging.

Principles: In heterogeneous, anisotropic media, $\underline{D}$ relates the flux of spin-labeled protons to their concentration gradient. Since $\underline{D}$ is symmetric and positive-definite, its three mutually orthogonal eigenvectors, $\varepsilon_1, \varepsilon_2$, and ε_3, define the principal axes and its three positive eigenvalues, λ_1, λ_2, and λ_3, are the diffusivities in these directions [2]. Continuum models of diffusion in heterogeneous media [3] suggest that the principal axes of $\underline{D}$ coincide with those of the grain or fiber and the principal diffusivities of $\underline{D}$ are related to the structure, geometry, and diffusivity of the various microscopic compartments within the heterogeneous medium.

The diffusion ellipsoid: In heterogeneous, anisotropic media [3], the macroscopic effective self-diffusion tensor, $\underline{D}$, appears in the conditional probability density function, which is the probability that a particle at x at time t was at x_0 at t = 0:

$$\wp(x \mid x_0,t) = \frac{1}{\sqrt{|\underline{D}|(4\pi t)^3}} \exp\left(\frac{-(x-x_0)^T \underline{D}^{-1} (x-x_0)}{4t}\right). \quad (1)$$

Setting the quadratic form to 1/2, i.e.,

$$\frac{(x-x_0)^T \underline{D}^{-1} (x-x_0)}{2t} = 1 \quad , \quad (2)$$

defines a diffusion ellipsoid whose principal axes constitute the local "fiber" frame of reference, and whose j^{th} major axis is the mean distance a spin-labeled proton diffuses in the j^{th} principal direction, $\sqrt{2\lambda_j \Delta}$, during the diffusion time, Δ.

The scalar invariants: Three scalar invariants of $\underline{D}$, I_1, I_2, and I_3, are:

$$\begin{aligned} I_1 &= \lambda_1 + \lambda_2 + \lambda_3 = \mathrm{Tr}\,\underline{D} \\ I_2 &= \lambda_1\lambda_2 + \lambda_3\lambda_1 + \lambda_2\lambda_3 \\ I_3 &= \lambda_1\lambda_2\lambda_3 = |\underline{D}| \quad . \end{aligned} \quad (3)$$

They have the desirable properties of being independent of the coordinate system in which $\underline{D}$ is measured, and insensitive to the scheme by which the λ_i are numbered, making them (or functions of them), ideal weighting factors in structural NMR imaging.

Data analysis: Diffusion ellipsoids for pork loin are constructed from two apparent self-diffusion tensors, $\underline{D}^{0°}$ and $\underline{D}^{41°}$, estimated from spin-echo experiments [1]:

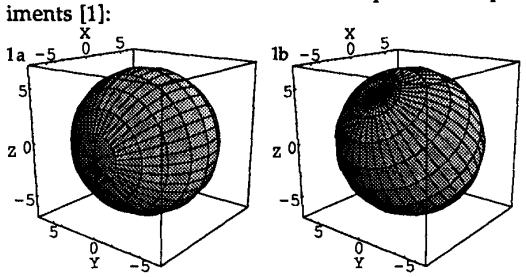

Fig. 1a,b: Diffusion ellipsoids of a pork loin sample. Laboratory coordinates, x, y, and z are in μm. The eigenvector corresponding to the largest eigenvalue defines the polar axis.

In Fig 1a, the grain of the sample was nearly aligned with the magnet's x axis. Eigenvalues (principal diffusivities) of $\underline{D}^{0°}$ are $\{\lambda_1 = (1.0406\pm0.0007)10^{-5}, \lambda_2 = (0.944\pm0.001)10^{-5}, \lambda_3 = (0.8532\pm0.0006)10^{-5}\}$ (cm²/sec). In Fig. 1b, the same sample is rotated approximately 41° in the z-x plane. Eigenvalues of $\underline{D}^{41°}$ are $\{\lambda_1 = (1.0119\pm0.0003)10^{-5}, \lambda_2 = (0.9343\pm0.0006)10^{-5}, \lambda_3 = (0.8767\pm0.0018)\ 10^{-5}\}$ (cm²/sec).

Discussion: The eigenvectors that define the fiber frame follow the sample when it is rotated. This is represented by the tipping of the polar axis. The scalar invariants of $\underline{D}$ differ by no more than 1% in both cases because they are intrinsic to $\underline{D}$, independent of the sample's orientation in the magnet. Both ellipsoids are nearly spherical, presumably because the diffusion time, Δ = 22.5 ms, corresponding to a mean diffusion distance of 4.7 μm, is too short for the majority of spin-labeled protons to encounter diffusional barriers.

Although a single voxel was used in this study, these principles can be generalized to multiple voxels. One could envision 3-D fiber maps [4] or diffusion ellipsoids displayed in each voxel, connected like link sausages that follow fiber tracts.

Conclusion: Constructing the diffusion ellipsoid requires knowledge of all diagonal and off-diagonal elements of $\underline{D}$. Inherently, $\underline{D}$ contains unique directional, structural and anatomical information *within a voxel* that scalars such as T_1 or T_2 do not - information that is embodied in the diffusion ellipsoid and scalar invariants.

References:

1. Basser, P. J., et al., submitted SMRM 1992.
2. Carslaw, H. S., Jaeger, J. C., Oxford Press, 1959.
3. Crank, J., Oxford Press, 1975.
4. Douek, P., et al., *J. Comput. Assist. Tomogr.* 15, 923, 1991.

SMRM, 1992.

A Precise and Fast Temperature Mapping Method Using Water Proton Chemical Shift

Y.Ishihara,A.Calderon,H.Watanabe,K.Mori,K.Okamoto,Y.Suzuki,K.Sato
K.Kuroda*,N.Nakagawa*,S.Tsutsumi*
TOSHIBA R&D Center,Kawasaki 210,JAPAN
*Faculty of Engineering,Osaka City University,Osaka 558,JAPAN

Introduction

Mapping the temperature distribution inside a body enables one to diagnose disorders such as metabolic and blood circulation abnormalities, since body temperature is closely related to physiological functions. In addition, non-invasive temperature monitoring during hyperthermia is highly desirable.

Recently, non-invasive thermometries using NMR parameters (ρ,T_1,T_2,D[1]) have been reported. It is difficult, however, to accurately measure the body temperature using only the above-mentioned parameters, as the temperature dependence for individual parameters varies from organ to organ and tissue to tissue.

We have considered the temperature dependence of the water proton chemical shift[2] and verified that this relationship is independent of biological tissue differences in-vitro[3]. Knowledge of these properties enables more accurate temperature measurements. We propose here a fast and precise temperature mapping method using field echo phase mapping, which is based on just such chemical shift properties. This method permits the measurement of temperature differences in the object. Using phantom experiments the validity of this method is shown.

Principle

The local magnetic field $\Delta B_0(\vec{r})$ can be represented as the sum of the field inhomogeneity $\delta B_0(\vec{r})$ and the chemical shift field $Bc(T(\vec{r}))$, which depends on the temperature distribution $T(\vec{r})$:

$$\Delta B_0(\vec{r}) = \delta B_0(\vec{r}) + Bc(T(\vec{r})) \qquad [1]$$

where $\delta B_0(\vec{r})$ is produced by the field error of the magnet and the magnetic susceptibility of the sample.

Variations in the chemical shift field $\Delta Bc(T(\vec{r}))$ are obtained by subtracting the field distribution at a reference temperature T_0 from the distribution after a change in temperature. $\Delta Bc(T(\vec{r}))$ can be calculated from the phase difference $\Delta\theta(\vec{r})$, which is rapidly measured using field echo phase mapping. The temperature distribution can then be calculated using the following equation:

$$[T(\vec{r})-T_0(\vec{r})] = \alpha\Delta Bc(T(\vec{r})) = \alpha\Delta\theta(\vec{r})/\gamma Te \qquad [2]$$

where α is the temperature dependent coefficient of the water proton chemical shift, and Te is the echo time.

Method

The experiment for the temperature mapping was performed using a 4.7 T MRI system, a 120 mm diameter QD-BC, and a 40 mm diameter spherical phantom filled with a 1 % NaCl solution. Inductive heating using a continuous wave at 200 MHz and 10 W was applied to the phantom to produce the change in temperature. After heating for 10 minutes the temperature inside the phantom increased about 10 ℃ from an initial temperature T_0 of 30 ℃. The inner temperature distribution of the phantom was then measured after each successive minute during the cooling process. The following measurement conditions were used: TR/TE 115/13 ms, matrix size 128 x 128, FOV 85 x 85 mm, slice number 5, slice thickness 3 mm, and acquisition time 15 s. The temperature dependence of the water proton chemical shift was estimated using thermocouples placed within the phantom.

Results

The temperature dependence of the water proton chemical shift was found to be linear with a correlation coefficient of -0.998, and can be expressed as $\Delta\delta(\Delta T) = -(0.0091\pm0.0003)\Delta T - (0.006\pm0.003)$. Figure 1 shows the profiles obtained from converting phase differences into temperature according to the obtained temperature dependence. The changes in temperature following spontaneous cooling were observed. The measurement accuracy was determined from the reproducibility of the results and better than ± 1 ℃. This reproducibility is dependent on the image S/N and the stability of the system.

Conclusions

A new temperature measurement procedure using field echo phase mapping gives high accuracy and rapid measurements. This method can be used for mapping the body's internal temperature distribution with high accuracy since the temperature dependence of the water proton chemical shift is independent of the tissue type[3]. This is especially useful when monitoring body temperature during hyperthermia. It is, however, necessary to evaluate the magnetic susceptibilities, pH, and blood flow effects on the temperature dependence of the water proton chemical shift in living systems.

References

1. LeBihan,D.,Delannoy,J.,Levin,R., 7th Ann.SMRM Meeting,881,1988
2. Hindman,J.C.,J.Chem.Phys.44,4582,1966
3. Kuroda,K.,Miki,Y.,Nakagawa,N.,Tsutsumi,S., Ishihara,Y.,Suzuki,Y.,Sato,K.,Medical& Biological Engineering&Computing 29,1991

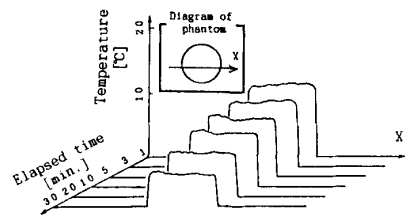

Figure 1. Profiles of temperature changes inside the phantom after heating

SMRM, 1993.

Identification and Characterization of the Ischemic Penumbra of Acute Human Stroke using Echo Planar Diffusion and Perfusion Imaging.

Steven Warach, MD. PhD, Piotr Wielopolski, PhD, Robert R. Edelman, MD
Departments of Neurology and Radiology, Beth Israel Hospital, Harvard Medical School, Boston, MA, USA

Introduction. A penumbra of partial ischemia has long been hypothesized to surround the central core of ischemia in acute stroke. This ischemic penumbra has served as a rationale for the development of early pharmacological interventions aimed at limiting the infarct size in stroke Although its existence has been implicated by PET studies, it has never been directly demonstrated in human stroke.

Methods. Eight patients with acute cerebral infarctions have been studied to date with combined perfusion and diffusion imaging. Time from onset of symptoms to first MR study ranged from 3-48 hours. Several patients were studied more than once. Studies were performed on a 1.5T whole body imager with the capability of echo planar imaging (Siemens Medical Systems, Erlangen, Germany). Multislice EPI diffusion weighted imaging was performed using a spin echo sequence, and TE = 100 msec, 128 x 128 matrix, 5mm slice thickness. The diffusion gradient strength was varied to give b values of 0, 34, 137, 307, 546, 854, and 1205 sec/mm^2. Multislice dynamic blood volume imaging was performed with an EPI FID sequence (TE = 60, 128 x 128 matrix, slice thickness 5-10 mm), during which an intravenous bolus (20cc) of gadolinium-DTPA was injected. At each slice position an image was acquired every 1.5 to 3 seconds. An initial screening diffusion sequence with b=1205 sec/mm^2 was performed to localize the infarct using 25-30 contiguous axial 5mm slices. The remainder of the exam focused on the slices containing the infarct as well on several slices above and below.

Results. Three distinct regions could be identified both qualitatively and quantitatively: normal brain, the core of the infarct, and an intermediate zone. On diffusion weighted images of some patients an intermediate zone appeared along the periphery of the infarct intermediate in intensity between the normal brain and the hyperintense core of the acute infarct (example in Figure 1). This intermediate zone did not evolve into an infarct on follow-up scans.

Dynamic blood volume imaging demonstrated progressively delayed passage of contrast as the core of the infarct is approached. Qualitatively, this is best appreciated when displaying the images as a cine loop. Quantitatively, there is a rightward shift and broadening of the curve of the change in signal intensity over time as region-of interest measurements are made progressively closer to the core of the stroke; there is also a lower precontrast signal intensity closer to the core, suggesting reduced deoxyhemaglobin in the penumbra. Figure 2 illustrates the results for a patient 23 hours after stroke onset. The penumbra is demonstrable as long as a week after onset of focal ischemia and has been observed to persist for this length of time without progression to infarction or without neurological symptoms.

Conclusion. We have found evidence of the ischemic penumbra using MR diffusion and dynamic blood volume imaging. The results to date indicate that not only may persistent partial ischemia cause evolution of an infarct, but may be present asymptomatically subacutely. Further study may determine whether the subacute penumbra is a risk for further infarction and potentially amenable to therapeutic intervention outside the hyperacute period.

FIGURE 1

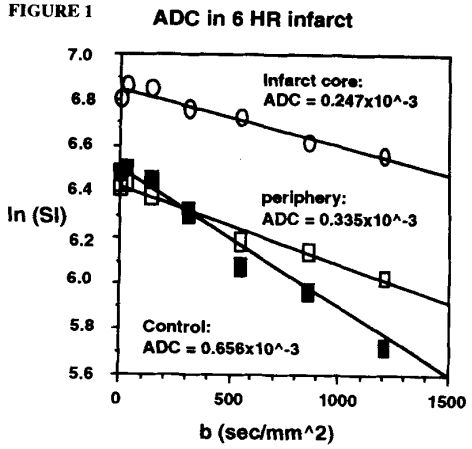

FIGURE 2

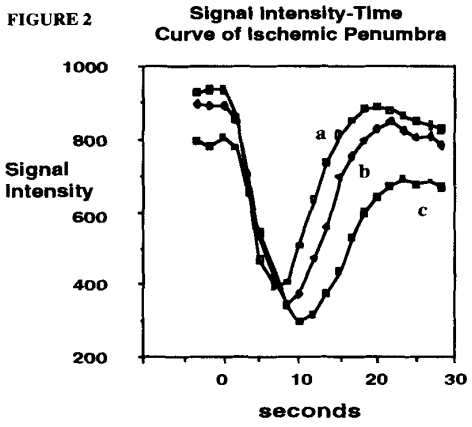

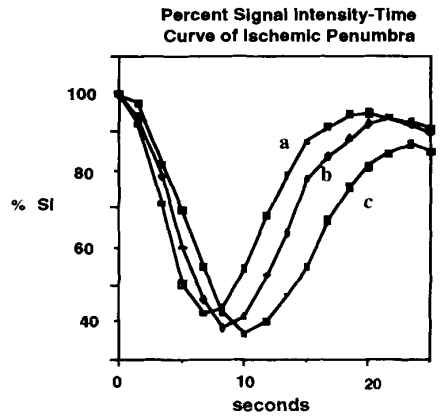

a, b, and c are from regions of interest progressively closer to ischemic core

SMRM, 1993.

(k,t)-Space Sampling Considerations for Imaging of Time-Varying Functions

Zhi-Pei Liang and Paul C. Lauterbur
Biomedical Magnetic Resonance Laboratory, University of Illinois, Urbana, IL 61801

Introduction

K-space sampling requirements for imaging of stationary objects are well understood. In dynamic imaging, the object is modeled by a time-varying function describing the spatiotemporal distribution, and the k-space treatments are often not adequate. Recently, Xiang and Henkelman have elegantly described motion artifacts associated with imaging of time-varying functions in the (k,t)-space setting [1]. In this paper, we will discuss the (k,t)-space sampling requirements for exact recovery of the spatiotemporal distribution. Such a theory can give the optimal ordering of phase encodings. It will also provide some insights into how to improve imaging efficiency and reduce motion artifacts.

Theory

For simplicity, we consider one-dimensional imaging using phase encoding. After taking into account the dynamic changes during the imaging process, the image function becomes a two-dimensional function, $I(x,t)$, of two independent variables: space (x) and time (t). In practice, a sequence of M snapshot images $I(x,t_n)$ is desired to define the spatiotemporal distribution. Assuming that each of these images has spatial resolution of $1/(N\Delta k)$, one has to instantaneously acquire N phase encodings, giving the ideal (k,t)-space coverage in Fig. 1. But because of dynamic changes taking place from one encoding to another (the so-called time-sequential constraint), (k,t)-space is effectively sampled as in Fig. 2, which is called lexicographic sampling in signal processing [2, 3]. Whether or not we can recover the desired spatiotemporal distribution from this set of time-sequentially sampled data points is dependent on the temporal-frequency distribution of the dynamic changes. Based on multidimensional sampling theory [4], the Fourier transform of the sampled data is a periodic function, as depicted in Fig. 3 where the vertical axis represents the temporal-frequency distribution; $\vec{u}_1 = [u_{11}, u_{12}]^t$ and $\vec{u}_2 = [u_{21}, u_{22}]^t$ are related to $\vec{v}_1 = [v_{11}, v_{12}]^t$ and $\vec{v}_2 = [v_{21}, v_{22}]^t$ by the following matrix equation

$$\begin{bmatrix} u_{11} & u_{21} \\ u_{12} & u_{22} \end{bmatrix} = \begin{bmatrix} v_{11} & v_{21} \\ v_{12} & v_{22} \end{bmatrix}^{-1} \qquad (1)$$

Assume that the maximum temporal-frequency of the dynamic changes is f_M and the time interval between two successive encodings is Δt. The Nyquist sampling criterion requires that $N\Delta t \leq 1/f_M$ for an aliasing-free reconstruction. In practice, this condition is often not met, and one has to sacrifice spatial resolution (reduce N) to reduce this aliasing artifact. This limitation can be alleviated by using different sampling patterns or by making use of the temporal-frequency distribution of the dynamic changes. For example, bit-reversed sampling and random sampling [3] (Fig. 4) can lower the sampling frequency below the Nyquist rate and hence reduce aliasing artifact.

If a time-varying image function is known to have high temporal frequency components only in a limited region within the field-of-view (FOV), as often the case in task-activated functional imaging, one can choose the $\vec{u}_1$ and $\vec{u}_2$ vectors optimally such that aliasing would not create image artifacts. An example is shown in Fig. 5 where the time-varying function has dynamic changes of a large frequency range only in the central region; one can still extract the desired image function from the aliased (but not overlapped) pattern using a special low-pass filter. The required sampling vectors $\vec{v}_1$ and $\vec{v}_2$ in (k,t)-space can be determined from equation (1).

Conclusion

Sampling is a fundamental operation in MR imaging systems and has been treated in k-space. For imaging of time-varying functions, the sampling requirements for exact image recovery should be cast in (k,t)-space. Such a treatment offers theoretical insights into how to optimally order the phase-encodings for improving imaging efficiency and reducing motion artifacts. It may also prove useful for a variety of dynamic imaging applications, such as dynamic studies of contrast agents and functional imaging.

Acknowledgements

The authors wish to thank Prof. Yoram Bresler of the Electrical and Computer Engineering Department for helpful discussions. This work was supported by the Whitaker Foundation, NSF STC grant NSF-DIR-89-20133, NIH Grants PHS-5-P41-RR05964 and 1S10RR06243, ONR grant N00014-92-J-1160, the National Center for Supercomputing Applications, the Beckman Institute, and the Servants United Foundation.

References

[1] Q.-S. Xiang and R. M. Henkelman, *Magn. Reson. Med.*, Vol. 29, 422-428, 1993.
[2] E. Dubois, *Proc. IEEE*, vol. 73, 502-522, 1985.
[3] J. P. Allebach, *J. Opt. Soc. Am.*, vol. 71, 99-105, 1981.
[4] D. E. Dudgeon and R. M. Mersereau, *Multidimensional Digital Signal Processing*, Prentice-Hall, Inc., New Jersey, 1984, pp. 36-47.

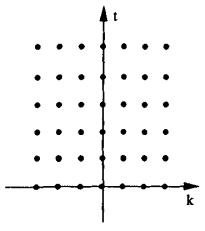

Fig. 1

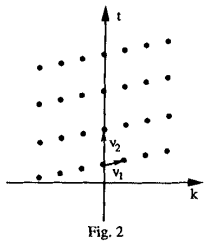

Fig. 2

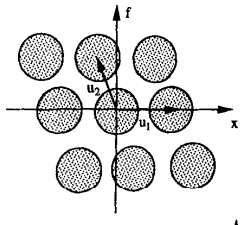

Fig. 3

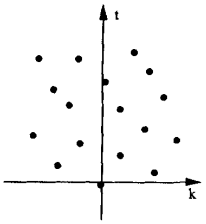

Fig. 4

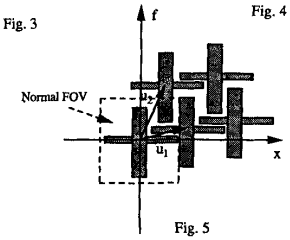

Fig. 5

SMR, 1994.

Applications of EPISTAR for mapping functional changes in relative cerebral blood flow.

S. Warach, D.G. Darby, V. Thangaraj, A.C. Nobre, J.A. Sanes, R. R. Edelman. Beth Israel Hospital, Harvard Medical School, Boston, MA, and Brown University, Providence, RI, USA

Introduction EPISTAR is a method of non-invasive qualitative cerebral blood flow mapping using proximal 180 degree RF tagging of inflowing arterial spins and echoplanar readout of a distal slice alternating with and subtracted from similarly acquired images not preceded by the inversion pulse (Edelman et al, this volume). Several features make this technique appealing as a potential method of localizing flow related changes in local brain activity; in particular, the method is relatively insensitive to small head movements and detects flow related changes primarily on the arterial and capillary side of circulation, without obvious contamination from venous signal.

Methods Studies were performed on a 1.5T whole body imager with the capability of echo planar imaging (Siemens Medical Systems, Erlangen, Germany). Over 40 studies of healthy volunteers were performed with various sensory, motor, and cognitive paradigms. Typical parameters were 8-10 mm thick slice, with a 90mm inversion slab centered 65 mm proximal to the imaging slice, 128 x 128 matrix, FOV 32 x 32 cm, inversion time (inflow time) 950 ms, TE 16 ms, 36 - 48 acquisitions, for acquisition times of approximately 1 - 2 minutes for each EPISTAR image. Difference images and percent difference images were derived with the aid of filters to minimize the contribution of background noise. Flow related changes were localized to their anatomical source by superimposition of EPISTAR difference map onto images acquired using a 3D MPRAGE sequence.

Results Initial experiments confirmed that standard sensory-motor paradigms give localized changes in expected regions of cortical grey matter: unilateral motor task to contralateral motor strip (see FIGURE 1), 8 Hz flashing lights to bilateral visual cortex, hemifield alternating checkerboard to contralateral visual cortex. In addition, contralateral basal ganglion activation was observed during a motor task. Study of a simple lateral saccadic eye movement task, revealed consistent changes on the precentral gyrus, supplementary motor area, and visual association areas, rather than the classic 'frontal eye fields'. Simple movements of fingers and wrist revealed a pattern of response in primary motor cortex suggestive of multiple, overlapping sites of activation for each movement. Changes related to language processing have also been demonstrated.

Conclusion EPISTAR has been demonstrated to map functional changes in relative cerebral blood flow onto the brain, and has begun to reveal new insights into the study of cognitive-motor networks in the brain.

FIGURE 1A. Axial EPISTAR image with TI=950 ms during rest in normal volunteer. Arrow points to region that will have increased flow related signal during finger tapping (FIGURE 1B, below)

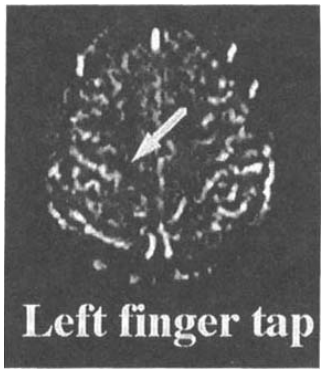

FIGURE 1B. EPISTAR image as in FIGURE 1A in same subject during rapid alternalting finger tap of left hand. Arrow points to region of increased flow related signal.

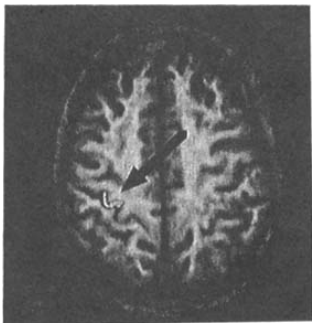

Figure 1C. Overlay of filtered EPISTAR difference image onto T1-weighted image localizes increased blood flow to anterior bank of central sulcus (motor cortex).

Practice Makes Perfect: A Functional MRI Study of Long Term Motor Cortex Plasticity

Peter Jezzard*, Avi Karni#, Gundela Meyer$, Michelle Adams#, Anna Prinster*, Leslie Ungerleider# and Robert Turner†

*Laboratory of Cardiac Energetics, NHLBI, #Laboratory of Neuropsychology, NIMH, National Institutes of Health, Bethesda, MD, USA, $University of La Laguna, Tenerife, Spain, and †Institute of Neurology, London WC1, UK

INTRODUCTION

Functional MR imaging using BOLD contrast has been shown to provide a method for indirectly studying neuronal activation via its effect on the cerebral vasculature (1). We have used this technique to study cortical reorganization and plasticity associated with a learned motor task which was practiced daily over a period of 4 to 6 weeks. Functional MRI maps generated whilst the subject was performing a sequence of finger-to-thumb opposition were compared with activation maps generated whilst the subject was performing a control sequence which contained the same component movements, but in an unpracticed order.

METHOD

The motor sequences used consisted of finger movements in which the fingers of the non-dominant hand (the left hand in the 4 subjects studied here) were touched against the thumb in a specified sequence. In Sequence A the order of finger movements was 4,1,3,2,4 (numbering the fingers from index to little), and in Sequence B the order was 4,2,3,1,4. Each subject was randomly assigned one of the above sequences to be practiced for ten to twenty minutes each day, the other sequence served as a control and was to be performed only during scanning. Subjects were scanned once a week for 4-6 consecutive weeks in a 4 Tesla MRI system, equipped with echo planar imaging capabilities (sequence parameters: gradient-echo 64x64 EPI, TR 2 secs, TE 26 ms, slice thickness 5 mm, 4 parasagittal contiguous slices centered about Right 30 mm, FOV 160 mm). Each study consisted of 4 experimental runs of 64 images per slice, each experimental run therefore lasting 4.5 minutes. The general paradigm for each run was rest-X-rest-Y-rest, where X and Y were, respectively, AB, BA, AB and BA. For all subjects control runs were collected which were either AA, or BB, or both. During all scanning sessions a metronome was used to pace the sequence of finger movements at a rate of 2 taps per second in order to control for differences in the speed of performance of each sequence.

The data were processed using software written at NIH in Interactive Data Language (Research Systems, Inc. CO). First, a pixel-by-pixel Z-map (2) was computed, in which each of the two motor task intervals was individually compared to the average of the rest intervals. Second, a pixel-by-pixel percentage change of signal intensity was calculated, again for each motor task period relative to the average of the rest intervals. Comparisons were then made, always within the same experimental run, between the number of pixels exceeding threshold in the primary motor area (M1) for tasks X and Y (arbitrary thresholds of $Z > 2.0$ and $\Delta\% > 2.0$ were chosen). Performance data were collected throughout the study period, specifically before each scanning session.

RESULTS

At the start of the study (week 0), we found no statistically significant difference between the size of regions in M1 above threshold for sequences A and B. By week 4, however, the MRI data showed a statistically significant increase in the area activated above threshold in M1 for the practiced sequence versus the unpracticed sequence in all 4 subjects. Performance measurements, correspondingly, showed superior performance for the trained versus the untrained task after 4 weeks (68 versus 36 cycles per minute) but not at week 0 (32 versus 33 cpm). Data from one of the subjects are shown in Figure 1, in which the number of pixels exceeding threshold in the primary motor area is shown for the paradigm order AB and BA (in which A was the practiced task).

An additional phenomenon observed was an effect related to the ordering of the sequences within each experimental run. In all subjects we found that a given sequence consistently gave a smaller area in M1 if it was second in the paradigm (position Y) than if it was first (position X). The size of this effect was gauged by running the paradigms AA or BB in each experimental session. This "ordering" effect suggests a possible short-term habituation mechanism and may confound the learning effect if not counter-balanced by performing the paradigm in both orders. However, by week 4, this ordering effect was overridden by the learning effect.

DISCUSSION

We found that the area of cortical activity in M1, as derived from the region of cerebrovascular response measured by BOLD EPI, significantly increased in size for the execution of simple opposition finger movements arranged in a specific sequence following four weeks of daily practice. These results agree with results recently reported using the technique of trans-cranial magnetic stimulation (3). However, our results were obtained by comparing the practiced sequence to a control task consisting of the same component movements: a result that suggests that the M1 plasticity is highly specific for sequence and not component movements, in agreement with our performance results (4). We also found a short-term within-session effect of task repetition, suggesting habituation in M1. This latter effect should be controlled for in the design of imaging studies of this comparative nature.

REFERENCES

1. K. Kwong *et al.*, PNAS USA **89**, 5675 (1992); S. Ogawa *et al.*, PNAS USA **89**, 5951 (1992)
2. D. LeBihan *et al.*, Proc. of the 12th Meeting of the SMRM, **1**, 11 (1993)
3. A. Pascual-Leone *et al.*, Neurology, **43**, A157 (1993)
4. A. Karni *et al.*, Soc. Neuroscience Abstr. (submitted)

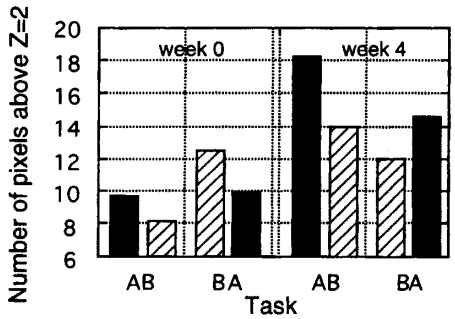

Figure 1: Number of pixels above Z=2.0 in M1 for the trained sequence (A) becomes larger than for the control sequence (B) [$p<0.001$]. Results from task orders AB and BA are shown for week 0 and week 4. Note that the ordering effect has been overridden by the learning effect by week 4. Data from subject HW. Similar results were obtained with the percent map analysis.

SMR, 1995.

Magnetic Resonance Imaging of Acoustic Strain Waves

R Muthupillai, DJ Lomas, PJ Rossman, JF Greenleaf, A Manduca, SJ Riederer, RL Ehman
Department of Diagnostic Radiology, Mayo Clinic, Rochester, MN, USA

Introduction

Palpation is a physical examination technique that assesses the elastic moduli of tissue. It is one of the most effective methods for detecting tumors in parts of the body that are accessible to the physician's hand. A medical imaging technique capable of sensitively mapping tissue moduli would be of great interest.

The propagation characteristics of shear and longitudinal strain waves directly reflect viscoelastic properties. Prior efforts to exploit this relationship have involved methods such as doppler ultrasound interrogation of tissue subjected to harmonic mechanical excitation ("sonoelasticity") [1] or direct ultrasound imaging of tissue displacements in response to intermittent mechanical pressure transients ("elastography") [2]. These techniques are limited by the need for an "acoustic window" and data-analysis difficulties. An NMR spectroscopy technique [3] has been proposed for observing the effect of mechanical waves, but its sensitivity and practicality have yet to be determined. A phase-contrast MR technique employing non-harmonic mechanical excitation has also been proposed [4] and like elastography, may require knowledge of boundary conditions in order to estimate the mechanical moduli.

The purpose of this work was to evaluate a different MRI approach for quantitatively mapping the propagation characteristics of acoustic strain waves within tissues. The method employs cyclic gradient waveforms and phase-locked acoustic shear waves to constructively build up phase shifts. One of our hypotheses is that the method can measure very small displacements. Preliminary analysis suggested that detection of harmonic displacements of *less than 1 μm* is possible.

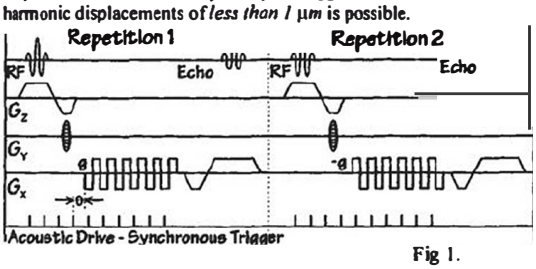

Fig 1.

Methods

A phase-contrast gradient echo imaging sequence was developed with adjustable-frequency motion-sensitizing gradients. Each phase encoding view is acquired twice, using cyclic gradients (g) of alternating polarity [Fig 1]. This "balanced" phase-contrast acquisition yields two phase images, which are subtracted to eliminated static phase errors, while doubling the observed phase shift due to harmonic strain. Trigger pulses synchronize an oscillator/amplifier unit that drives an electromechanical actuator coupled to the surface of the object to be imaged. The frequency and number of gradient cycles are adjustable.

Consider the specific case in which the spins undergo simple harmonic motion, about a mean position $\vec{r}_o$. From the Larmor equation, it can be shown that the observed phase accumulated by a spin undergoing such a motion in the presence of the synchronously cycling gradient waveform is given by:

$$\phi(\vec{r},\theta)=\frac{4\gamma N T}{\pi}\left(\vec{G}\cdot\vec{\xi}_o\right)Sin\left(\vec{k}\cdot\vec{r}+\theta\right) \qquad (1)$$

where $\vec{k}$ is the wave number, $\vec{\xi}_0$ is the displacement amplitude, N is the number of gradient cycles, and T is the period. The phase shift is multiplied many times by the gradient reversals.

Images of propagating shear waves were obtained in agarose gel phantoms and animal organ specimens on a 1.5T imager. Calculated displacements were independently measured with a laser optical technique. The typical number of gradient cycles, N, was 10-20. Acquisition time was 15-25 seconds.

Results

A typical shear wave image is illustrated in figure 2. A 500 Hz acoustic excitation was applied at two separate points on the surface of a gel phantom. The resulting complex interference pattern is clearly depicted in this phase image. The wave amplitude in the lower third of the phantom near the midline is less than 300 *nanometers*. By changing the phase relationship (θ) between the acoustic trigger pulses and gradient cycles in progressive steps, it was possible to generate a series of images which, displayed "cine" fashion, graphically demonstrate the pattern of wave propogation.

Fig. 3 demonstrates the capacity of the shear wave images to reveal mechanical characteristics. The wavelength of the shear waves is proportional to the square of the shear modulus. The images demonstrate a much longer wavelength in areas of stiff (tumor-like) gel than in adjacent softer gel, where the wavelength is shorter.

Experiments were performed with mechanical wave frequencies from 120 Hz to 1.1 kHz, with the performance of the gradient subsystem defining the upper limit. Comparison of measurements of shear modulus calculated from the phase images revealed good correlation with measurements obtained using a mechanical testing machine.

Experiments to assess the sensitivity of the method demonstrated that at 500 Hz, wave patterns with displacement amplitudes of less than *50 nanometers* were clearly depicted.

Discussion

The experiments confirm the hypothesis that the proposed technique quantitatively depicts the characteristics of propagating shear waves. Hence, the method shows promise as a potential technique for "palpation by imaging." Potential applications may include detection of tumors in breast, liver, kidney, and prostate. Tissue characterization parameters that might be assessed include shear modulus, attenuation, and dispersion. Preliminary organ and in vivo imaging experiments are promising, but have indicated that adequate driver power is critical due to higher tissue viscous loss.

A second area of application may be to use the imaging method as as an industrial design tool to study mechanical vibrations in objects. The flexible orientation of the shear-sensitizing gradient offers the possibility of resolving all components of the strain dyadic non-invasively.

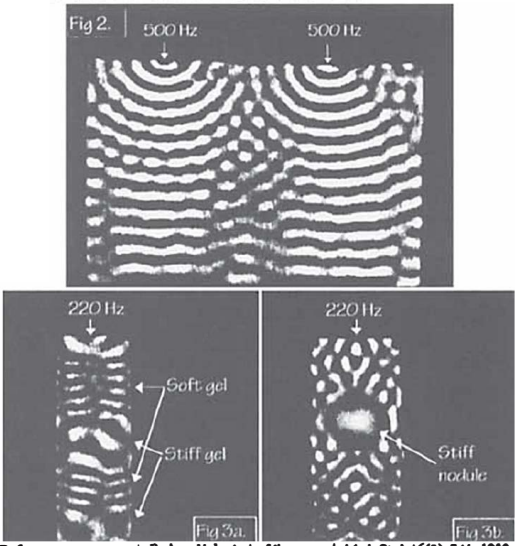

References:
1. Parker, K.J. et al., *Ultrasound Med. Biol.* 16(3), 241, 1990.
2. Ophir, J. et al., *Ultrasonic Imaging*, 13, 111, 1991.
3. Lewa, C.J., de Certaines, J.D., *JMRI*, 5(2), 241, 1995.
4. Plewes, D.B., Betty, I., Soutar, I., *Proc. of SMR CA*, 1994.

SMR, 1995.

HIGH RESOLUTION MEASUREMENT OF CEREBRAL PLASMA FLOW, MEAN TRANSIT TIME AND VOLUME USING DYNAMIC IMAGING OF Gd-DTPA BOLUS PASSAGES.

L Østergaard†‡, RM Weisskoff, DA Chesler, K Kwong, G Sorensen, TL Davis, JL Boxerman, C Gyldensted†, BR Rosen.
Massachusetts General Hospital, NMR Center, Department of Radiology, Charlestown, Massachusetts,
†Department of Neuroradiology and ‡PET Center, Aarhus University Hospital, Denmark.

Introduction

One of the main goals of functional NMR is high resolution measurement of regional Cerebral Blood Flow (rCBF), regional Cerebral Blood Volume (rCBV) and Mean Transit Time (MTT). Determining these quantities by deconvolving tissue concentration-time curves with an arterial input function after bolus-injection of an intravascular contrast agents has a number of inherent mathemathical difficulties due to the lack of *a apriori* knowledge on the vascular structure(1). In this study, we analyzed a number of model assumptions and mathematical approaches to perform high resolution measurements rCBF, rCBV and MTT from Gd-DTPA bolus passages.

Background.

Using The Central Volume Theorem (2) for non-diffusible tracers, Gd-DTPA bolus passage concentration time curves have previously been used to calculate rCBV. Attempts to calculate involves knowledge of vascular structure through the *residue function* R(t) since this determines how the observed tracer is retained in the vasculature. The concentration $C_{VOI}(t)$ of tracer within a given VOI is given by

$$C_{VOI}(t) = F_t \int_0^t C_a(\tau) R(t-\tau) d\tau \qquad (1)$$

where F_t is tissue flow, $C_a(t)$ is the arterial input and R(t) is the residue function of the tissue vasculature. The Mean Transit Time (MTT) of the tracer is given by

$$MTT = \frac{rCBV}{F_t} \qquad (2)$$

Materials and Methods

Images were obtained using a GE Signa 1.5 Tesla imager retrofitted for EPI capabilities (Instascan, Advanced NMR). Data were obtained from two groups: (1) patients having MRI according to a routine cerebral perfusion protocol and (2) normal volunteers (N=6) participating in clinical testing of Sprodiamide (Sterling Winthrop). Patients recieved 0.2 mmol/kg Gd-DTPA delivered by a power-injector (Medrad) at a rate of 5 ml/sec in an antecubital vein. Normal volunteers recieved 0.3 or 0.5 mmol/kg Sprodiamide at a rate of 5 or 10 ml/sec. Echo Planar Imaging was performed using TR = 1.5 sec (patients) or TR = 1.0 sec (normal volunteers) and TE = 75 msec. Image resolution was 1.6 by 1.6 mm with a slice thickness of 5 mm.

Arterial input values for deconvolution were determined from susceptibility effects around large vessels(3). We used techniques independent of vascular structure (Fast Fourier Transform (FFT), Singular Value Decomposition(SVD) and reguarization) to numerically deconvolve Eq. 1. for R(t), F_t, CBV and MTT on a regional basis as well as on a pixel to pixel basis. Deconvolution was also performed using a model assuming well-mixed vascular compartments (exponential residue function).

Results

It was possible to perform deconvolution of tissue response curves on a pixel-to-pixel basis (0.01cc) using model dependent and, to some degree, model independent approaches(SVD, regularization). The latter was done using uniform smoothing. For normal volunteers(N=6), MTTs were of the order of 1.9 ±0.9(SD)sec for gray matter (occipital cortex) and 3.1±0.7 sec for white matter. The gray/white flow ratio was 3.7±0.9 and the corresponding CBV ratio 2.5±0.6. Figure 1 shows the result of deconvolving the tissue response curve with an arterial input function on a pixel to pixel basis in a tumor patient. Figure 2 shows the corresponding CBV map. Notice a small region of high flow within the tumor region.

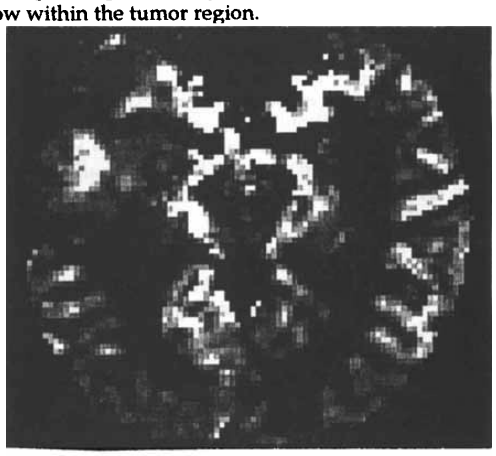

Figure 1. CBF

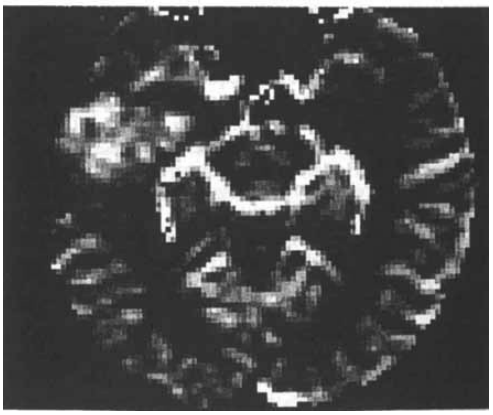

Figure 2. CBV

Conclusion

EPI-imaging of Gd-DTPA bolus passages with subsequent deconvolution with an arterial input function can be used for quantitative imaging of CBF, CBV and MTT using NMR. We are presently performing Monte Carlo simulations to evaluate the deconvolution techniques with respect to their ability to reproduce tissue residue functions, MTT, CBV and CBF.

References

1. Lassen NA *J Cereb. Blood Flow Metab.* **4** 633-634 (1984).
2. Meier P, Zierler KL. (1954). *Appl Physiol* **6**:731-744 (1954).
3. Villringer A, Rosen BR, Belliveau JW, Ackerman JL *et al. MRM* **6**: 164-174 (1988).

ISMRM, 1997.

Shading Artifacts in Phase Contrast Angiography Induced by Maxwell Terms: Analysis and Correction

Matt A. Bernstein[1], Xiaohong Zhou[1], Kevin F. King[1], Alexander Ganin[1], Norbert J. Pelc[2], and Gary H. Glover[2]

[1]GE Medical Systems, Milwaukee, WI, U.S.A.

[2]Lucas MR Center, Dept. of Radiology, Stanford University, Stanford CA, U.S.A.

Introduction

Whenever a linear gradient is activated, additional magnetic fields with non–linear spatial dependence result. This is a consequence of Maxwell's equations: $\nabla \times \mathbf{B} = \mathbf{0}$, (assuming no true or displacement current), and $\nabla \bullet \mathbf{B} = 0$. These additional magnetic fields are called Maxwell terms, and have been discussed in the literature[1–5]. Here we consider the effect of Maxwell terms on phase contrast imaging in greater detail.

Methods

Assuming symmetry of G_x and G_y, the spatially quadratic Maxwell magnetic field B_E is

$$B_E(x,y,z,t) = \frac{1}{2B_0}\left\{\left(G_x^2 + G_y^2\right)z^2 + G_z^2\frac{x^2+y^2}{4} - G_z z\left(G_x x + G_y y\right)\right\} \quad (1)$$

where B_0 is the main magnetic field, and x,y, and z are the magnet–based coordinates. (To our knowledge the xz and yz terms have not been previously described in the MR literature.) The phase accumulation is

$$\phi(x,y,z) = \gamma \int B_E(x,y,z,t)\, dt \quad (2)$$

After the phase difference operation, the residual Maxwell phase error for phase contrast is

$$\Delta\phi(x,y,z) = \phi(x,y,z,fe_1) - \phi(x,y,z,fe_2) \quad (3)$$

where fe is the flow encoding index (e.g. "bipolar up" or "bipolar down").

Results

Figure 1 shows typical data. Here the G_y is causing a z^2 phase error. The FoV is 32cm, and the VENC=5cm/s. The solid line is calculated from Eq. 3, with *no* adjustable parameters. The +'s represent measured data.

Discussion

There are several artifact avoidance and artifact correction methods that are feasible:

1) Use of symmetric lobes ($G(fe_1) = -G(fe_2)$) eliminates phase errors from self–squared terms (like G_x^2), but does not necessarily address the cross terms (G_zG_x and G_zG_y).

2) Playing G_z non–concurrently with G_x and G_y eliminates the cross terms, but can increase minimum TE and sequence time.

3) The amplitude of the gradient lobes can be de–rated, although this also increases minimum TE and TR. Figure 2 shows a sagittal scan of a normal volunteer at 1.5T: VENC=30cm/s, 24 FoV, 50mm thick, 256x192, 8 Nex, no post processing correction. a) 22mT/m, 77T/m/s, TE=6.6ms, b) 11mT/m, 77T/m/s TE=7.7ms.

4) The phase error can be fit [6] with a polynomial. If u and v are the readout and phase encode directions, it can be shown that the general (including off–center FoV) Maxwell phase error is of the form

$$\Delta\phi(u,v) = \alpha u + \beta v + \gamma u^2 + \delta v^2 + \epsilon uv + \zeta, \quad (4)$$

which can be fit with linear regression. A disadvantage to this method is possible contamination to the fit from the desired, flow–related phase.

5) Since the pulse sequence "knows" the gradient waveforms, it can calculate the phase error with Eq. 3, and pass this information to the reconstruction program. The reconstruction program (or other post–processor) can then apply the phase correction in the image domain. Although somewhat engineering intensive, this is the preferred method since it has no fundamental drawbacks.

Conclusion

With strong gradients and/or small B_0, Maxwell term phase errors can be appreciable, because the error field B_E/B_0 is a quadratic function of the ratio of the applied gradient amplitude to B_0 (Eq. 1). Low VENC's and large FoV's aggravate the problem. The phase errors can be minimized with pulse sequence design, or eliminated with post–processing corrections.

References

1. DG Norris, SMRM 1985 abstract # 1037
2. RM Weiskopf, JJ Dalcanton, RR Rzedzian SMRM 1990 abstract 457.
3. R Coxon and P Mansfield SMRM 1989, abstract 361.
4. DG Norris, JMS Hutcheson, MRI 8, 33–37, (1990).
5. R.M. Weiskopf, MS Cohen, RR Rzedzian. MRM 29, 796–803 (1993).
6. MA Bernstein, and NJ Pelc U.S. Patent #5,226,418.

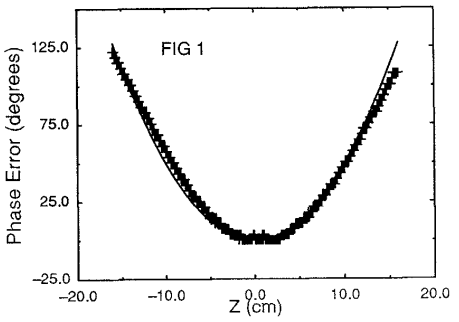

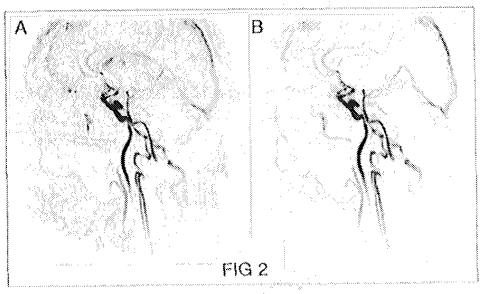

FIG 2

ISMRM, 1997.

A Biomechanical Interpretation of the BOLD Signal Time Course: the Balloon Model

R.B. Buxton*, E.C. Wong*† and L.R. Frank*
Departments of *Radiology and †Psychiatry, University of California, San Diego 92103

Purpose: To develop a quantitative model for the transient changes of the BOLD signal in terms of underlying physiological processes accompanying brain activation.

Background: The BOLD signal time course during brain activation often exhibits transient features at the onset and end of the stimulus: an initial dip [1], corresponding to an initial increase in local deoxyhemoglobin observed with optical techniques [2]; a post-stimulus undershoot [3]; and more rarely an initial overshoot followed by a much weaker plateau and a strong post-stimulus undershoot [4]. These transient effects have been interpreted as evidence for an uncoupling of flow and oxygen metabolism (e.g., the dip is an initial increase in oxygen metabolism prior to the flow increase [2]). However, two lines of thought have led us to question these interpretations. First, the simultaneous effects of dynamic changes in blood volume and oxygenation, which have opposite effects on the BOLD signal, have not been investigated. Second, we recently argued that the large flow changes observed in brain activation can be explained as a tight coupling of flow and metabolism in the presence of an intrinsic limitation on the delivery of oxygen, so that a large flow change is required to provide a small increase in oxygen metabolism [5]. Thus our goal is to answer two basic questions: 1) Can transient BOLD effects be attributed to blood volume changes?, and 2) Can these effects occur in the presence of tight coupling of flow and metabolism?

Model: We assume that the BOLD signal change is primarily due to venous blood changes and includes both an extravascular [6] and an intravascular [7] component, leading to a signal change that depends on two time-dependent quantities: q(t), the total deoxyhemoglobin in the tissue voxel, and v(t), the venous volume. We model the venous compartment as an expandable balloon fed by the output of the capillary bed. The volume of the balloon changes when the inflow, F_{in}, is not matched by the outflow, F_{out}. $F_{in}(t)$ is treated as an arbitrary function of time that drives the system, and F_{out} is assumed to be a function of the venous volume. Then after an increase in F_{in}, the venous balloon swells and the pressure increases until F_{out} matches F_{in} (a new steady-state). The amount of swelling that occurs will depend on the pressure/volume curve of the venous compartment. Treating the balloon as a well-mixed compartment, the equations for q(t) and v(t) are:

$$\frac{dq}{dt} = \frac{1}{t_0}\left[f_{in}(t)\frac{E(t)}{E_0} - f_{out}(v)\frac{q(t)}{v(t)}\right] \qquad \frac{dv}{dt} = \frac{1}{t_0}\left[f_{in}(t) - f_{out}(v)\right]$$

where t_0=mean transit time through the venous compartment at rest, E(t)=net oxygen extraction fraction, and E_0=E(0). All other variables are normalized to their rest values, so that $q(0)=v(0)=f_{in}(0)=f_{out}(v(0))=1$. By our model of tight coupling of flow and oxygen metabolism E is a function of $f_{in}(t)$ which can be approximated as $E(f)=1-(1-E_0)^{1/f}$ [5]. Variable patterns of response will then be created for different functional forms of $f_{out}(v)$ (i.e., different pressure/volume curves for the venous compartment).

Results: The curves shown below were calculated with t_0=2 sec and E_0=0.4, and $f_{in}(t)$ was assumed to be trapezoidal. In each panel the upper half shows the time courses of f_{in}, f_{out}, blood volume v, and total deoxyhemoglobin q. The bottom half shows the BOLD signal time course, and the assumed curve $f_{out}(v)$ is shown as an inset. The left panel shows a simple BOLD response for a linear pressure/volume curve. For the second set the flow change is identical but the pressure/volume curve is nonlinear and the maximum volume change is larger. There is an initial dip in the signal corresponding to a slight increase in deoxyhemoglobin, a reduction of the plateau level, and a post-stimulus undershoot. The initial dip occurs when f_{out} is slow to follow the increase of f_{in} because of the shallow slope of the flow/volume curve, leading to a rapid rise in blood volume. This decreases the extravascular signal, but not the intravascular component, which may account for why the initial dip is less pronounced at lower fields where the intravascular component makes a larger contribution to the signal change [7]. The post-stimulus undershoot occurs in the absence of a corresponding flow undershoot when the blood volume returns to the resting value more slowly than the flow. Even the unusual time courses [4] showing an initial overshoot, a return to near baseline, and a post-stimulus undershoot, can be produced by this model (right panel) with a larger volume change. For this example we introduced some hysteresis which roughly approximates the stress-relaxation effects measured in venous vessels [8].

Conclusions: A simple biomechanical model can produce large transient undershoots and overshoots in the BOLD signal depending on the relative time course of flow and volume changes. Furthermore, these transient effects are consistent with continuous tight coupling of flow and oxygen metabolism [5]. We should be cautious about interpreting measurements of deoxyhemoglobin content from optical measurements or BOLD measurements in terms of physiological changes; radically different deoxyhemoglobin time courses can be produced by relatively minor differences in the separate time courses of blood flow and volume.

1) Ernst T *MRM*:146 (1994); 2) Malonek D *Science* 272:551 (1996); 3) Davis TL SMR Proc, pg 69 (1994); 4) Frahm J *MRM* 35:143 (1996); 5) Buxton RB *J CBF and Metab* (in press) (1996); 6) Ogawa S *Biophys J.* 64:803 (1993); 7) Boxerman JL *MRM* 34:4 (1995); 8) Pedley T. The Fluid Mechanics of Large Blood Vessels. Cambridge University Press, Cambridge (1980).

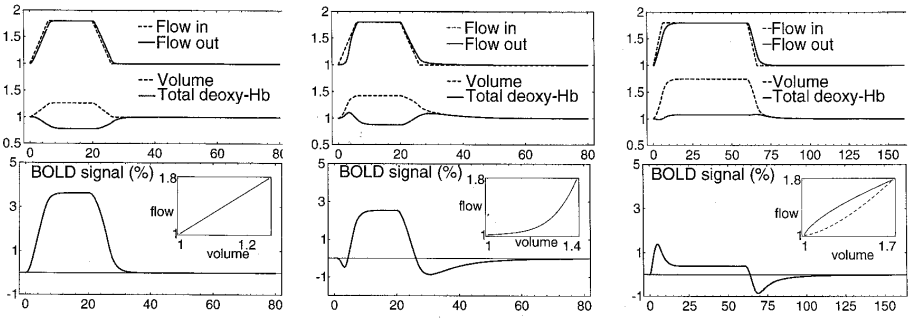

ISMRM, 1997.

SiMultaneous Acquisition of Spatial Harmonics (SMASH): Ultra-Fast Imaging with RF Coil Arrays

D.K. SODICKSON AND W.J. MANNING
Cardiovascular Division, Beth Israel Deaconess Medical Center and Harvard Medical School, Boston, MA

Introduction

A common feature of nearly all the fast MR imaging techniques now in use is that they all acquire data in a sequential fashion. Whether the *k*-space matrix is filled in a rectangular raster pattern, a spiral pattern, a rapid series of line scans, or some other novel trajectory, it is always acquired one point and one line at a time.

In this report, we present a fast imaging technique which allows some significant fraction of signal data points to be acquired *in parallel*, rather than sequentially in time. Several fast imaging schemes have been proposed to date using simultaneous data acquisition in multiple RF coils (1,2, 3,4). The technique described here, dubbed SiMultaneous Acquisition of Spatial Harmonics (SMASH), reduces image acquisition times by a multiplicative factor without a significant sacrifice in spatial resolution or signal-to-noise ratio, essentially by scanning many lines of *k*-space at a time. The SMASH procedure operates by using linear combinations of simultaneously acquired signals from multiple surface coils with different spatial sensitivities to generate multiple data sets with distinct offsets in *k*-space. The full *k*-space matrix may then be generated with only a fraction of the usual number of gradient phase encoding steps, and the total image acquisition time may consequently be reduced by the same fraction. A two-fold savings in acquisition time is demonstrated here using a three-element phased array coil, and substantially larger factors are expected for appropriate coil designs.

Methods

The SMASH technique reduces image acquisition times by exploiting spatial information inherent in the geometry of a surface coil array. Partial signals are acquired simultaneously in the component coils of an array, and the remainder of the *k*-space matrix required for image production is reconstructed after the fact, using linear combinations of the component coil signals to substitute for spatial modulations normally produced by phase encoding gradients.

The MR signal for a plane with spin density $\rho(x,y)$ takes the form

$$S(k_x,k_y) = \iint dxdyC(x,y)\rho(x,y)\exp\left\{-ik_x x - ik_y y\right\}, \qquad [1]$$

where $C(x,y)$ represents the sensitivity function for the receiver coil used to detect the signal. In a linear surface coil array with adjacent components, each coil j has a distinct but overlapping sensitivity $C_j(x,y)$. In the SMASH approach, signals from the various array components are combined to produce overall sensitivity variations across the image plane of the form

$$C^{tot}(x,y) = \sum_j n_j C_j(x,y) = \exp(imK_y y). \qquad [2]$$

By virtue of these sinusoidal spatial modulations, each combined data set is shifted in *k*-space by an amount $-mK_y$, precisely the same shift which would be produced by evolution in a *y* gradient of magnitude $\gamma G_y t_y = -mK_y$:

$$S(k_x,k_y) = \iint dxdy\rho(x,y)\exp\left\{-ik_x x - i(k_y - mK_y)y\right\} = \tilde{\rho}(k_x,k_y - mK_y). \qquad [3]$$

If a total of N spatial harmonics are generated using linear combinations of coil signals, then N extra lines in *k*-space may be reconstructed for each application of a phase encoding gradient. The full signal matrix may therefore be generated in $1/(N+1)$ of the usual acquisition time.

Results

Figure 1 shows a successful application of the SMASH technique *in vivo*. Image (a) is a coronal slice through the brain of a healthy adult volunteer, taken with a conventional turbo spin-echo sequence in a total acquisition time of 71 seconds. (FOV = 200 mm, matrix size = 256 x 256, slice thickness = 10mm, number of signal averages = 8). Image (b) was acquired in half the time (i.e. 35 seconds) with half the number of phase encoding steps, and was then reconstructed using the SMASH procedure.

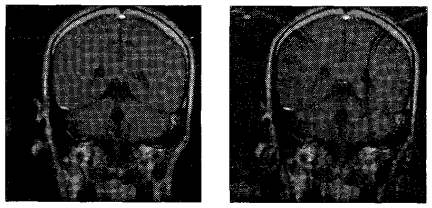

a **Figure 1**: a) Reference image (71 sec). b) SMASH image (35 sec). b

In both cases, the receiver coil was a linear array of three slightly overlapped component coils, with a total spatial extent of 400 mm. The image plane was centered above the middle coil, 80 mm from and parallel to the plane of the array. **Figure 2** shows the spatial variations in net sensitivity across the image plane for two linear combinations representing the two spatial harmonic modulations used for SMASH reconstruction. The raw data for component coil sensitivities were obtained from phantom images, and the optimal weights for spatial harmonic generation were determined using a gradient-descent fitting algorithm. The residual foldover artifacts in Image 1b are due primarily to imperfections in the zeroth harmonic fit, which may in turn be traced to sensitivity variations in the non-optimized coil array. A coil array designed with spatial harmonic generation in mind would circumvent these artifacts.

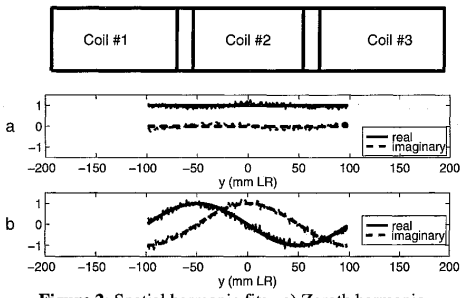

Figure 2: Spatial harmonic fits. a) Zeroth harmonic. b) First harmonic.

Conclusions

As a partially parallel imaging strategy, SMASH may be integrated with many of the fastest existing imaging sequences. A factor of two time savings is demonstrated here with standard equipment, but in principle, there is no limit to the number of lines that may be scanned simultaneously, provided coil arrays with sufficient numbers of components are constructed. The resultant savings in acquisition time are expected to be of particular value in areas such as cardiovascular MR, where physiologic motion makes fast imaging a necessity.

References

1. M. Hutchinson, U. Raff, Fast MRI data acquisition using multiple detectors. *Magn Reson Med* **6**, 87-91 (1988).
2. D. Kwiat, S. Einav, G. Navon, A decoupled coil detector array for fast image acquisition in magnetic resonance imaging. *Med Phys*, **18**:251-265 (1991).
3. J. W. Carlson, T. Minemura, Imaging time reduction through multiple receiver coil data acquisition and image reconstruction. *Magn Reson Med* **29**, 681-688 (1993).
4. J. B. Ra, C. Y. Rim, Fast imaging using subencoding data sets from multiple detectors. *Magn Reson Med* **30**, 142-145 (1993).

ISMRM, 1997.

MR Imaging of the Human Lungs Using Hyperpolarized ^{129}Xe Gas

JP Mugler, III[1], B Driehuys[2], JR Brookeman[1], GD Cates[2], SS Berr[1], RG Bryant[1], TM Daniel[1], EE de Lange[1], CJ Erickson[2], W Happer[2], DP Hinton[1], T Maier[1], BT Saam[2], KL Sauer[2], ME Wagshul[3]

[1]*University of Virginia Health Sciences Center, Charlottesville, VA,* [2]*Princeton University, Princeton, NJ*
[3]*State University of New York at Stony Brook, Stony Brook, NY*

INTRODUCTION

Recent research has demonstrated the feasibility of performing magnetic resonance imaging using laser-polarized ^{3}He and ^{129}Xe gases. Although ^{129}Xe imaging of relatively small volumes [1-3] has been performed, imaging of larger volumes, namely the human lungs, has not been possible because methods for generating sufficient quantities of hyperpolarized xenon did not exist. We present the first results obtained using a new method for xenon laser-polarization that provides liter quantities of hyperpolarized gas.

METHODS

Using a high-volume production method of laser-polarized ^{129}Xe, which is described in detail elsewhere [4], between 300 cm^3 and 500 cm^3 of hyperpolarized gas was accumulated for each experiment. Estimated polarizations ranged from 0.1% to 2.4%.The gas was transported to the imager in a small plastic bag and then inhaled by the volunteer in one large breath. Imaging commenced immediately following gas inhalation.

Two healthy volunteers participated in the imaging experiments which were performed using a 1.5 T commercial whole-body imager (Magnetom Vision, Siemens Medical Systems, Iselin, NJ), modified to operate at 17.6 MHz by the addition of a broadband RF amplifier and a ^{129}Xe volume RF coil. Coronal (two volunteers) and axial (one volunteer) images of the lungs were acquired using a two-dimensional low-flip angle gradient-echo pulse sequence (FLASH) with the following parameters: TR/TE 190 ms / 5.6 ms, flip angle 9^{o} (sequential phase encoding) or 12^{o} (centric phase encoding), matrix size 64 x 128, voxel size 6.6 mm x 13.3 mm x 20 mm or 6.6 mm x 6.6 mm x 20 mm, and NEX 1. Eleven contiguous sections were collected during a 12 second breath-hold. For the coronal image sets, corresponding proton images were acquired using a low-flip angle FLASH sequence and the body RF coil.

RESULTS

All three image sets depicted the full extent of the left and right lungs, with the exception of the most superior portions of the lungs which extended near the end of the RF coil. The axial image sections and the central sections of the coronal image set demonstrated relatively well-defined edges at the lung surfaces. In two of the image sets, signal was also apparent in the trachea.

The images showed some lung structure, although less than recently demonstrated with hyperpolarized ^{3}He imaging [5,6]. The principal reason for this difference is the factor of 5 increase in the in-plane voxel dimension for the xenon images compared to the helium images because of the lower available signal. Several factors contribute to the large signal level difference: (1) gas polarization values were 5-20 times lower for the xenon images, (2) inhaled gas volumes were 1.5-3 times lower for the xenon images, and (3) the gyromagnetic ratio for ^{129}Xe is 2.8 times lower than that for ^{3}He. The maximum S/Ns for the three xenon image sets were 32 (1.8 cm^3 voxel, centric encoding), 9 (1.8 cm^3 voxel, sequential encoding), and 28 (0.9 cm^3 voxel, centric encoding).

Several of the images demonstrated regional signal intensity variations. However, because the sample size is small and the breathing maneuvers were not carefully controlled in these preliminary studies, we are hesitant to draw a conclusion regarding the significance of these observed intensity variations.

Ghosting artifacts were apparent in some of the coronal images (centric phase-encoding order) for both volunteers, but not in any of the axial images (sequential phase-encoding order). We believe that these artifacts were caused by bulk mixing of the (heavier) xenon gas with the other lung gases just after inhalation.

Figure 1 shows three contiguous coronal xenon lung images, as well as corresponding proton images. Comparing the xenon and proton images, we see good correlation between the gas-space signal void in the proton images and the gas-space signal in the xenon images, although an exact correspondence is not expected since the xenon and proton images were acquired in two separate breath-hold periods.

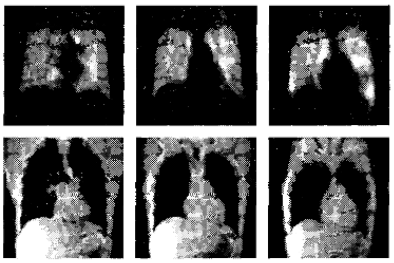

FIGURE 1: Contiguous coronal ^{129}Xe lung images (upper panel) and corresponding ^{1}H images (lower panel) of a healthy human volunteer.

CONCLUSIONS

We have obtained the first ^{129}Xe imaging results from the human lungs. With polarization levels of approximately 2%, we were able to obtain a voxel volume of 0.9 cm^3 with a S/N of 28. With anticipated improvements in the polarization system, pulse sequences, RF coils, and breathing maneuvers, these results suggest the possibility for ^{129}Xe gas-phase imaging of the lungs with a resolution approaching that of current conventional thoracic proton imaging.

REFERENCES

1. Albert MS, Cates GD, Driehuys B, et al. Nature 1994; 370:199-201.
2. Sakai K, Bilek AM, Oteiza E, et al. J Magn Reson, Series B 1996; 111:300-304.
3. Wagshul ME, Button TM, Li HF, et al. Magn Reson Med 1996; 36:183-191.
4. Driehuys B, Cates GD, Miron E, et al. Appl Phys Lett 1996; 69:1668-1670.
5. MacFall JR, Charles HC, Black RD, et al. Radiology 1996; 200:553-558.
6. Kauczor HU, Hofmann D, Kreitner KF, et al. Radiology 1996; 201:564-568.

ISMRM, 1998.

LASER: Adiabatic Single Shot Localization with J-Refocusing

L. DelaBarre and M. Garwood
Center for Magnetic Resonance Research and Department of Radiology,
University of Minnesota, Minneapolis, Minnesota, 55455, USA

Introduction:

A Carr-Purcell (CP) train of 180° pulses has long been known to suppress J-modulation and diffusion effects[1]. Recently, a CP version of the PRESS sequence has been proposed to achieve J-refocusing for localized ^{1}H spectroscopy[2]. Here we describe a robust CP sequence for localized ^{1}H spectroscopy which exploits adiabatic passage pulses to eliminate flip angle errors and to greatly reduce voxel displacements caused by chemical shift, while using low peak RF power. This sequence has been christened LASER: Localization by Adiabatic SElective Refocusing.

Methods:

The pulse sequence begins with a nonselective adiabatic half-passage (AHP) pulse for excitation, followed by 12 adiabatic full-passage (AFP) pulses which make up the CP portion of the sequence (Figure 1). The 180° (AFP) pulses are grouped into 3 sets of 4; whereby each set defines a slice perpendicular to the other two slices. The AHP pulse excites everything in the sample. Brief spoiler gradients before and after the AFP pulses eliminate signals outside the three intersecting orthogonal slices. In the present implementation, the AFP pulses were based on the hyperbolic secant (HS) pulse[3] which permits a highly square slice profile with low peak power. The phase of the AFP pulses were prescribed according to the MLEV-4 scheme[4], which further sharpened the edges of the slice profiles and compensated for pulse imperfections. Although the sequence is shown with 4 HS pulses defining each slice, any even number of AFP pulses can be used. In the present experimental implementation of LASER for ^{1}H spectroscopy, water signal was suppressed by applying a train of frequency-selective adiabatic pulses[5] in front of the excitation (AHP) pulse.

Results:

The ability of LASER to refocus J modulation was verified using phantoms containing glutamate. *In vivo* results are shown in figures 2 and 3. These data were collected using a 9.4T horizontal bore magnet fitted with a 300 mT/m gradient insert, and a 20 mm transceive surface coil placed over the rat's head. Figure 2 shows an image of a voxel from the rat brain acquired with a gradient-echo tacked onto the end of the LASER sequence. Readout projections are shown to exemplify the sharp voxel profiles. Figure 3 shows a ^{1}H spectrum of the (4 mm)^3 voxel acquired with water suppression, TR/TE = 3000/36 ms, and NEX=256. Despite the use of a relatively long TE, no peaks exhibited anti-phase character (i.e., J-refocusing was achieved).

Discussion:

LASER is an adiabatic sequence that selects a sharply defined voxel and suppresses J-modulation and diffusion effects. By using only B_1-insensitive adiabatic pulses, LASER does not require fine tuning of the RF power (or flip angles). Preliminary human experiments indicate that LASER can be implemented within FDA limits on SAR.

References:

1. Allerhand, A., *J Chem Phys* **44**, 1 (1966).
2. Hennig, J., et al., *Magn Reson Med*, **37**, 816 (1997).
3. Silver, M. , et al., *J Magn Reson*, **59**, 347 (1984).
4. Levitt, M. and R. Freeman, *J Magn Reson*, **43**, 502 (1981).
5. de Graaf, R.A. et al. *J Magn Reson B*, **113**, 35 (1996).

Acknowledgments:

This work is supported by NIH grants RR08079 and CA64338 and the W. M. Keck Foundation.

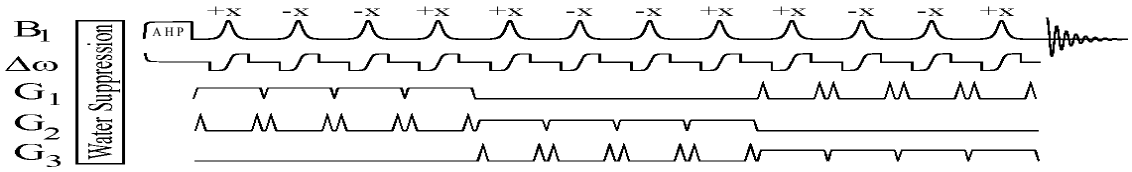

Figure 1: Pulse sequence diagram of LASER. The Δω function shows the frequency modulation of the adiabatic pulses.

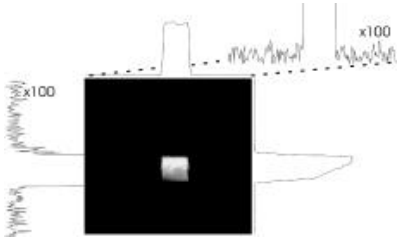

Figure 2: Image of the LASER voxel in the caudate of a rat brain. Projections show the sharpness of the voxel boundaries and a lack of contamination from signals outside the voxel. FOV = 25 x 25 mm.

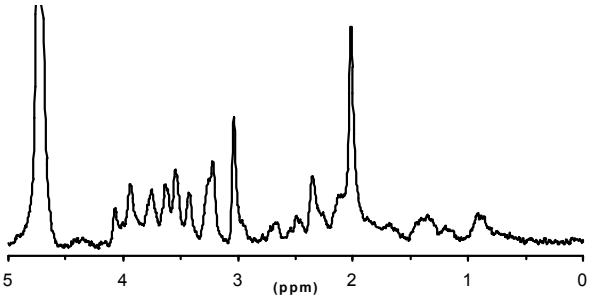

Figure 3: ^{1}H spectrum of the LASER voxel shown in figure 2 acquired with TR/TE = 3000/36 ms, NEX=256. AFP pulses were 2 ms long with bandwidth = 12.5 kHz.

ISMRM, 1998.

Coil Sensitivity Encoding for Fast MRI

Klaas P. Pruessmann, Markus Weiger, Markus B. Scheidegger, Peter Boesiger
Institute of Biomedical Engineering and Medical Informatics, University and ETH Zürich, Switzerland

INTRODUCTION

As suggested earlier by various authors [1-5] the sensitivity of a receiver coil may be regarded as a modification of the harmonic encoding functions in Fourier imaging. According to this view parallel acquisition with an array of receiver coils yields distinct spatial information in each channel. However, special image reconstruction methods are required in order to take advantage of sensitivity encoding for faster imaging.

The techniques described in [1-4] are based on the image domain formulation of Fourier aliasing. *In vivo* feasibility has been reported for the SMASH method [5] which uses the k-space formalism for image reconstruction.

Taking the image domain approach, in this work we introduce a scheme of acquisition and reconstruction steps called 'SENSE', short for SENSitivity Encoding. Given a receiver array it enables the reduction of scan time in any standard Fourier imaging mode. As compared to previously proposed image domain techniques [1-4], SENSE exhibits crucially improved *in vivo* practicability due to a generalized approach to the inversion problem and to an advanced *in vivo* reference strategy. Together with the method an SNR analysis is presented as well as a selection of phantom and *in vivo* results.

METHODS

Using an array of M receiver coils the duration of a standard Fourier scan is reduced by increasing the distance of readout lines in k-space by a real number $L \leq M$. Reconstruction of single coil images by FFT yields a reduced FOV with each pixel representing the superposition of N equidistant voxels in the object, where $N < L+1$. Foldover in corresponding pixels of the M single coil images is described by

$$\vec{a} = S\,\vec{b} \qquad (1)$$

where a_i is the pixel value in the i-th coil image, S_{ij} is the complex sensitivity of the i-th coil at the position of the j-th out of N voxels, and b_j is the tissue contrast function at the j-th position. The vector b is determined according to

$$\left|S\vec{b} - \vec{a}\right| = min \quad \Rightarrow \quad \vec{b} = S^{+}\vec{a} \qquad (2)$$

where S^+ denotes the pseudoinverse of the M×N matrix S. This inversion is performed for each pixel in the reduced field of view, yielding a representation of the tissue contrast function in the full FOV at preserved resolution.

Good knowledge of the matrix S is essential. In addition to actual imaging, low-resolution full-FOV single coil images of arbitrary contrast are acquired simultaneously as references. Raw sensitivity maps are obtained through division by either the 'sum-of-squares' of the single coil references or by an optional body coil reference. In the latter case reconstructed images will automatically be intensity corrected. Refinement of raw maps is crucial for image quality. It is achieved by a local polynomial fit procedure including thresholding, smoothing and extrapolation.

Compared to an array image obtained with full phase encoding the SNR of a reconstructed image is reduced approximately by

$$\frac{SNR_{full}}{SNR_L} = G\sqrt{L} \qquad (3)$$

where $G \geq 1$ is a local geometry factor reflecting the degree of linear dependence of the coil sensitivities at superimposed positions. The G factor is calculated from the matrix S only, thus enabling a priori estimates of SNR and optimal choice of L. G is minimized by excluding those voxels from inversion which lie outside of the object according to the reference images. Thereby, local SNR is significantly improved and sensitivity extrapolation may be restricted to a short, reliable range.

RESULTS

The proposed methods were evaluated experimentally on a 1.5 T Philips Gyroscan NT system. Fig. 1 demonstrates unfolding and intensity correction in a quality phantom using five surface coils positioned around the object. Fig.2 shows a brain image acquired with a reduction factor of L=2.0 using only two coils, and a short axis heart image acquired with five coils and L=2.9. Using the same setup single-shot EPI data were collected from a transverse heart slice in 31 ms per image (L=2.5) yielding images of acceptable quality with a resolution of 2.3×2.9mm.

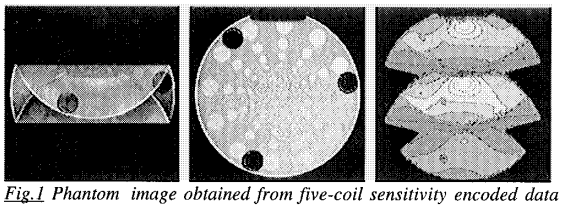

Fig.1 Phantom image obtained from five-coil sensitivity encoded data 2.9-fold undersampled in phase encoding direction.
Left: 'sum-of-squares' from single coil images. Middle: Reconstruction.
Right: map of G-factor reflecting local noise enhancement.

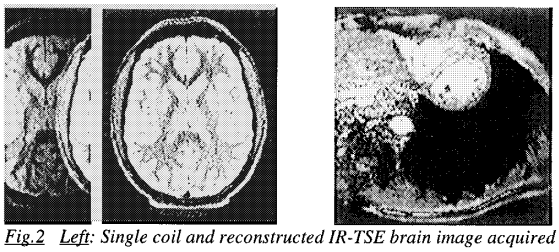

Fig.2 Left: Single coil and reconstructed IR-TSE brain image acquired with a two coil array in 85 s instead of 170 s for full Fourier encoding.
Right: Short axis half Fourier EPI heart image from a multi-phase series acquired with a five coil array in 7 instead of 17 heart beats.

DISCUSSION

It has been demonstrated that the discussed method is feasible *in vivo* and enables considerable reduction of scan time. No residual foldover artifacts are observed. Optimized non-integer reductions are possible and no particularly shaped coil sensitivities are required. Nevertheless, the coil arrangement is a major determinant of SNR and will be subject to further studies.

The sensitivity encoding concept is naturally impaired by the need for fairly good sensitivity maps. However, practicability is improved considerably by the use of low resolution references and automated map refinement. Extrapolation allows sensitivity maps to be applied also to slightly changing tissue configurations as encountered in cardiac imaging. Thus, successive imaging is enabled with only one initial reference scan. 3D sensitivity maps may be a major future improvement.

Clearly, SENSE is only appropriate if the need for scan speed outweighs SNR concerns. Therefore, it appears most promising for real-time and rapid imaging, especially using single-shot strategies which strongly benefit from shorter echo trains.

REFERENCES

1. Hutchinson, M. et al., MRM 6:87-91 (1988).
2. Kelton, J. R. et al., Proceedings of 8th SMR, 1172 (1989).
3. Ra, J. B. et al., Proc.ISMRM 1240(1991)
4. Ra, J. B. et al., MRM 30:142-145 (1993).
5. Sodickson, D. K. et al., MRM 38:591-603 (1997).

ISMRM, 1998.

Fiber-Tractography via Diffusion Tensor MRI (DT-MRI)

Peter J. Basser
Section on Tissue Biophysics and Biomimetics, NICHD, NIH, Bethesda, MD

Purpose

To propose a methodology to calculate continuous fiber-tract trajectories from measured diffusion tensor MRI data, and a rationale for determining fiber tract continuity.

Introduction

In normal and pathological tissues, fiber tract trajectories would provide valuable new microstructural information. In aging and development it would provide a means to follow changes in fiber-architecture. DT-MRI (1) is now the first noninvasive imaging modality capable of generating such fiber-tract trajectories. This is because in each voxel, the fiber tract direction is parallel to the eigenvector, ε_1, associated with the largest eigenvalue, λ_1, of the local diffusion tensor, $\underline{\mathbf{D}}$ (1). However, ε_1 measured by DT-MRI are inherently discrete, noisy, voxel-averaged estimates of the "true" direction vectors (2). To date, it has not been feasible to reconstruct continuous fiber tract trajectories from the measured ε_1. However, a new, efficient $\underline{\mathbf{D}}$-field processing methodology that we just developed, generates a continuous diffusion tensor field, $\underline{\mathbf{D}}(\mathbf{x})$, from measured DT-MRI data (3) from which a continuous ε_1-field map can be calculated. Then, the method below can be used to calculate fiber tract trajectories, and assess fiber tract continuity.

Theory

The fiber tract trajectory vector, $\mathbf{r}(s)$, is parameterized by arc length, s. We solve the linear forced vector differential equation on the left below for $\mathbf{r}(s)$ (4):

$$\frac{d\mathbf{r}(s)}{ds} = \mathbf{t}(s); \quad \mathbf{t}(s) = \varepsilon_1(\mathbf{r}(s))$$

The key new idea presented on the right above is to equate the normalized eigenvector of $\underline{\mathbf{D}}(\mathbf{r}(s))$, $\varepsilon_1(\mathbf{r}(s))$, (associated with the largest eigenvalue of $\underline{\mathbf{D}}(\mathbf{r}(s))$, $\lambda_1(\mathbf{r}(s))$, and the unit vector, $\mathbf{t}(s)$, tangent to the fiber tract trajectory vector, $\mathbf{r}(s)$.

Methods

Numerical methods must be used to obtain $\mathbf{r}(s)$ from $\underline{\mathbf{D}}(\mathbf{x})$. Starting at a point $\mathbf{x}_0$ on $\mathbf{r}(s)$, we evaluate $\underline{\mathbf{D}}(\mathbf{x}_0)$, calculate $\varepsilon_1(\mathbf{x}_0)$ (which is parallel to the slope of $\mathbf{r}(s)$ at $\mathbf{x}_0$), and approximate the position of a nearby point on $\mathbf{r}(s)$, $\mathbf{x}_1$, using a Taylor series expansion of $\mathbf{x}$ about $\mathbf{x}_0$: $\mathbf{x}_1 = \mathbf{x}_0 + \delta\mathbf{x}$ ... Since the correction, $\delta\mathbf{x}$ is parallel to the fiber tract direction at $\mathbf{x}_0$, $\delta\mathbf{x} = \alpha\, \varepsilon_1(\mathbf{x}_0)$, where α is a (small) constant. These steps are repeated for a new point, $\mathbf{x}_1$; the process is then iterated. This is Euler's method. While easy to implement, there is no way to correct its prediction of $\mathbf{r}(s)$, leading to accumulated errors (5). However, using our continuous representation of $\underline{\mathbf{D}}(\mathbf{x})$, we can now calculate second and higher derivatives of $\varepsilon_1(\mathbf{x})$ at any point, and thus improve accuracy by employing higher order correction schemes, e.g., Runge-Kutta methods (5).

Results

To test their fidelity and spatial frequency response, a family of analytical 3-d $\underline{\mathbf{D}}(\mathbf{x})$ maps was synthesized with fiber tract direction fields having a (a) non-zero divergence (converging or diverging fiber pattern), (b) non-zero curl (circulating, open or closed fiber pattern), or (c) periodic or uniform fiber directional pattern. Fig 1 shows a fiber tract trajectory, $\mathbf{r}(s)$, calculated from such a test map in which all three Euler angles of $\underline{\mathbf{D}}(\mathbf{x})$: $\phi(\mathbf{x})$, $\varphi(\mathbf{x})$, and $\theta(\mathbf{x})$, varied continuously through the image volume.

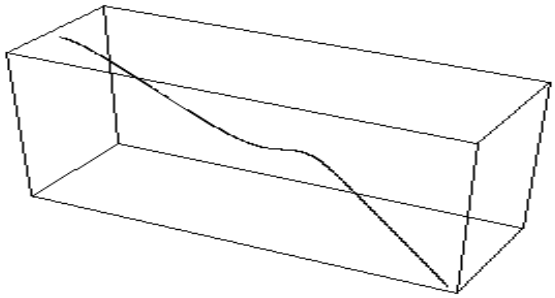

Fig 1. Computed 3-d fiber tract trajectory from synthetic $\underline{\mathbf{D}}(\mathbf{x})$ image.

Predictably, however, we were unable to follow the fiber-tract trajectory through singularities (sources or sinks) in the fiber direction field. Closed and open fiber paths could be followed reliably, though, provided that the step size was small compared to the local radii of curvature.

Discussion and Concluding Remarks

Two paradigmatic problems arise in this emerging field of *DT-MRI Fiber Tractography* in trying to assess fiber-tract continuity or functional connectivity. One is an initial value problem--to follow a fiber trajectory starting from one point on it. Another is a two-point boundary value problem--to establish whether two points (or regions) are connected by a single fiber-tract (or set of fiber tracts). Note, if these regions are connected by fiber tracts that cross, branch, merge or fan out, causing "powder averaging" of the $\underline{\mathbf{D}}$-field at these points (6), then without additional *a priori* or *a posteriori* information about the distribution of fiber tract directions within these voxels, tracing fibers through them is problematic. In functional PET and MRI studies, "activity" is often reported simultaneously in different brain regions following stimulation. Here, it is naive to imagine that DT-MRI alone can provide an anatomical basis for simultaneous activation by establishing connections between these regions via gross neural pathways. Nevertheless, using the new methodology presented here, determining fiber trajectories in large coherently oriented white matter tracts, such as the spinal cord, corpus callosum, and pyramidal tracts, as well as in other ordered soft tissues, is now feasible.

References

1. Basser, PJ et al., *Biophys. J.*, 66, 259-267, 1994.
2. Basser, PJ et al., *J. Magn. Reson* , B 103, 247-54, 1994.
3. Aldroubi, A et al, in prep., 1998.
4. Kreyszig, E, *Differential Geometry*, 1991.
5. Press, WH et al., *Numerical Recipes in C*, 1992.
6. Pierpaoli, C et al., *Magn. Reson. Med.*, 36, 893, 1996.

ISMRM, 1998.

3D Reconstruction of Axonal fibers from Diffusion Tensor Imaging using Fiber Assignment by Continuous Tracking (FACT).

S. Mori[1], R. Xue[2], B. Crain[3], M. Solaiyappan[1], V.P. Chacko[1], and P.C.M. van Zijl[1]
Department of Radiology[1], Biomedical Engineering[2], and Pathology[3], Johns Hopkins University, School of Medicine, Baltimore, MD 21205, USA

Introduction

Diffusion-weighted MRI allows *in vivo* mapping of the diffusional properties of brain water and has revealed a high degree of diffusional anisotropy in white matter (1). Despite many studies of this anisotropy and the production of vector pictures showing fiber orientation within voxels of image planes, the actual reconstruction of neuronal projections by tracking of these vectors has never been accomplished. In the present study, we demonstrate an approach called Fiber Assignment by Continuous Tracking (FACT), which is able to achieve such 3D tracking of axonal projections (2). The results are subsequently validated by *in situ* tracking of known fiber tracts in rat and sheep brains.

Materials and Methods

MRI studies: Rat and sheep brains fixed in formalin were subjected to the study using 9.4 and 4.7 T GE Omega imagers, respectively. A diffusion-weighted 3D spin-echo sequence was used to record images that were diffusion-weighted along ten independent axes. An additional image with the least diffusion-weighted image was also recorded and six independent tensor elements were calculated for each pixel. A data size of 128 x 64 x 64 was acquired and zerofilled to obtain final resolution of 256 x 128 x 128. FOV was 32 x 16 x 16 mm (rat) or 90 x 60 x 54 mm (sheep).

Tracking: One of the difficulties in the post-processing reconstruction of 3D fiber structures from diffusion tensor MRI data is related to decision-making for the connections between voxels in the image. This is illustrated in Fig. 1a, where the fibers (long curved arrows) are assumed to be confined to the 2D plane and the calculated fiber direction within each voxel is indicated by a straight open arrow. Starting from the voxel with an asterisk, tracking should follow the bold curved arrow. The most intuitive way to perform this tracking is by connecting each voxel to the adjacent one at which the fiber direction is pointing. However, when using this approach, the tracking (indicated by the dotted voxels) often deviates from the true fiber orientation, because the choice of direction is limited (26 in the case of 3D). This problem is avoided when tracking a continuous rather than a discrete number field (Fig. 1b). Here, tracking is initiated from the center of a voxel and proceeds according to the vector direction. At the point where the track leaves the voxel and enters the next, its direction is changed to that of the neighbor. Due to the presence of continuous intercepts, this tracking now connects the correct voxels and the actual fiber (bold straight arrows) can be assigned. We therefore dubbed this approach FACT (Fiber Assignment by Continuous Tracking).

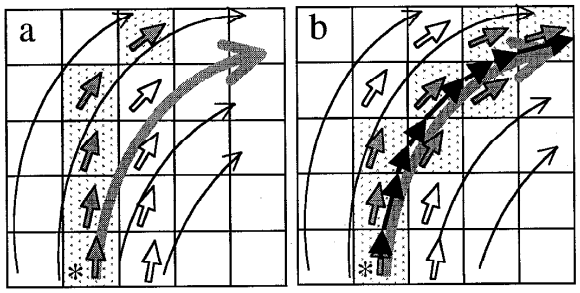

Fig. 1: Tracking of fibers using information from diffusion tensor imaging in a discrete (a) and continuous (b) number field.

Results and Discussion

An example of the 3D fiber reconstruction is shown in Fig. 2. For clarity, only the internal capsule is shown. More than 10 prominent axonal projections (optic tract, fimbria, internal and external capsule, genu and splenium corpus callosum, anterior commissure, stria terminalis, fornix, stria medullaris, medial forebrain bundle, and olfactory tract) were reconstructed from the rat and sheep brains. The slice-by-slice comparison with brain atlases confirmed that the MRI results precisely reflect the structures of the known axonal projections.

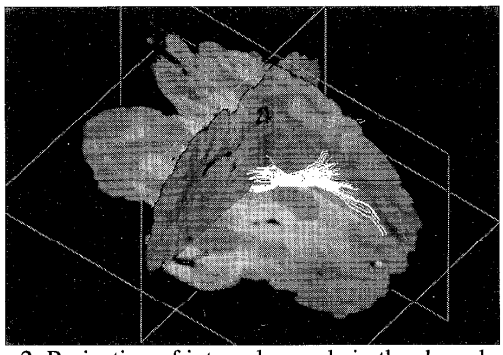

Fig. 2: Projection of internal capsule in the sheep brain.

1: Basser, P.J. et. al, Biophys.J. 66,259-267(1994), Peirpaoli, et.al., Radiology, 201,637-648(1996)
2: Mori et. al, Annal. Neurol. in press (1999)

ISMRM, 1999.

Segmented TrueFISP Cine Imaging of the Heart

J. Bundy[1], O. Simonetti[1], G. Laub[1], J.P. Finn[2]

[1]*Siemens Medical Systems and* [2] *Northwestern University Radiology Department, Chicago IL*

Purpose

The purpose of this study was to develop a segmented TrueFISP[1] pulse sequence for cine imaging of the heart with short TR while maintaining high blood/myocardium contrast. Short TR can be used to achieve shorter breath-holds, or higher temporal or spatial resolution than possible with standard segmented FLASH techniques.

Introduction

Breath-hold cine imaging of the heart is widely used to evaluate cardiac function by MRI. The temporal and spatial resolution of this technique are limited by the total acquisition time which must be within a comfortable breath-hold (15 – 20 heartbeats). Spoiled gradient echo sequences which rely on inflow enhancement for blood/myocardium contrast are typically used. As gradient performance improves, the minimum TR attainable in such a sequence decreases. However, inflow enhancement is diminished at shorter TR's causing saturation of the blood signal and reduction of blood/myocardium contrast. At very short TR, it may be advantageous to exploit the difference in blood and myocardium relaxation times rather than rely on inflow enhancement. Blood has a significantly lower T1/T2 ratio than myocardium. At very short TR, TrueFISP is sensitive to T1/T2 and potentially offers higher contrast-to-noise than FLASH as well as inherent motion insensitivity[2].

For these reasons, TrueFISP has been utilized for real-time cardiac fluoroscopy[3,4], but at relatively low temporal and spatial resolution. In this work, we apply the TrueFISP technique in a segmented k-space, breath-hold acquisition, taking advantage of the short TR and inherently high contrast between blood and myocardium to achieve faster scan times than standard FLASH techniques.

Methods

The segmented True FISP sequence was implemented on a 1.5T Magnetom Sonata (Siemens Medical Systems, Iselin NJ) with a high performance gradient system (40 mT/m amplitude, 200 T/m/sec slew rate). The sequence is based on a breath-hold, ECG-triggered, segmented k-space acquisition with echo-sharing[5] to improve temporal resolution. The basic TrueFISP timing module used has TR=4.0 ms and TE=2.0ms. Pulse sequences with 11, 15, and 19 lines per segment and corresponding temporal resolution of 24, 32, and 40 msec were implemented. To achieve and maintain the steady state required by TrueFISP, RF and gradient pulsing are applied for one preparatory heartbeat and then constantly applied without interruption throughout the entire acquisition. Typical imaging parameters for the 19 line per segment sequence are 133 x 256 pixels with dimensions of 2.0mm x 1.25mm x 6 mm slice thickness acquired in 7 heartbeats. The flip angle (α) was 50° and receiver bandwidth was 780 Hz/pixel. This sequence was compared to a segmented FLASH with TR 8.0 msec, TE 4.0 msec, α = 20 °, and 230 Hz/pixel bandwidth. A CP 4-channel phased array body coil was used.

Results

Image examples of short-axis and 4-chamber views obtained in a volunteer are shown in Figures 1 and 2.

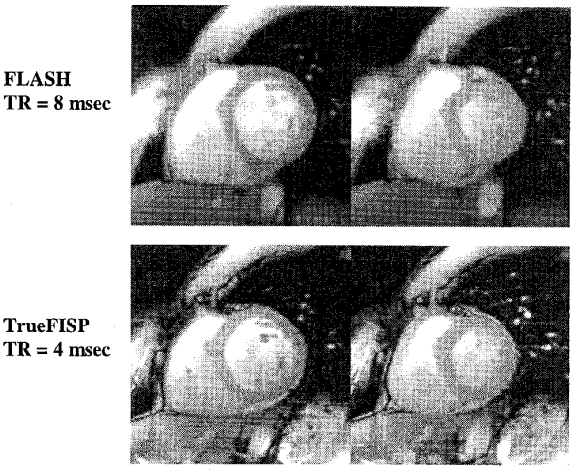

Figure 1. Two time frames (left = end-diastole, right = end-systole) comparing segmented FLASH (top) and segmented TrueFISP (bottom). Contrast between the blood and the myocardium is maintained at shorter TR using the TrueFISP acquisition. Acquisition time for FLASH images was 20 seconds compared to 10 seconds for TrueFISP. Temporal resolution (40 msecs) and spatial resolution are equivalent.

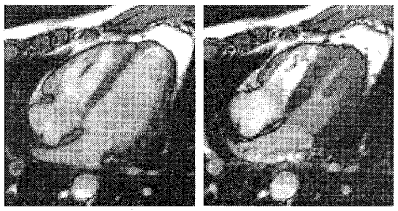

Figure 2. Two time frames (left = end-diastole, right = end-systole) from segmented TrueFISP cine with TR 4.0 msec showing high blood/myocardium contrast in 4-chamber view.

Discussion

The standard FLASH cine sequence has a TR of 8 msec not due to gradient limitations, but to maintain sufficient inflow enhancement. TrueFISP cine demonstrated equivalent blood myocardium contrast throughout the cardiac cycle at half the TR of FLASH. This factor of two time savings can be used to shorten the breath-hold as shown in the example, or to increase either spatial or temporal resolution in the same breath-hold period. The reduced reliance on inflow enhancement of TrueFISP is also advantageous in long-axis orientations which often suffer from saturation of blood signal in FLASH. TrueFISP is sensitive at high field to B_0 inhomogeneity, but this problem is reduced at the short TR's possible with high performance gradient hardware.

True FISP allows us to take advantage of short TR imaging without sacrificing blood/myocardium contrast.

References

1. A. Oppelt et al., *Electromedica* 54, 15 (1986).
2. Y. Zur, et al., *Magn. Reson. Med.*, 16:444-459, 1990.
3. O. Heid, *5th ISMRM*, 1997.
4. M. Griswold et al., *Radiology*, Vol. 209(P), pp.245-246, 1998.
5. G. Laub, *12th SMRM*, p. 478, 1993.

ISMRM, 2000.

Mapping fiber orientation spectra in cerebral white matter with Fourier-transform diffusion MRI

V.J. Wedeen, T.G. Reese, D.S. Tuch, M.R. Weigel, J.-G. Dou, R.M. Weiskoff‡, D. Chessler
MGH-NMR Center, Department of Radiology, Massachusetts General Hospital and the Harvard Medical School, Boston MA
and Epix Medical, Cambridge, MA‡

What diffusion tensor MRI gives with one hand it takes away with the other, awakening hopes of cerebral tractography but excluding any possibility of accurately resolving tract intersections.

The present study describes methodology to image *a distribution of fiber orientations within each voxel*, mapping within each MRI voxel the 3D probability density function (PDF) of proton diffusion with q-space diffusion MRI with Fourier transform (FT) encoding and reconstruction. We find that these distributions while consistent with diffusion tensor MRI frequently show multiple white matter orientations within each voxel and that these often correspond to known cerebral white matter tract intersections.

Methods

Diffusion-weighted single-shot echo-planar NMR images are acquired for several hundred values of the diffusion-encoding spatial modulation **q** comprising points of an isotropic 3D grid contained within a spherical volume of radius r

$$\mathbf{q} = (a\,\mathbf{q}_x, b\,\mathbf{q}_y, c\,\mathbf{q}_z);$$
$$a, b, c \text{ integers and } a^2 + b^2 + c^2 \le r^2 \qquad [1].$$

where the $\mathbf{q}_i$ denote unit phase-encodings in the respective coordinates. At each voxel, the signal data $S(\mathbf{q})$ comprise a sampling of the 3D Fourier transform of the probability density function of spin translation

$$\mathcal{P}(\Delta\mathbf{r}) = \langle P(\mathbf{y} | \mathbf{y} + \Delta\mathbf{r}, \tau)\rangle \qquad [2]$$

where $P(\mathbf{y}|\mathbf{y} + \Delta\mathbf{r}, \tau)$ is the conditional displacement probability density from location $\mathbf{y}$ to point $\mathbf{y} + \Delta\mathbf{r}$ at the given mixing time τ and the angle-bracket denotes an average over the observed spins within a voxel. Then $\mathcal{P}(\Delta\mathbf{r})$ in each voxel is the inverse 3DFT ($\mathcal{F}$) of the signal

$$\mathcal{P}(\Delta\mathbf{r}) = \mathcal{F}[S(\mathbf{q})] \qquad [3].$$

Imaging in vivo, the phase of $S(\mathbf{q})$ is confounded by macroscopic motion, but $\mathcal{P}(\Delta\mathbf{r})$ may be accurately reconstructed using the surprising result that functions that can arise as probability densities of diffusion, free or restricted, isotropic or anisotropic, observed at any time τ, always have Fourier transforms that are *real* (because the PDF is symmetric) *and positive* (because the PDF represents the exponential of a Hermetian exchange matrix). Whence

$$S(\mathbf{q}) = |S(\mathbf{q})| \qquad [4]$$

and we reconstruct the PDF directly as the (discrete) inverse 3DFT of the amplitudes

$$\mathcal{P}(\Delta\mathbf{r}) = \mathcal{F}[|S(\mathbf{q})|] \qquad [5].$$

Results

Cerebral Fourier diffusion MRI studies were acquired in normal volunteers at 1.5T using single-shot echo-planar spin-echo pulse sequence augmented by diffusion encoding gradient pulses of peak intensity $|\mathbf{G}|_{MAX}$ = 40 mT m^{-1}, TR/TE/τ = 2 R-R intervals (peripheral pulse trigger)/176 ms/66 ms and spatial resolution = (4 mm)^3. Data were acquired for N = 500 values of **q** representing the interior of the sphere of radius r = 5 grid units, where the grid spacing $|\mathbf{q}_i|$ = 70 radian mm^{-1}. This maps PDF-space with isotropic spatial resolution of $2\pi|5\mathbf{q}_i|^{-1}$ = 9 μm and field-of-view $\pi|\mathbf{q}_i|^{-1}$ = 90 μm. At maximum, diffusion sensitivity $b_{MAX} \approx |5\mathbf{q}_i|^2 2\tau/3 \approx 20{,}000$ s mm^{-1}.

Figure 1 illustrates for one voxel the signal amplitudes and their Fourier transform, the PDF. Signal amplitudes show a complex non-Gaussian structure revealed in the PDF to arise from two distinct orientational limbs corresponding to fibers of two orientations. Figure 2 shows an image of diffusion probability densities for a coronal slice through the brainstem; intersection of the corticospinal tract with fibers of the middle cerebellar peduncle yields PDF's resembling '+' signs with maximum diffusion in the fiber directions, superior-inferior and left-right, respectively. More superiority, PDF's at the intersection of the corona radiata, corpus callosum and superior longitudinal fasicle show the expected 3-way crossing. These features were confirmed in multislice multi-axial imaging across subjects.

Fig. 1. Signal amplitudes $|S(\mathbf{q})|$ in 5 data planes of 3D q-space for one voxel (left) and its 3DFT, the diffusion PDF, represented by $\mathcal{P}(\Delta\mathbf{r}) = const.$ (right), exhibit complex non-gaussian structre.

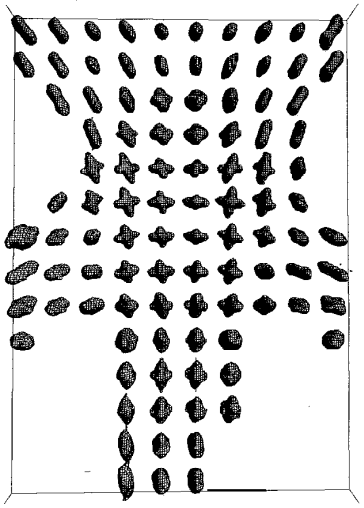

Fig. 2. Map of diffusion PDF's at intersection of corticospinal tract (orientations sup.-inf.) and pontine decussation (left-right).

Discussion

A limitation of present methodology is its insensitivity to unsymmetric internal spin motion such as perfusion and streaming or 'effective' motion produced by asymmetric relaxation sinks. Typically, the present method will detect the spatially symmetric part of such motion, however more complex transport effects are also possible.

Detection of intravoxel diffusion heterogeneity depends on the existence of distinct microenvironments whose size exceeds the diffusion length at the given timescale τ, and the PDF finally oberved at each location is simply the algebraic sum of such small-scale contributions. The efficacy of present fiber orientation mapping rests in part on the geometry of the 3DFT: given a fiber bundle with some orientation, high signal (low attenuation) occurs in the 2D plane of q-directions orthogonal to the fibers, converted by 3DFT into a high signal in precisely the fiber direction, concentrating signal energy like a matched filter.

Based on the present study, diffusion tensor MRI can be viewed as a second-order approximation of a 3D displacement probability distribution that can be imaged in full with Fourier methods. The potential of Fourier diffusion MRI for cerebral tractography will depend on the still unknown degree to which cerebral white matter tracts are separable by local orientation, and doubtless tracts will not be so separable.

Acknowledgement

Supported by NIH 1R01 HL5627 and the Sol Goldman Charitable Trust

ISMRM, 2000.

2D and 3D Segmented TurboFLASH for the Visualization of Myocardial Injury

Orlando Simonetti[1], PhD, Raymond J. Kim[2], MD, David S. Fieno[2], MS, Hanns Hillenbrand[2], MD, Edwin Wu[2], MD, Jeffrey M. Bundy[1], PhD, J. Paul Finn[2], MD, Robert M. Judd[2], PhD
Siemens Medical Systems[1] and Northwestern University Medical School[2], Chicago, IL

Purpose: The ability to detect and delineate myocardial injury by MRI is directly influenced by the imaging pulse sequence employed. The goal of this study was to design and implement 2D and 3D segmented inversion-recovery turboFLASH[1] MRI pulse sequences for the visualization of myocardial injury, to compare this technique to other MRI approaches in a canine model of ischemic injury, and to evaluate its utility in patients with coronary artery disease.

Methods: Two-dimensional (TR/TE 8.0/4.0, 230 Hz/pixel, 23 lines per segment) and three-dimensional (TR/TE 3.4/1.2, 390 Hz/pixel, 64 lines per segment) segmented inversion recovery turboFLASH sequences were implemented on a Siemens Magnetom Sonata MRI system (Siemens AG, Erlangen, Germany) with high performance gradient system (40mT/m amplitude, 200T/m/sec slew rate). Six dogs and 18 patients were studied. The ten pulse sequences listed in Table 1 were tested in dogs with surgically produced myocardial infarction. 2D segmented turboFLASH was compared to both T2-weighted imaging without contrast agent injection, and T1-weighted imaging following injection of 0.2 mmol/kg Prohance (Bracco Diagnostics, Princeton, NJ. In patients, the segmented turboFLASH technique was used to acquire contrast-enhanced images 19±7 days following myocardial infarction documented by serum enzymes.
Signal intensities in remote and infarcted regions of myocardium were measured in dogs and patients. Image enhancement and contrast-to-noise ratios were calculated and compared for all ten of the pulse sequences tested in dogs. The 3D segmented turboFLASH technique designed to achieve full coverage of the heart in a single breath-hold was also tested in two dogs and two patients.

Results: Canine results are summarized in Table 2.

Sequence	Δ% INF / REM		Contrast-to-NR	
	Mean	SEM	Mean	SEM
T2 TSE	94.2	46.7	4.19	3.79
T2 STIR	120.1	88	3.16	2.75
T1 SE	67.2	36.7	2.95	2.3
T1 TSE	64.7	22.1	5.97	2.21
T1 IR-TSE	497.3	211.5	5.89	1.7
MD-FLASH	140.1	61	8.3	3.61
True FISP	148.1	45.1	14.44	5.98
IR TFL (Null Pre)	111 6	42 7	8 21	2.44
IR TFL (Null Post)	510 4	256 6	10 14	3 59
Seg IR TFL (Null Post)	1080 4	524 1	18 93	7 31

Table 1. Summary of results obtained from the ten pulse sequences tested in canine model of myocardial infarction. Mean and standard error of mean are listed for % increase of infarcted tissue signal (INF) over remote signal (REM) and contrast-to-noise ratio.

Using 2D inversion-recovery segmented turboFLASH with the inversion time (TI) set to null post-contrast normal myocardium, the image intensity in infarcted myocardium was 1080%±214% higher than remote. This was nearly twice that of the next best sequence tested ($p<0.05$ compared to all other sequences). Similarly, the contrast-to-noise ratio was higher than the other sequences. Single-shot inversion recovery turboFLASH with TI set to null *post*-contrast myocardium (IR TFL (Post)) demonstrated a five-fold increase in enhancement over single-shot turboFLASH with TI set to null *pre*-contrast myocardium (IR TFL (Pre)). In the 18 patients, the intensity in infarcted myocardium using segmented turboFLASH was 485±43% higher than remote. One patient example is shown in Figure 1. Similar results were obtained in limited testing of the 3D version of the same technique. One 3D example in an animal model of infarction is shown in Figure 2.

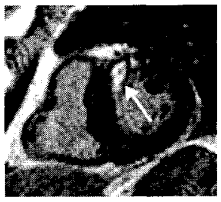

Figure 1: Example of post-contrast 2D segmented IR-turboFLASH image of antero-septal MI in a patient.

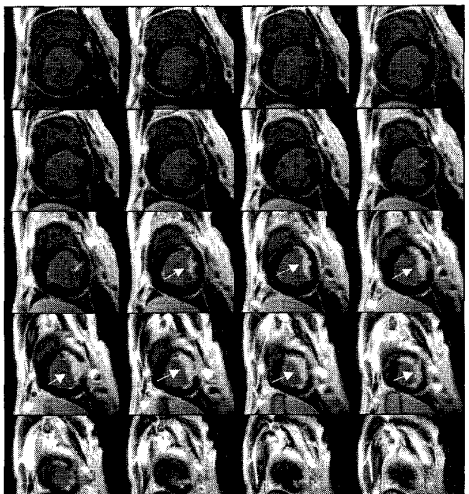

Figure 2: Example of 3D breath-hold segmented turboFLASH. 20 out of 32 partitions are shown. In this animal, a lateral wall infarct is clearly depicted.

Conclusions: Inversion-recovery segmented breath hold turboFLASH demonstrated a significant improvement in contrast over previously described techniques and can be used to generate high-contrast 2D and 3D breath-hold images of myocardial injury.

References:

1. Edelman et al.. Radiology. 1990;177:515-521.

ISMRM, 2000.

T_2 reveals spatial collagen architecture in articular cartilage: a comparative quantitative MRI and polarized light microscopic study

M.T. Nieminen[1], J. Rieppo[1], J. Töyräs[2], J.M. Hakumäki[3], M.J. Silvennoinen[3], M.M. Hyttinen[1] H.J. Helminen[1] and J.S. Jurvelin[2]
[1]Department of Anatomy, University of Kuopio; [2]Department of Clinical Physiology and Nuclear Medicine, Kuopio University Hospital;
[3]NMR Research Group, A. I. Virtanen Institute for Molecular Sciences, University of Kuopio, Kuopio, Finland.

Introduction

Functional competence of articular cartilage is mainly determined by the organization, content and interactions of collagen, proteoglycans (PGs) and extracellular fluid. Characterization of cartilage constituents *in vivo* is essential for the detection of early stages of degenerative joint disease (osteoarthrosis).

In articular cartilage, type II collagen forms a highly organized, anisotropic three-dimensional fibrous network, where the fibril orientation changes depthwise from the surface to subchondral bone. It is suggested that T_2 relaxation is closely related to fibril arrangement [1,2]. In this study, a quantitative spatial approach was conducted to verify the relationship between T_2 and collagen fibril orientation as measured by quantitative polarized light microscopy, a method for analysis of tissue structural organization.

Methods

Osteochondral plugs from healthy articular cartilage (ϕ=6mm, n=9) were prepared for MR microscopic and polarized light microscopic (PLM) analyses from patellae of 1 to 3-year-old bulls, one sample per patella.

The MR microscopic measurements were performed at 9.4T with a 16mm high resolution spectroscopy probe. Cartilage T_2 maps were obtained from spin-echo measurements with TR/TE=2500/14, 24, 34 and 44ms, 1mm slice thickness and 20mm FOV with 256^2 resolution at 25±1°C. Cartilage surface was oriented normal to the B_0 field. For each sample, a T_2 profile across cartilage thickness was calculated from a 1mm wide area.

After MR measurements, samples were fixed in formalin, dehydrated and mounted in paraffin. For each sample, 5µm-thick microscopic sections were cut and PGs were digested with hyaluronidase to reveal the collagen network. Samples were analyzed in four vertically randomized orientations using a computer assisted polarized light microscope to obtain a mean optical retardation (OR) profile of collagen from cartilage surface to subchondral bone. OR of polarized light, i.e. birefringence, is known to reflect sensitively the degree of collagen orientation [3].

Results

The intermediate cartilage zone is characterized by non-ordered collagen fibrils. Therefore, a maximum T_2 and minimum optical retardation are observed in this zone. These landmarks were used to match spatial T_2 and high resolution OR data for quantitative comparison.

A structural similarity was observed between T_2 maps and PLM images (Fig. 1). After reducing spatial PLM resolution to match MR resolution, a reproducible inverse relation between T_2 relaxation and OR was detected (Fig. 2A). Consequently, a linear positive correlation between T_2 and 1/OR was established in each sample (Fig. 2B), with r=0.93±0.02 (n=9). Pooling data from all samples (n=194) resulted in r=0.69.

Discussion

Maximum contrast between T_2 laminae is observed when cartilage surface is aligned at 0 or 90° in reference to B_0. This starting point gives potential to observe the possible relationship between T_2 and the birefringence of oriented tissue.

The results reveal a close relationship between MR and PLM imaging modalities. Experimental evidence is presented that cartilage T_2 follows sensitively collagen fibril arrangement. Both techniques reflect primarily changes in collagen orientation, but secondary contributors may also exist. Only moderate correlation between the pooled T_2 and 1/OR data suggests that it may be inaccurate to quantitatively predict one parameter by using the other.

A second T_2 maximum was often observed in the deep cartilage zone, which was systematically detected also by 1/OR maximum in PLM. This extra lamina is located near the cartilage-subchondral bone-interface and may associate with collagen fibrils bending around the hypertrophied chondrocytes. This demonstrates that the collagen network structure in the deep zone may diverge from the conventional conception of highly parallelly organized collagen fibrils.

Although a perfect relationship does not exist between cartilage T_2 and PLM, the spatial agreement of these two totally different techniques reveals that T_2 changes in normal articular cartilage reflect sensitively architectural changes in collagen fibril arrangement.

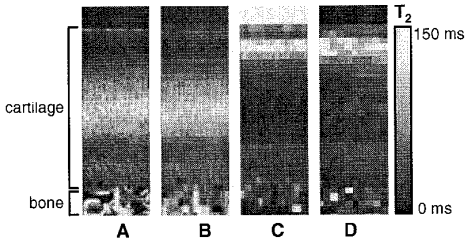

Fig. 1: PLM image with original high resolution (A), OR (B) and 1/OR (C) images with vertical resolution similar to MR image, and T_2 map (D) from a representative sample.

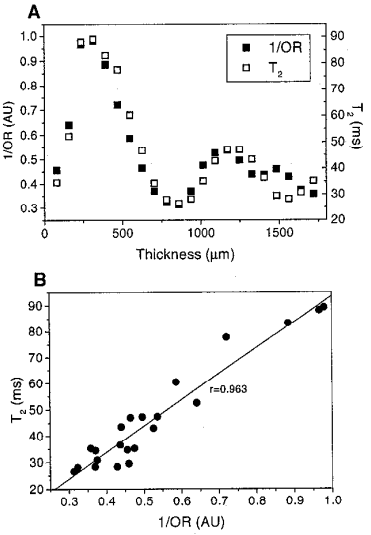

Fig. 2: (A) T_2 and 1/OR profiles as a function of thickness from cartilage surface, and (B) T_2 plotted as a function of 1/OR for a representative sample.

References

1. Goodwin, D.W., Dunn, J.F., *Top. Magn. Reson. Imaging*, 9, 337-47, 1998.
2. Xia, Y., *Magn. Reson. Med.*, 39, 941-9, 1998.
3. Arokoski, J.P. et al., *Ann. Rheum. Dis.*, 55, 253-64, 1996.

Acknowledgments

This study was supported by the Graduate School for Musculoskeletal Diseases, Kuopio University Hospital (EVO 5103), Kuopio and TEKES, Helsinki, Finland.

ISMRM, 2000.

Proton Chemical Exchange Dependent Saturation Transfer (CEST): Evaluation as a Mechanism for Non-Metal Based Exogenous MRI Contrast Agent

K.M. Ward, A.H. Aletras, R.S. Balaban

Lab of Cardiac Energetics, National Heart Lung and Blood Institute, NIH, Bethesda MD

Purpose To evaluate proton chemical exchange dependent saturation transfer (CEST) as a method of generating exogenous MRI contrast. To define chemical groups suitable as exogenous CEST contrast agents under *in vivo* pH and temperature conditions.

Introduction Most MR contrast agents are dependent on the T1 or T2* relaxation properties of metal chelates or metal particles which can be limited in their use at high concentrations by toxicity or T2* effects (most T1 agents). The goal of this study was to evaluate the use of saturation transfer with specific chemical groups as a non-metal based MR contrast agent. The idea is to find chemical groups with the appropriate proton exchange and chemical shift properties at physiological pH and temperature that will function as effective saturation transfer partners with water. A thousand-fold enhancement of the exchange site proton signal can result via the reduction in the water signal (M_S/M_0) based on the following equations:

$$M_S/M_0 \sim [1/(1+k_1 T_{1w})] \quad (1)$$

$$k_1 = (1/\tau_{CA})[\text{agent}][n] \quad (2)$$

where M_S and M_0 is the water signal with and without saturation of the exchange site, T_{1w} is the T1 of water protons, k_1 is the pseudo first order rate constant, τ_{CA} is the site proton lifetime, [agent] is the mole fraction of the agent relative to water protons, and [n] is the number of exchange sites per mole of agent. [1]. An ideal contrast agent requires the following: 1) Slow to intermediate exchange rate. (i.e. $\tau_{CA}\,\Delta\omega_{CA} >$ 1 where $\Delta\omega_{CA}$ is the chemical shift difference between the site and water [2]). 2) Large $\Delta\omega_{CA}$ to support a high exchange rate and improve specificity due to B_0 in-homogeneity can be > 2 ppm. 3) High solubility. 4) Low toxicity. 5) Defined tissue distribution. To stay in slow exchange, τ_{CA} must be rather long reducing the effect of each exchange site. Given a $\Delta\omega_{CA}$ of 5 ppm, $\tau_{CA}\,\Delta\omega_{CA}$ ~10, and an Ms/Mo of 0.9 requires [agent] to be >10 mM . These concentration estimates were confirmed in our studies outlined below. Based on these considerations we searched for compounds with proton chemical exchange sites with large $\Delta\omega_{CA}$, high solubility and appropriate chemical exchange rates to just maintain within the slow exchange limits at physiological pH (7.4) and temperature (37°C).

Methods Solutions were dissolved in HPLC grade water with inorganic phosphate buffers to maintain pH. Magnetization transfer spectra were collected at 7T using a Bruker AC-300 wide bore spectrometer at 37°C. Studies were conducted using a steady-state irradiation (15 sec) over a range of frequencies ± 8 ppm from water. The M_s data were plotted as a function of the irradiation frequency in the magnetization transfer spectra. MR images were collected on a custom designed 4T system. See figure legends for details.

Results/Discussion Several classes of chemical exchange sites were evaluated. Sugar hydroxyl groups provided good chemical exchange sites at pH 7 (M_S/M_0 0.89-0.68; 250 mM sugar) but their $\Delta\omega$ values (< 2 ppm) were too small. Sugar polymers, such as dextran, maintained these chemical exchange and shift properties but with much higher [n] reducing the osmotic load. Therefore, polymerization will be a useful approach for reducing the osmotic load of CEST agents. Backbone amino acid amino and the arginine R group, guanidinium , protons provided a better model with 2–3 ppm shifts, but were in fast exchange at pH 7.0. These studies revealed that indole ring NH groups had useful properties with $\Delta\omega_{CA}$ >5 ppm and reasonable exchange rates at pH 7.0. We evaluated additional ring-NH groups: nucleosides, their pyrimidine and purine bases, as well as derivatives of barbituric acid and imidazole. Several of these compounds revealed promising properties with $\Delta\omega_{CA}$ >3.0 ppm and M_S/M_0 values in the range of 0.7 (62.5 mM). Barbituric acid is presented in detail in this report.

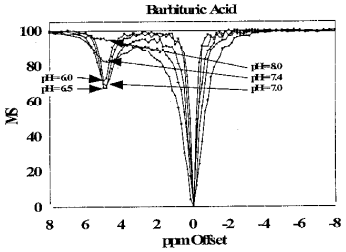

Figure 1A: Saturation transfer spectrum of barbituric acid (62.5 mM, T=37°C, pH = 6.0, 6.5, 7.0, 7.4, 8.0)

Figure 1B: Image of barbituric acid solutions (62.5 mM, pH = 6.5, 7.0, 7.4) and 500 mM NH_4Cl submerged in water and irradiated at 900 Hz at 4T. NH_4Cl was used to test the specificity of the effect.

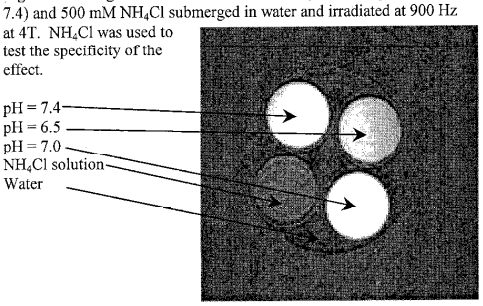

The magnetization transfer spectrum of barbituric acid (62.5 mM) as a function of pH is presented in Figure 1A . The CEST effect is clearly seen in the 5 ppm region. The $1/\tau_{CA}$ was 18.4/M/sec at pH 7. Concentration, temperature, saturation power and buffer effects were also characterized for this molecule (data not shown). Figure 1B is a difference image (M_0-M_s) collected with a 5.3 ppm irradiation. All three solutions of barbituric acid were enhanced over the surrounding water and NH_4Cl controls. Note that the contrast effect could be turned off and on depending on the saturation pulse, which is not possible with metal-based T1 or T2 agents.

Barbituric acid was a model compound used in this study, but is not considered the "ideal" compound. Barbituric acid is pharmacologically inactive with an LD50>5g/kg [3]. Substitution at a side group not involved in chemical exchange is used to manufacture a wide variety of active drugs; this same site could be used to polymerize the compound to eliminate the osmotic stress associated with mmoles of exchange sites. We have infused barbituric acid in rabbits as isotonic concentrations (~150 mM) with minimal short-term physiological perturbations suggesting that there is nothing inherently toxic, in the short term, with this type of molecule. These studies reveal that CEST is a feasible mechanism to generate new exogenous contrast agents that can be "turned" off and on using the saturation pulse. In addition, since these compounds do not require a metal, it may be more feasible to get the agents into cells using preexisting transport pathways.

References *1. Guivel-Scharen, V., Sinnwell, T., Wolff, S., and Balaban, R.,* J. Magn. Res.,*133:36;1998. 2. Dwek, R.,* Nuclear Magnetic Resonance (N.M.R.) in Biochemistry. Applications to Enzyme Systems, *(Oxford UK ,1973) 3. Goldenthal, E., Toxicol. Appl. Pharmacol., 18:185;1971.*

ISMRM, 2000.

3D MR Tracking of Magnetically Labeled Oligosphere Transplants: Initial *In Vivo* Experience in the LE (Shaker) Rat Brain

J.W.M. Bulte[1], S.-C. Zhang[2], P. van Gelderen[3], B.K. Lewis[1], I.D. Duncan[2], J.A. Frank[1].

[1]*Laboratory of Diagnostic Radiology Research (CC) and* [3]*In vivo NMR center (NINDS), National Institutes of Health, Bethesda, MD;* [2]*Department of Medical Sciences, School of Veterinary Medicine, University of Wisconsin, Madison, WI.*

Introduction

Multipotent stem cells are present in the nervous system (1), and have recently been isolated from the human brain (2). They can be established as permanent cell lines and induced to become oligodendroglial cells in the form of free-floating oligospheres following growth factor treatment (3). The adult brain retains the potential to generate these type of cells, and following transplantation they have proven to exhibit extensive myelination capacity (4). It has also been demonstrated that by incorporating a magnetic label into glial cells it is possible to visualize cell spread and the induced myelination non-invasively using MRI (5). Using magnetically labeled oligospheres, we now show that these cells can be monitored *in vivo* repeatedly, in order to make a momentary "snapshot" of their precise spatial migration and distribution at a particular given time. This development is of crucial importance if such stem cell-based therapies are going to be pursued in humans.

Materials and Methods

Oligospheres (OS) were prepared as described (3), and transfected with the LacZ reporter gene in order to track down cell migration histochemically following MRI. OS were co-cultured with MION-46L-OX-26 (5) or a rhodamin-fluorescent derivative at a dose of 25 µg Fe/ml for 24h. In this way, magnetic tagging is achieved by specific targeting and uptake through the transferrin receptor. Magnetic tagging was always verified by Prussian Blue staining. Approx. 1-1.5 x 10^5 labeled OS cells in 2-3 µl medium were transplanted into the intracerebroventricular region (6) of neonatal (P0) Long Evans (LE) shaker rats and normal littermates (n=17).

Rat pups were imaged at 1.5 T using a quadrature wrist coil with several different T1w, PD/T2W, FSE, and T2*w pulse sequences. 2D images were obtained at 2 mm slice thickness, and a 1.2 mm thick 3D SPGR data set was obtained. In order to allow repeated scanning, all scans were performed using isoflurane anesthesia. 3D multi gradient echo MR images were also obtained at 313 µm isotropic resolution using a 4.7 T GE CSI Omega NMR spectrometer and a 1.5 inch diameter home-made surface coil. The 4.7 T scan parameters were: FOV=6x3x3 cm; matrix=192x96x96; NEX=1; TR=100 msec; TE= 6 msec; n echoes=6, flip angle = 15 deg.

Results and Discussion

The first images at approx. 2 weeks post-transplantation showed a localized distribution of cells around the injection site. The injection site could always be identified by its "blooming effect" on gradient echo images. At 3-4 weeks post-transplantation, further cellular spread could be observed inside the white matter areas of the corpus callosum, internal capsule, and hippocampus (Fig. 1). The extend of cellular spread in normal littermates was greater than for the shaker animals; a similar finding was observed previously for the spinal cord (5). Since shaker animals are myelin-deficient and oligodendrocytes stop dividing once they myelinate, we hypothesize that the reduced temporal-spatial migration in the shakers can be explained by a cellular "switch-off" that interferes with cellular expansion and motility. Studies of the long-term survival and –migration kinetics are currently in progress.

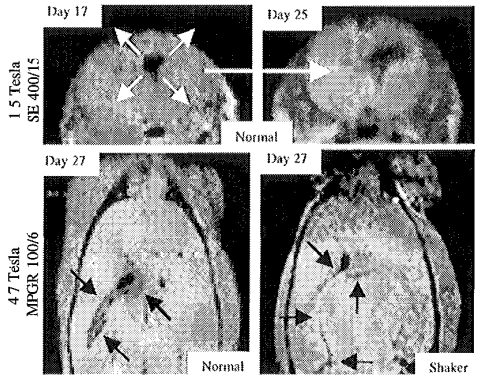

Fig. 1

Conclusions

These results are a first demonstration of the feasibility of dynamic MR imaging (dMRI) of migrating cells relevant to therapeutic intervention. Moreover, this approach has proven to also work using a clinically approved magnet and field strength, and may thus help guide further advances in stem-cell based therapies.

References

1. R. McKay. *Science* **276**, 66 (1997)
2. P.S. Eriksson, et al., *Nature Med.* **4**, 1313 (1998).
3. S.-C. Zhang et al. *J. Neurocytol.* **27**, 475 (1998).
4. S.-C. Zhang, et al. *Proc. Natl. Acad. Sci USA* **96**, 4089 (1999).
5. J.W.M. Bulte et al. *Proc. Natl. Acad. Sci. USA*, in press.
6. B. Yandava et al. *Proc. Natl. Acad. Sci USA* **96**, 7029 (1999).

ISMRM, 2001.

Push-button PPA Reconstructions: GeneRalized Autocalibrating Partially Parallel Acquisitons (GRAPPA)

Mark GRISWOLD[1], Peter JAKOB[1], Robin HEIDEMANN[1], Mathias NITTKA[2], Jianmin WANG[2], Berthold KIEFER[2], Axel HAASE[1],

[1]Universität Würzburg, Physikalisches Institut, EP5, Am Hubland, 97074 Würzburg, Germany; [2] Siemens Medical, Erlangen, Germany

Introduction

In the last few years, many partially parallel acquisition (PPA) techniques have been proposed. These techniques use information in an RF coil array to partially replace a fraction of the phase encoding steps that would normally be acquired using gradient methods. PPA techniques such as SMASH and SENSE have both been previously used to improve imaging speed with good results [1,2]. However, the vast majority of these proposed techniques, including the recently proposed hybrid technique [3], require detailed coil sensitivity mapping procedures. This requirement can be difficult to meet in many instances, such as lung imaging, where the signal from the lung is very low but non-zero, and in EPI imaging, where image distortions cause misregistrations between the acquired coil maps and the reconstructed image. For these reasons, autocalibrating techniques such as AUTO-SMASH [4], and the recently proposed VD-AUTO-SMASH [5], have increased relevance.

In this abstract we propose a more generalized extension of VD-AUTO-SMASH, GeneRalized Autocalibrating Partially Parallel Acquisitions (GRAPPA). GRAPPA is shown to provide up to 5-fold lower artifact power and higher SNR for the same acquired data set when compared to VD-AUTO-SMASH. The combination of the simple autocalibration method with a magnitude based sum of squares reconstruction results in a push-button technique which requires absolutely no user intervention for robust reconstructions.

Theory

The GRAPPA reconstruction can be broken down into the following steps:

1) As in VD-AUTO-SMASH, GRAPPA is based on the acquisition of a block of extra lines in the center of k-space for determination of the reconstruction parameters.

2) A sliding block reconstruction is used, as shown in Figure 1b. This method extends the VD-AUTO-SMASH approach (Fig 1a) to include more than one line in each linear combination. As in VD-AUTO-SMASH, the block of extra acquired lines can be used in the final image reconstruction to provide better image quality with lower artifact powers.

3) Finally, the GRAPPA reconstruction is performed separately for each coil in the array. This is done by setting the target functions in the fit to be a line acquired in one coil, instead of the sum of the lines from all of the coils. This process is repeated for each coil in the array, resulting in unaliased images from each component coil, which can then be combined using a sum of squares algorithm.

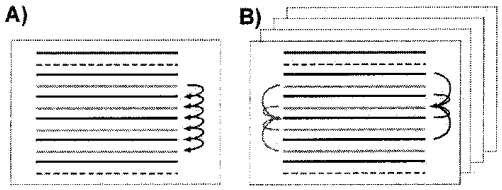

Figure 1. A) Schematic diagram of VD-AUTO-SMASH (B) Schematic diagram of GRAPPA which is performed separately in each coil in the array.

Methods

This method was implemented on a 1.5T Siemens Quantum Symphony system equipped with eight receiver channels using eight element head and body arrays. In each case, 16-64 lines with full sampling density were used for determination of the reconstruction parameters. In all images presented in this study, a block containing four acquired lines was used in each reconstruction of each block. Several different imaging sequences, including single shot HASTE and EPI and contrast enhanced 3D FLASH, were examined throughout the body.

Results and Discussion

GRAPPA provided robust reconstruction in each area of the body tested without any user intervention and without the increased imaging time needed for acquisition of a full coil sensitivity map. The GRAPPA reconstruction provided excellent results in the lung and abdomen, as shown below. Notice the increased resolution in the GRAPPA images compared to the reference images, even though they were acquired in the same imaging time [6]. The lung images in particular are extremely difficult to reconstruct using any other technique which is based on coil sensitivity mapping due to the low, but non-zero signal in the lung. Besides the images shown here, GRAPPA provided high quality images even in cases of severe EPI distortions and in cases where phased-sum based methods [1,3-5] resulted in severe phase cancellation artifacts. Artifact power measurements using simulated image acquistions demonstrate that GRAPPA provides up to 5-fold lower artifact power compared to VD-AUTO-SMASH, while at the same time providing a higher SNR due to the sum of squares reconstruction. Based on these results, GRAPPA appears to be ready for routine clinical applications where fast imaging and robust push-button reconstructions are required.

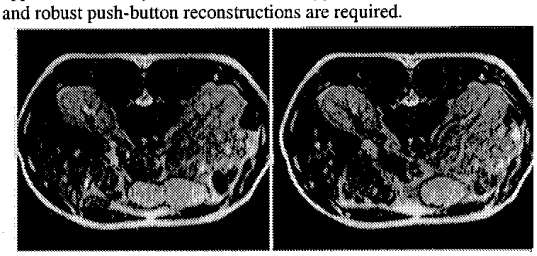

Figure 2. Non-breathhold single shot HASTE images in the abdomen. TR=3.5 ms. Acquisition time=252ms (L) Full time reference, matrix=128x256 (R) GRAPPA, acceleration factor 2, matrix=256x256.

Figure 3. Single shot IR-HASTE images in the lungs, Acquisition time=252ms (top) Reference, matrix=128x256 (bottom) GRAPPA, acceleration factor 2, 256x256. Phase encode direction is horizontal.

References

1. SODICKSON, et. al. *MRM* 38:591-603 (1997)
2. PRUESSMANN, et. al. *MRM*, p. 579 (1999)
3. SODICKSON, *Proc of ISMRM*, p. 272 (2000)
4. JAKOB, et. al., *MAGMA* 7:42-54 (1998)
5. HEIDEMANN, et. al., *Proc of ISMRM*, p. 274 (2000)
6. GRISWOLD, et. al., *MRM* 41:1236-45 (1999)

ISMRM, 2001.

Dynamic Imaging by Temporal Modeling with Principal Component Analysis

Ananya Sen Gupta[1], Zhi-Pei Liang[1]

[1]University of Illinois at Urbana-Champaign, Department of Electrical and Computer Engineering, Beckman Institute of Advanced Science and Technology, 405 N. Mathews Av., Urbana, IL USA;

Introduction

Dynamic imaging with good spatial and temporal resolution can provide a valuable diagnostic tool for various clinical applications. Several fast imaging techniques have been proposed to improve temporal resolution, notably Echo-Planar Imaging (EPI) and recently SMASH (SiMultaneous Acquisition of Spatial Harmonics) [3]. Reduced-encoding techniques like Keyhole [1] have also been used for further improvement in temporal resolution. In this paper, we propose a new reduced-encoding scheme using temporal modeling to generate MR movies of the beating heart with good spatial and temporal resolution. No assumption is made about periodicity or quasi-periodicity of cardiac motion. Simulation results demonstrate that the method can reconstruct high-resolution movies with sparsely sampled ($\boldsymbol{k},t$) space data.

Methods

The proposed technique is based on the concept of temporal modeling [2]. Specifically, we represent the time-varying image function I(x,t) in terms of the following generalized series:

$$I(\boldsymbol{x},t) = \sum_i c_i(\boldsymbol{x})\varphi_i(t) \qquad (1)$$

where $c_i(\boldsymbol{x})$ is the amplitude parameter corresponding to the basis function $\varphi_i(t)$. If we consider the intensity of every pixel to vary in time independently of others, we need as many basis functions as there are pixels in the high-resolution image. However, in most practical situations, we can partition the dynamic image into several independent motion regions or "*moxels*" such that intra-moxel dynamic information is fairly "homogenous". This means it is sufficient to represent the image dynamics by as many basis functions as the number of independent motion regions. This significantly reduces the number of model coefficients needed and hence the number of encodings to estimate them. More specifically, we can express $I(\boldsymbol{x},t)$ as:

$$I(\boldsymbol{x},t) = \sum_{i=1}^{N} c_i(\boldsymbol{x})\varphi_i(t) \qquad (2)$$

where N is the number of moxels in the image, which is usually much smaller than the total number of pixels. Taking the spatial Fourier transform yields:

$$S(\boldsymbol{k},t) = \sum_{i=1}^{N} \alpha_i(\boldsymbol{k})\varphi_i(t) \qquad (3)$$

To use this model for dynamic imaging we need to collect sufficient data to determine both the basis functions and time series coefficients. A representative ($\boldsymbol{k},t$) space coverage scheme is shown in Fig 1.

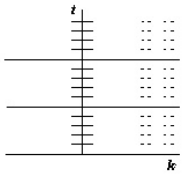

Fig 1. ($\boldsymbol{k},t$) space coverage of proposed method

The central ($\boldsymbol{k},t$) space is densely sampled to capture most of the contrast dynamics. Additional data at the higher spatial frequencies are collected with high temporal resolution to provide more information on the object motion [2].

The basis functions $\{\varphi_i(t)\}$ are derived from the set of signals$\{S(\boldsymbol{k}_i,t)\}$ with high temporal resolution. To do so, we apply principal component analysis (PCA) to $\{S(\boldsymbol{k}_i,t)\}$. PCA extracts the eigenvectors which are used as the basis functions $\{\varphi_i(t)\}$ of the model in Equation (3). It is noteworthy that the basis functions need not follow a harmonic model, which means the temporal model can also capture non-periodic motion of the moxels. The amplitude parameters $\alpha_i(\boldsymbol{k})$ can be solved using the following matrix equation:

$$\begin{bmatrix} \phi_1(t_1) & \phi_2(t_1) & \dots & \phi_N(t_1) \\ \phi_1(t_2) & \phi_2(t_2) & \dots & \phi_N(t_2) \\ \vdots & \vdots & \dots & \vdots \\ \phi_1(t_M) & \phi_2(t_M) & \dots & \phi_N(t_M) \end{bmatrix} \begin{bmatrix} \alpha_1(\boldsymbol{k}) \\ \alpha_2(\boldsymbol{k}) \\ \vdots \\ \alpha_N(\boldsymbol{k}) \end{bmatrix} = \begin{bmatrix} S(\boldsymbol{k},t_1) \\ S(\boldsymbol{k},t_2) \\ \vdots \\ S(\boldsymbol{k},t_M) \end{bmatrix}$$

where M is the number of sparse data frames. After fitting sparse ($\boldsymbol{k},t$) space data over the set of basis functions to estimate the amplitude parameters $\{\alpha_i(\boldsymbol{k})\}$, at every $\boldsymbol{k}$-space location, the time signal $S(\boldsymbol{k},t)$ can be synthesized using Equation (3). The synthesized data set will have both high spatial and temporal resolution and can be used to generate high resolution movies using the conventional FFT method.

Results and Discussion

A set of representative simulation results from a real cardiac data set (79 frames of 256-by-256 encodings) obtained by SMASH imaging is presented. The SMASH data set is deliberately decimated to only 8 frames while retaining dense data over 8 encodings. PCA is carried out over the dense data and the basis functions corresponding to the five most significant singular values are estimated. Then the sparse data is fitted over the generalized series model and interpolated to synthesize the lost data. Fig 2 shows three different original frames, followed by the constructed frames. Error images for the proposed method are also shown.

(a) ***(b)*** ***(c)***

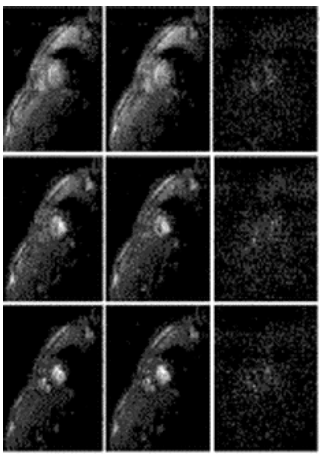

Fig 2. Simulation results for three different frames: *(a): original, (b): reconstructed, (c): error*

The proposed method increases the temporal resolution by a factor of R where R is the relative sampling ratio between the dense and sparse data in ($\boldsymbol{k},t$) space. Based on our simulation studies, a factor of 4 to 10 improvement can be obtained with minimal image errors.

Conclusion

A novel temporal modeling approach has been proposed to improve temporal resolution of cardiac imaging. The proposed technique makes no assumption about the nature of cardiac motion and can handle intra and inter-plane motion. It can be used in combination with any existing fast imaging technique to provide real-time cardiac imaging.

References

[1]Van Vaals et al., Proc. 10th SMRI,44,1992.
[2]Liang et al., Int' J Imaging Syst Techn., 8:551-557 (1997).
[3]Sodickson et al., MRM 38:591-603 (1997).

ISMRM, 2002.

Theory and experimental verification of transmit SENSE

Ulrich Katscher[1], Peter Börnert[1], Christoph Leussler[1], Johan van den Brink[2]
[1]Philips Research Hamburg, Roentgenstrasse 24-26, D-22335 Hamburg, Germany;
[2]Philips Medical Systems, Prof. Holstlaan 6, 5656 AA Eindhoven, The Netherlands

The ideas of parallel imaging techniques, designed to shorten the acquisition time by the simultaneous use of multiple receive coils, can be adapted for parallel transmission of spatially selective multi-dimensional RF pulses. In analogy to data acquisition, a multi-dimensional RF pulse follows a certain trajectory in k-space. Shortening this trajectory shortens the pulse duration. The use of multiple transmit coils, each with its own time-dependent waveform and spatial sensitivity, compensates for the missing parts of k-space. This results in a maintained spatial definition of the pulse profile while its duration is reduced.

Introduction

Multi-dimensional spatially selective RF pulses [1,2] have found a large number of useful applications in magnetic resonance imaging (MRI) [3,4]. The basic idea of a spatially selective RF pulse is the simultaneous application of RF energy in presence of an appropriate gradient waveform. A shortening of these RF pulses without losing spatial resolution (e.g., to overcome T_2^* - problems for 3D spatially selective RF pulses) would be very desirable. Fortunately, the MR physics of RF pulses show strong similarities to the principles underlying MR imaging. Recent developments of parallel imaging [5,6] aim at reducing the total measuring times in MR imaging applications. In analogy to these principles, this work describes the shortening of the k-space trajectory of multi-dimensional RF pulses ("transmit SENSE"). This is achieved by using a number of different transmit coils, each transmitting a different RF waveform, to compensate for the lack of k-space coverage.

Theory

Let R be the number of transmit coils with known, arbitrary but different sensitivity profiles $S_r(\mathbf{x})$, $r=1 \ldots R$, and the corresponding unknown individual pulse profiles $P_r(\mathbf{x})$ within the excitation FOV. The superposition of all the individual pulse profiles should yield the desired pulse profile $P_{des}(\mathbf{x})$

$$P_{des}(\mathbf{x}) = \sum_{r=1}^{R} S_r(\mathbf{x}) P_r(\mathbf{x}) \quad . \tag{1}$$

Transforming into k-space, Eq. (1) gives

$$p_{des}(\mathbf{k}) = \sum_{r=1}^{R} s_r(\mathbf{k}) \otimes p_r(\mathbf{k}) \quad . \tag{2}$$

Discretizing the k-space, the integral in Eq. (2) can be expressed by a matrix/vector multiplication

$$\mathbf{p}_{des}(\mathbf{k}) = \sum_{r=1}^{R} \mathbf{s}_r(\mathbf{k}-\mathbf{k}')\,\mathbf{p}_r(\mathbf{k}') \quad . \tag{3}$$

Assuming that the pulse profiles are defined on a NxN matrix in the spatial domain, $\mathbf{p}_{des}$ and $\mathbf{p}_r$ are vectors with $N^2 = M$ components. The matrices $\mathbf{s}_r$ have the size MxM . Now the special case of an R-fold reduction of the transmit duration is introduced. This reduction takes place by reducing the k-space trajectory $\mathbf{k}'$. Thus, the $\mathbf{p}_r$ become vectors with M/R components, the size of the rectangular matrices $\mathbf{s}_r$ is Mx(M/R). The reduced-sized variables $\mathbf{p}_r$ and $\mathbf{s}_r$ can be combined to single full-size variables $\mathbf{p}_{full}$ and $\mathbf{s}_{full}$ introducing $\mathbf{k}''$ containing R times the trajectory k'. Thus, Eq. (3) can be rewritten without the sum over the coils

$$\mathbf{p}_{des}(\mathbf{k}) = \mathbf{s}_{full}(\mathbf{k}-\mathbf{k}'')\,\mathbf{p}_{full}(\mathbf{k}'') \quad . \tag{4}$$

The unknown $\mathbf{p}_{full}$ can now be calculated by a straight-forward matrix inversion or with the help of regularization techniques. Afterwards, the pulse profiles for the individual transmit coils $\mathbf{p}_r$ have to be extracted from $\mathbf{p}_{full}$. The final waveforms $\mathbf{B}_{1,r}(t)$ can be deduced from $\mathbf{p}_r(\mathbf{k}')$ according to ref. [1].

Methods

Simulations have been performed using different coil sensitivities and pulse profiles $P_{des}(\mathbf{x})$. Additionally, initial experiments have been performed on a Philips Gyroscan NT15 to confirm the outlined theory. Due to the lack of two different simultaneously active transmit channels a switchable loop that couples to the body coil was mounted on a phantom. This loop can be opened and closed by an external trigger to change the corresponding transmit sensitivities in two successively performed single experiments. The corresponding two sensitivities were measured and served as input for the calculation of two different $\mathbf{B}_{1,r}$ waveforms for an undersampled spiral k-space trajectory k' (8 revolutions, 512 points) and a circular, homogeneous pulse profile $P_{des}(\mathbf{x})$ defined on a 32x32 matrix. Two experiments were performed at different transmit coil sensitivities using the different waveforms successively to image the excitation profiles. The pulse duration of these waveforms was half as long as the duration of a waveform, which would excite the same pattern without transmit SENSE. The images were added afterwards to mimic a simultaneous excitation.

Results

The numerical simulations show a good agreement between the desired pulse profile $P_{des}(\mathbf{x})$ and the combined images of the pulse profiles of the individual coils. Fig. 1 shows the example of a circular, homogeneous pulse profile $P_{des}(\mathbf{x})$ for an undersampled spiral k-space trajectory k' and hyperbolic coil sensitivities. Besides small oscillations, all undersampling artifacts of the pulse profiles of the individual coils (Fig. 1a/b) cancel by combining them to the final image (Fig. 1c).

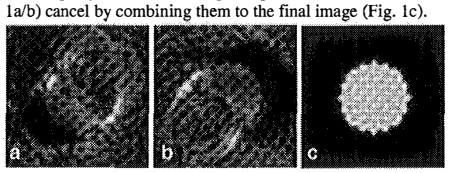

Fig.1: Numerical results. a/b: Pulse profile of first/second reduced waveform. c: Adding the pulse profiles of the reduced waveforms yields the desired pulse profile.

Fig. 2a/b shows the images of the two experiments and the sum of the two images (Fig. 2c). Inside the pulse profile, the combined image has the desired constant shaped, while the shape in the single coil images is convex and concave, respectively. Outside the phantom, however, some spiral undersampling artifacts remain. This may be explained by the fact that the measured different sensitivities are close to linear dependency.

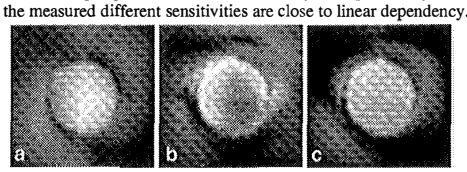

Fig.2: Initial experimental results. a/b: Pulse profile of first/second reduced waveform. c: Adding the pulse profiles of the reduced waveforms yields the desired pulse profile. The inadequate coil sensitivities lead to remaining subsampling artifacts

Conclusion

The presented approach describes the feasibility of transmit SENSE, that shows the potential of shortening multi-dimensional RF pulses using multiple transmit coils. Instead of shortening the RF pulse, one could also improve the spatial resolution of the pulse profile. Furthermore, a reduction factor lower than the number of coils can be used, as in parallel imaging. The ability of transmit SENSE to shorten multi-dimensional RF pulses could be very interesting to make 3D RF pulses feasible even in case of fast T_2^* relaxing species or strong main field in homogeneities.

Acknowledgments

We thank Miha Fuderer, Julius Cohen, and Kay Nehrke for valuable discussions.

References

1. Pauly J et al., *J. Magn. Reson.* 81: 43, 1989.
2. Hardy CJ et al., *J. Magn. Reson.* 82: 647, 1989.
3. Yang GZ et al., *MRM* 39: 833, 1998.
4. T. S. Sachs TS et al., *MRM* 32: 639, 1994.
5. Sodickson DK et al., *MRM* 38: 591, 1997.
6. Pruessmann KP et al., *MRM* 42: 952, 1999.

ISMRM, 2002.

Detection of pH Effects in the Water Signal through Selective Saturation Transfer via Exchangeable Amide Protons of Mobile Intracellular Proteins; *P*rotein *P*roton *T*ransfer *I*maging (*PPTI*).

Jinyuan Zhou,[+*] Jean-Francois Payen,[+%] David A. Wilson,[#] Richard J. Traystman,[#] Peter C. M. van Zijl[+*]

Departments of [+]Radiology and [#]Anesthesiology, Johns Hopkins University Medical School, Baltimore, Maryland.
[*]F.M. Kirby Research Center for Functional Brain Imaging, Kennedy Krieger Institute, Baltimore, Maryland.
[%]Department of Anesthesiology, The Grenoble University School of Medicine, 38000, Grenoble, France.

ABSTRACT

We demonstrate the possibility to selectively detect transfer of saturated exchangeable amide protons from mobile intracellular proteins to water. A procedure is given to separate this protein proton transfer (PPT) effect from BOLD and conventional MT effects. To demonstrate the principle, PPT spectra in the rat brain (n = 15) were measured *in vivo* and postmortem. Exchange rates of the amide protons were measured using proton exchange spectroscopy and pH was quantified using phosphorus spectroscopy. The PPT effect during this physiological change was on the order of 1-2%. This proton transfer procedure should be useful to image pH effects and intracellular protein content *in vivo*.

INTRODUCTION

Presently there are no MR imaging methods to spatially assess differences in pH and protein content via the water signal. However, it was recently demonstrated by Mori et al. (1) that the exchangeable protons visible around 8.3 ± 0.5 ppm in the proton spectra of brain and cancer cells are sensitive to pH changes, in line with knowledge from high-resolution NMR protein studies (2,3). We recently assigned this resonance to the combined amide proton signals of intracellular proteins (4) using selective inversion transfer from water to these protons (5). Using small molecules in solution, Ward et al. (6) recently demonstrated that the inverse process of saturation transfer from exchangeable protons to water can be used for sensitivity enhancement. Especially large effects have been demonstrated for amide protons (7), which have a favorable exchange rate range (10-100 s^{-1}) under physiological conditions. We hypothesized that it should be possible to detect the intracellular amide protons via this process, which should depend on endogenous protein concentration and amide proton exchange rate, and thus pH.

MATERIALS AND METHODS

Sprague-Dawley rats (350-500 g) were anaesthetised using pentabarbital (i.v.) and mechanically ventilated. Experiments were performed on a horizontal bore 4.7 T GE CSI animal imager (40 cm bore). A proton surface coil (inner diameter 3 cm) was used for RF transmission and reception. For the phosphorus experiments a double-tuned (31P/1H) coil was used. In the MT experiments, a train of 400 Gaussian pulses (duration 6.6 msec, delay 3.4 msec, total duration 4 sec) was used for off-resonance irradiation. Each single pulse within the Gaussian pulse train has a flip angle of 180°, corresponding to an average RF power of about 50 Hz. Two- or four-shot spin-echo EPI with TE = 50 ms was used for data acquisition. The imaging matrix was 64×64, FOV was 40×40 mm^2, and the imaging slice thickness was 2 mm. The raw data set was corrected for spatial magnetic field inhomogeneity on a pixel by pixel basis. Five ROIs covering the whole brain were chosen for quantitative analysis. WEX (water-exchange-filter) spectroscopy (5) was used to measure the exchange rates of the amide protons. All MRI and MRS experiments were performed both in vivo and after cardiac arrest.

RESULTS & DISCUSSION

Standard MT-ratio (normalized with respect to unsaturated) spectra *in vivo* (solid) and postmortem (dashed) are shown in Fig. 1a. The difference in these curves is due to the BOLD effect, changes in the shape of the direct saturation curve and potential MT changes. To selectively assess only the PPT effect, we performed an asymmetry analysis by subtracting MT ratios obtained at the negative offset minus those at the corresponding positive offset. The resulting curves are shown in the bottom-left corner. Fig. 1b shows a close-up of the results of subtracting the *in vivo* difference spectrum from the postmortem difference spectrum.

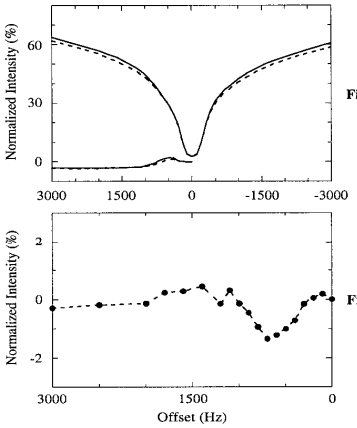

Fig. 1a

Fig. 1b

The maximum change in the difference signal intensities is found at 700 Hz from water. Using 4.75 ppm for water, this corresponds closely to the broad amide proton frequency (8.25 ppm), supporting our hypothesis. Using WEX spectroscopy (5), the exchange rates of the amide protons in the proton spectra were found to be 23.9 ± 5.3 sec^{-1} *in vivo* and 12.5 ± 2.3 sec^{-1} postmortem (n = 5). The total protein signal as determined from integration of the amide peak after complete inversion transfer in the WEX spectra did not change significantly.

The intracellular pII values determined using 31P spectra were 7.15 ± 0.09 and 6.65 ± 0.10 in vivo and postmortem, resp. This is in good agreement with literature data on rat brain ischemia (8) showing an *in vivo* pH_i of 7.05 under normal conditions and pH_i = 6.44 during prolonged ischemia, where continued lactate formation may cause lower pH than in postmortem tissue. Decreased pH in the brain accompanied the decreased exchange rates for the amide protons (23.9 to 12.5 sec^{-1}), resulting in a decreased off-resonance saturation transfer from the exchangeable protons. As a result, the imaging signal intensities (water MR signals) increased at the side of the positive offsets, and the asymmetry difference spectrum decreased for the postmortem brain. The experimental results are in a good agreement with the theoretical prediction.

In conclusion, off-resonance saturation transfer via amide proton exchange can be used to detect pH effects in the brain. The results of further quantitative PPT analysis should provide an approach to image pH effects *in vivo*.

REFERENCES

1) Mori et al., MRM 40 (1998) 36: 2) Liepinsh et al., MRM 35 (1996) 30; 3) Mori et al., JACS, 119 (1997) 6844; 4) van Zijl et al., MRM, under revision; 5) Mori et al., JMR. B 110 (1996) 96; 6) Ward et al., JMR 143(2000) 79. 7). Goffeney et al., JACS 123(2001)8628. 8) Kintner et al., J Neurochem 72(1999)405.

We acknowledge Dr. V.P. Chacko for building the double-tuned 31P/1H coil. Supported by NIH grant RO1 NS31490.

ISMRM, 2003.

Mechanisms of Indomethacin-Induced Alterations in Choline Phospholipid Metabolism of Non-malignant versus Malignant Human Mammary Epithelial Cells

K. Glunde[1], V. Chacko[1], Z. Bhujwalla[1]

[1]Johns Hopkins University School of Medicine, Baltimore, Maryland, United States

Abstract

Distinct differences characterize the choline metabolite profile of malignant human mammary epithelial cells (HMECs) compared to normal HMECs. Treatment with the non-steroidal anti-inflammatory agent indomethacin changes this profile toward a pattern more typical of non-malignant HMECs. Metabolites produced from [1,2-^{13}C]-choline using ^{1}H and ^{13}C NMR spectroscopy, and gene expression levels using microarray technology were analyzed following indomethacin treatment of breast cancer cells. Indomethacin induced diverse changes at the gene expression level. Enzymes involved in choline metabolism were not affected at the transcriptional level. Changes in choline phospholipid metabolites following indomethacin treatment were most likely due to increased membrane turnover.

Introduction

Breast carcinogenesis is accompanied by increasing phosphocholine (PC) and decreasing glycerophosphocholine (GPC) levels [1]. Indomethacin, a non-steroidal anti-inflammatory agent and non-specific cyclooxygenase (COX) inhibitor, has been shown to change this profile toward a pattern more typical of non-malignant HMECs [2]. Indomethacin also reduced the invasive and metastatic behaviour of human breast cancer cells, and decreased tumor angiogenesis and growth [3]. To understand mechanisms underlying the increase of GPC relative to PC following treatment with indomethacin in HMECs, we performed ^{1}H and ^{13}C NMR spectroscopy of cells labeled with [1,2-^{13}C]-choline and as well microarray-based gene expression analysis of breast cancer cells treated with indomethacin. The non-malignant human mammary epithelial cell line MCF-12A was compared with the human breast cancer cell lines MCF-7 and MDA-MB-231. Long-term and short-term incubation with [1,2-^{13}C]-choline was performed to distinguish between anabolic and catabolic pathways of choline metabolism.

Methods

For long-term experiments, cells were exposed to fresh cell culture medium containing 100 µM [1,2-^{13}C]-choline for 24 h to build up a labeled phosphatidylcholine (PtdCho) pool. For short-term experiments, fresh medium without labeled choline was added. Then, cells were incubated with 300 µM indomethacin in medium containing 100 µM [1,2-^{13}C]-choline for 3 h. Lipid and water-soluble cell extract fractions were obtained using a dual-phase extraction method [4]. The samples were dissolved in deuterated solvents. Composite pulse ^{1}H-decoupled ^{13}C NMR spectra and fully relaxed ^{1}H NMR spectra of the water-soluble metabolites and the lipids were measured on a 500 MHz MSL Bruker spectrometer. ^{13}C NMR spectra were corrected for saturation and NOE effects. Total RNA was isolated from MDA-MB-231 cells following 2 h indomethacin treatment. Microarray analysis was perfomed with the Human Genome U133 GeneChip Set containing 39,000 transcripts.

Results

^{13}C and ^{1}H NMR spectra of the water-soluble fractions demonstrated that both breast cancer cell lines, MCF-7 and MDA-MB-231, accumulated high PC levels, depleting most of the free intracellular choline (Cho) (Figure 1) whereas normal HMECs contained similar amounts of PC and free choline (Figure 1). The ^{13}C-enrichment in PC was significantly higher in long-term compared to short-term [1,2-^{13}C]-choline exposure in the breast cancer cells, but not in non-malignant cells. During long-term [1,2-^{13}C]-choline exposure, all HMEC lines built up fractional ^{13}C-enrichment in the PtdCho pool, as calculated from ^{13}C NMR spectra of the lipid fractions. Short-term exposure resulted in no detectable ^{13}C-enrichment in the PtdCho pool. Treatment with 300 µM indomethacin for 3 h caused a significantly decreased [PC]/[GPC] ratio in all three HMEC lines as observed in ^{1}H NMR spectra of long-term as well as short-term experiments. The ^{13}C-enrichment in the PC pool remained relatively constant during indomethacin treatment compared to control in the long-term experiments whereas it decreased in the short-term experiments. Indomethacin treatment also resulted in increased free choline levels in the breast cancer cell lines which was not detected in non-malignant HMECs. Results of the microarray analysis of gene expression after 2 h treatment with indomethacin revealed that 86 cDNA/genes, such as transcription factors, differentiation factors, cytokines, and transporters were least twofold over- or underexpressed after 2 h of indomethacin treatment. Twofold or higher changes were not detected in the messenger RNA expression levels of genes/proteins directly involved in choline phospholipid metabolism.

Figure: Representative ^{13}C (a) and ^{1}H (b) NMR spectra of the water-soluble fractions of non-malignant HMECs (MCF-12A: lower panel) compared to human breast cancer cells (MCF-7: central panel, MDA-MB-231: upper panel) after long-term exposure (24+3h) to [1,2-^{13}C]-choline

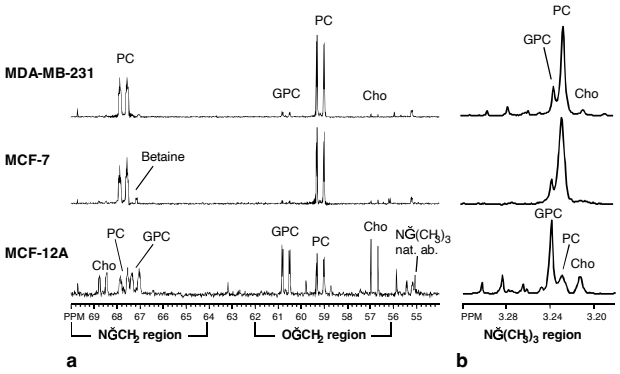

Discussion

The depletion of free choline and the appearance of PC in MCF-7 and MDA-MB-231 cells support previous observations [5] that breast cancer cells exhibit a higher rate of choline phosphorylation by choline kinase compared to normal HMECs (Figure 1). The reduction of the fractional ^{13}C-enrichment of the PC pool in the short-term experiments in malignant HMECS may be due to a higher phospholipase D or C activity in these cancer cells.

Treatment with indomethacin resulted in a decreased [PC]/[GPC] ratios in both normal and malignant HMECs as reported previously [2]. Free choline that most likely originated from catabolic processes increased after indomethacin treatment in the breast cancer cells but not in the non-malignant HMECs. The decrease in total PC and the absence of free choline in the short-term ^{13}C NMR spectra suggest that indomethacin also upregulated the anabolic pathway.

The microarray-based gene expression analysis revealed that mRNA for none of the enzymes that are directly involved in choline phospholipid metabolism were over- or underexpressed by twofold or higher at the gene expression level. Changes in choline phospholipid metabolites most likely occurred from changes in enzyme activity rather than enzyme expression. However, twofold or higher over- or underexpression was detected in 86 cDNAs/genes after 2 h of indomethacin treatment of MDA-MD-231 human breast cancer cells suggesting that indomethacin causes diverse changes at the transcriptional level.

References

[1] Aboagye EO and Bhujwalla ZM, *Cancer Res* **59**, 80 (1999) [2] Natarajan K *et al*, *Advan Enzyme Regul* **40**, 271 (2000) [3] Reich R *et al*, *Prostaglandins* **51**, 1 (1996) [4] Tyagi RK *et al*, *MRM* **35**, 194 (1996) [5] Katz-Brull R and Degani H, *Anticancer Res* **16**, 1375 (1996) This work was supported by NIH 1R01 CA82337. We thank Dr. Francisco Martinez Murillo, Dr. Venu Raman, and Dr. Ioannis Stasinopoulos for expert technical assistance in performing the microarray data analysis and Mr. Gary Cromwell for maintaining the cell lines.

ISMRM, 2003.

Vascular-Space-Occupancy (VASO) Dependent fMRI

H. Lu[1], X. Golay[1], J. Pekar[1], P. van Zijl[1]

[1]Dept of Radiology, Johns Hopkins University & F.M. Kirby Research Center, Kennedy Krieger Institute, Baltimore, MD 21205, United States

ABSTRACT: We introduce a new fMRI methodology that maps blood volume changes during brain activation, without need for exogenous contrast agents. Vascular water is selectively labeled by nulling its signal independent of inflow and oxygenation. During visual activation, these vascular-space-occupancy (VASO) dependent fMRI signal changes show a negative cross-correlation with the stimulus paradigm, consistent with increased blood volume and reduced tissue volume in the parenchyma. We derive the theory describing the effect, characterize its spatial characteristics and hemodynamic response, and compare it to the BOLD effect and to a blood flow based method. Results show high spatial and temporal specificity.

INTRODUCTION: Most fMRI studies employ BOLD contrast. However, blood oxygenation changes not only influence MRI signals in and around microvessels close to the activation site, but also in and around veins draining from it. To improve the spatial specificity of fMRI, it would be helpful to have contrast that only reflects microvascular expansion or contraction. To accomplish such VAscular Space Occupancy (VASO) dependent contrast, we designed a labeling technique in which the blood-water signal is nulled independent of inflow (spatially non-selective inversion) and oxygenation. Here we demonstrate the feasibility of VASO-fMRI for visual stimulation, and compare performance with BOLD-fMRI and pulsed arterial spin labeling (TILT; (1))

THEORY: The vascular space occupancy of a microvessel *i* (*i = arteriole, capillary or venule)*, ξ_i , is its cerebral blood volume (CBV) fraction in the parenchyma: $\xi_i = CBV_i/V_{par} = CBV_i/(V_{tissue} + \Sigma CBV_j)$, in which V_{par} is parenchymal volume. For optimum blood nulling for the particular field strength (T_{1blood} = 1400 ms; $T_{1tissue}$(gray matter) = 1000 ms at 1.5T), and gradient echo detection at the shortest TE to minimize extravascular BOLD effects, the VASO signal change is: $\Delta S/S = (\xi^{rest} - \xi^{act})/(1-\xi^{rest})$.

METHODS: A 1.5T Philips scanner with body transmit and quadrature head receive was used. Nominal resolutions were 2x2x5 mm^3 for high-resolution fMRI (Fig. 1) and 3.75x3.75x5 mm^3 for measuring hemodynamic responses (Fig. 2). For the latter, TR = 2s, TI = 665 ms (time after adiabatic inversion), TE = 10 ms, FA = 90, GRE-EPI detection, 146 images per fMRI scan. Subjects (n = 8) gave consent. Blue-yellow checkerboard stimulation (8 Hz, 25° angle, 30s) with 50s recovery; 3 trials per experiment and 30s extra rest to get used to scanner noise at the beginning. Data processing: 5 mm Gaussian filter, AIR re-alignment, box-car correlation threshold +/- 0.18 (0.18 for BOLD, TILT; -0.18 for VASO), 3-voxel cluster, $p < 0.005$.

RESULTS and DISCUSSION: Fig. 1 shows a high-resolution VASO image. The activation localizes well within gray matter. The hemodynamic response is negative, corresponding to vasodilation. The magnitude of the signal changes was in agreement with simulations using the above model. Fig. 2 compares the hemodynamic responses of VASO (CBV-based), BOLD (oxygenation-based) and TILT (blood flow based). VASO and TILT signals start to increase before BOLD, while the VASO signal returns to baseline at a slower rate than TILT. BOLD returns to baseline at the same speed as TILT but continues with a post-stimulus undershoot, which has been explained by delayed compliance of venous vessels (2, 3). These data indicate a temporal resolution of VASO that is at par with flow changes and faster than BOLD. When comparing voxels, BOLD had the highest number, but the hemodynamic expect VASO to become a useful tool for fMRI and blood volume imaging.

REFERENCES:

1. Golay et al. JMRI 9: 454-461 1999. 2. Buxton et al. MRM 39: 855-864 1998. 3. Mandeville et al. JCBFM 19: 679-689 1999

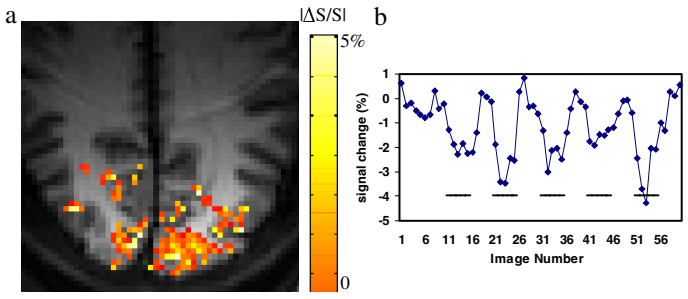

Fig. 1: High-resolution VASO-fMRI (visual stimulation, 5 blocks) and temporal evolution of signal changes. Due to the inversion preparation, VASO has high tissue contrast (white matter bright, blood spaces dark, gray matter is gray).

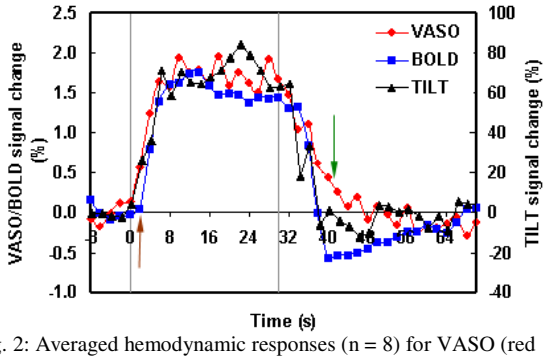

Fig. 2: Averaged hemodynamic responses (n = 8) for VASO (red diamonds), BOLD (blue squares), and TILT (black triangles). VASO signal time-course was flipped in sign for easier comparison with the positive signal changes of TILT and BOLD.

ISMRM, 2003.

Quantifying Non-Gaussian Water Diffusion by Means of Pulsed-Field-Gradient MRI

J. H. Jensen[1], J. A. Helpern[1]
[1]New York University School of Medicine, New York, New York, United States

SYNOPSIS

The extent to which water transport in a tissue deviates from homogeneous, Gaussian diffusion can be quantified by a dimensionless statistical measure referred to as the excess kurtosis. By using pulsed-field-gradient spin echo MRI data acquired with large diffusion sensitizing gradients, we show how to estimate the excess kurtosis. In particular, the excess kurtosis can be approximately determined from the lower order terms of an expansion in the gradient strength of the logarithm of the signal intensity. This result is applied to estimate the excess kurtosis in healthy adult and newborn human brain and ischemic rat brain tissue.

INTRODUCTION

When water diffusion in a tissue is homogeneous and Gaussian, then the logarithm of the signal intensity obtained with a conventional diffusion-weighted imaging sequence depends linearly on the square of the strength of the diffusion sensitizing gradients. However, substantial departures from linearity are observed in the brain when large gradients are applied (1-3), suggesting a deviation from simple Gaussian diffusion. This deviation can be quantified with a standard, dimensionless statistical measure called the excess kurtosis (4,5). For Gaussian diffusion, the excess kurtosis vanishes. If the excess kurtosis is negative, the distribution of diffusion paths is more sharply peaked than for Gaussian diffusion, while a positive excess kurtosis indicates that the distribution is less sharply peaked. The excess kurtosis can be estimated from an expansion of the logarithm of the signal intensity in powers of the gradient strength. The excess kurtosis is therefore an experimentally measurable parameter that can be used to quantitatively characterize non-Gaussian water diffusion in tissues.

THEORY

For diffusion in one dimension, the excess kurtosis over a time interval t is defined by

$$K(t) = \{\langle [x(t) - x(0)]^4 \rangle / \langle [x(t) - x(0)]^2 \rangle^2\} - 3 \qquad [1]$$

where the angle brackets indicate an averaging over all the diffusion paths $x(t)$. Now consider a conventional pulsed-field-gradient spin echo sequence used for diffusion-weighted imaging (1-3). The logarithm of the signal intensity S has the expansion

$$\ln[S(b)] = \ln[S(0)] - bD_{app} + (1/6)\, b^2 (D_{app})^2 K_{app} + O(b^3) \qquad [2]$$

with $b = (\gamma\delta g)^2 (\Delta - \delta/3)$. Here g is the gradient strength, γ is the proton gyromagnetic ratio, Δ is the time interval between the centers of the diffusion sensitizing gradient pulses, and δ is the duration of each pulse. In carrying out this expansion, Δ and δ are assumed to be fixed. Equation [2] defines the apparent diffusion coefficient D_{app} and the apparent excess kurtosis K_{app}.

If confounding effects, such as inhomogeneous T_2 relaxation, are negligible, then one can demonstrate that $K_{app}(\Delta,\delta) = K(\Delta) + O(\delta)$, where K is the excess kurtosis in the direction of the diffusion gradients. This shows that K_{app} approaches the true excess kurtosis as δ goes to zero. In practice, K_{app} obtained with a small value of δ/Δ provides a good approximation for K. The dependence of K_{app} on the gradient orientation can be described by a tensor with 15 independent components.

RESULTS

By applying Eq. [2] to published data (1-3), the excess kurtosis can be estimated for various types of brain tissue (Table 1). These results indicate that water diffusion is less Gaussian in white matter (WM) than gray matter (GM), less Gaussian in adult brain than in newborn brain, and less Gaussian in ischemic brain than in normal brain. The large magnitudes of the variations suggest profound differences in tissue structure. Properties that affect the excess kurtosis include cell membrane permeabilities and intracellular water diffusion coefficients.

Table 1

	Apparent Excess Kurtosis in the Brain					
Reference	Adult GM	Adult WM	Newborn GM	Newborn WM	Normal Rat	Ischemic Rat
1					0.53 ± 0.05	1.42 ± 0.10
2	0.66 ± 0.28	1.03 ± 0.27				
3	0.78 ± 0.12	1.42 ± 0.11	0.29 ± 0.09	0.34 ± 0.09		

REFERENCES

1. Pfeuffer J, Provencher SW, Gruetter R. *MAGMA;* **8**:98-108 (1999).
2. Clark CA, Le Bihan D. *Magn Reson Med;* **44**:852-859 (2000).
3. Mulkern RV, Vajapeyam S, Robertson RL, Caruso PA, Rivkin MJ, Maier SE. *Magn Reson Imaging;* **19**:659-668 (2001).
4. *CRC Standard Math Tables, 25th Edition.* Beyer WH, ed. (West Palm Beach, FL: CRC Press, 1978) p 508.
5. Press WH, Teukolsky SA, Vetterling WT, Flannery BP. *Numerical Recipes in C: The Art of Scientific Computing.* (New York: Cambridge University Press, 1992) p 612.

ISMRM, 2004.

MR Elastography of in vivo Human Liver

M. Dresner[1], J. Fidler[1], R. Ehman[1]
[1]Mayo Clinic, Rochester, MN, United States

Introduction: Previous studies of ex vivo specimens have established that fibrosis is associated with increased liver stiffness (1). MR Elastography (MRE), an emerging technique for quantitating tissue mechanical properties, is applied to in vivo human liver to determine the feasibility of measuring liver stiffness in vivo. MRE experiments commonly experience signal loss artifacts near electromechanical drivers, which have limited adequate data acquisition for some applications, motivating consideration of novel vibration sources. To provide the necessary control over the relative phase between vibration and motion sensitization, pulse sequence triggers of wave generation have been used, but these enforce longer scan TRs for low-frequency acquisitions. The challenges of this work were to accomplish liver MRE within a breathold utilizing a novel displacement source in order to limit motion and driver artifacts.

Methods: MR Elastography techniques described previously (2-3) were adapted for this study to assess an organ that requires breathold scans and is protected from direct shear by the ribcage. MRE experiments were performed in five healthy volunteers (age 23-45, three males, two females) after obtaining informed consent. Shear displacements were generated by the top surface of a passive speaker connected by plastic tubing to a 30 cm diameter audio speaker generating 50-100 Hz acoustic vibrations. The active speaker, located 3 meters from the magnet bore, was enclosed in stiff plastic to channel the pressure variations into the tube. The passive speaker was placed on a ramp which aims the vibrations at the liver while allowing the speaker to be positioned below the ribcage (Figure 1a) for greater volunteer comfort. While triggered-wave experiments allowing adequate wave travel time to reach the liver would have required a TR of 100 msec or more, the TR can be set to an integer multiple of the wave period if the speaker operates continuously for the duration of each image acquisition. This continuous mode of operation was used with TRs of 40 and 25 msec for frequencies of 50 and 80 Hz, respectively, for breathold times of 7-10 seconds per offset. A fixed gap of five seconds between offset acquisitions was implemented for the volunteer to reestablish end-inspiration breathold. Eight phase offsets were acquired for each volunteer using 1 period of motion-sensitizing gradient and a matrix size of 256 x 64, an FOV of 24-32 cm and 10 mm thick sagittal sections. T2-weighted FSE images were collected at the same section locations to provide anatomy information to complement the elastograms. The wave images were processed with the Local Frequency Estimator and also by manual estimation of wavelength from image profiles. The LFE shear stiffness estimates were thresholded on the basis of displacement SNR so that only areas of adequate wave penetration are visible.

Results: No artifacts were detected in the vicinity of the displacement source using a gradient echo acquisition. Images acquired during 8-10 second breatholds were acceptably free of motion artifacts. Displacement images at 80 Hz showed only 1-2 cm of penetration into the liver before attenuation to noise levels in the livers of 5 healthy volunteers. Anatomical and 50 Hz displacement images are displayed in Figure 1 for a 45 year old healthy male volunteer. The stiffness estimates were performed manually from line profiles in the direction of wave propagation, although good agreement was observed with SNR-thresholded LFE estimates. The average over the volunteers was 1.93 ± 0.23 kPa at 50 Hz; 80 Hz stiffness estimates averaged 1.80 ± 0.98 kPa. The displacement amplitude in the image in Figure 1 has a maximum value of 90 microns; no discomfort was reported by the volunteers.

Discussion/Conclusions: The feasibility of in vivo liver MRE has been established. Methodological improvements in displacement generation allowed placement of the wave source immediately adjacent to the tissue of interest, and improved scan timing has reduced subject motion related to long breathold scans. Our results are comparable to previously published liver specimen studies (4-5). MR Elastography has potential for imaging human liver stiffness in vivo.

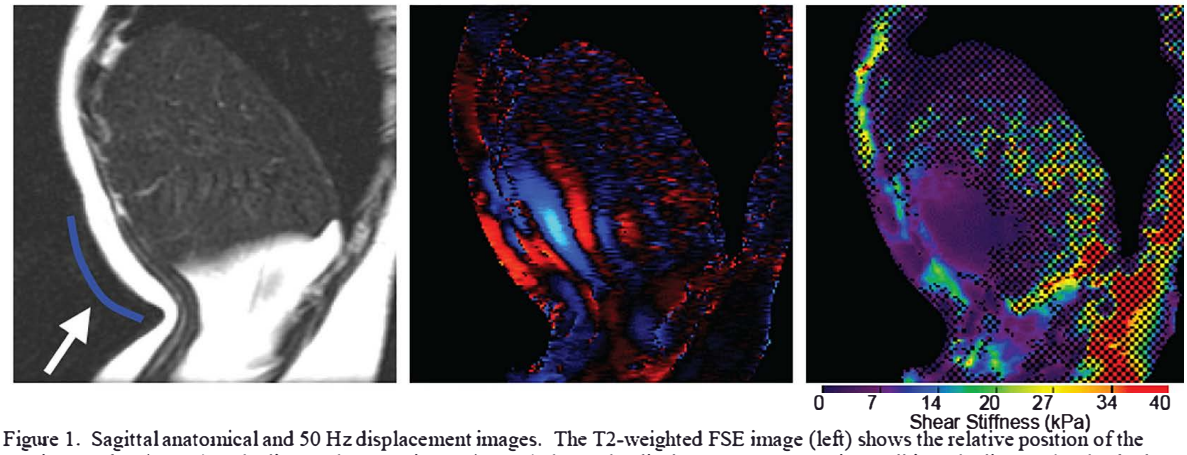

Figure 1. Sagittal anatomical and 50 Hz displacement images. The T2-weighted FSE image (left) shows the relative position of the passive speaker (arrow) to the liver. The wave image (center) shows the displacements propagating well into the liver. The checked areas on the LFE-derived stiffness map (right) represent regions with insufficient displacement SNR for stiffness characterization.

References: 1) Yeh et al., Ultr.Med.Biol., 2002 2) Dresner et al., JMRI, 2001. 3) Muthupillai et al. Science, 1995.
4) Shi et al., Ultr. Imaging, 1999. 5) Kruse et al. Phys. Med. Biol., 2000.

ISMRM, 2005.

Pseudo-continuous Flow Driven Adiabatic Inversion for Arterial Spin Labeling

D. M. Garcia[1,2], C. de Bazelaire[1,3], D. Alsop[1,3]

[1]Radiology, Beth Israel Deaconess Medical Center, Boston, MA, United States, [2]Electrical Engineering and Computer Science, Massachusetts Institute of Technology, Cambridge, MA, United States, [3]Harvard Medical School, Boston, MA, United States

Introduction: Flow driven adiabatic inversion (1) has been used to continuously label arterial blood for arterial spin labeling perfusion and angiography studies. Continuous ASL (2) produces the largest ASL signal change, potentially the greatest SNR, and can be advantageous for other reasons as well. Continuous labeling has drawbacks, however. It requires near continuous wave RF transmit capability that is often not available on imagers. Multi-slice implementations of continuous ASL (3-7) suffer from signal attenuation, velocity sensitivity or imperfect static tissue subtraction or require special hardware and labeling geometries. Here we propose and implement a method for flow driven adiabatic inversion that employs repeated RF pulses rather than continuous RF. This method potentially overcomes a number of the limitations of previous implementations of continuous ASL.

Theory: It has previously been shown that repeated application of RF pulses support a steady state in the absence of T1 and T2 decay (8). Magnetization oriented along this steady state direction at the midpoint between two pulses will return to this orientation after the next pulse. The angle of the steady state is determined by the phase shift experienced during the time between pulses, ϕ, and the flip angle of the RF, α. If the phase shift or phase is slowly varied, such that the change in the steady state angle is slow, then the magnetization tends to follow the steady state solution.

$$M_z = \frac{\pm M_0 \sin\alpha \sin\frac{\phi}{2}}{\sqrt{(1-\cos\alpha)^2 + \sin^2\alpha \sin^2\frac{\phi}{2}}}$$

The z magnetization for the steady state solution is given by the equation to the left and its value is plotted for a 22.5° flip angle, figure 1. Magnetization with near zero phase shift will be in the transverse plane while magnetization with 180° phase shift will be nearly along the z axis. Gradually changing the phase shift from –180° to 180° will cause an inversion. Hence the behavior of this pulsed experiment is very similar to the continuous irradiation used for flow driven adiabatic inversion except that the solution is periodic in ϕ, for the pulsed solution. The periodicity can be eliminated, however, if the RF pulse is sufficiently selective such that the RF is negligible at frequencies corresponding to the other inversion planes.

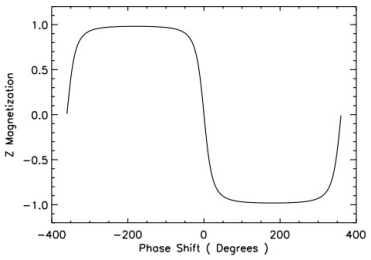

Figure 1: The steady state solution for Mz with repeated pulses as a function of the phase shift between pulses.

Using these concepts one can design a flow driven adiabatic inversion strategy using pulsed RF and gradients. In the pulse sequence of figure 2, selective RF pulses are applied at equal spacing. For the control, we choose to maintain a 180° phase shift for all positions. This is achieved by alternating the sign of the RF from pulse to pulse and assuring there is zero average gradient between each pair of pulses. The control is shown with dashed lines in figure 2 whenever it deviates from the label. For the label, we add some imbalance in the gradients to causes a position dependent phase shift. The average gradient over the time between pulses should be comparable to the value used for continuous flow driven adiabatic inversion and the average B1 over the same time interval should be comparable to the continuous case.

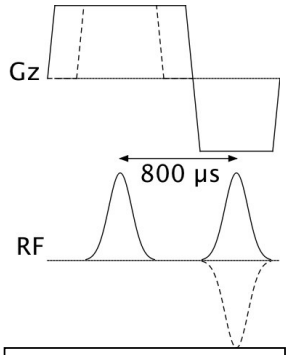

Figure 2: One cycle of the repeated pattern of RF and gradient pulses used for pseudocontinuous ASL. Where the control sequence deviates from the label is shown with a dashed line.

Methods: The sequence of figure 2 was implemented on a GE 3 Tesla scanner. 500µs Hanning window shaped pulses were used for the RF, a gradient amplitude of 0.6 G, an average B1 of 20 mG, and an average gradient of 0.15 G were employed for the labeling. The labeling was performed prior to image acquisition with a gradient echo echoplanar image acquisition. A post-labeling delay of 1.2 s and a labeling duration of 1.5 seconds were selected. Studies were performed in 2 normal volunteers following a protocol approved by our institution's human subject study review board. Imaging was performed with labeling applied below the imaged slab and also with the labeling above the head, in order to assess subtraction errors.

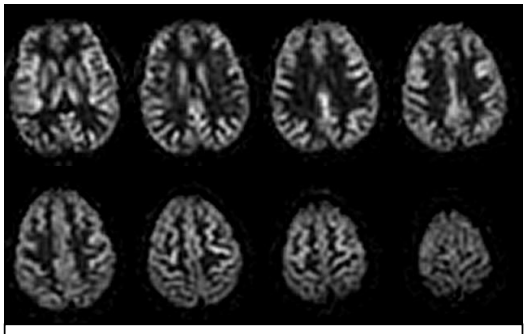

Figure 3: Example perfusion images acquired using the pseudocontinuous inversion labeling strategy.

Results: Difference images showed clear signatures of perfusion, figure 3, with higher perfusion in gray matter than white matter. When labeling was performed above the brain, no measurable signal was observed.

Discussion: Pseudo-continuous flow driven adiabatic inversion was successful at both labeling arterial spins and controlling for off-resonance errors. Further work will assess the relative efficiency of this and other approaches to continuous ASL.

References: 1. Dixon et al. MRM. 3:454-62 (1986) **2.** Williams et. al. Proc. NAS. 89:212-16 (1992) **3.** Alsop et. al. Radiology. 208: 140-16 (1998) **4.** Talagala et. al. ISMRM 1998 #381 **5.** Alsop et. al. ISMRM 2001 #1562 **6.** Silva et. al. MRM. 33(2):209-14 (1995) **7.** Zaharchuck et. al. MRM. 41(6):1093-8 (1999) **8.** Alsop. MRM. 37:176-84 (1997).

ISMRM, 2005.

APD-based PET for combined MR-PET imaging

R. Grazioso[1], R. Ladebeck[2], M. Schmand[1], R. Krieg[2]
[1]Detector R&D, CPS Innovations, Inc., Knoxville, TN, United States, [2]MRE-MI, Siemens Medical Solutions, Erlangen, Germany

Abstract: We propose a MR-compatible PET detector using avalanche photodiodes (APDs) in a light-sharing readout scheme. A prototype APD-based PET detector block has been designed, built and tested for PET performance inside and outside a magnetic field. The block design consists of an 8 x 8 array of 2 mm x 2 mm x 20 mm LSO crystals coupled to a lightguide and read out by a 2 x 2 array of APDs. The APDs used are manufactured by Hamamatsu Corp. (Model # S8664-55). The average pixel energy and timing resolution (measured against plastic/PMT) were 16-18% and 1.8-2.0 ns, respectively. The detector block has been tested in a 0.4 Tesla static magnetic field with no degradation of position resolution or energy resolution. These results are promising and are comparable to other APD-based PET designs. For the full paper, we will show results from a prototype detector operating in a whole body MR scanner.

Introduction: Recently, there has been exciting work in combined MR-PET imaging [1,2] though the idea has been around for quite sometime [3,4]. Historically, there has been two main ideas on how to achieve a PET image within an MR bore: 1) using optical fibers to transport the light from scintillators to magnetically-sensitive photomultiplier tubes (PMTs) and 2) using magnetically insensitive photosensors, such as APDs, coupled to scintillators inside the MR bore. We believe the latter option will be more cost-effective while still producing better results.

Preliminary Results: An APD-based block detector has been built consisting of an 8 x 8 array of 2 mm x 2 mm x 20 mm LSO crystals. This array was coupled to a lightguide and read out by a 2 x 2 array of APDs as shown in Figure 1. The APDs used in these measurements were manufactured by Hamamatsu Corp. (model # S8664-55) and have an active area of 5 mm x 5 mm with an overall package size of 9.0 mm x 10.6 mm. The average pixel energy and timing resolution (measured against a plastic scintillator on a PMT) were 16-18% and 1.8-2.0 ns, respectively. This block design was chosen for these measurements based on previous work by [5].

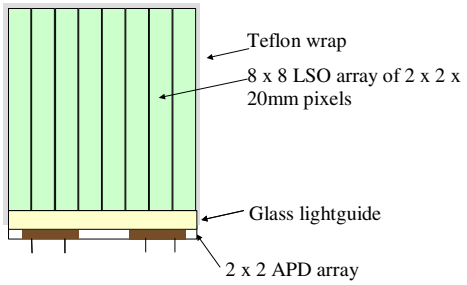

Figure 1. Drawing of an 8 x 8 LSO array coupled to a glass lightguide and read out by a 2 x 2 APD array. The entire array is wrapped with a few layers of Teflon.

This block was also tested in a magnetic field to determine the effect of a magnetic field on APD performance. The block was tested inside the bore of a permanent magnet that has a field strength of approximately 0.4 Tesla. The experimental setup is shown in Figure 2. The detector block, as described above, was placed inside the bore of the magnet with the electronics displaced far enough away so as not to be disturbed by the magnetic field. These measurements were made inside a light-tight box that is temperature controlled and set to 21° C. Measurements were made with and without the APD block inside the bore of the magnet. The position profiles, identifying the 8 x 8 array of crystals, are shown in Figure 3. The position profile is a 2D image that represents the crystals in the array that are being irradiated by a 511 keV flood source. The position profile on the left is the block outside of the magnetic field and the position profile on the right is the block inside the magnet bore. There is no qualitative difference between these two position profiles. Energy resolutions and 511 keV photopeak positions were recorded for each crystal in the array. The average energy resolution and 511 keV photopeak position for the array outside the magnetic field were 17.0% and 536 channel compared to 17.0% and 540 channel for the array inside the magnetic field. These results show there is no degradation in light collection performance of the APDs. Timing resolution measurements were not performed due to the sensitivity PMTs have within a magnetic field, but since there was no light loss we can safely assume the timing resolution of the block in the magnetic field would be identical to previous measurements.

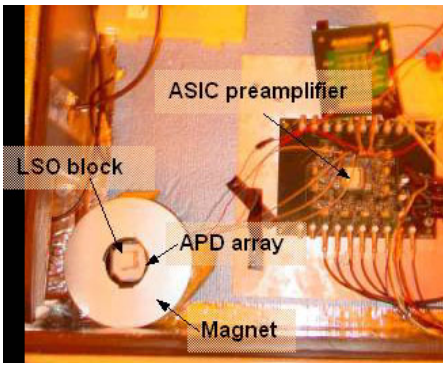

Figure 2. Photograph showing experimental setup of measurements with the APD detector in a permanent magnet.

Future Work: Detector prototypes will be built consisting of multiple blocks in one package. This module will be tested for PET performance in a benchtop setting and then tested within a whole body MR scanner. Data will be presented from measurements showing the effects the different magnetic fields (B_0, Gradients and RF) have on the PET detector, as well as, any effects the PET detector has on the magnetic fields and subsequent MR images. We will also evaluate possible RF shielding options for mutual compatibility. These results will be reported and compared to previous MR-PET prototypes.

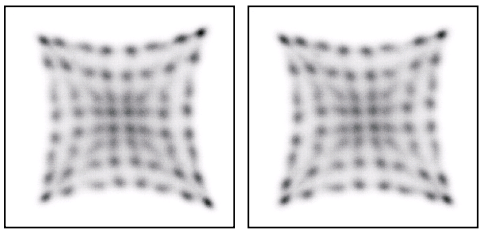

Figure 3. Position profile of an 8 x 8 LSO array outside of the magnetic field (left) along with a position profile of the same array inside the magnetic field (right).

[1] Design and Development of an MR Compatible PET Scanner for Imaging Small Animals, J. E. Mackewn, et al., 2004.

[2] Development and Evaluation of a LSO-APD Block-Detector for Simultaneous PET-MR Imaging, B. J. Pichler, et al., 2004.

[3] Engineering Considerations for a MR-PET Scanner, B. E. Hammer, 1995.

[4] Development of a PET Detector System Compatible with MRI/NMR Systems, Y. Shao, et al., 1997.

[5] APD performance in light sharing PET applications, R. Grazioso, et al., 2003.

ISMRM, 2006.

7T Body Imaging: First Results

T. Vaughan[1], C. Snyder[1], L. DelaBarre[1], L. Bolinger[2], J. Tian[1], P. Andersen[1], J. Strupp[1], G. Adriany[1], K. Ugurbil[1]

[1]Radiology, University of Minnesota, Minneapolis, MN, United States, [2]National Reserch Council-Canada, Winnipeg, MB, Canada

Objective: To investigate the feasibility of whole body imaging at 7T.

Introduction: Whole body imaging and its clinical applications have been commercially developed for 3T. Body imaging has been demonstrated in research applications to 4T.[1] Major MRI system manufacturers are now supporting 7T whole body MRI systems for human head imaging. Are 7T systems capable of human body imaging as well? The aim of this study is to find out.

Methods: The methods consisted of modeling, hardware development and data measurement.

Modeling: Initial modeling used the Remcom Finite Difference Time Domain method to numerically predict RF field and loss contours in the NLM Visual Human digital atlas. Figure 1 shows such a scale model of an adult male loading a TEM body coil. The electrical dimesions of the coil are: i.d. = 57.5cm, o.d. = 62.5cm, active element length = 33cm, cavity length = 100cm.

Hardware Development: 7T equipment specific to human body imaging is not commercially available. Therefore, an initial effort was made to build the necessary means in house. The MRI system used for the study is a Magnex 7T, 90cm bore magnet with Magnex whole body gradients and shims (i.d.= 63cm). A Varian Inova console was used, together with a custom, 8kW solid state RF power amplifier from Communications Power Corporation (CPC). An actively detuned, 300 MHz. RF body coil of the model dimensions was built together with its PIN detuning circuits and system control interface as shown in Figure 2. The details of this device can be found in the first reference. Specialty 300 MHz receive circuits such as the 4-element stripline dual breast array show in Figure 5 also were developed together with the necessary PIN decoupling circuits and multi-channel, digital receivers.

Measurement: Due to the limited peak power available (approximately 4 kW at the coil) and the signficant high frequency load losses predicted, initial measurements employed low tip angle sequences of long pulse widths. For an initial mapping of the RF "landscape" in the body at 300 MHz, coronal, saggital, and transaxial images were acquired with the body coil switched to transmit and receive mode, without the use of additional receiver coils. The common parameters used for acquiring the gradient echo, whole body images of Figure 3 were: 256x256 matrix , 3mm thick slice, 2 ms windowed sinc RF pulse, flip angle = 25 degrees. Specific to the coronal images: TR/TR = 60/4 ms 50x35 cm, NT=4, scan time = 110 sec. The sagittal images were acquired by: TR/TE = 50/4 ms, 50x35 cm, NT=2, scan time 55 sec., and the transaxial images required: TR/TE = 50/4 ms 35x35 cm NT=4 Scan time 110 sec. Additionally, the body coil was used as an actively detuned, homogeneous transmitter for breast imaging with the local receiver coils shown in Figure 5. The acquisition parameters for this gradient echo sequence were: 256x128 matrix, 42cm/25cm, 3mm thick slice, 2 ms windowed sinc RF pulse, TR/TE = 50/5 ms, flip angle = 20 degrees, scan time 12 sec.

Results and Discussion: The models predicted significant RF artifacts in at least one sharp line running longitudinally through the body, primarilly due to destructive interference of the short (12cm) wavelengths in the high water content tissue dielectrics at 300MHz. Imaging proved these predictions generally correct. See Figure 3. Also shown in the Figure 3 images are what appear to be susceptibility artifacts possibly due to gas pockets in the bowel. Apparent susceptibility artifacts were also noted near the body, between the breasts in female subjects. See Figure 4. B_0 phenomena were not modeled for this investigation.. The RF power (SAR) used to acquire the images was estimated by: Average SAR = 996 W peak power * 0.2789 (sinc Se power ratio) = 277.7 Watts * 2ms/50ms = 11.1 W per slice in each TR. 11.1 * 5 slices = 55.5W, or less that 1.0 W/kg for most adults, well within the FDA guideline for human torso imaging. The observed artifacts and RF power requirements however do not appear to preclude the possibility of useful whole body imaging for at least some applications at 7T. Breast imaging for example is a strong candidate. Scout imaging combined with low gamma spectroscopy of almost any organ or tissue might prove highly successful at 7T. Furthermore, recent work suggests that at least some of the artifacts observed at 7T may be manipulated or removed by RF field shimming for targeting localized regions of interest. [1]

Conclusions: These preliminary results demonstrate that safe and successful whole body imaging at 7T may be feasible.

Reference: Vaughan, Adriany, Snyder, et.al., Efficient High Frequency Body Coil for High Field MRI. MRM 52:851-859 (2004)

Acknowledgements: NIH-R33 CA94318, NIH-R01 CA94200-01A1, NIH- R01 EB000895-04, NIH-P41 RR08079

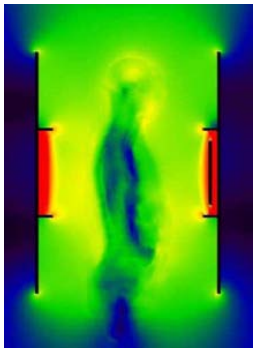

Figure 1. Model Body in Coil

Figure 2. 300 MHz TEM Body Coil

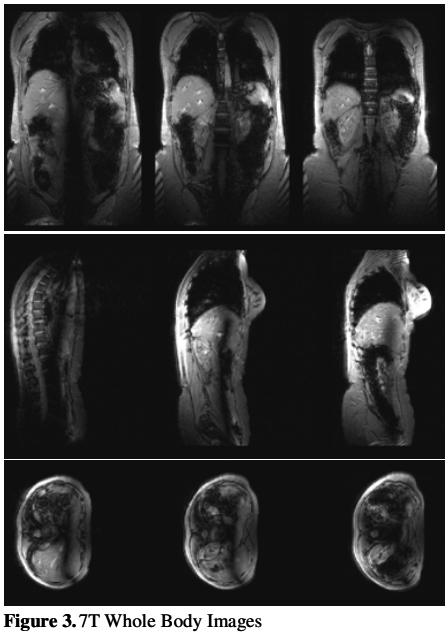

Figure 3. 7T Whole Body Images

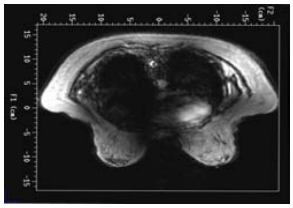

Figure 4. 7T Chest Image (with heart)

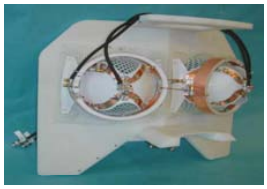

Figure 5. 300MHz Breast Array

Figure 6. Breast Images from Coil above

ISMRM, 2006.

Simultaneous slice excitation and reconstruction for single shot EPI.

R. G. Nunes[1], J. V. Hajnal[1], X. Golay[2], D. J. Larkman[1]

[1]Imaging Sciences Department, MRC Clinical Sciences Centre, Hammersmith Hospital, Imperial College London, London, United Kingdom, [2]MRI Facility, Singapore Bioimaging Consortium, Singapore, Singapore

Introduction and Background: Partially Parallel Imaging (PPI) is highly effective for reducing acquisition time in multi shot MRI because the speed up factor equals the reduction in the number of shots required to construct a non aliased image. For single shot EPI reduction in the number of phase encodes has a lesser impact on scan time due to the relative length of the preparation phases and the readout. Typically scan time is only decreased by 20-30% with a speedup factor of 2. Image artefacts are reduced due to the reduced length of the readout window. Where time is critical a better strategy for single shot imaging is to excite multiple slices simultaneously. This, combined with unfolding using PPI, has been demonstrated before[1]. The method provides a direct speedup factor (factor 2 for two slices etc) and carries with it the additional benefit of not suffering from the $\sqrt{r}$ (r=speedup factor) penalty in SNR that is associated with other PPI methods. However, the method does not perform well with standard enveloping array coils when transverse slice geometries are used because of a lack of variation in coil sensitivity in the through slice (z) direction. PPI reconstruction of closely spaced slices results in prohibitively high g-factors. Attempts have been made to tackle this problem: CAIPIRINHA[2] uses shot by shot modulation of the RF pulse to synthesise shifts in plane of one slice by half a field of view (fov) to improve PPI unfolding performance. RF encoded [4] and hardware [3] solutions have also been proposed, however the former are not suitable for single shot imaging (EPI) and the latter are largely unpractical. We propose a different method to introduce an arbitrary shift between two simultaneously excited single shot EPI slices, allowing them to be separated by PPI with acceptable g-factors.

Theory and Methods: Simultaneous slice excitation pulses were produced by modulating the single slice time domain RF pulse by $\cos(\omega t)$ which by the the Fourier convolution theorem produces two slices excited at +/-ω, where ω determines the slice separation. If PPI is applied to multislice excited data directly, then in the transverse geometry, for small slice spacing the g-factor is prohibitive because of the similarity of the coil sensitivities at the locations of the superimposed pixels. Since the coils have much greater differential sensitivity in plane than through plane, we seek to introduce a differential in plane shift between the two excited slices. This is achieved during readout by creating a k-space phase ramp in the direction of desired shift using a scheme proposed for FLASH imaging [3] that was modified for single shot EPI. To produce the phase ramp an additional set of blip gradients is required in the through slice direction with the same timing as the in plane phase encode blips. These introduce an accrual of phase throughout the readout producing a shift which is proportional to the magnitude of the through slice field at the location of the slice. Slices further from isocentre experience greater fields and therefore greater shifts. The differential shift between two slices a fixed distance apart is constant regardless of their proximity to isocentre. Such simultaneously excited slices can be separated using standard PPI algorithms by modifying the input and reference data to conform to the standard field of view reduction formalism usually considered in PPI. This approach is similar to that described in the context of fat artefact removal [4]. In a fully sampled image, the signal intensity S_1 in a pixel where there is a superposition of signals x_1 in slice1 and x_2 in slice2, imaged with coil j can be written as $S_j=C_{j1}x_1+C_{j2}x_2$, where C_{j1} represents the sensitivity of the coil at slice 1 and C_{j2} the sensitivity at slice 2. This equation is the SENSE equation and with multiple coils the problem can be solved. The in plane difference in position between the locations of x_1 and x_2 is not necessarily half a field of view as in traditional SENSE with factor two pixel degeneracy. It can be chosen at will according to the selected differential shift. The data can be made to fit the usual formalism by constructing reference data from standard coil sensitivity data for each slice position shifted by the known differential shift. Reconstruction uses a standard SENSE algorithm.

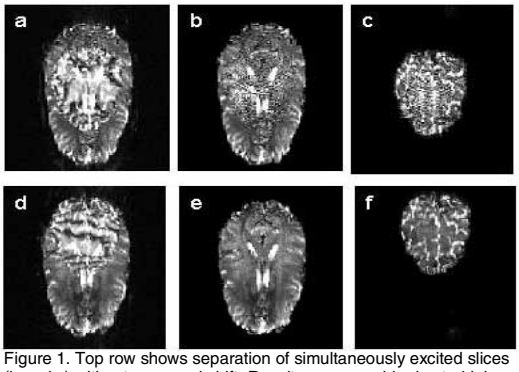

Figure 1. Top row shows separation of simultaneously excited slices (b and c) without proposed shift. Results are unusable due to high g-factor noise. e and f show results of proposed method.

Methods: The principle was tested by simulation and experiment. The data presented is a full practical implementation. At present this has been tested on phantoms and 3 healthy volunteer subjects. Acquisition: 240mm FoV, 4mm slice thickness, 4mm gap, TE/shot duration 196/54, 128x128 matrix. The multi-slice excitation has a slice separation of 32mm and was the same duration as the single slice excitation. For testing purposes a 5 slice acquisition was used resulting in 9 unique slice locations with one slice acquired twice with each part of the RF pulse for comparison. Data reconstruction was performed using a standard SENSE reconstruction algorithm in the manner described. All data were acquired on a Philips 3T Intera.

Results: Figure 1a) shows an acquisition where two slices were excited without additional blips in the slice direction and figure 1d) shows the differential effect of these blip gradients. It is important to note that as the shifts required to control the g-factor are relatively small (32 pixels in this case) the blips are small in area, introducing negligible slice dephasing. Comparison of the regions of the image where the slices do not overlap demonstrate this. Figure 1b and c show the results separated using SENSE, The peak g-factor is 37.2 the mean g-factor is 7.4. These images are not interpretable.. Figure 1 e and f show the same slices excited with the slice blips on and separated using SENSE with modified reference data . The reconstructions are faithful to the anatomy and have peak g-factor 1.8 mean g-factor 1.2 resulting in fully diagnostic images.

Discussion: For many applications time per acquired slice is critical. For example in the recently published method for model free quantitative arterial spin labelling (qASL) [5], coverage of the brain is limited by the lifetime of the tagging pre-pulse, dictated by the T1 of the blood. A typical exam with a total scan time limited to 10-12mins only achieves coverage of 4 slices, which with 6mm slice thickness and a 2mm gap samples only a 32mm slab of the brain. By using the method presented here, the volume of brain measured in the example above would double. As the two slices would have been excited simultaneously (double the number of spins) there would be no $\sqrt{r}$ term in the PPI SNR equation. This is vital for SNR limited applications like qASL. Although in plane shifts serve to reduce the g-factor, introducing these shift can cause through slice de-phasing. Use of a pre-winder gradient ensures that the centre of k-space is fully refocused, but some spatial frequency dependent de-phasing may be seen introducing blurring in the phase encode direction. The greater the slice separation the smaller the blip gradient needed and the less this artefact manifests. As can be seen in the examples successful separation of even closely space slices can be achieved with little loss of image quality. In conclusion we have demonstrated by simulation, in phantoms and in vivo that this methodology provides a flexible framework for PPI based separation of signals in simultaneously excited slices. The method can also be applied with slice shifts in the frequency encode direction, potentially allowing both separation of simultaneously excited slices and reduction in echo train length in the phase encode direction using PPI unfolding in two orthogonal directions.

Acknowledgements: We acknowledge grant support of the EPSRC and Philips medical systems

References:[1].Larkman, D.J., et al.,. J Magn Reson Imaging, 2001. **13**(2): p. 313-7.[2].Breuer, F.A., et al.,. Magnet Reson Med, 2005. **53**(3): p. 684-691.[3].Weaver, J.B., Magn Reson Med, 1988. **8**(3): p. 275-84.[4].Larkman, D.J., et al . *ISMRM*. 2005.[5.]Petersen, Lim, and Golay,. ISMRM, 2005: p. Abs 34.

ISMRM, 2006.

Rapid MR Imaging with "Compressed Sensing" and Randomly Under-Sampled 3DFT Trajectories

M. Lustig[1], D. L. Donoho[2], J. M. Pauly[1]

[1]Electrical Engineering, Stanford University, Stanford, CA, United States, [2]Statistics, Stanford University, Stanford, CA, United States

Introduction

Recently a rapid imaging method was proposed [1] that exploits the fact that sparse or compressible signals, such as MR images, can be recovered from randomly under-sampled frequency data [1,2,3]. Because pure random sampling in 2D is impractical for MRI hardware, it was proposed to use randomly perturbed spirals to approximate random sampling. Indeed, pure 2D random sampling is impractical, however, randomly under-sampling the phase encodes in a 3D Cartesian scan (Fig. 1) is practical, involves no overhead, is simple to implement and is purely random in two dimensions. Moreover, scan-time reduction in 3D Cartesian scans is always an issue. We provide a method to evaluate the effective randomness of a randomly under-sampled trajectory by analyzing the statistics of aliasing in the sparse transform domain. Applying this method to MR angiography, where images are truly sparse, we demonstrate a 5-fold scan time reduction, which can be crucial in time-limited situations or can be used for time resolved imaging

Theory

Medical images in general, and specifically angiograms, often have a sparse representation using a linear transform (wavelets, DCT, finite differences, etc.)[1]. Under-sampling the Fourier domain results in aliasing. When the under-sampling is random, the aliasing is incoherent and acts as additional noise interference in the image, but more importantly, as incoherent interference of the sparse transform coefficients. Therefore, it is possible to recover the sparse transform coefficients using a non-linear reconstruction scheme [1-4] and consequently, recover the image itself. The interference in the sparse domain is a generalization of a point-spread function (PSF) and is computed by $I(n,m)=<Sig(x_n),Sig(x_m)>$ where x_n is the n^{th} transform coefficient, and $Sig\{x_n\}$ is the normalized projection of the transform coefficient onto the under-sampled Fourier space. The success of the reconstruction will depend on the sparsity of the coefficients and that the interference $I(n,m)$ be small and have random statistics [2,3]. The interference can be used as a design criteria or a test for a practical randomly under-sampled trajectory. As an example, we analyzed the statistics of the interference of wavelet coefficients (See Fig. 2), leading to a conclusion that for images sparsified by wavelets, random sampling should have variable density sampling, with increased density toward the center of k-space.

Methods

Angiograms are truly sparse, with high signal from blood vessels and low background signal. To test our proposed trajectory, we considered an SSFP angiogram data set[6]. By post processing, we simulated a randomly under-sampled 3D Cartesian trajectory by removing phase encodes (Fig. 1), sampling more densely towards the center of k-space. We reconstructed from 5%, 9%, 13%, 20%, 30%, 50%, 80% percent of the data respectively using L_1 Total Variation(TV) [1-4] and compared the results to zero-filling the missing data, and a low-resolution acquisition with the same number of phase encodes.

Results and Discussion

Fig 3. illustrates a region of interest in the maximum intensity projection (MIP) of the reconstructions for different under-sampling ratios. As expected, reconstruction by zero filling is severely degraded by aliasing artifacts and most vessels do not show in the MIP for high under-sampling ratio. The low resolution reconstruction also exhibits narrowing of vessels due to smoothing of the edges. On the other hand, the L_1 reconstruction was able to recover the sparse signal and produces a similar quality MIP to the fully sampled reconstruction starting from only 20% of the data. In conclusion, L_1 –penalized image reconstruction recovers sparse images even with severe undersampling. We also showed a method to evaluate random sampling schemes. Our method is computationally intensive. In the current, Matlab™ implementation we are able to reconstruct a 128x128x256 image in a matter of 120 minutes, this can be improve by newly proposed reconstruction algorithms [4,5]. This type of approach can be used either to speed scan time or gain more spatial or temporal resolution.

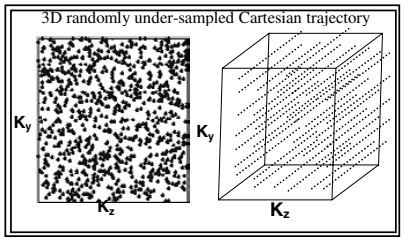

Figure 2: *Random under-sampling by randomly removing phase-encodes*

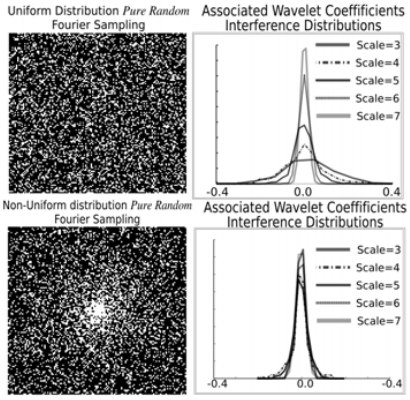

Figure 1: *Wavelet coefficients interference distribution. Large scale wavelets corresponds to low freq. image features, small scale to high freq. Top: Interference is random and Gaussian distributed. Low frequencies interfere more than high frequencies. Bottom: Variable density random sampling "equalizes" the distributions such that the interference is small and similar for all scales.*

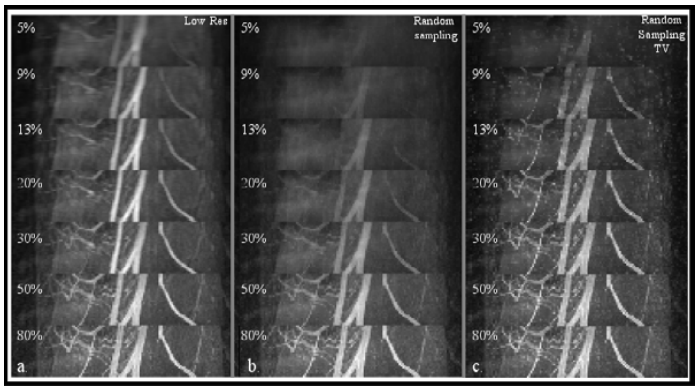

Figure 3: *Reconstruction from randomly under-sampling phase encodes in 3D Cartesian acquisition. Left: Recon. from only low-res information. Middle: Recon. by zero- filling missing random phase encodes. Right: L_1 Total Variation recon. from randomly under-sampled data The percentage represents amount of phase encodes used in the reconstructions .*

References

1] Lustig et al. 13th ISMRM 2004:p605

[2] Candes et al. "Robust Uncertainty principals". Manuscript.

[3] Donoho D. "Compressesed Sensing". Manuscript.

[4] Candes et al. "Practical Signal Recovery from Random Projections" . Manuscript.

[5] M. Elad, "Why Simple Shrinkage is Still Relevant for Redundant Representations?" Manuscript.

[6] Bangerter et al. 12th ISMRM:2004, p.11

ISMRM, 2006.

Detection of orientation specific activation zones in human V1 using fMRI

E. Yacoub[1], K. Ugurbil[1], N. Harel[1]
[1]Center For Magnetic Resonance Research, University of Minnesota, Minneapolis, MN, United States

Introduction:

There have been several previous studies in humans and animals which have successfully used fMRI to map high resolution functional architecture in the brain at the level of cortical columns (1-2). Animal studies using fMRI have been able to map both orientation columns (3-4) as well as ocular dominance columns (ODC) (5) using several different contrasts. In humans, ocular dominance columns have been demonstrated using fMRI, however, attempts to *directly* map orientation columns have never been done. With the ability to do longitudinal studies in humans, fMRI maps can be robustly established and the reliability assessed. With this, apriori maps of ocular dominance columns, which we have previously demonstrated, can be used to predict an expected spatial organization of orientation columns. In this work, we demonstrate directly for the first time in humans, the existence of orientation specific activation using high resolution fMRI at high magnetic fields.

Background:

Neurons in visual area V1 are selective for the orientation of a bar presented within their receptive field. Neurons with preference for similar orientation are clustered together, forming columns that run orthogonal to the cortical surface. Using anatomical techniques (6) ocular dominance columns have been previously demonstrated in the human post-mortem brain. Histological staining for the enzyme cytochrome oxidase enhances regions that are metabolically active relative to resting regions. Such post-mortem histological studies in humans that lost one eye demonstrated stripes of active regions corresponding to their functional eye within visual area V1. In contrast, to date there has been *no* verification of the existence of orientation columns in humans, although based on the data from animal models they are believed to exist. Post-mortem studies are not capable of depicting the existence of these columns, as there is no obvious clinical syndrome that would make a specific group of these columns inactive. More specifically, unlike ocular dominance columns, orientation columns have no anatomical basis, and therefore can only be observed via functional properties of the neurons. Non-invasive mapping techniques with high degrees of spatial specificity, such as the techniques proposed in this study, present a unique opportunity to explore functional architecture of the human brain that before were unattainable.

Methods:

Studies were conducted at 7T using slab selective FOV reduction for HSE (TR/TE 6000/50 ms) with 3 image segments. The spatial resolution was: 0.5 x 0.5 x 3 mm^3 with minimal resolution loss due to EPI blurring along the phase encode direction. To minimize the effects of motion; subjects used a bite bar, image registration of small motion was used within and between scans, and scans with large amounts of motion and / or significant mis-registration problems, were discarded. The visual stimuli were presented through fiber optic video goggles (Avotec, inc.). Subjects initially participated in ocular dominance column studies and brought back for repeated studies to assess the reproducibility of the functional maps. Following successful differential mapping of ocular dominance columns, subjects were again brought back to attempt to map orientation specific regions using the same anatomical slice. Initial studies were conducted using a series of drifting bars alternating between 2 orientations (0 and 90 degrees) while presented binocularly. The activation maps were analyzed similarly to the ODC data. Functional maps from the different days and the different paradigms were registered to the same anatomical location.

Results:

The results from one subject are shown below. Figure 1a displays a differential ODC map (i.e. right eye minus left eye (red and blue) with a confidence of 85%. These maps of alternating ODC patterns have previously been demonstrated to be highly reproducible (7). In contrast, when the activation pattern for a drifting bar stimulus for 0 degrees is compared to 90 degrees (Fig. 1b; green and pink) an entirely different fMRI activation pattern appears. Clusters of pixels with similar orientation preference appear to run orthogonal to the ODCs as expected from known cortical architecture in animal models.

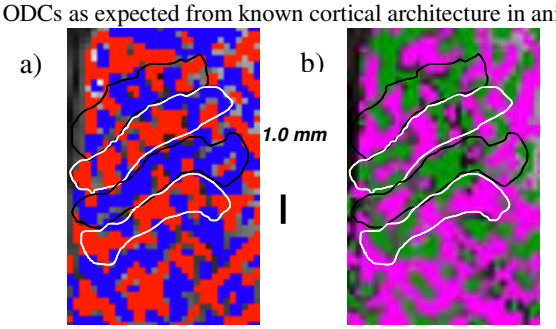

Conclusions:

We demonstrate here for the first time, the existence of cortical regions in human visual cortex which are orientation specific (i.e. 0 degrees vs. 90 degrees). In addition, we have registered these maps to ODC maps which show the anticipated spatial relationship between these sets of visual cortical columns. We are currently conducting studies to obtain multiple orientations using phase encoding techniques.

Fig.1 a) Results from single sessions of ODC studies (red & blue) and orientation studies (b) (green and pink) from the same subject. The ODC outlines are registered to the same locations on the orientation maps.

References: **1**. *Menon et al 1997* **2**. *Cheng et al 2001* **3**. *Kim et al 2004* **4**. *Duong et al 2001* **5**. *Harel et al 2002* **6**. *Horton et al 1990.* **7**. *Yacoub et al 2005*

Acknowledgements: R01MH70800-01, P41-RR008079, The Keck Foundation, The MIND institute.

ISMRM, 2007.

High-Field MRI of Brain Cortical Substructure Based on Signal Phase

J. H. Duyn[1], P. van Gelderen[1], T-Q. Li[2], J. A. de Zwart[1], A. P. Koretsky[2], and M. Fukunaga[1]

[1]Advanced MRI, LFMI, NINDS, National Institutes of Health, Bethesda, MD, United States, [2]LFMI, NINDS, National Institutes of Health, Bethesda, MD, United States

INTRODUCTION

The spatial resolution of clinical brain MRI is limited to about 1 mm^3 (1 μl), which is not optimal for measuring the fine-scale differences in cortical morphology across functional regions or between normal and pathological tissue. Although recent developments in high field MRI technology and array detectors have allowed a reduction of the voxel volume to below 0.1 μl [1], the generation of strong cortical contrast has proven challenging. Recently, susceptibility contrast was used to improve detection of venous structures and iron rich brain regions such as the substantia nigra and the globus pallidus [2]. Here, we investigate whether susceptibility contrast at high field allows improved measurement of cortical morphology.

METHODS

MRI experiments were performed on a 7.0 T GE Signa MRI scanner, receiving signals from 16 channels of a 24-channel receive-only detector array. Six normal volunteers (3 male, 3 female) in the age range of 25-52 years were scanned under an IRB approved protocol. Axial gradient echo (GRE) acquisitions were performed with TE=28-31 ms, TR=500-800 ms, flip angle 30-50 degrees (adjusted at center of brain), slice thickness 1 mm, field of view 240×180 mm^2, matrix size 1024×768, bandwidth 32 kHz, and first order flow compensation on all imaging gradients. The total scan time was 6.5 – 10 minutes. Multiple slices were acquired throughout the brain with varying inter-slice gap. For comparison, 3D MPRAGE scans were performed with TE=5.4 ms, TR=11.3 ms, flip angle 14, slice thickness 1 mm, field of view 240×180 mm^2, matrix size 512×384, bandwidth 62.5 kHz, TI=1.2 s, overall TR=3 s, scan time 20 minutes. Prior to the anatomical scans, higher (second) order B_0 shims were adjusted to minimize macroscopic susceptibility effects. In addition, during each scan, real time higher order shimming was performed to compensate for B_0 fluctuations related to the respiratory cycle [3]. Images were reconstructed using phase sensitive combina of the individual coil data [4] using the separately acquired coil sensitivity reference data. Susceptibility images were derived from the GRE phase data after removal of macroscopic phase variation with eight-order 2D polynomial fitting.

RESULTS AND DISUSSION

A dramatic contrast was observed in the GRE phase data, indicating frequency differences of up to 5 Hz between cortical grey matter (GM) and underlying white matter (WM) (Figs. 1-2). CSF phase was similar to that of WM. Similar GM-WM differences were seen in all subjects. In motor cortex parallel to B_0, the frequency difference ranged from 3-5 Hz in the central layers, corresponding to a susceptibility difference of 0.01-0.02 ppm. At 5 Hz frequency difference, the estimated *CNR* gain over magnitude data was about 9-fold. *CNR* values in peripheral and central regions for MPRAGE were around 1.5:1 and 8:1 respectively, compared to 3:1 and 20:1 for GRE phase data. When taking into account the 2-3 times longer scan time and 4 times lower resolution, the inherent *CNR* of MPRAGE data was 10-12 fold lower than that of GRE phase data. Interestingly, in many cortical regions including the motor cortex and visual cortex, phase variations across the cortical thickness were observed, suggesting a layer-specific contrast (Fig. 2). The hypo-intensity seen in the primary visual cortex is suggestive of the line of Gennari, a feature that has been observed previously with T_1-weighted MRI [5,6] at lower resolution. These results indicate that high field MRI combined with multi-channel detection and phase-based contrast allows *in-vivo* brain imaging with unprecedented *CNR* and resolution.

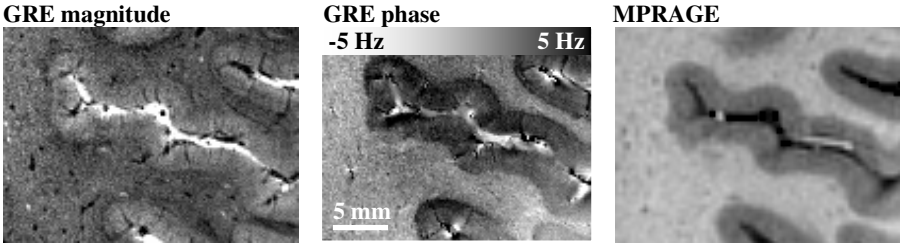

Figure 1

The susceptibility related phase effects observed in this work could originate from a variety of sources, including variations in iron content, myelin content, and deoxy-hemoglobin. Post-mortem iron and myelin stains and histochemistry on the same tissue might elucidate the relative contributions of these mechanisms.

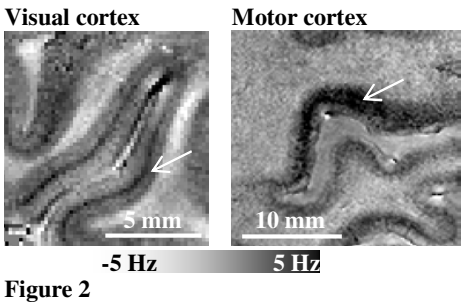

Figure 2

REFERENCES

[1] Li TQ, et al., (2006): Neuroimage 32(3):1032-40
[2] Haacke EM, et al., (2005): Magn Reson Imaging 23(1):1-25
[3] van Gelderen et al., Magn Reson Med (in press)
[4] de Zwart JA,et al., (2002): Magn Reson Med 47(6):1218-27
[5] Clark VP, et al., (1992): Cereb Cortex 2(5):417-24
[6] Barbier EL, et al., (2002): Magn Reson Med 48(4):735-8

ISMRM, 2008.

gagCEST & NOE: Assessment of Glycosaminoglycan Concentration in Vivo

W. Ling[1], R. R. Regatte[2], G. Navon[1], and A. Jerschow[3]

[1]Tel Aviv University, Israel, [2]Medical School, New York University, New York, NY, United States, [3]New York University, New York, NY, United States

Introduction

GAG is essential for human musculoskeletal function, cell regulation, and spinal function. Proteoglycans (PGs), the functioning unit with high [GAG], play vital functions in diarthrodial joints and IVD (1). Thus, quantification of [GAG] in vivo is desirable for OA and disk degenerative diseases, which are both characterized by the loss of PGs in cartilaginous tissues. Based on our spectroscopic study (2) on cartilage, both amide proton (-NH, δ=+3.2ppm) and hydroxyl protons (-OH δ=+1.0~+1.9ppm) from GAG are exploited to be as CEST agents (3, 4).The annulus fibrosus and nucleus pulposus of IVD also demonstrates similar behavior as cartilage. Moreover, the contribution of the nuclear Overhauser effect (NOE) from slow motion of GAG was found to act like chemical exchange protons in z-spectroscopy, leading to additional diagnostic ability.

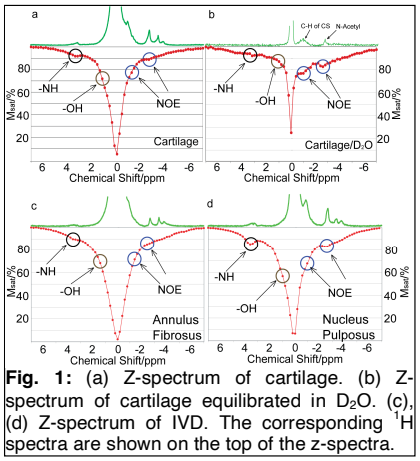

Fig. 1: (a) Z-spectrum of cartilage. (b) Z-spectrum of cartilage equilibrated in D_2O. (c), (d) Z-spectrum of IVD. The corresponding ^1H spectra are shown on the top of the z-spectra.

Materials and methods

NMR/MRI Sample preparation: The bovine cartilage samples were cut to into a 5 mm NMR tube. The 60 min trypsinization (0.2 mg/mL trypsin, Aldrich-Sigma) was performed a cartilage 60mins×3 times. In cartilage D_2O equilibration experiments, the fresh cartilage was immersed in PBS/D_2O for 24 hours. [^{23}Na] in fresh cartilage was calibrated. 1 human subject with occasional knee pain was under MR investigation.

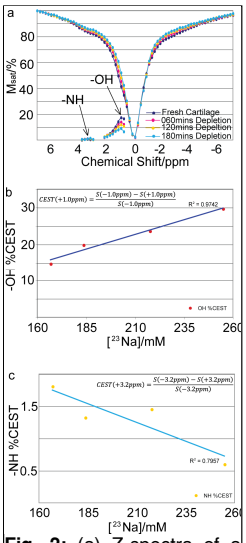

Fig. 2: (a) Z-spectra of a cartilage trysinization series. (b) -OH CEST vs. [^{23}Na], as assessed via ^{23}Na NMR spectroscopy. (c) -NH CEST vs. [^{23}Na], as assessed via ^{23}Na NMR spectroscopy.

NMR experiments: NMR Data were acquired at a 500 MHz Bruker Avance spectrometer equipped with a BBO probe. The temperature of the sample was stabilized at 310 K. The T_1 of bulk water was measured by saturation recovery. For the CEST experiments, continuous wave irradiation was used with irradiation power and duration varying according to the system of interest, followed by a 5° pulse. For the z-spectra, a total of 71 spectra were collected with 100 Hz shift in offset frequency per step. The saturation duration and power levels of the presaturation were as follows: For Figure 1: 10 s and 50 Hz; For Figure 2: 4 s and 250 Hz.

MRI experiments: The MRI experiments were performed on a 3.0 T clinical Siemens MR scanner. The CEST imaging sequence was performed with a train of ten 180° Gaussian pulses with pulse length 31 ms and average saturation power 35 Hz. Slice thickness = 3 mm; acquisition matrix = 256x128; FOV = 150 mm x 150 mm.

Results and Discussion

The exchangeable protons of the PG molecules have been identified in a previous article (2). Figure 1a shows the z-spectrum from a piece of bovine cartilage: the chemical exchange sites are at δ=+3.2 and +1.0 ppm; additionally, two sites at δ=-2.6 ppm and -1.0 ppm are identified as NOE sites. These two sites correspond to the CH and N-acetyl residues in GAG, respectively (2). The NOE enhancement is expressed as $NOE_{water}=T_1\times\sigma$. The NOE sites were confirmed by Figure 1d, which shows the z-spectrum of cartilage equilibrated in D_2O. The presence of bulk D_2O significantly reduces the appearance of the dips at the chemical exchangeable sites, while it enhances the NOE sites as shown in Figures 1b. The enhancement can partly be attributed to the increase of T_1 in bulk D_2O compared to that in bulk H_2O: 2.1 s in native cartilage and 4.0 s in D_2O-equilibrated one. Figure 1c and 1d show z-spectra of annulus and nucleus region of IVD. Figure 2 shows the z-spectra acquired from a piece of a sequentially trypsinized cartilage. Figure 2b shows CEST(δ=+1.0 ppm) vs. [^{23}Na]. The linear relationship demonstrates that the -OH can be employed as a reliable CEST agent. In Figure 2c, however, -NH CEST(δ=+3.2 ppm) shows only about 1~2 % effect, much smaller than that from –OH, hence –NH CEST is less reliable. The high concentration (200~300 mM) and high chemical exchange rate ($k_{-OH}\approx1000s^{-1}$) of –OH easily overrides the NOE contributions at δ=-1.0ppm, and results in an overall substantial CEST effect (15%~30%). Figure 3a shows in-vivo results of –OH CEST on a patellofemoral human knee joint, which shows a clear demarcation of a cartilage lesion on the medial facet. The regional variation of the GAG concentration is clearly demonstrated in Figure 3b. These results are consistent with the one from Figure 2b. Thus, the CEST difference image demonstrates its ability to detect localized GAG concentration distributions and hence the pathological state of cartilage in vivo.

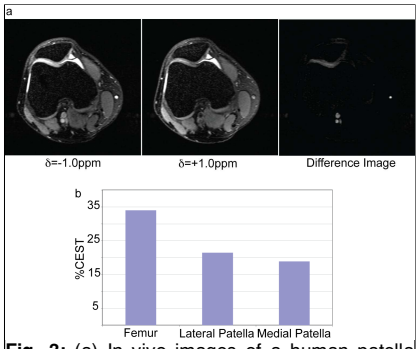

Fig. 3: (a) In vivo images of a human patella with irradiation at δ= -1.0 ppm, δ= +1.0 ppm, and the difference image. (b) The extracted CEST contrast.

Conclusion

We have demonstrated that –OH at δ=+1.0 ppm, among other labile protons, can be used to monitor GAG concentration in cartilage in vivo. The applicability of the method extends also to IVD diseases, as shown in Figs. 1c and 1d. The negative NOE observed in this work results from the interaction of water and non-exchangeable GAG protons with low mobility, which is likely to hold at lower magnetic fields, e.g. clinical scanners. Moreover, NOE is likely to contribute to the low efficiency of some –NH CEST based applications in vivo, but may lead to additional diagnostic methods for macromolecules, but may lead to additional diagnostic methods for macromolecules (5).

References

1. Roughley PJ (2006) *Eur. Cell Mater.* **12,** 92-101.
2. Ling W, Regatte RR, Schweitzer ME, & Jerschow A (2007) *NMR Biomed.* **20,** in press.
3. Ward KM, Aletras AH, & Balaban RS (2000) *J. Magn. Reson.* **143,** 79-87.
4. Zhou J & van Zijl PCM (2006) *Prog. NMR Spectr.* **48,** 109-136.
5. Hubbard PL, Närväinen J, Kauppinen RA, & Morris GA (2007) in *Proc. Intl. Soc. Mag. Reson. Med.* (ISMRM, Berlin, Germany), p. 3464.

ISMRM, 2008.

Traveling wave MR on a whole-body system

D. O. Brunner[1], N. De Zanche[1], J. Paska[2], J. Fröhlich[2], and K. P. Pruessmann[1]

[1]Institute for Biomedical Engineering, University and ETH Zurich, Zurich, Switzerland, [2]Laboratory for Electromagnetic Fields and Microwave Electronics, ETH Zurich, Zurich, Switzerland

Introduction: RF probe design faces novel problems in ultra-high field MRI due to decreased wavelengths. The RF fields produced by classical RF probes such as volume resonators or surface coil arrays suffer from interference effects appearing as dark holes and bright spots. Furthermore, the efficiency of RF probes is lowered as the reactive region of their electro-magnetic fields becomes significantly smaller than the object size. The robustness of such probes with respect to changes of loading and cable routing is also crucial to provide optimal performance and safety. For these reasons we propose to deliberately leave the near-field RF regime and explore MR probe design based on propagating waves. In this work, experiments and simulations are performed demonstrating the feasibility, effectiveness and advantages of a novel family of RF probe devices based on traveling RF waves guided by the cylindrical RF shield that usually lines the bore of MRI systems.

Theory: A propagating plane wave in free space would have maximum homogeneity and transverse polarization up to arbitrarily small wavelengths. Indeed, a freely propagating wave cannot be established inside the bore of an MR magnet. However, a traveling wave can still be guided by the bore and its RF shield. The modes of the empty bore of typical whole-body 7T systems (see Fig. 1 a) have cutoff frequencies slightly above the proton Larmor frequency. Therefore filling the bore with lossless dielectric material (in addition to the subject or sample, Fig. 1 c) reduces the cutoff frequencies of the first modes sufficiently ([2]) to support wave propagation at the proton frequency.

In order to prevent axial standing waves stemming from reflections due to guided mode mismatches at the dielectric interfaces of the subject, a dielectric load tapering towards the subject should be placed at the center of the bore (Fig. 1 d). Additionally, the dielectric loading can be used to shape the transverse field pattern of the mode. Such a setup could provide highly homogenous RF fields in the axial direction if the standing wave ratio can be kept low enough. Furthermore the field patterns (dominated by the mode structure of the loaded bore) are expected to be largely independent of the probing device, which could ease the safety assessment of novel probe designs.

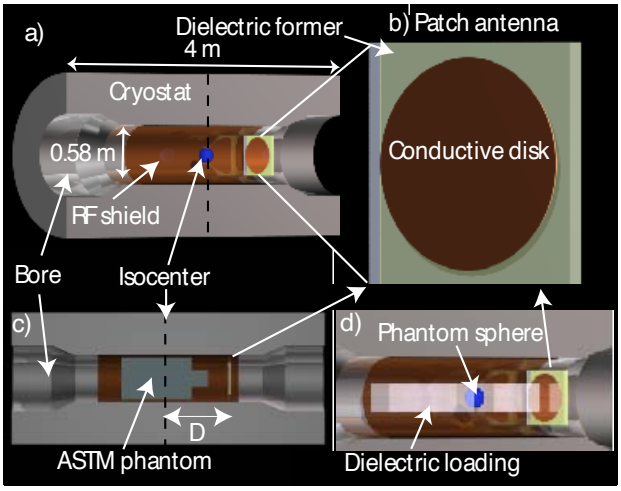

Figure 1: Drawings of the experimental setup

Methods: Two RF probes were constructed, a 350 mm diameter circular patch antenna [1] with quadrature driving ports on a PMMA former (400 mm side length, 30 mm thick) with copper backplane (see Fig. 1 b) and a pair of crossed folded dipole antennas of 250 mm length driven in quadrature. The ports of the patch antenna were matched by attaching the feeding posts directly to 50 Ω impedance points on the disk [1]. Imaging experiments were carried out on a 7T Philips Achieva whole-body system using standard quadrature RF coil interfaces. The RF probes acted as transmit-receive devices in all experiments, and in reception the two quadrature channels were acquired independently. For imaging, a standard small flip-angle gradient-echo sequence (FLASH) was used without averaging.

Experiments and Results: For all experiments the antennas were placed at one end of the bore's RF shield at 65 cm distance from the isocenter (Fig. 1). Using the patch antenna, a central coronal image was taken from a 15 cm saline water sphere placed at isocenter without dielectric load (Fig. 2 d). The same image was taken using 10 3-litre demineralized water containers for dielectric loading (see Fig. 1 d) and replacing the patch by the folded dipole (Fig. 2 e,f). It is seen that the dielectric matching affects the excitation pattern greatly. However, exchanging the RF probe did not change the received image significantly. Using the dielectric loading, coronal images of 9 kiwi fruit (Actinidia Chinensis) arranged in a 3×3 array were acquired. The resulting high resolution (0.375 x 0.375 x 2 mm^3) image in Fig. 2 a) shows excellent SNR with a probe that is actually 60 cm away from the sample. Figure 2 b) shows a transverse slice placed as marked by the dashed line in Fig. 2 a), illustrating homogeneous coverage also in the third dimension. Whole-body imaging was mimicked using a standardized ASTM [3] phantom. Figure 2 c) shows the resulting coronal image acquired using the maximum possible FOV of 500 mm with an in-plane resolution of 1 mm. The coverage thus achieved is visibly inhomogeneous but nevertheless remarkable for "whole-body" imaging at 7T.

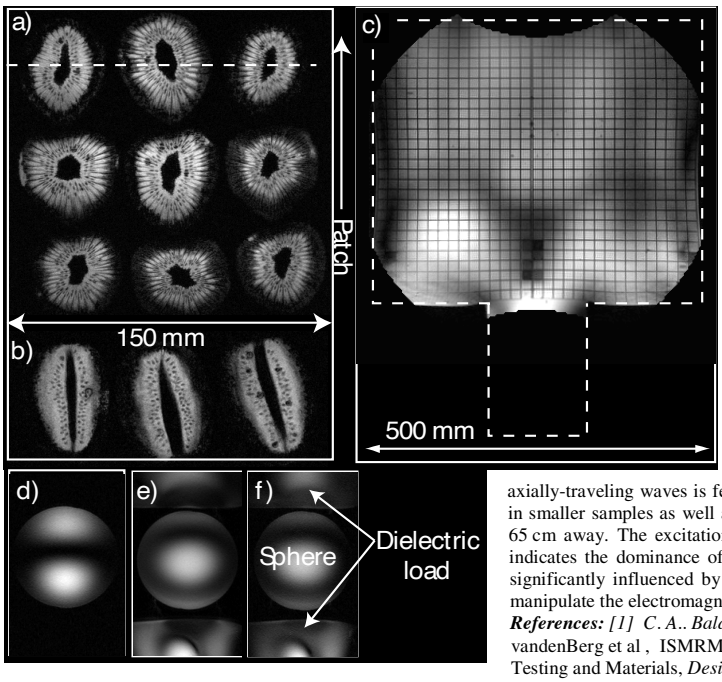

Figure 2: Imaging results

Simulations: Electromagnetic model calculations were carried out using CST Microwave studio®. The results confirmed that although the empty bore has a cutoff frequency of about 303 MHz, very little dielectric loading allows a traveling wave to be established. Furthermore it was found that the transverse field distribution can be altered and unwanted reflections can be lowered by tapering the dielectric interfaces of the subject.

Conclusion: It has been shown that MR excitation and detection by axially-traveling waves is feasible and quite efficient at 7T. High SNR and good coverage was achieved in smaller samples as well as in a whole-body phantom, using an antenna that was placed a remarkable 65 cm away. The excitation pattern produced does not significantly depend on the probe used which indicates the dominance of the mode structure of the loaded bore system. The mode structure can be significantly influenced by dielectric loading of the bore thus allowing various degrees of freedom to manipulate the electromagnetic fields for optimal imaging performance.

References: *[1] C. A.. Balanis, Antenna Theory: Analysis and Design*, Wiley (1997), [2] C.A.T vandenBerg et al , ISMRM workshop Advances in high field MRI Asilomar [3] American Society for Testing and Materials, *Designation: F 2182 – 02a - Standard Test Method for Measurement of Radio Frequency Induced Heating Near Passive Implants During Magnetic Resonance Imaging*

ISMRM, 2008.

High Resolution Human Brain Susceptibility Maps Calculated from 7 Tesla MRI Phase Data

K. Shmueli[1], P. van Gelderen[1], T-Q. Li[1], and J. H. Duyn[1]

[1]Advanced MRI Section, Laboratory of Functional and Molecular Imaging, National Institute of Neurological Disorders and Stroke, National Institutes of Health, Bethesda, Maryland, United States

Introduction: Utilizing the phase in susceptibility-weighted MRI has yielded increased image contrast (**1**). However the phase is affected by tissue orientation, geometry and main magnetic field strength and phase changes extend beyond areas of altered susceptibility. Measurement of the underlying tissue magnetic susceptibilities is therefore desirable since the susceptibility is an intrinsic property of tissue that reflects its composition more closely than the MRI phase. Recent theoretical developments (**2-4**) make calculation of tissue susceptibilities from phase images a new prospect. Here we applied these methods to calculate susceptibility images from high-resolution phase images of the human brain (both ex vivo and in vivo).

Methods: All images were coronal multislice gradient echo images acquired on a 7 Tesla GE system using 16 channels of a (Nova Medical) head coil. Images of a preserved human brain section in fomblin were acquired with 147 μm in-plane resolution, 0.5 mm slice thickness, 0.5 mm gap, 23.2 ms TE and 1.03 s TR. Here, 25 repeated images from a single coil were added together to increase the SNR. In vivo images of a normal volunteer's brain were acquired with 430 μm in-plane resolution, 0.5 mm slice thickness, 0.1 mm gap, 30 ms TE, 2.1 s TR (and SENSE rate 2). After unwrapping the phase by fitting polynomials up to order 5 (ex vivo) or using FSL prelude (**5**) (in vivo), macroscopic background phase variations were removed by subtracting either the fitted phase (ex vivo) or the phase smoothed with a 10-voxel-wide boxcar average (in vivo). Regions (such as blood vessels) in which Iresidual phaseI > π-2 were masked with zeroes as this had been found to reduce artifacts in the susceptibility maps. The equation below (**2-4**) was applied to sub-sections of the resulting residual phase images, where FT denotes a Fourier Transform, χ is the susceptibility, ϕ is the image phase, γ is the proton gyromagnetic ratio, B_0 is the main magnetic field strength, k_z is the z-component of k-space, and $K^2 = k_x^2 + k_y^2 + k_z^2$. To avoid problems as K^2 tended to zero, the k-space deconvolution filter was truncated at a value of 1. Calculations were performed using 2D and 3D regions of phase data with a 2D and 3D FT respectively.

$$\chi = FT^{-1}\left[FT\left(\frac{\varphi(x,y,z)}{-\gamma * B_0 * TE} \right) * \left(\frac{1}{\frac{1}{3} - \frac{k_z^2}{K^2}} \right) \right]$$

Results: **Figure 1** shows the 2D region from images of the preserved human brain in which the susceptibility was calculated. The magnitude image (**A**) shows standard susceptibility-weighted or T_2^* contrast while the phase image (**B**) (scaled between ± 7 Hz) shows variable contrast: the most superficial cortical layer is bright and the deeper layer is darker when they run parallel to B_0 (arrow 1). However this contrast is reversed when the layers are perpendicular to B_0 (arrow 2). The contrast of these layers is more consistent in the susceptibility image (**C**) (scaled between ± 13 x 10^{-9}) in which alternating phase patterns around vessels (or other small regions of altered susceptibility) appear as small homogenous regions (arrows 3). **Figure 2** shows one coronal slice from the 3D region in which the in vivo susceptibility of human brain was calculated. A dark band near the GM-WM border (arrows and tracings in zoomed images **a, b** and **d**) is more clearly visible in the susceptibility image calculated in 3D (**D**) (± 18 x 10^{-9}) than in either the susceptibility image calculated in 2D (**C**) or the magnitude (**A**) or phase (**B**) (± 5 Hz) images.

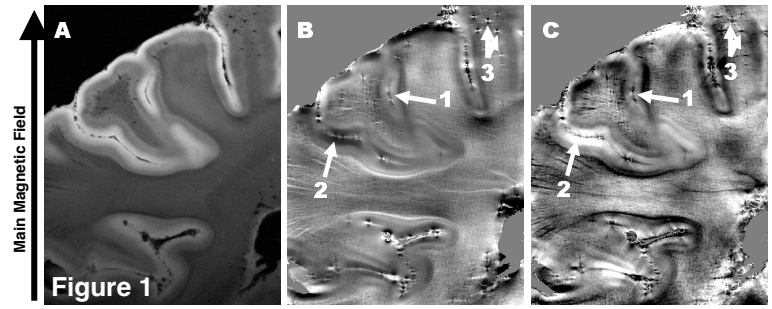

Figure 1

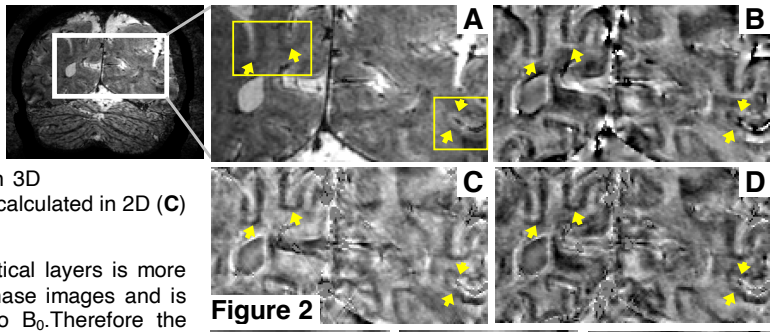

Figure 2

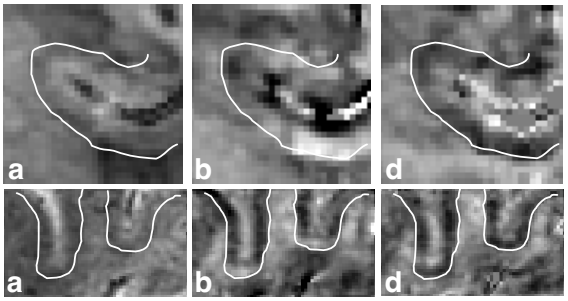

Images **a, b** and **d** are zoomed regions (yellow boxes) of **A, B** and **D**: magnitude, phase and susceptibility calculated in 3D

Discussion and Conclusions: The contrast of cortical layers is more consistent in the susceptibility images than in the phase images and is independent of the structures' orientation relative to B_0.Therefore the susceptibility images seem to overcome some of the shortcomings of phase images. Figure 2 shows that using 3D data for the susceptibility calculation improves the conspicuity of cortical layers in the images. This new source of contrast shows promise for revealing fine scale brain structure. Further work is necessary to determine the most widely applicable parameters for smoothing the phase data and truncating the deconvolution filter.

References: **1.** J.H. Duyn et al. *PNAS* **2007**, 104(28), 11796-801 **2.** E.M. Haacke et al. *MRI* **2005**, 23, 1-25 **3.** J.P. Marques and R. Bowtell *Conc. in MR* **2005**, 25B(1), 65-78 **4.** R. Salomir et al. *Conc. in MR* **2003**, 19B(1), 26-34 **5.** M. Jenkinson *MRM* **2003**, 49(1), 193-7 and http://www.fmrib.ox.ac.uk/fsl/

ISMRM, 2008.

Multiple Orientation Acquisition to Invert Dipole Field for Quantitative Susceptibility Mapping

T. Liu[1,2], P. Spincemaille[2], L. de Rochefort[2], B. M. Kressler[1,2], and Y. Wang[1,2]

[1]Biomedical Engineering, Cornell University, Ithaca, NY, United States, [2]Radiology, Weill-Cornell Medical College, New York, NY, United States

Introduction

An important source of contrast in MRI is magnetic susceptibility [1], and its corresponding magnetic field can be mapped from the MR phase images. However, quantifying arbitrary susceptibility distributions by inverting the measured magnetic field remains challenging because it is intrinsically ill-posed. Some theoretical approaches have been proposed and remain to be validated experimentally [1] [2]. Here, we analyze the ill-posed problem and present a novel method to stabilize it by imaging the object at multiple orientations with respect to B_0. Preliminary data indicates that this multiple orientation approach stabilizes the inversion process and allows voxel-based susceptibility quantification.

Theory

In the presence of inhomogeneous susceptibility variations $\chi(\vec{r})$ within a uniform magnetic field $\overrightarrow{B_0} = B_0 \vec{z}$, the relative magnetic difference field (*RDF*) is given by the convolution [3] $RDF(\vec{r}) = B_z(\vec{r})/B_0 - 1 = FT^{-1}\left(1/3 - k_z^2/k^2\right) \otimes \chi(\vec{r})$, where B_z is the magnetic field component along $\vec{z}$, *FT* is the Fourier Transform, and k denotes components in the Fourier domain. Accordingly, the convolution kernel has zeros on a cone surface at the magic angle (54.7° from B_0). Therefore, directly inverting *RDF* to get $\chi(\vec{r})$ involves calculating $\left(1/3 - k_z^2/k^2\right)^{-1}$ on k-space, which is not defined at those zeros.

If the object is rotated N times with respect to B_0, an equivalent rotation of the *RDF* in the object frame is given by replacing $\left(1/3 - k_{axis}^2/k^2\right)$ in the previous expression, where k_{axis} is the rotated Fourier domain coordinates along B_0 with respect to the object. Then for each point X(k) in k-space, the following linear problem can be solved $\left[\left(1/3 - k_{axis1}^2/k^2\right),...,\left(1/3 - k_{axisN}^2/k^2\right)\right]^T \mathrm{X} = \left[FT(RDF_1),...,FT(RDF_N)\right]^T$. In an ideal environment without noise, if the number of orientations is greater than or equal to 3, then no more rank-deficiency exists for the system, except for k=0. In practice, the field measured from the signal phase has a non-homogeneous noise variance that is inversely proportional to the signal amplitude *S* [4]. In this situation, the following weighted linear system can be solved in image space to account for noise: $S \cdot RDF(\vec{r}) = S \cdot FT^{-1}\left(1/3 - k_{axis}^2/k^2\right) \otimes \chi(\vec{r})$.

Methods

A water phantom containing 7 test tubes (Fig. 1) was used. Tubes were filled with water for a reference scan, and then filled with different concentrations of gadolinium solutions. The experiment was conducted on a 1.5T GE Signa system using a standard 3D fast gradient echo. A 192*192*28 matrix size covered the entire phantom with an isotropic resolution of 0.5mm. Bandwidth was 62.50kHz, TR=50ms and flip angle 30° . 4 TE were used (3, 4, 5 and 6ms). The phantom was rotated in-plane 3 times by 120° increments. *RDF* maps were obtained by linear fitting the phase evolution as a function of echo time, and by subtracting the reference map. A dedicated registration algorithm based on best correlation search between intensity images (rotation/translation) was used to relocate the object with different orientations within the same frame (±0.5degree, ±0.5 voxel size).

Both k-space direct inversion and image space iterative method were implemented. For direct inversion, *RDF* was additionally masked in the noisy air region to reduce noise influence. As an explicit inversion is not feasible for the image space method, an *LSQR* algorithm was used. To assess the precision of the proposed techniques, mean susceptibility values inside the tubes were measured and compared to the expected values.

Results

The measured *RDF* (Fig. 2) shows conspicuous dipolar pattern surrounding the tubes with different gadolinium concentrations and noisy region outside water dish. Both direct inversion and iterative method gave satisfactory images (Fig. 3 and 4). Different Gd concentrations were clearly resolved and no streaking artifacts were observed. While both methods gave linear results ($R^2 \approx 1$), the direct inversion was fast and tended to underestimate susceptibility, and the iterative method took several minutes and provided a good measurement of susceptibility (slope close to 1).

Discussion and Conclusion

An inversion technique based on imaging from multiple orientations was proposed to quantify arbitrary susceptibility distribution. Consistent susceptibility distributions were obtained with a good contrast. While sampling from more directions may lead to better inversion performance (data not shown), a minimum of 3 orientations is required to remove any rank-deficiency, otherwise no meaningful map was obtained. Nevertheless, a small underestimation was obtained that, besides experimental errors in the phantom preparation, could come from the limited information available (the field is not probed everywhere), misregistration, discretization or partial volume errors. The observed bias may be explained by the fact that k-space center is forced to be zero as every offset solution is suitable.

This technique could be used on small objects that can be rotated inside the bore or on open magnets. In addition, it may provide a simple tool for molecular and cellular or small animal imaging.

References

[1] Haacke et al., MRI: 23:1-25, 2005. [2] Li et al., MRM: 51:1077-82, 2004. [3] Salomir R, et al. Concept Magnetic Res: 19B:26-34, 2003. [4] Conturo, T.E. MRM: 15: 430-37, 1990

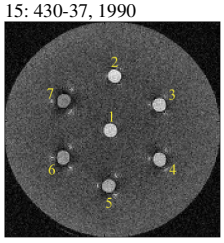

Fig.1. Phantom with Gd. Gd concentrations from #1 to #7 are 5mM to 35mM with 5mM increments.

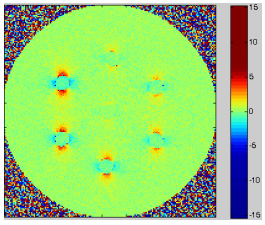

Fig. 2. One slice of RDF map. Unit in ppm

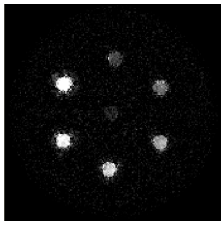

Fig. 3. Reconstruction from k-space direct inversion. Air region was set to zero for display purpose

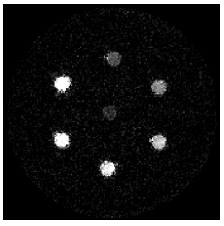

Fig. 4. Reconstruction from iterative method. Air region was set to zero for display purpose

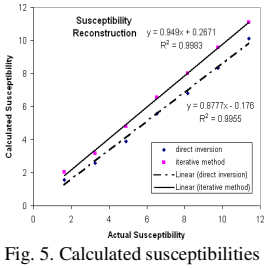

Fig. 5. Calculated susceptibilities versus actual susceptibilities.

ISMRM, 2008.

fMRI with 16 fold reduction using multibanded Multislice sampling

S. Moeller[1], E. Auerbach[1], P-F. van de Moortele[1], G. Adriany[1], and K. Ugurbil[1,2]

[1]Center for Magnetic Resonance Research, University of Minnesota, Minneapolis, MN, United States, [2]High-Field Magnetic Resonance Center, Max Planck Institute for Biological Cybernetics, Tubingen, Germany

Introduction: The use of partial parallel imaging (PPI) is usually associated with a loss in SNR which can be estimated as the product between *g*-factor and the square root of data reduction R, $g\sqrt{R}$ [1]. However, the SNR loss is limited to g only when the reduction of gradient encoding is performed with multi-band RF excitation pulses [2]. The use of multi-band excitation was initially proposed for spine imaging [3], and the aliasing was solved using a SENSE formulation (for Cartesian undersampling) for directly resolving aliased pixels. Later alternative methods that shift the aliasing between slices have been proposed [4, 5]. The use of multi-band pulses does increases average SAR [2] relative to single-band excitation, but for e.g. GE-EPI this is not a serious limitation – even at high and ultra-high fields. It has been shown that the use of PPI in GE-EPI fMRI is very favorable [6], since the statistical power is not reduced by $g\sqrt{R}$, in particular when the temporal noise is dominated by non-thermal noise. This paper investigates the use of multiband multislice GE-EPI to fMRI.

Background: With a 16-channel head coil at 7T, it has been shown that a reduction of 4 in the PE direction is associated with a mean g-factor of ~1.36 [6], providing a net SNR loss of 2.7. For multi-band acquisitions the corresponding g-factors have been evaluated for aliasing of coronal slices, and a separation of 35 mm is feasible with acceptable g-factors [mean 1.7, max 3]. Separating aliased slices is normally formulated in terms of a SENSE type reconstruction, but similar to the technique from e.g. [7], a GRAPPA type reconstruction can be used by reformatting the data. In addition to aliasing from the multi-band pulse, reduced sampling can be used in the phase encoding direction.

Methods: Imaging experiments were performed on a 7 Tesla magnet (Magnex Scientific, UK) equipped with a Siemens (Erlangen, Germany) TIM console, Siemens Avanto body gradient hardware, and an 8 kW RF amplifier. A 16-channel transmit/receive head coil [8] was used, with the RF power split evenly among the channels(Werlatone, Brewster, NY, USA). Multi-band excitation pulses were created by combining standard 5-lobe sinc pulses, with frequency offsets (phase ramps) applied to each constituent pulse to realize a spacing of 35 mm between bands. FLASH images (T_E/T_R = 3.4/210 ms, 10º FA, 1×1×5 mm resolution, 28 slices) were acquired for localization of anatomy. Functional images were acquired using GE-EPI (T_E/T_R = 25/1500 ms, 15º FA, 2×2×5 mm resolution, 28 slices, 100 repetitions). The readout direction was placed in the head-foot direction to facilitate full use of the 16 circumferentially placed elements for acceleration. Reconstructions using GRAPPA and SENSE were performed offline. Phase-correction lines were acquired prior to each acquisition, and a non-linear phase correction was applied. We have investigated the use of multi-band excitation for fMRI. Additionally, we have evaluated three different reconstruction approaches: 1D GRAPPA in the PE direction & 1D SENSE in the slice direction, 2D SENSE, and 1D GRAPPA in the PE direction & 1D GRAPPA in the slice direction.

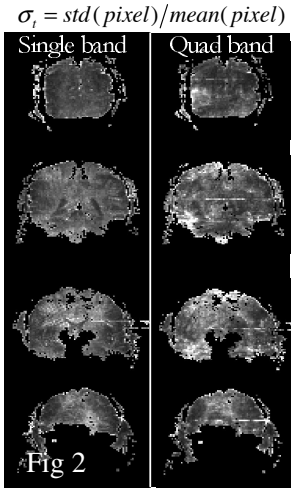

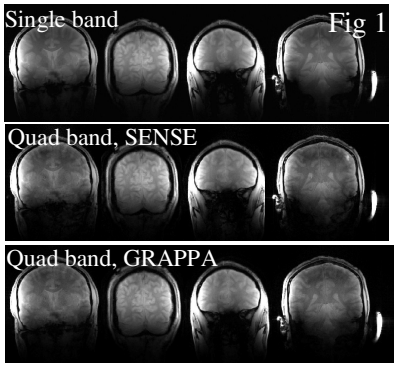

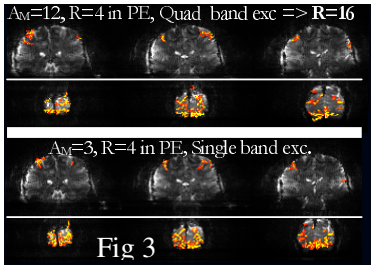

Results and Discussion: FLASH images acquired with single- and quad-band pulses, reconstructed with SENSE and GRAPPA respectively are shown in Figure 1. GE-EPI images have been evaluated for temporal stability, and normalized temporal noise maps indicate that the 1D GRAPPA in the PE direction and 1D GRAPPA in the slice direction provides the least noise amplification. These maps are shown for 4 slices in Figure 2. The temporal fluctuations with a quad-band excitation, relative to a single-band excitation, had only an average increase of 17%, with 7% of the voxels having an increase greater than 200%. This is consistent with non-uniform g-factor noise amplification. The increase in temporal fluctuations is offset by the gain in coverage justifying the use of multi-band excitation for fMRI studies. Functional activation maps from a 150 sec (30 s on/30s off) finger-tapping motor task with 8 Hz flashing-light visual stimulation are shown in Figure 3. The experiment was performed with and without the use of quad-band excitation; in both cases a total of 28 slices were acquired. Figure 3 shows activation maps for a subset of 6 coronal slices from both, covering the primary visual and motor areas. The quad-band acquisition exhibited lower t-scores overall, but similar robust, statistically-significant activation was observed for both acquisitions. The maximal aliasing was A_M=3 and A_M=12 for the single and quad band experiments respectively. We have found that multi-band excitation enables the extension of traditional multi-slice GE-EPI to cover the whole brain with reduced T_R. The combination of 2 orthogonal reduction directions and increased SNR from separate excitations, makes an effective undersampling factor of 16 feasible.

References: [1] Pruessmann, MRM 1999. [2] Kyriakos, NMR Biomed 2006. [3] Larkman, JMRI 2001. [4] Paley, MRM 2006. [5] Breuer, MRM 2006. [6] Moeller, MRM 2006, [7] Blaimer, MRM 2006. [8] Adriany, ISMRM2005, 2005.

Acknowledgement: BTRR - P41 RR008079, MIND Institute, P30 NS057091

ISMRM, 2009.

System for MRI guided Radiotherapy

J. Overweg[1], B. Raaymakers[2], J. Lagendijk[2], and K. Brown[3]
[1]Philips Research Europe, Hamburg, Germany, [2]University Medical Center Utrecht, Utrecht, Netherlands, [3]Elekta, Crawley, United Kingdom

INTRODUCTION

The adverse side effects of gamma-ray radiotherapy can be reduced significantly by combining the treatment system with a real-time imaging system, used to precisely steer the radiation beam. MRI is a particularly attractive imaging modality for this, due to its excellent soft tissue contrast. A project is underway to combine a cylindrical, closed bore high-field MRI system with a 6 MeV Linac radiation source (fig. 1) [1]. A key feature of the concept is that the Linac is located on the outside of the MRI magnet. The gamma beam passes through the scanner to reach the patient inside the bore. This abstract describes some of the modifications to the MRI scanner needed to make it compatible with this application.

METHODS/DESIGN

The MRI system has to be modified in several respects to allow co-operation of a linear accelerator:

1. The magnet, gradient coil and all other system components in the central plane of the system has to be transparent to gamma rays. A number of relatively thin cylindrical walls, such as those of the outer vacuum container of the cryostat, are acceptable but superconducting coil bundles or thick gradient coil conductors would cause too much (inhomogeneous) absorption and scatter. The required width of the radiation window is approximately 150 mm at the windings of the magnet and 200 mm at the inner boundary of the gradient coil, preferably extending over (nearly) the full circumference of the system.
2. The stray field of the magnet has to be minimized along the path of the electron beam in the Linac, in particular at the gun section. This low-field zone can also be used to locate other parts of the Linac (e.g. a microwave circulator) that would not work in a strong field.

The magnet requirements can be fulfilled by not too drastic modifications of a conventional 6+2 section 1.5 T MRI magnet design. By shifting the shield coils towards the midplane and slightly modifying the number of turns of these coils, it is possible to create a ring-shaped field-free zone at a radius of 1.7-2.0 meters (Fig. 2). It is not easily possible to extend the low field region inward to the outer surface of the cryostat. The multi-leaf collimator of the Linac must be made from non-magnetic materials. Sensors and actuators should either be made field-resistant or moved radially outward. In order to retain the magnet's homogeneity on increasing the central gap width, a pair of small additional coils can be added, adjacent to the central sections. Alternatively, the inner radius of the central coils may be increased. The field pattern generated by the optimized split magnet design does not differ significantly from that of a standard magnet. A complete split of the cryostat, with vacuum-insulated walls bounding the central gap, would require a separation of the central magnet sections by at least 250 mm. Such a large separation would involve a major redesign of the magnet, leading to significantly increased conductor cost. The heat load on the cryostat by the gamma beam passing through is negligible, so the cryogenic performance and quench stability of the magnet will not be impaired by the combined operation.

The gradient coil has a central gap free of windings of 200 mm width. The main and shield saddle coil conductors of the transverse channels are interconnected by conductors running over the flanges bounding the central gap [2,3]. The coil also features some radial interconnections at the outer flanges of the coil (Fig. 3). The coil was designed by modeling the stream function on a surface mesh, minimizing the coil's magnetic stored energy while satisfying constraints on primary gradient field in the imaging volume and field contributions of induced eddy-currents [4]. With inner/outer diameters 700/850 mm the stored energy of the transverse channels is 7.8 Joule at a gradient amplitude of 10mT/m. This is 40% more than of an un-split coil with the same size and performance. Although there are no shielding conductors in the gap area, the field contribution from eddy currents induced in the magnet bore tube is of the same order of magnitude as seen in un-gapped actively shielded gradient coils. Both coil halves were manufactured using standard materials and manufacturing technology. The two halves are rigidly linked by means of a 5 mm thick GRP cylinder located on the outer periphery of the coil. This interconnection is thin enough that gamma ray absorption/scatter is acceptable but provides sufficient stiffness to the cylinder to withstand the Lorentz forces acting on it.

The RF coils and RF shields located inside the gradient coil do not contain any thick copper parts or lumped components in the region where the gamma beam passes through.

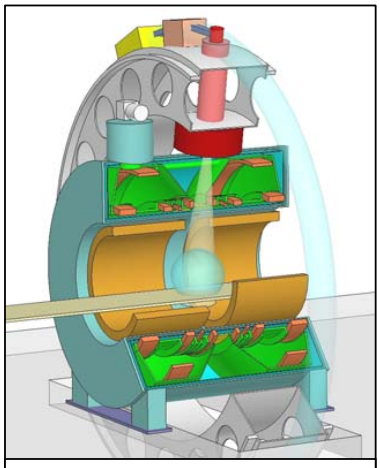

Fig. 1 combined MRI/Linac system

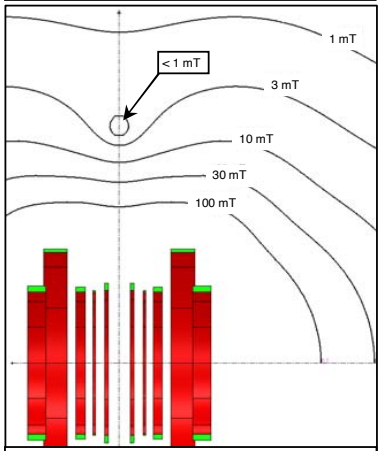

Fig. 2 low field region outside magnet

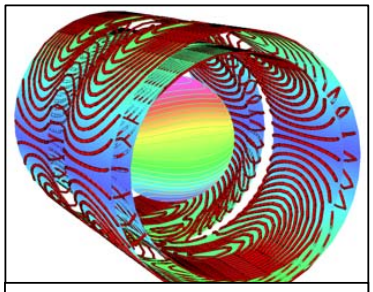

Fig. 3 split gradient coil

RESULTS

First tests of simultaneous operation of the modified MRI system and a Linac gamma source radiating through the magnet are expected to be carried out in the first half of 2009.

REFERENCES

[1] Lagendijk J.J.W. et al. Radiother Oncol (2007), doi:10.1016/j.radonc.2007.10.034
[2] Overweg, J.A. et al., WO patent 2008122899A1
[3] Green, D. et al., Proc Int. Soc. Mag. Reson. Med. 16 (2008) 352
[4] Peeren, G.N., J. Comput. Phys. 191 (2003) 305

ISMRM, 2009.

Accelerated MR parameter mapping using compressed sensing with model-based sparsifying transform

M. Doneva[1], J. Sénégas[2], P. Börnert[2], H. Eggers[2], and A. Mertins[1]
[1]University of Luebeck, Luebeck, Germany, [2]Philips Research Europe, Hamburg, Germany

Introduction: The estimation of MR parameters, such as the relaxation times T_1, T_2 and diffusion coefficients D, requires the acquisition of multiple images at different sequence parameters, which is often associated with long acquisition times. These data show a high temporal correlation, which can be described by a model facilitating accelerated image acquisition by data undersampling as shown in [1]. Recently, Compressed Sensing (CS) [2-4] was demonstrated for image reconstruction from incomplete k-space data. In this work we show that prior knowledge about the data can be used to define a model-based sparsity transform for improved CS reconstruction for MR parameter estimation.

Theory: CS relies on two premises: data compressibility and incoherent sampling. In Cartesian sampling, incoherence can be achieved by random undersampling in the phase encoding direction. An important factor for the quality of CS reconstruction is the appropriate choice of a sparsifying transform. Transforms like wavelets or finite differences can be applied to sparsify a large class of signals. In parameter estimation, there is a strong correlation of the data in the temporal dimension described by the underlying model. We use that knowledge to define a sparsifying transform by means of Principal Component Analysis (PCA). This is demonstrated here for T_2 mapping, in which the signal is described by an exponential decay. However, the method is not restricted to exponentials and could be generalized for other models.

The model-based sparsity transform is obtained as follows. Training data S are generated, based on a uniformly distributed set of T_2 times covering a broad range of values. The matrix S contains a set of exponentials corresponding to these T_2 in its columns. The matrix U, taken from the Singular Value Decomposition (SVD) of the correlation matrix $R = SS^H = U\Sigma U^H$ achieves a compact representation of the training set and also of any other exponentially decaying signal with T_2 in the given range. The reconstruction was performed by solving the unconstrained optimization problem:

$$\text{minimize } \|F_u x - y\|_2^2 + \lambda_1 \|U^H x\|_1$$

Here, x is the image, y is the measured data, F_u is the undersampled Fourier operator, and λ_l is a regularization parameter.

Methods: The proposed approach was demonstrated for multi-echo spin-echo measurements for T_2 mapping in the brain (32 echoes, 5ms echo spacing, FOV 250mm, 6mm slice thickness, 256×256 matrix, TR = 1000ms), measured on 1.5T clinical scanner (Achieva, Philips Healthcare). For each echo, different sets of 64 phase encodings (reduction factor of 4) were randomly chosen with higher sampling density near the k-space origin. The data were CS reconstructed with the PCA-based operator as a sparsifying transform in the temporal dimension, using nonlinear conjugate gradient. The training set used to determine U contained 1000 exponentials with T_2 values uniformly distributed in the range 10-300ms. CS reconstruction with wavelet (Daubechies 4) and total variation (TV) constraints [4] was performed on the same data for reference.

Results: Fig. 1 shows the images for several echo times obtained with CS reconstruction using wavelets and TV, and CS with the model-based PCA transform, obtained after 150 iterations. The model-based approach achieves better reconstruction with a normalized RMS error of 0.0529 compared to the wavelet-TV CS with an error of 0.3764. Fig. 2 shows the original and CS reconstructed signal for several pixels with different T_2 for the 32 echoes. The model-based reconstruction reduces the aliasing and results in a signal very close to the original for all T2 times. Fig. 3 shows the T_2 map, obtained from the model-based CS reconstruction, which is very similar to the full dataset map.

Conclusions: We have demonstrated a Compressed Sensing reconstruction with a new, model-based sparsifying transform that exploits the underlying model in MRI parameter estimation to efficiently reconstruct an image series for T2 mapping from reduced number of phase encoding lines. The model-based PCA sparsity transform allows improved reconstruction from reduced amount of data compared to the wavelet-TV CS reconstruction. The ability to reduce scan time could be of interest for a number of applications.

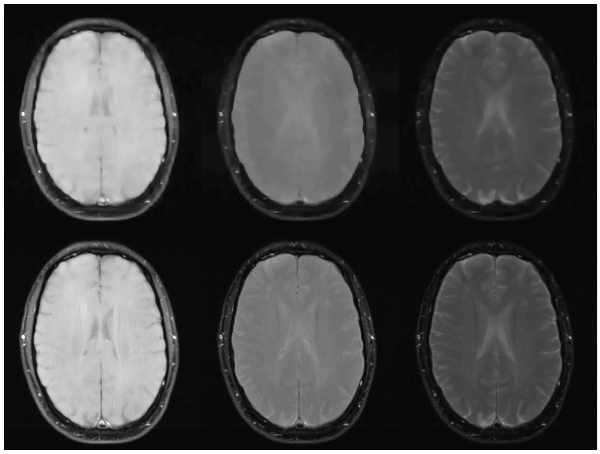

Fig. 1. Reconstruction from undersampled data with reduction factor of 4. Top: CS reconstruction with wavelet and TV constraints Bottom: CS reconstruction with model-based PCA transform

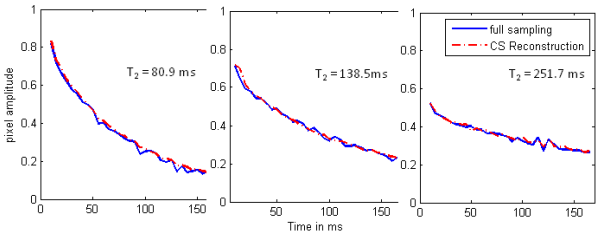

Fig. 2. Temporal signal evolution for different T_2. CS reconstruction of undersampled data with reduction factor 4 leads to very good approximation of the fully sampled data

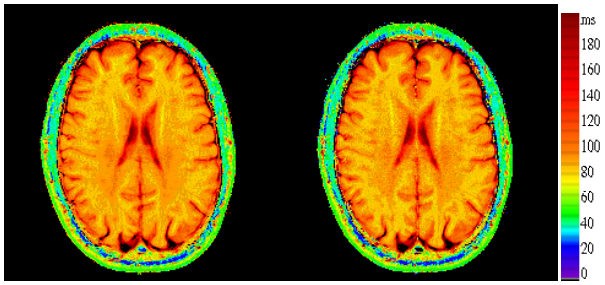

Fig. 3. T2 maps. Left is shown the map obtained from the CS reconstruction with acceleration factor 4, right is the map from the full dataset. The normalized RMS error is 0.0539

References: [1] Senegas J et al Proc ISMRM 2008 p.1394;
[2] Candes E et al, IEEE Tran Info Theo 2006, 52: 489-509;
[3] Donoho D, IEEE Tran Info Theo 2006, 52: 1289-1306;
[4] Lustig M et al, MRM 2007, 58: 1182-1195

ISMRM, 2010.

B_1 mapping by Bloch-Siegert shift

L. Sacolick[1], F. Wiesinger[1], W. Dixon[2], I. Hancu[2], and M. W. Vogel[1]
[1]GE Global Research, Garching b. Munchen, Germany, [2]GE Global Research, Niskayuna, NY, United States

INTRODUCTION: A wide variety of B_1 mapping methods have been developed to date, but problems with scanning time, accuracy over only a narrow range of B_1, and sensitivity to B_0, T_1, and TR have prevented any one method from becoming dominant. Here, we present a novel fast B_1 mapping method based on the Bloch-Siegert shift. The term Bloch-Siegert shift describes the effect where spin precession frequency shifts in response to an off-resonance RF pulse (1). This frequency shift is proportional to the square of the B_1^+ field and to the frequency difference between the RF pulse and resonance. An RF pulse at off-resonance frequency ω_{RF} is placed into an imaging sequence following excitation. The Bloch-Siegert frequency shift ω_{BS} results in a B_1^2-dependent phase φ_{BS}. Two images are acquired: with the pulse applied symmetrically around the water resonance at +/- ω_{RF}. The phase difference between these two images is proportional to the square of the B_1 magnitude.

A.

$$\varphi_{BS} = \int_0^T \omega_{BS}(t) = \int_0^T \frac{(\gamma B_1(t))^2}{2\omega_{RF}(t)}$$

$$\varphi_{BS} = B_{1,peak}{}^2 \int_0^T \frac{(\gamma B_{1,normalized}(t))^2}{2\omega_{RF}(t)} dt \;, \qquad \varphi_{BS} = B_{1,peak}{}^2 \times K_{BS}$$

B.

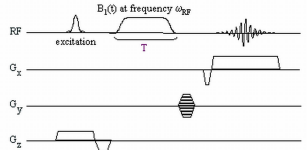

C.

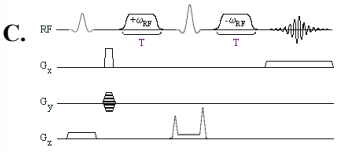

D.

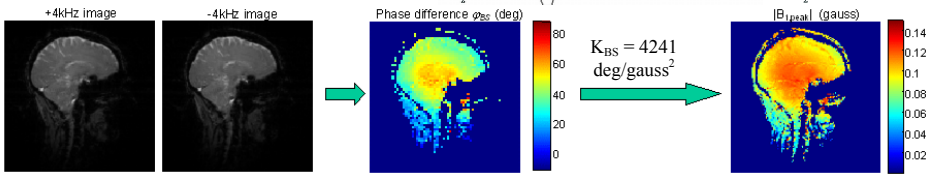

Figure 1a. Bloch Siegert phase shift φ_{BS} for an RF pulse with normalized pulse shape $B_{1,\,normalized}$, and maximum $B_{1,peak}$, length T, and off-resonance frequency ω_{RF}. K_{BS} is the relationship between Bloch-Siegert phase shift and B_1 magnitude (degrees/gauss^2) **b.** Gradient and **c.** Spin echo sequence incorporating off-resonance Fermi RF pulses. **d.** Two images acquired with the sequence in **b.**, the phase difference, and calculated B_1 map. 128x128 resolution, 0.5cm slice thickness, TE/TR = 13/50 msec, scan time = 12.8 sec.

METHODS/RESULTS: The gradient and spin echo Bloch-Siegert sequences were implemented on 3T GE Signa Excite HD and DVMR systems. The off-resonant RF pulses used in these sequences were 8 msec (grad. echo) and 6 msec (spin echo) Fermi pulses, 4 kHz off-resonance. These pulses produce Bloch-Siegert phase shifts of 4241 (8 msec) and 3180 (6 msec) degrees/gauss^2. Two images were acquired with the Fermi pulses having opposite +/- ω_{RF} frequencies. The phase difference is then 2x the Bloch-Siegert phase shift, removing transmit, B_0, receive, and other sequence related phases that are the same in both scans.

A. Double angle 13 min.

B. Bloch-Siegert 25.6 sec

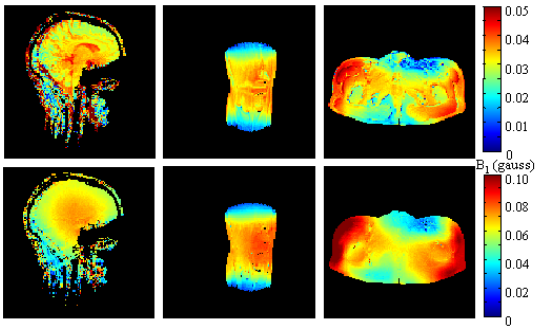

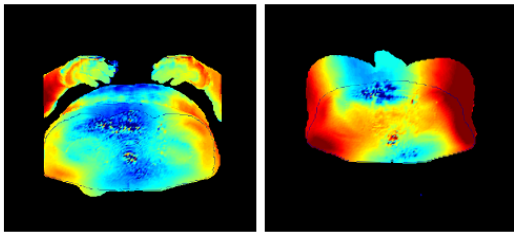

C. Multi-slice, spin echo Bloch-Siegert B1 maps, lower abdomen, 3T body Tx coil.

Figure 2a. 128x128 double angle B_1 maps, 45°, 90° average flip angles over the slice, TR = 3 sec. **b.** 128x128 Bloch-Siegert maps (brain, knee: grad. echo sequence, TE/TR = 12/100 ms), abdomen: spin echo sequence, TE/TR = 28/100 msec. **c.** 3D rendering of two multi-slice lower abdomen B_1 maps from a whole-body Tx coil. Slices were acquired interleaved, with 128x128 in plane resolution, 30 slices (left) and 18 slices (right) of 1 cm thickness. TE = 28, TR = 3sec (left), 1.8 sec (right).

DISCUSSION: The Bloch-Siegert shift has long been overlooked outside of decoupling in spectroscopy (2) and multi-band RF pulse design (3). The B_1-dependence of this effect gives a fast, accurate, robust, and conceptually straightforward method for measuring B_1 maps. This B_1 mapping method is insensitive to T_1, TR, chemical shift, inhomogeneous B_0, and magnetization transfer. While the Bloch-Siegert shift is B_0 dependent, the phase difference between two scans with the RF applied symmetrically around resonance is independent of B_0, for B_0 offset << ω_{RF}. The Fermi pulse used here is often used similarly in magnetization transfer sequences. Magnetization transfer is observed as a magnitude difference between scans with and without the pulse. No phase contribution from magnetization transfer is evident in the in-vivo scans or in milk phantom experiments or has been reported. The 8 msec, 4 kHz pulse demonstrated here provides easily detectable phase shift over a wide range of B_1. The upper bound on B_1 amplitude that can be detected is 0.21 gauss- where phase wrapping begins for this particular RF pulse. At the lower bound, the Bloch-Siegert phase shift falls within the level of image phase noise. In the in-vivo experiments shown here we found a lower limit of approximately 0.03 gauss. However, the lower bound depends on the SNR of the base images and the phase stability of the transmit RF chain. Scan time in most cases is limited at low field by a tradeoff between scan acceleration and image SNR, and at high field (≥ 3 Tesla) by clinical SAR limits. All B_1 mapping demonstrated here falls well within the SAR limits as measured by conventional power monitoring. This method is compatible with EPI, spiral readout, or other imaging acceleration methods, which can additionally reduce scan time and/or SAR.

ACKNOWLEDGEMENTS AND REFERENCES: This research was supported by NIH grant 5R01EB005307-02

1. Siegert A, Bloch F. Phys Rev 1940;57:522-527. **2.** Vierkotter SA. J Magn Reson 1996;118:84-93. **3.** Steffen M, Vandersypen LMK, Chuang IL J Magn Reson 2000;146:369-374.

ISMRM, 2010.

Blipped CAIPIRHINA for simultaneous multi-slice EPI with reduced g-factor penalty

K. Setsompop[1,2], B. A. Gagoski[3], J. Polimeni[1,2], T. Witzel[1], V. J. Wedeen[1,2], and L. L. Wald[1,2]
[1]Radiology, A. A. Martinos Center for Biomedical Imaging, Massachusetts General Hospital, Charlestown, MA, United States,
[2]Harvard Medical School, Boston, MA, United States, [3]EECS, Massachusetts Institute of Technology, Cambridge, MA, United States

Introduction: The acquisition of simultaneous slices using EPI with either wideband methods (1-3) or parallel imaging multi-slice methods (4-7) has the potential to increase the temporal sampling rate of fMRI or the number of diffusion directions obtained per unit time in diffusion imaging (DI). Unlike conventional parallel imaging with EPI, which does not significantly increase the number of slices per second, simultaneous multi-slice methods do not undersample the data, instead they unalias simultaneously excited slices. This leads to an R fold reduction of time and an SNR reduction given simply by the g factor, rather than g√R. Thus, the same data is acquired in significantly shorter time, providing the potential to increase the SNR per unit time for high-resolution whole-head fMRI, or DI where TRs >> T_1 are generally required.

With parallel imaging methods, the unaliasing problem is difficult in closely spaced simultaneously excited slices, resulting in high g factors. Unfortunately, the traditional CAIPIRINHA scheme (5) for introducing a FOV/2 shift in the phase direction of alternate slices utilizes RF phase cycling of the excitation pulses and is not applicable to single-shot EPI. A method to use a set of constant slice-select gradient blips (G_z) simultaneously with the EPI phase encoding blips (G_y) to achieve CAIPIRINHA-style shifts (6) introduces undesirable "tilted voxel" problem similar to the wideband methods (1-3). Here, we introduce a blipped CAIPIRINHA scheme where the blips in the slice-select gradient are cycled in amplitude to impart a phase on each line of kspace that produces the modulation needed for the CAIPIRINHA shift scheme, but does not accrue significant phase over the EPI readout, eliminating "tilted voxel" problem and its spatial resolution filtering effect.

Theory: In ref. (6), to achieve an inter-slice image shift in the PE direction, gradient blips in the slice-select direction (G_z) are introduced simultaneously with the conventional EPI G_y blips. The addition of constant amplitude G_z blips results in a rotation of the phase encode direction into the slice direction rendering slice and PE directions non-orthogonal (the gradients vectors add), resulting in the undesirable pixel tilt artifact. The tilt-effect produces a voxel blurring artifact (6), where the phase shifts introduced to the k_y lines cause through-plane dephasing within each excited slice. An initial G_z pre-wind gradient refocuses the dephasing at the center of kspace, but the dephasing accumulates for high k_y lines introducing a blurring filter in the y direction of the image. To address this, we developed a novel G_z blipping scheme that provide an inter-slice image shift (e.g. of FOV/2), but does not produce a phase accumulation in k_y, and thus eliminates the through-plane dephasing and associated blurring/voxel tilt artifact. In this strategy, subsequent G_z blips act to un-wind the through-plane dephasing of the previous blip as well as producing the required phase shift between the adjacent slices needed for the inter-slice image shift. By replacing a constant phase accumulation across k_y with back-and-forth jumps, we eliminate the accumulation of through-plane dephasing and its associated blurring filter. The scheme is shown schematically in Fig. 1 for FOV/2 and FOV/3 image shift cases.

FIGURE 1

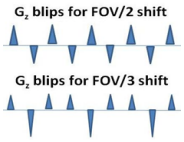

Methods: We tested our blipped CAIPIRINHA acquisition on two volunteers using Siemens TIM Trio scanner with a 32-channel head array coil. A slice-GRAPPA reconstruction technique similar to that used in ref. (7-8) was implemented. The method was demonstrated with **(i)** 3 simultaneously acquired multi-slice SE-EPI acquisition which utilizes R=3 slice-Grappa, and **(ii)** 6 simultaneously acquired multi-slice GE-EPI acquisition which utilizes R=3 slice-Grappa together with Simultaneous Image Refocusing (SIR) (9) to achieve an extra R=2 multiplicative acceleration factor. Additionally, R=2 inplane-Grappa was employed to counteract lengthen echo-spacing due to SIR (~50% longer esp was required) providing a net 50% improvement in susceptibility induced distortion. Because of the inplane acceleration, an intra-slice image shift of ¼ rather than ½ FOV was used to prevent voxels with same in-plane (x,y) locations of adjacent image slices from overlapping. The parameters for the two acquisitions were: **(i)** slice-Grappa inter-slice gap = 40mm; FOV = 208x208x120 mm; Partial Fourier = ¾; matrix = 104x78x20; resol= 2mm iso; TR/TE = 3s/96 ms; for **(ii)** slice-Grappa inter-slice gap = 40mm; FOV = 208x208x120 mm; Partial Fourier = ¾; matrix = 104x52x10; resol= 2mm iso; TR/TE = 0.77s/33 ms; Flip angle = 51.8° (Ernst angle). All RF pulses were designed using SLR algorithm (10) with frequency modulation and summation to produce simultaneous multi-slice excitation. Verse (11) was applied to reduce SAR while keeping each RF pulse to within 4 ms.

FIGURE 2

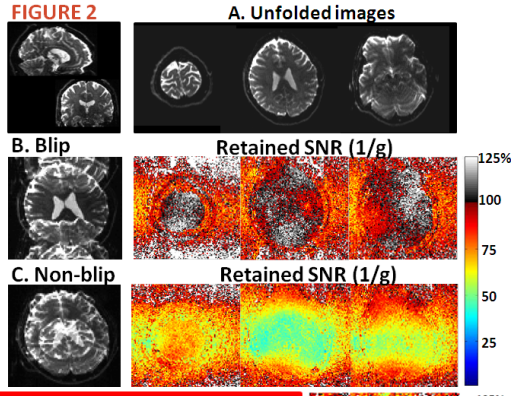

Results: Fig. 2 shows results of 3x slice-Grappa SE-EPI: Fig. 2A. left: coronal and sagittal views of the unaliased 3D stack of slices, right: an unaliased slice group. Fig.2B. left: blipped-CAIPIRINHA folded images, right: Retained SNR (1/g) calculated via pseudo-multiple replica method(12) Fig.2C. left: non-blip folded images, right: Retained SNR. The retained SNR from blipped CAIPIRINHA acquisition is substantially higher than the non-blip case. In some regions the retained SNR is greater than unity indicating some noise cancellation in the reconstruction process as previously demonstrated in low R inplane Grappa acquisition (13). Note that in order to perform the same inter-slice image shift acquisition using method in ref. (6), voxel tilt would cause signal from one voxel to smear over ~3.5 voxels. Fig. 3 shows results from 6x multi-slice GE-EPI, left: coronal and sagital views of unfolded slice stack, center: a set of 6 unaliased slices from 2 SIR multislice groups (red and yellow), right: Retained SNR of blipped and non-blip acquisitions from a representative slice. Again blipped CAIPIRINHA acquisition results in substantially higher retained SNR. Noted that as a result of short TR, low contrast between gray and white matter can be observed.

FIGURE 3

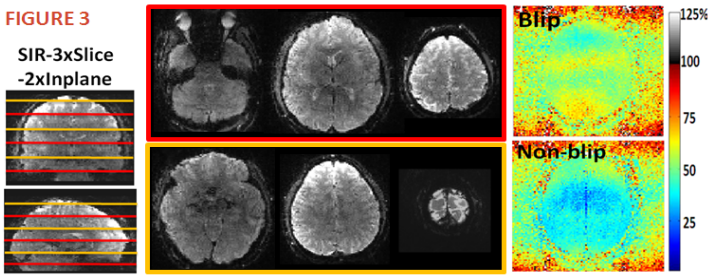

Conclusion: In this work we introduced blipped CAIPIRIHINA EPI acquisition and demonstrated its associated low g-factor penalty and 3x acceleration of the slices per second of acquisition. Given the benefit achieved, this method could help enable fast high-resolution whole-head fMRI and HARDI/Q-ball and DSI style diffusion imaging acquisitions.

Support: NCRR P41RR14075 and NIBIB R01EB006847. **References: 1.** Weaver JB. et al, MRM 1988:8:275. **2**. Paley MN. et al, MRI 2006:24:557. **3.** Wu EL. et al, ISMRM 2009p.2678. **4.** Larkman DJ. et al, JMRI 2001:13:313 **5.** Breuer FA. et al, MRM 2005:53:684 **6.** Nunes RG. et al ISMRM 2006p.293 **7.** Moeller S. et al, ISMRM 2009p.1544 **8.** Blaimer M. et al, JMRI 2006:24:444 **9.** Feinberg DA. et al, MRM 2002:48:1 **10.** Pauly J. et al IEEE TMI 1991:10:53 **11.** Conolly SM. et al, JMR1988:78:440 **12.** Robson PM et al, MRM 2008:60:895 **13.** Polimeni JR. et al, ISMRM 2008p.1286

ISMRM, 2012.

MR Fingerprinting (MRF): a Novel Quantitative Approach to MRI

Dan Ma[1], Vikas Gulani[1,2], Nicole Seiberlich[1], Jeffrey Duerk[1], Mark Griswold[1,2]

[1]Department of Biomedical Engineering, Case Western Reserve University, Cleveland, OH, United States; [2]Dept. of Radiology, University Hospitals of Cleveland and Case Western Reserve University, Cleveland, OH, United States

Introduction: Conventional MRI attempts to generate pure "weighted" images that depend only on one or two parameters of interest. Much of the MR pulse sequence development at ISMRM is directed at generating a constant signal level over time to acquire a weighted image as quickly as possible, It is well known that this is difficult to achieve (e.g. pure T2 weighting in a fast spin echo sequence) and is limited in the presence of motion or phase changes. Here we propose a new concept for MRI based on recent advances in Compressed Sensing which we call MR fingerprinting (MRF). MRF is based on a change in perspective: instead of providing a constant signal level over time, we use a sequence that attempts to generate a different signal evolution for each tissue with different relaxation parameters. We then use a pattern recognition based reconstruction to derive quantitative estimates of the underlying relaxation parameters. This is analogous to matching fingerprints (MR signal) to a database (dictionary), and by extension retrieving a host of additional personal information such as identity, address, phone number, etc. (T_1, T_2, diffusion coefficient, etc.). Here we show that these estimates are independent of B_0 and B_1 variations using a sequence with very low SAR. We initially demonstrate this MRF concept by generating quantitative MR images in a clinically feasible time.

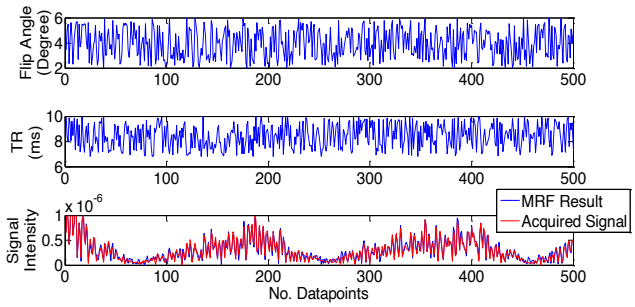

Figure 1: Flip angle (a) and TR (b) were randomly varied from one TR to the next in random the TrueFISP sequence. An example time course (c) from reconstructed images shows oscillating signal evolution.

Methods: The goal of an MRF sequence is to provide a unique signal evolution in each tissue type by varying the basic sequence parameters. One example of this type of sequence is to use random TrueFISP, which was chosen for the first demonstration of MRF due to extensive existing knowledge about the evolution of the TrueFISP signal evolution. Figure 1 demonstrates a sequence where 500 data points for each pixel were acquired. For each data point, we randomly varied the TR (range: 6.8-10ms) and flip angle (range: 2-6 degrees), and an inversion pulse was added every 200 TRs. Using such a sequence, the signal varies wildly from one TR to the next (see Figure 1C). To determine the relaxation parameters, pattern recognition of the signal time course is completed using Orthogonal Matching Pursuit (OMP) [2,3], which can resolve the correct signal and obtain multiple parameters simultaneously. OMP involves building a dictionary that contains all expected signal evolutions based on the designed sequence parameters (TR, TE, flip angle, B_0) by using a Bloch simulation. This method was evaluated in a phantom study, where 10 cylindrical phantoms constructed with varying concentrations of $GdCl_3$ (Aldrich) and agarose (Sigma) to yield T_1 and T_2 values ranging from 67 to 1700 ms and 30 to 300 ms, respectively. The phantom was scanned using a 1.5T Siemens Espree (Siemens Medical Solutions). Around 15000 characteristic parameter sets (T_1 from 50 to 2000 ms, T_2 from 20 to 400 ms, and off-resonance from -40 to 40Hz) were used to simulate possible signal time courses using Bloch simulations of the spin evolution, and were stored in the dictionary. OMP was then used to select the elements from the dictionary that best represent the acquired signals, yielding the corresponding T_1, T_2, proton density, and off-resonance maps. As a gold standard comparison, a standard spin-echo sequence was performed to quantify T_1 and T_2 separately (T_1 quantification: 13 TRs ranging from 50 to 5000ms, TE = 8.5 ms; T_2 quantification: 15 echoes with TE=15-225 ms with 15ms increment). T_1 and T_2 maps of the spin echo sequences were obtained by fitting the time courses on a pixel-by-pixel basis using a three-parameter nonlinear least squares fit. Square regions of interest (ROI) were chosen from each of the cylinders and the mean MRF values were compared with the values from the standard measurements.

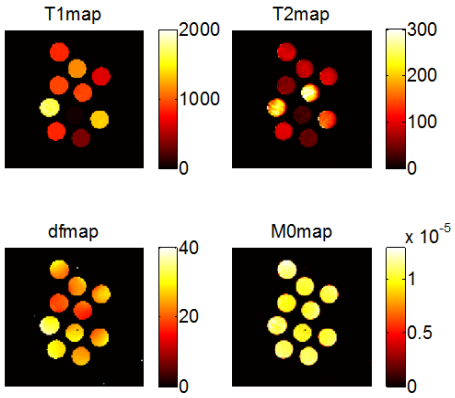

Figure 2: T_1, T_2, M_0 and off-resonance maps generated from the MRF phantom experiment.

Results and Discussion: Figure 1C shows the signal time course from one pixel of the reconstructed MRF series and its corresponding dictionary match. The T_1, T_2, M_0, and off-resonance maps generated from MRF are shown in Figure 2. In Figure 3, T_1 and T_2 values obtained from MRF methods are compared with the values from standard spin-echo sequence measurements. As can be seen in Figure 3, Both T_1 and T_2 values are in good agreement with the traditional measurement even though the MRF sequence used only very low flip angles. In addition, we simultaneously obtained a map of off-resonance. The concept of MRF uses a completely different approach to experimental design in MRI, where the sequence design is optimized not towards yielding individual images with various weightings, but rather towards generating unique signal timecourses that can be matched with a compressed sensing approach to the corresponding parameters to yield the underlying tissue parameters. The method is robust as long as the designed sequence provides unique signal evolution curves for different tissues, and the chosen reconstruction method is able to generate the required parameter maps. In addition, because a single preparation is avoided, the equilibrium signal state is never reached, which allows for continuous scanning to assess measure multiple parameters at once. Also, since the reconstruction is probabilistic, MRF may be less susceptible to motion. The presented sequence design is but one of the infinite sequence designs possible and to be explored, that could yield quantification of any of the various parameters which affect the MR signal without errors due to B_0, B_1 and other effects.

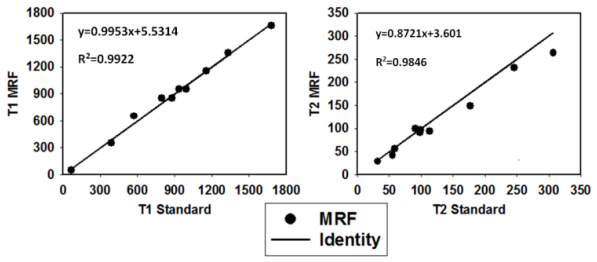

Figure 3: T_1 (left) and T_2 (right) values from MRF are compared with values measured from standard spin-echo sequences

Reference: [1] Schmitt et al. Magn Reson Med. 2004, 51:661-667; [2] Tropp J el al. IEEE Trans Inf Theory 2007, 53:4655-4666. [3]Doneva et al. Magn Reson Med. 2010, 64:1114-1120. **Acknowledgements**: The authors would like to acknowledge funding from Siemens Medical Solutions and NIH grants 1RO1HL094557, 5K99EB011527, and 1KL2RR024990.

ISMRM, 2016.

Learning a Variational Model for Compressed Sensing MRI Reconstruction

Kerstin Hammernik[1], Florian Knoll[2], Daniel K Sodickson[2], and Thomas Pock[1,3]

[1]*Institute for Computer Graphics and Vision, Graz University of Technology, Graz, Austria,* [2]*Center for Biomedical Imaging and Center for Advanced Imaging Innovation and Research (CAI2R), Department of Radiology, NYU School of Medicine, New York, NY, United States,* [3]*Safety & Security Department, AIT Austrian Institute of Technology GmbH, Vienna, Austria*

Synopsis

Compressed sensing techniques allow MRI reconstruction from undersampled k-space data. However, most reconstruction methods suffer from high computational costs, selection of adequate regularizers and are limited to low acceleration factors for non-dynamic 2D imaging protocols. In this work, we propose a novel and efficient approach to overcome these limitations by learning a sequence of optimal regularizers that removes typical undersampling artifacts while keeping important details in the imaged objects and preserving the natural appearance of anatomical structures. We test our approach on patient data and show that we achieve superior results than commonly used reconstruction methods.

Purpose

In this work, we propose a novel Compressed Sensing (CS) MRI reconstruction method by learning optimal regularization that can effectively avoid undersampling artifacts while preserving the natural image appearance. Existing methods are based on simple regularizers such as Total Variation (TV)[1] or sparsity in the wavelet domain[2]. However, these handcrafted models are too simple to capture the characteristic structure of complex anatomies. Additionally, application of CS in clinical practice is still challenging due to expensive computations, parameter selection and limited applicability to 2D Cartesian protocols. To overcome these limitations, we propose to learn a set of filters and corresponding penalty functions of a variational model.

Methods

Following the recent work of Chen et al.[3] for image denoising, we propose to generate a sequence $\{u_t\},\ t = 0 \dots T-1$ of reconstructed images by minimizing a sequence of simple quadratic energies $\{E_t\}$:

$$u_{t+1} = \arg\min_u E_t(u, \theta_t) = \langle s_t(u_t), u - u_t \rangle + \frac{1}{2} \|u - u_t\|_2^2,$$

where $s_t(u_t)$ are learned functions defined below. The minimizers of the quadratic energies form a gradient step with gradients $s_t(u_t)$:

$$u_{t+1} = u_t - s_t(u_t).$$

Inspired by classical CS regularization approaches, we define functions $s_t(u_t)$ as gradients of following variational model:

$$E_t(u) = \frac{\lambda_t}{2} \|Au - f\|_2^2 + \sum_{i=1}^{N_k} \phi_{i,t}\left(k_{i,t} * u\right).$$

The first term enforces data consistency to measured k-space data f using the linear forward sampling operator A that implements pointwise multiplications with coil sensitivity profiles and FFTs. The second (regularization) term convolves the image u with N_k filter kernels $k_{i,t}$ and then applies differentiable penalty functions $\phi_{i,t}$. The influence of both terms is controlled via a regularization parameter λ_t. We now define $s_t(u_t)$ as gradients of the variational model:

$$s_t(u_t) = \nabla E_t(u)|_{u=u_t} = \lambda_t A^T\left(Au_t - f\right) + \sum_{i=1}^{N_k} \bar{k}_{i,t} * \phi_{i,t}'\left(k_{i,t} * u_t\right),$$

where A^T denotes the backward operator, which performs inverse FFTs and combination of coil images, $\bar{k}_{i,t}$ denote the filter kernels $k_{i,t}$ rotated by 180° and $\phi_{i,t}'$ are the first derivatives of the penalty functions $\phi_{i,t}$. Hence, we can interpret our method as a specialized convolutional neural network performing a fixed number of learned gradient descent steps starting from an initial solution u_0 (see Figure 1).

To learn the parameters of our network, we minimize the following loss function over a set of S training images:

$$\min_{\theta} \frac{1}{2} \sum_{s=1}^{S} \|u_{T,s}(\theta) - g_s\|_2^2,$$

where $u_{T,s}$ denotes the output of the network after T steps and g_s denotes the reference images. The vector $\theta = \{\lambda_t, k_{i,t}, \phi_{i,t},\, i = 1...N_k,\, t = 0...T-1\}$ holds all unknown parameters of our network. After training, the learned network can be efficiently applied to new k-space data as it performs only T steps of simple operations.

Experimental Setup

We scanned 10 knee patients on a clinical 3T system (Siemens Magnetom Skyra) using a 15-channel knee coil. The study was approved by the IRB and written informed consent was obtained. A coronal PD weighted Cartesian 2D TSE sequence was used with following sequence parameters: TR=2690ms, TE=33ms, matrix size 320×320, $0.4 \times 0.4\mathrm{mm}^2$, 34 $3\mathrm{mm}$ slices, acceleration factor $R = 2$. This clinical protocol delivers reference images without aliasing by using conventional parallel imaging (PI) reconstruction from the scanner vendor.

We conduct the training on a subset of 40 images from 4 different patients. This data is additionally undersampled for an acceleration factor of $R = 6$. The training and parameter initialization of the network is performed similar to Chen et al.[3]. We train 48 filters of size 7×7, their corresponding penalty functions and the regularization parameter λ_t for each of $T = 15$ steps.

Results

For evaluation, we apply the learned network to $R = 2$ and $R = 6$ data from 6 patients that was not used for training, covering a wide range of anatomical knee structures. We compare our method to zero-filled initialization, iterative CG-SENSE[4] and TV-regularized combined CS and PI[1] reconstructions. Figure 2 depicts the results for $R = 2$. As expected, all methods perform equally well. When the acceleration factor is pushed to $R = 6$, CG-SENSE and TV cannot remove all artifacts as illustrated in Figure 3. This is also depicted in Figure 4 that shows several reconstructed slices of a single patient. Although TV-regularized reconstructions still include residual aliasing at this level of regularization they already look unnatural due to the piecewise-constance assumption and small low-contrast features vanish. Our learning approach leads to artifact-free and natural results with a reconstruction time of 1.78 seconds for a single 320×320 slice.

Discussion and Conclusion

In this work, we presented a novel approach for CS reconstruction to learn optimal regularization of a variational model. This allows for highly efficient reconstruction of new k-space data in terms of both image quality and runtime. The impact of our algorithm is visible for high acceleration factors where we achieve visually superior results compared to CG-SENSE and TV. While conventional CS reconstruction methods use handcrafted regularizers that are not particularly suitable for 2D Cartesian sequences which are still essential in clinical practice, our learned network enables the separation of characteristic undersampling artifacts from the natural appearance of MR images.

Acknowledgements

We acknowledge grant support from the Austrian Science Fund (FWF) under the START project BIVISION, No. Y729, NIH P41 EB017183 and R01 EB000447.

References

1. Block K T, Uecker M, and Frahm J. Undersampled radial MRI with multiple coils. Iterative image reconstruction using a total variation constraint. Magn Reson Med, 2007, 57, 1086-1098.

2. Lustig M, Donoho D, and Pauly J M. Sparse MRI: The application of compressed sensing for rapid MR imaging. Magn Reson Med, 2007, 58, 1182-1195.

3. Chen Y, Yu W, and Pock T. On learning optimized reaction diffusion processes for effective image restoration. IEEE Conference on Computer Vision and Pattern Recognition (CVPR), 2015, 5261-5269.

4. Pruessmann K P, Weiger M, Boernert P, and Boesiger P. Advances in sensitivity encoding with arbitrary k-space trajectories. Magn Reson Med, 2001, 46, 638-651.

Figures

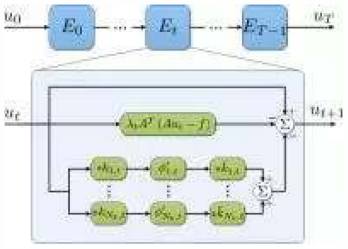

Figure 1: Network structure. To reconstruct an image u_T, we propagate the image $u_0 = A^T f$ through T steps of the network which correspond to quadratic energies E_t (blue). During a training process, optimal filter kernels $k_{i,t}$, penalty functions $\phi_{i,t}$ and the regularization parameter λ_t (green) are learned for each update step.

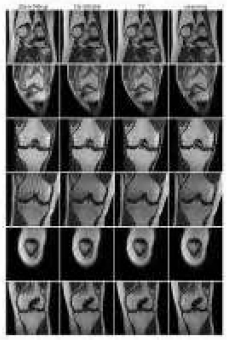

Figure 2: Comparison of reconstruction methods for $R = 2$. Each slice is taken from a different patient. Since this is the same acceleration as in the conventional clinical protocols, all methods perform equally well, as expected.

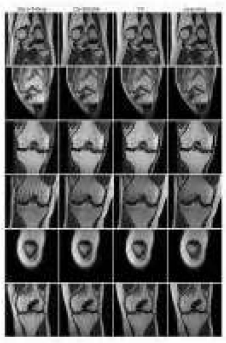

Figure 3: Comparison of reconstruction methods for acceleration factor $R = 6$. Each slice is taken from a different patient. CG-SENSE and TV show residual aliasing artifacts and the TV result exhibits the characteristic blocky appearance. In comparison, image quality of our learning approach is similar to the $R = 2$ case.

Figure 4: Comparison of reconstruction methods for acceleration factor $R = 6$ for different anatomical knee structures of a single patient. CG-SENSE and TV contain residual aliasing and detectability of low-contrast features is reduced for TV. Our learning method shows artifact-free reconstructions.

ISMRM, 2016.

Exploiting deep convolutional neural network for fast magnetic resonance imaging

Shanshan Wang[1], Zhenghang Su[1,2], Leslie Ying[3], Xi Peng[1], and Dong Liang[1]

[1]*Shenzhen Institutes of Advanced Technologies, Shenzhen, China, People's Republic of,* [2]*School of Information Technologies, Guangdong University of Technology, Guangzhou, China, People's Republic of,* [3]*Department of Biomedical Engineering and Department of Electrical Engineering, The State University of New York, Buffalo, NY, United States*

Synopsis

This paper proposes a deep learning based approach for accelerating MR imaging. With the utilization of a large number of existing high-quality MR images, we train an off-line convolutional neural network (CNN) to identify the mapping relationship between MR images obtained from zero-filled and fully-sampled k-space data. Then the trained CNN is employed to predict an image from undersampled data, which is used as the reference in solving an online constrained imaging problem. Results on in vivo datasets show that the proposed approach is capable of restoring fine details and presents great potential for efficient and effective MR imaging.

INTRODUCTION

Signal processing based MR image reconstruction from reduced samples have played an essential role in accelerating MR scans in recent years [1,2]. A foundation for the success of these methods is the utilization of prior information on MR images, such as sparsity [3], low-rank [4], manifold fitting [5] and generalized series [6]. Nevertheless, despite all the achievements obtained by the existing methods, the exploited priors are still quite limited to the knowledge about the target image or very few reference images. Based on the observation that the anatomic structure of the same organ/tissue between different people are quite similar, we try to learn an off-line prior model to aid online fast imaging by taking advantage of the enormous images acquired each day. Specifically an off-line convolutional neural network is trained to describe the end-to-end mapping between zero-filled and fully-sampled MR images. The network is not only capable of restoring the details and fine structures of the MR images, but is also compatible with online constrained reconstruction model for efficient and effective MR imaging.

THEORY AND METHOD

The proposed method consists of two main parts: the off-line training and online imaging. In the off-line settings, consider T pre-acquired MR images u_t reconstructed from fully-sampled data, we design and train an L-layer convolutional neural network $\begin{cases} C_0 = x \\ C_l = \sigma(W_l * C_{l-1} + b_l), l \in 1, 2, \ldots, L-1 \\ C_L = \sigma(W_L * C_{L-1} + b_L) \end{cases}$ by minimizing $\mathrm{argmin}_\Theta \left\{ \frac{1}{2\mathrm{T}} \sum_{t=1}^{T} \|C(z_t;\Theta) - u_t\|_2^2 \right\}$ where z_t is the zero-filled MR image generated as the direct inverse of the undersampled data and C means the end-to-end mapping function with hidden parameters $\Theta = \{(W_1, b_1), \ldots, (W_l, b_l), \ldots, (W_L, b_L)\}$. Once we learned the hidden parameters $\hat{\Theta}$ from the pre-acquired datasets, we can reconstruct MR images by considering the online constrained optimization problem $\mathrm{argmin}_u \left\{ \|C(F^H f; \hat{\Theta}) - u\|_2^2 + \lambda \|f - PFu\|_2^2 \right\}$, where f means the undersampled data, P is the undersampling diagonal mask, F denotes the full Fourier encoding matrix normalized as $F^H F = I$ and H represents the Hermitian transpose operation. As we can see, the first term in the cost function promotes the similarity between the network prediction and the target image, and the second term enforces the data fidelity in k-space. As a simple least squares problem, we can give an analytical solution $Fu(k_x, k_y) = \begin{cases} S(k_x, k_y) & , \text{ if } (k_x, k_y) \notin \Omega \\ \frac{S(k_x,k_y) + \lambda S_0(k_x,k_y)}{1+\lambda} & , \text{ if } (k_x, k_y) \in \Omega \end{cases}$, where $S_0(k_x, k_y) = FF_M^H f$, $S(k_x, k_y) = FC(F^H f; \hat{\Theta})$; and Ω means the sampled locations.

EXPERIMENT

The training data consists of over 500 fully sampled MR brain images we collected from a 3T scanner (SIEMENS MAGNETOM Trio). Informed consent was obtained from the imaging subject in compliance with the Institutional Review Board policy. Undersampled measurements were retrospectively obtained using the 2D Poisson disk sampling mask. To increase the robustness of the proposed approach, we further generate more samples by separating the image pairs into 33×33 sub-image pairs, among which 90% are used for updating

the network dataset and the rest 10% for validating the training process. We use three layers of convolution for the network. The first layer consists of 64 filters with the size of 9×9, while the second layer has 32 filters of size 5×5 and the last layer is one filter with size 5×5 . The filter weights of each layers are initialized by random values from a Gaussian distribution with zero mean and standard deviation 0.001. The bias is all initialized as 0. The training takes about three days, on a workstation equipped with 128G memory and a processor of 16 cores (Intel Xeon (R) CPU E5-2680 V3 @2.5GHz).We evaluated the proposed approach on a fully sampled transversal brain dataset which was acquired on a 3T scanner (SIEMENS MAGNETOM Trio) with a 12-channel head coil by T2-weighted turbo spin-echo (TSE) sequence (TE=91.0ms, TR=5000ms, FOV=20×20 cm, matrix=256×270, slice thickness=3mm) and a sagittal brain image which was acquired on a GE 3T scanner (GE Healthcare, Waukesha, WI) with a 32-channel head coil by 3D T1-weighted spoiled gradient echo sequence (TE=minimum full, TR=7.5ms, FOV=24 24cm, matrix=256×256, slice thickness=1.7mm). Undersampled measurements were retrospectively obtained using the 2D Poisson disk sampling mask.

RESULTS AND DISCUSSION

The first row of Fig. 1 presents the test results of the proposed method on the transversal brain at the acceleration of 5. It can be observed that the zero-filled images are very blurry with some details lost. After being put through the network, some fine structures and textures are restored and the noise is reduced. Further combining with the online constrained imaging model, we can reconstruct an image quite close to the reference one. For a close-up look, the zoom-in results have also been presented for the transversal brain. We also have presented the sagittal brain reconstruction at the acceleration of 3. According to Fig. 1k, we can see the difference image is noise-like and consists of only the contour information. There are no obvious details and structures lost. It demonstrates that the proposed network is capable of restoring the details and fine structures which are discarded in the zero-filled MR image. Furthermore, although the off-line training takes roughly three days, under the same GPU configurations, it takes far less than 1 second for each online MR reconstruction case.

CONCLUSION

We propose to design and train an off-line convolutional neural network to aid online fast MR imaging. Experimental results on two in vivo datasets have shown that the network is capable of restoring fine structures and details while removing noise, and have demonstrated great potential for efficient and effective MR imaging.

Acknowledgements

Grant support : China NSFC 61471350, the Natural Science Foundation of Guangdong 2015A020214019, 2015A030310314, the Basic Research Program of Shenzhen JCYJ20140610152828678, JCYJ20140610151856736 and the youth innovation project of SIAT under Y4G0071001 and US NIH R21EB020861 for Ying.

References

[1] Caballero J et al. ISMRM, p1560, 2014. [2] Ravishankar S et al., IEEE TMI 30(5):1028-1041, 2011. [3] Liu Q et al. IEEE TIP, 22(12):4652-4663, 2013. [4] Haldar J et al. ISBI, 857-860, 2011. [5] Shi C et al. ISBI, 901–904, 2015. [6] Liang Z et al. IEEE TMI, 22(8): 1026–1030, 2003.

Figures

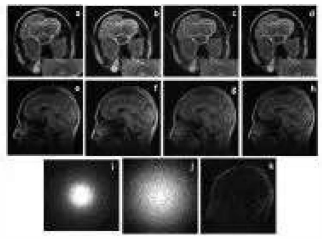

Fig. 1 Visual quality comparison: (a) and (e) Reference images, (b) and (f) Zero-filled MR images, (c) and (g) Image prediction from the network, (d) and (h) Reconstructed results, (i) the 5x-acceleration mask for the transversal brain, (j) the 3x-acceleration mask for the sagittal brain, and k) reconstruction error of the sagittal brain

ISMRM, 2016.

Learning-based Reconstruction using Artificial Neural Network for Higher Acceleration

Kinam Kwon[1], Dongchan Kim[1], Hyunseok Seo[1], Jaejin Cho[1], Byungjai Kim[1], and HyunWook Park[1]

[1]*KAIST, Daejeon, Korea, Republic of*

Synopsis

A long imaging time has been regarded as a major drawback of MRI, and many techniques have been proposed to overcome this problem. Parallel imaging (PI) and compressed sensing (CS) techniques utilize different sensitivity of multi-channel RF coils and sparsity of signal in a certain domain to remove aliasing artifacts that are generated by subsampling, respectively. In this study, an artificial neural networks (ANN) are applied to MR reconstruction to reduce imaging time, and it is shown that the ANN model has a potential to be comparable to PI and CS.

Introduction

A long imaging time has been regarded as a major drawback of MRI, and many techniques have been proposed to overcome this problem. Parallel imaging (PI) and compressed sensing (CS) techniques utilize different sensitivity of multi-channel RF coils and sparsity of signal in a certain domain to remove aliasing artifacts that are generated by subsampling, respectively. In addition, PI and CS have been combined to accelerate the imaging time.[1] Meanwhile, artificial neural networks (ANN) have been applied to various fields, which has shown superior performance by utilizing deep architecture and tremendous database. In this study, an ANN model is applied to MR reconstruction to reduce imaging time, and it is shown that the ANN model has a potential to be comparable to PI and CS.

Materials and Methods

Three typical brain imaging sequences such as T1-weighted (T1w), T2-weighted (T2w) and fluid attenuated inversion recovery (FLAIR) are commonly used. For the three imaging sequences, brain MR images from 12 subjects were obtained using Siemens Magnetom Verio 3T system. Three sequences were fully sampled with 216 phase encoding lines and 384 readout points, from which the experimental data were retrospectively subsampled to make database. Fig 1 shows schematic diagram of the proposed method. Learning and reconstruction are processed line by line because the aliasing artifacts from subsampling spread in phase encoding direction. The aliased image was divided into real and imaginary parts, and used as inputs of the ANN model. Sensitivity maps were estimated from 16 center lines by using ESPIRiT algorithm.[2] Likewise, the sensitivity maps are divided into real and imaginary parts and used as inputs of the model. Desired outputs were computed as follows:

$$I_d(x,y) = |\sum_{c=1}^{N} S_c^*(x,y) I_c(x,y)|$$

, where I_d, I_c, and S_c are the desired combined image, the obtained image from channel c, and the sensitivity map of channel c, respectively. In this study, four channels were used to reconstruct the images. Two models were learned according to two subsampling patterns that have the same acceleration factor (R=2.6024). The proposed method was implemented using the well-known Caffe package.[3] The ANN model was (216×16)-(864)-(864)-(864)-(216×1), where input matrix with 216×16 consists of real and imaginary lines of the aliased images and sensitivity maps for 4 channels, output matrix with 216×1 consists of aforementioned combined line, and three hidden layers have 864 nodes. Nodes between neighboring layers were fully connected, and rectified linear unit was used as an activation function. Total 648 image slices with 216×384 were used for learning the model, and aliased images that were not used for learning were used for test of the model to show the performance of the learned model. Various hyper parameters like learning rate, the number of iterations, and weight initialization were heuristically selected.

Results

As shown in Figs. 2 and 3, reconstructed T2w images from the proposed method and SPIRiT[1] are displayed when the regular subsampling pattern of Fig 2c and the irregular subsampling pattern of Fig 3c are used, respectively. In Fig 2d-e, visible errors from the proposed method are mainly in edges, but those of SPIRiT are distributed in center region that have small difference between coil sensitivity maps. Both methods can remove aliasing artifacts, but the reconstructed image from the proposed method looks more blurry whereas that from

SPIRiT looks noisy. In Fig 3b, the reconstructed image from SPIRiT becomes worse when the irregular subsampling pattern is used, even though the number of sampling lines is same as Fig 2b. However, the proposed method can remove aliasing artifacts and suppress noise well in Fig 3a.

Discussion and Conclusion

The proposed method utilizes the ANN model. The database for learning the model has profound information that can be used to remove aliasing artifacts and noise of the subsampled images. The ANN method utilizes coil sensitivity maps and subsampled data as input data, and learns relation between subsampled and full-sampled data as prior information. Learning-based method depends on database, and it is difficult to collect many datasets sufficiently. In this study, although relatively small datasets are used, the proposed method can reconstruct the subsampled images well. The proposed method needs only a feedforward operation of ANN, which requires very short reconstruction time. The proposed method can reconstruct an image from irregularly subsampled k-space data, which could be useful in dynamic imaging that is differently sampled according to motion phases. For further works, more database would be used to improve the performance, and to correct MR artifacts like EPI ghost artifact.

Acknowledgements

This research was partly supported by the Brain Research Program through the National Research Foundation of Korea (NRF) funded by the Ministry of Science, ICT & Future Planning (2014M3C7033999) and Korea Health Technology R&D Project through the Korea Health Industry Development Institute (KHIDI), funded by the Ministry of Health & Welfare, Republic of Korea (grant number : HI14C1135).

References

1. Lustig M, el al. SPIRiT: Iterative Self-consistent Parallel Imaging Reconstruction From Arbitrary k-space. MRM. 2010;64:457-471. 2. Uecker M, el al. ESPIRiT- An Eigenvalue Approach to Autocalibrating Parallel MRI: Where SENSE Meets GRAPPA. MRM. 2014;71:990-1001. 3. Jia Y, el al. Caffe: Convolutional Architecture for Fast Feature Embedding. In: ACM Multimedia. 2014;675-678.

Figures

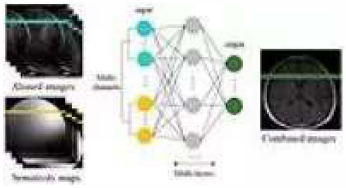

Schematic diagram of the proposed method. Colored circles mean each voxel of input and output images, and gray circles mean nodes of hidden layers in ANN.

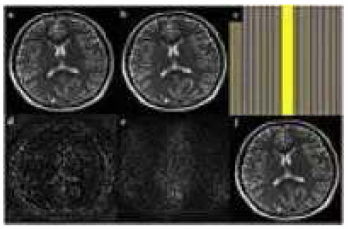

Reconstructed T2w images from (a) the proposed method and (b) SPIRiT, (c) regular subsampling pattern (R=2.6024), corresponding difference images (d) and (e) between the reference full sampled image and the reconstructed images from (a) the proposed method and (b) SPIRiT, and (f) reference full-sampled image.

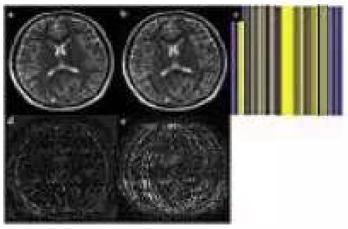

Reconstructed T2w images from (a) the proposed method and (b) SPIRiT, (c) irregular subsampling pattern (R=2.6024), corresponding difference images (d) and (e) between the reference full sampled image and the reconstructed images from (a) the proposed method and (b) SPIRiT.